UNIVERSITY OF GLASGOW

Wavelengths in bioconvection patterns

by

Reem Abdullah J Almahmud

A thesis submitted in partial fulfillment for the
degree of Doctor of Philosophy

in the
College of Science and Engineering
School of Mathematics and Statistics

December 2016

Declaration of Authorship

I, Reem Abdullah J Almahmud, declare that this thesis titled, 'Wavelengths in bioconvection patterns' and the work presented in it are my own. I confirm that:

- This work was done wholly or mainly while in candidature for a research degree at this University.
- Where any part of this thesis has previously been submitted for a degree or any other qualification at this University or any other institution, this has been clearly stated.
- Where I have consulted the published work of others, this is always clearly attributed.
- Where I have quoted from the work of others, the source is always given. With the exception of such quotations, this thesis is entirely my own work.
- I have acknowledged all main sources of help.
- Where the thesis is based on work done by myself jointly with others, I have made clear exactly what was done by others and what I have contributed myself.

Signed: _____

Date: _____

Abstract

Unicellular bottom-heavy swimming microorganisms are usually denser than the fluid in which they swim. In shallow suspensions, the bottom heaviness results in a gravitational torque that orients the cells to swim vertically upwards in the absence of fluid flow. Swimming cells thus accumulate at the upper surface to form a concentrated layer of cells. When the cell concentration is high enough, the layer overturns to form bioconvection patterns. Thin concentrated plumes of cells descend rapidly and cells return to the upper surface in wide, slowly moving upwelling plumes. When there is fluid flow, a second viscous torque is exerted on the swimming cells. The balance between the local shear flow viscous and the gravitational torques determines the cells' swimming direction, (gyrotaxis). In this thesis, the wavelengths of bioconvection patterns are studied experimentally as well as theoretically as follow;

First, in aquasystem it is rare to find one species lives individually and when they swim they can form complex patterns. Thus, a protocol for controlled experiments to mix two species of swimming algal cells of *C. rienhardtii* and *C. augustae* is systematically described and images of bioconvection patterns are captured. A method for analysing images using wavelets and extracting the local dominant wavelength in spatially varying patterns is developed. The variation of the patterns as a function of the total concentration and the relative concentration between two species is analysed.

Second, the linear stability theory of bioconvection for a suspension of two mixed species is studied. The dispersion relationship is computed using Fourier modes in order to calculate the neutral curves as a function of wavenumbers k and m. The neutral curves are plotted to compare the instability onset of the suspension of the two mixed species with the instability onset of each species individually. This study could help us to understand which species contributes the most in the process of pattern formation.

Finally, predicting the most unstable wavelength was studied previously around a steady state equilibrium situation. Since assuming steady state equilibrium contradicts with reality, the pattern formation in a layer of finite depth of an evolving basic state is studied using the nonnormal modes approach. The nonnormal modes procedure identifies the optimal initial perturbation that can be obtained for a given time t as well as a given set of parameters and wavenumber k. Then, we measure the size of the optimal perturbation as it grows with time considering a range of wavenumbers for the same set of parameters to be able to extract the most unstable wavelength.

Acknowledgements

First, I would like to thank Allah for everything in my life.

I would like to thank my family for their love and support.

I would like to thank the Saudi government for their financial support.

I would like to thank my supervisors Prof. Nicholas Hill and Prof. Martin Bees for their support and guidance throughout this thesis.

Contents

List of Figures

List of Tables

Abbreviations

E. coli	*Escherichia coli*
C. augustae	*Chlamydomonas augustae*
C. reinhardtii	*Chlamydomonas reinhardtii*

Symbols

Chapter 1

a	Cell length.
b	Cell width.
B	Gyrotactic orientation parameter.
C	Cell concentration.
C_0	Cells' geometric center.
$\mathbf{D}$	Cell diffusivity tensor.
D_H	The horizontal component of the cells' diffusivity tensor.
D_V	The vertical component of the cells' diffusivity tensor.
D_r	The rotational diffusion.
$\mathbf{E}$	The rate−of−strain tensor.
f	The probability density function.
$\mathbf{g}$	The acceleration due to gravity.
G	Cell's center of mass.
h	The distance between the geometric center C_0 and the center of mass G.
H	The suspension depth.
$\mathbf{J}$	The flux.
$\mathbf{k}$	The unit vector in the vertical direction.
k_c	Critical wavenumber.
L	The length scale.
$\mathbf{L}_T$	The total torque exerted on the cell.
$\mathbf{L}_g$	The gravitational torque.
$\mathbf{L}_v$	The viscous torque.
m	The cell mass.
n	Cell concentration (as Pedley and Kessler [86].)

p	The pressure
$\mathbf{p}$	The unit vector in the cell's swimming direction.
$\mathbf{q}, \mathbf{r}$	Two unit vectors perpendicular to each others and perpendicular to $\mathbf{p}$.
$\mathbf{P}, \mathbf{Y}, \mathbf{R}$	Tensors depending on the cell's surface geometry.
Re	Reynolds number.
R_c	Critical Rayleigh number.
$\mathbf{u}$	Fluid velocity.
$\mathbf{U}$	Fluid velocity.
v	Cell volume.
V_s	The mean of the cell swimming speed (as Pedley and Kessler [86]).
$\mathbf{V}_c$	The mean of the cell swimming velocity (as Pedley and Kessler [86]).
$\mathbf{V}_r$	The relative velocity (as Pedley and Kessler [86]).
α	The cell density relative to the fluid density.
α_0	Cell's eccentricity.
$\alpha_\parallel$	The resistance coefficient for a rotation about an axis parallel to $\mathbf{p}$.
$\alpha_\perp$	The resistance coefficient for a rotation about an axis perpendicular to $\mathbf{p}$.
μ	Fluid viscosity.
ρ	Fluid density.
τ	The direction correlation time.
ω	Fluid vorticity.
Ω	Cell's angular velocity.
$\Sigma^s, \Sigma^p, \Sigma^d,$	The stress tensors (as Pedley and Kessler [86]).

Chapter 2

a	The scale of the wavelet function.
$\mathbf{b}$	The location of the wavelet function.
C_a, C_r	The cell concentration of the green algae *C. augustae* and *C. reinhardtii*.
f	Continuous function.
$\mathbf{k} = (k_x, k_y)$	Wavevector.
$\mathbf{k}_\psi$	The wavevector associated with ψ_M.
$S_{a,\mathbf{b},\theta}$	The wavelet transform coeffecient.

θ	The direction of the wavelet basis function.
$\lambda_{I,\min}$, $\lambda_{I,\max}$	The minimum and the maximum values of the initial dominant wavelengths.
$\lambda_{\infty,\min}$, $\lambda_{\infty,\max}$	The minimum and the maximum values of the long term dominant wavelengths.
ψ	Wavelet function.
$\psi_{a,\mathbf{b},\theta}$	Wavelet basis functions.
ψ_M	The 2D complex Morlet wavelet.
ψ_0, $\psi_1, \cdot \psi_n, \cdot$	Orthonormal system of functions on $[0, 1)$.

Chapter 3

a_i	The relative swimming speed.
ax_i	The major cell axis.
bx_i	The minor cell axis.
B_i	The gyrotactic orientation parameter.
$\mathbf{D}_i$	The diffusivity tensor.
$\mathbf{D}_i^*$	The dimensionless diffusivity tensor.
$\mathbf{D}_{ir}$	The rotational diffusivity.
$\mathbf{E}$	The fluid rate−of−strain tensor.
f_i	The probability density function.
g	The acceleration due to gravity.
$\mathbf{k}$	The unit vector in the vertical direction.
k, l, m	The wavenumber in the x^*, y^*, z^* directions.
k_c	The critical wavenumber.
n_i	The cell concentration.
n_i^*	The dimensionless cell concentration.
n_i'	The perturbed cell concentration.
$\mathbf{p}_i$	The cell swimming direction.
P_e	The excess pressure above hydrostatic.
P_e^*	The dimensionless excess pressure above hydrostatic.
P_e'	The perturbed excess pressure above hydrostatic.
Re	The cell Reynolds number.
$\mathbf{U}$	The suspension velocity.
$\mathbf{U}^*$	The dimensionless suspension velocity.
$\mathbf{U}'$	The perturbed suspension velocity.

v_i	The cell volume.
V_{is}	The cell swimming speed.
$\mathbf{V}_{ic}$	The cell swimming velocity.
$\mathbf{V}_{ir}$	The cell relative velocity.
α_i	The density fluctuation.
α_{0i}	The cell eccentricity.
γ_i	The relative cell concentration.
ζ_i	The relative cell volume.
η_i	The relative gyrotactic.
λ_i	The deterministic stochastic parameter.
λ_c^d	The dimensional critical wavelength.
μ	The fluid viscosity.
ρ	The fluid density.
ρ_i	The cell density.
ϱ_i	The relative density difference.
σ	The time growth rate.
τ_i	The direction correlation time.
$\boldsymbol{\omega}$	The fluid vorticity.

Chapter 4

B	The gyrotactic orientation parameter.
$\mathbf{D}$	The diffusivity tensor.
$\mathbf{e}$	The rate−of−strain tensor.
E	The perturbed energy.
G	The dimensionless gyrotactic orientation parameter.
GE	The gained energy.
$\mathbf{k}$	The unit vector in the vertical direction.
$k_{\max}$	The dimensionless most unstable wavenumber.
L	Lagrange function.
n	The cell concentration.
n^*	The dimensionless cell concentration.
$\tilde{n}_p$	The perturbed cell concentration.

$\tilde{n}_p^j$	The perturbed cell concentration in the adjoint field.
$\mathbf{p}$	The cell swimming direction.
$\mathbf{p}$, $\mathbf{q}$, $\mathbf{r}$	Set of right handed unit vectors.
P_e	The excess pressure above the hydrostatic.
P_e^*	The dimensionless excess pressure above the hydrostatic.
$\tilde{P}_{ep}$	The perturbed excess pressure above the hydrostatic.
$\tilde{P}_{ep}^j$	The perturbed excess pressure above the hydrostatic in the adjoint field.
$\mathbf{U}$	The fluid velocity.
$\mathbf{U}^*$	The dimensionless suspension velocity.
$(\tilde{u}_p, \tilde{v}_p, \tilde{w}_p)$	The perturbed suspension velocity.
$\left(\tilde{u}_p^j, \tilde{v}_p^j, \tilde{w}_p^j\right)$	The perturbed suspension velocity in the adjoint field.
Ra	Rayleigh number.
s	The normalization factor.
S_c	Schmidt number.
v	The cell volume.
V_s	The cell swimming speed.
α_0	The cell eccentricity.
$\tilde{\theta}_p$	The perturbed swimming direction.
$\tilde{\theta}_p^j$	The perturbed swimming direction in the adjoint field.
$\lambda_{\max}$	The dimensionless most unstable wavelength.
$\lambda_{\max}^d$	The dimensional most unstable wavelength.
μ	The fluid viscosity.
ρ	The fluid density.
$\boldsymbol{\omega}$	The fluid vorticity.

To my family...

Chapter 1

Introduction

1.1 General background

Single-celled microorganisms are one of the oldest organisms on the planet Earth. Their formation started approximately 3−4 billion years ago (Schopf [101]). Although they constitute the vast majority of the Earth's biomass, they can not be seen by naked eye since their length scale is very small, typically of order 1 μm for bacteria and 10 μm for algae (Koch and Subramanian [66]). Over millions of years, enormous and diverse ranges of microorganisms have evolved, from the bacteria found in the stomachs of human beings to algae found in rivers and oceans around the world (Falkowski et al. [31], Ma et al. [77] and Finlay et al. [33]). Such microorganisms have a significant impact on ecosystems. For example, the algae in the sea photosynthesize by using CO_2 from the air as a source of carbon, and as consequence of this process they release O_2 (Arnold and Murray [5]). So, any variation in their population can have a long term affect on weather conditions. Moreover, it can cause an extinction of large species since microorganisms are at the bottom of the food chain (Compant et al. [23] and Fuhrman [35]).

Many microorganisms can be exploited in the industrial field. In the pharmaceutical industry, for instance, bacteria are widely used in manufacturing antibiotics (Drautz et al. [28]). They are also used to produce fertilizer (Popova et al. [92]) and in sewage

treatment (Horan [54]). However, a rapidly developing application of these microbic creatures is in the energy industry. Some species of microorganisms, such as *Entromorpha intestinalis*, can be used as a potential source of biofuel (Gnansounou and Roman [40], Jeong and Park [60] and Mendoza et al. [80]) that could be a substitution to fossil fuels.

Since 1675 when Anton van Leeuwenhoek first discovered them (Porter [93]), researchers have investigated their swimming behaviour and this investigation still continuous (Jeffery [58], Kessler [62], Lavandowsky et al. [71], Kessler and Hill [65], Hill and Häder [49], Silflow and Lefebvre [104], Berg and Anderson [15] and Lauga and Powers [70]). Such studies can provide the means to explore how they feed, mate and die, control light for photosynthesis, reproduce themselves to form colonies, and regulate their lives and consequently the lives of the larger creatures that feed on them.

Studies of the swimming behaviour of microorganisms have advanced significantly over the last 15 years. For example, E. Lauga [69] reviewed the biomechanics of bacterial motility. He highlighted the impacts of fluid dynamics relevant to the swimming of bacteria in viscous environments. He focused on the mechanics of single−celled behaviour with the aim of understanding the way the a single bacterium exploits the surrounding fluid together with the physical constraints the bacterium is subject to. One of his results is that the low Reynolds number hydrodynamics is at the heart of the fundamental physics of bacteria swimming. Also, although surrounding fluids play important roles in the life of bacteria, hydrodynamic forces on flagellar filaments and cell bodies also have to be balanced with forces associated with bending and twisting elasticity. DeLillo et al. [74] demonstrates that the fluid acceleration reorients gyrotactic plankton, triggering small−scale clustering by studying the distribution of the phytoplankton *Chlamydomonas augustae* within a rotating tank. Their results are that, when fluid acceleration and gravitational acceleration are on the same order, distribution of gyrotactic swimmers becomes significantly more clustered. However, it is noted that the turbulence in natural environments is too weak to reach the needed regime. Furthermore, it was highlighted that nonhomogeneous conditions, such as solid boundaries, may drive fluid acceleration induced cell clustering in the bottom boundary layer as a result

of the generation of intense vorticity at moderate Reynolds numbers. Son et al. [105] studied and analysed the motility adaptations of microorganisms. They investigated the motility strategies such as swimming in moving fluids, swimming in dense microbial suspensions, the hydrodynamic signature of microorganisms using dynamic microbial imaging. Also, they looked into the utilization of microfluids for the control of microbial environments. They concluded that the ability of microfluids to combine the dynamic imaging and environmental control has provided a tremendous way of capturing the fundamental nature of various dynamic microbial processes. Furthermore, it is noted that due to the temporally and spatially explicit understanding of microbial processes provided by dynamic imaging and microfluids, a vast range of microbial processes will benefit from the application of these approaches. All these studies and other similar studies in the field of the physics of microfluids have set the basic rules as well as open the gate to investigate other microbial natural phenomena such as bioconvection due to swimming behaviour of the microorganisms in response to some stimuli. In this thesis, to to study aspects of bioconvection, we shall take as the starting point, the assumption that all cells swim with a constant speed and that their orientation is given by a probability density function that satisfy a Fokker−Plank equation.

In a realistic aquasystem one usually finds two or more species living together. When at least one non−mutually buoyant species swims in a biased directions and accumulates, they can form intricate patterns, named bioconvection, that are influenced by many factors such as the relative concentration of each species and the total concentration of the suspension, light and suspension depth. One aim of this thesis is to illustrate the patterns observed in mixed species suspensions of swimming microorganisms experimentally, to demonstrate the effect of the relative and the total concentration in a layer of finite depth, as well as theoretically, to investigate the onset of bioconvection in uniform suspensions. This could help us to understand which species has the stronger impact on the process of pattern formation. This is the first time there has been a quantitative experimental study of mixed species rather than one species forming patterns, which this is the biological reality in the wild. This is supported by the first theoretical studies. Since earlier studies assumed that the system had reached the steady state before the instability arose which is considered unrealistic situation, a further aim is to investigate

the linear stability in a layer of a finite depth around a time−evolving basic state using the nonnormal modes. This enables us to estimate the most unstable wavenumber of bioconvection patterns. The non−normal analysis allows us to explore the mechanism underlying the initial growth of patterns on an evolving concentration profile.

1.2 Orientation mechanisms and cell swimming behaviours

In this thesis, the focus will be on swimming single-celled microorganisms. In general, microorganisms can be categorized into two major divisions: prokaryotic cells, such as *cynobacteria*, which are characterized by the lack of a nucleus; and eukaryotic cells which have a cell nucleus, such as the green algae. Microorganisms evolve with time according to geological, geochemical and biological processes (Falkowski et al. [31] and Ma et al. [77]). Recent genetic research has established a detailed phylogenetic tree. Hence, a precise classification based on genetic evidence can be specified (Woese [117]).

Motile microorganisms generally swim in a particular direction as a response to stimuli (Pedley and Kessler [87]). According to Henderson's dictionary, these directed motions are called taxes (Eleanor [30]). Many bacteria, such as *Escherichia coli* (Lauga and Powers [70]), swim towards regions of higher nutrient concentration to feed themselves. This response to chemical gradient is called chemotaxis (Berg and Brown [16] and Kundra et al. [67]). Some bacteria may respond to oxygen gradients by either swimming towards the upper surface if they use oxygen to metabolise fats and sugars, such as *Bacillus subtilis* (Czirók et al. [25]) or swimming down away from the upper surface if the oxygen causes damage to the cell. The bacterium is classified in this case as aerotactic (Taylor [108], Hong et al. [53] and Okon et al. [83]).

Some microorganisms respond to the light by either swimming towards light or away from it, such as *Euglena*, *Chlamydomonas* and several other species (Wager [114] and Kessler [64]). This is called phototaxis (Foster et al. [34], Forward [95] and Jékely et al. [59]). Many motile green algae are phototactic. They photosynthesize by converting light to energy and produce O_2 as a byproduct. Some microorganisms, such as *Chlamydomonas* (Pedley and Kessler [87]), have an asymmetric mass distribution. In other

words, the center−of −mass is displaced from the center−of−buoyancy. Hence, in the absence of other effects, the cells swim vertically upwards on average as a negative response to the acceleration due to gravity **g**. This mechanism is called gravitaxis (Häder et al. [46], Lebert et al. [73] and Roberts and Deacon [98]). However, in the presence of the fluid flow, a balance between the gravitational and the viscous torques biases the cell swimming direction. This mechanism is called gyrotaxis.

Despite the fact that different species of microorganisms have different cell morphology and swimming styles, they swim by waving, undulating and rotating their appendages at low Reynolds number, $Re \ll 1$. This is due to the fact that the product of their body length scale, L, together with their swimming velocity, $\mathbf{V}$, is small compared to the ambient kinematic fluid viscosity, $\nu = \frac{\mu}{\rho}$, where ρ and μ are the fluid density and viscosity, respectively (Purcell [94]). The Reynolds number, $Re = \frac{L\mathbf{V}\rho}{\mu}$, is a measure of the ratio between the inertial forces and the viscous forces. So, when this number is small, the viscous forces dominate. In this case, the dimensionless Navier−Stokes equation will be

$$-\nabla p + \nabla^2 \mathbf{u} = 0 \quad . \tag{1.1}$$

Equation (1.1) states that time has no effect and the reversible fluid flow prevents cells from moving if a reciprocal swimming is used. Because they retrace their trajectory when they reverse their motion. Hence, microorganisms have developed a range of non-symmetric swimming strokes in order to move in a desired direction (Purcell [94]). For example, the *paramecium* have an ellipsoidal cell body, of length $100 - 200$ μm, covered by thousands of approximately 10 μm long cilia that are uniformly distributed over the cell. These cilia beat at a frequency of 20 Hz to produce a sinusoidal wave of the cilia tips that help the cells swim with a speed of up to 500 μms^{-1} (Lauga and Powers [70] and Bary [9]; see Figure 1.1a) . In contrast, *spiroplasma* a bacterium, of width 150 nm and length of a few μms, moves by deforming its body as they have no cilia or flagella attached to their bodies to drive them in the surrounding fluid (Lauga and Powers [70] and Shaevits et al. [102]; see Figure 1.1(c)).

E. coli exhibits another type of non-symmetric swimming motion. This type of bacteria

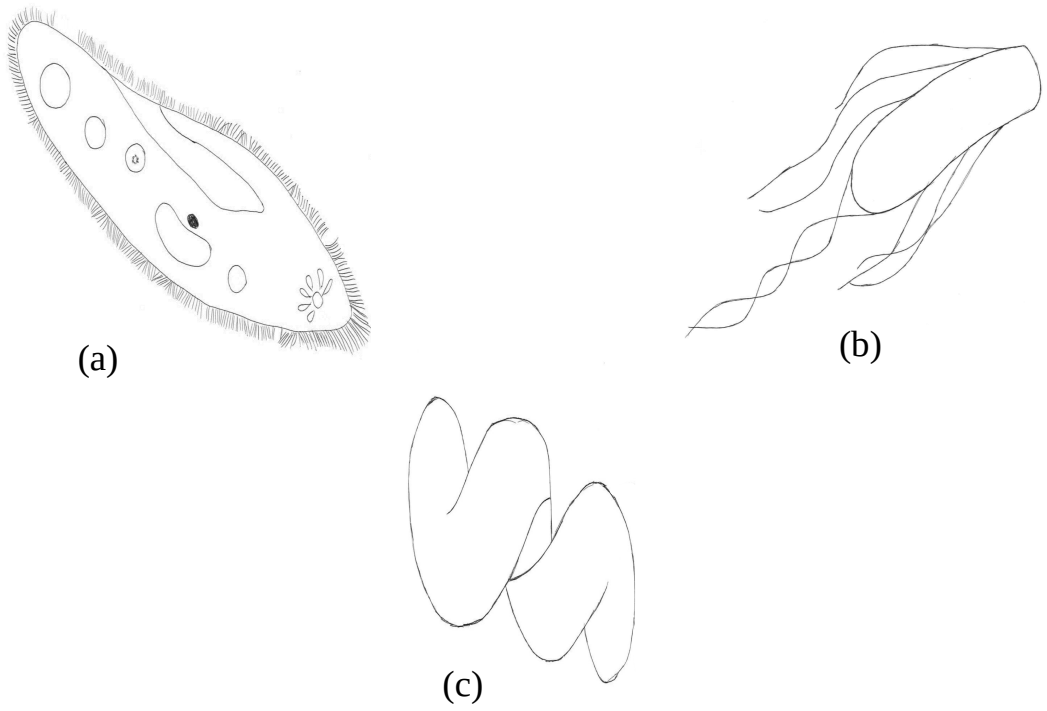

FIGURE 1.1: Diagram of some swimming microorganisms that exhibit different swimming styles. (a) *Paramecium* with its cilia distributed uniformly around the cell with a sinusoidal wave beating pattern to propel itself. (b) The bacterium *E. coli*, which has flagella attached to the cell that rotate in order to swim. (c) *Spiroplasma* a bacterium that moves in the surrounded fluid by deforming the cell body.

has 2 μm body and flagella that are hooked to a rotary motor embedded in the cell wall. The flagella are of 10 μm length and have a rigid helical structure that rotate to form a $3D$ helical motion causing the cells to swim with a typical speed of $25 - 35$ μms^{-1} (Lauga and Powers [70], Purcell [94], Bary [9] and Stocker and Durham [107]; see Figure 1.1(b)). Other microorganisms, such as *spermatozoa*, possess a long flexible flagellum that they undulate in a $2D$ whip−like motion to swim (Lauga and Powers [70]).

Our subject of study are the unicellular biflagellated green algae *Chlamydomonas augustae* (mistakenly referred to in earlier literature as *Chlamydomonas nivalis* Croze et al. [24]) and *Chlamydomonas reinhardtii*. They both have spheroidal bodies of length approximately $7 - 10$ μm and two flagella attached to the anterior end. The center of mass is displaced from the geometric center (Pedley and Kessler [87], Rüffer and Nultsch [97]; see Figure 1.2). They swim with a non−reversible breaststroke like motion. During

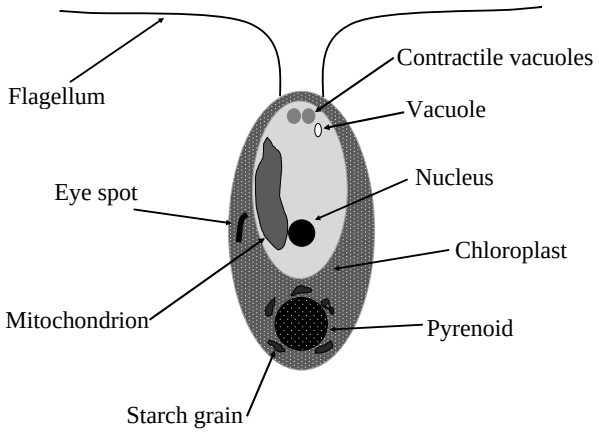

FIGURE 1.2: The cell structure of the green algae *Chlamydomonas*.

the effective stroke both flagella point vertically upwards, in the swimming direction. Then, the straight flagella beat backwards towards the cell body and the cell moves forward, while in the recovery stroke a bend passes from the base to the tip of the flagella to reset them in their original position. However, there is a significant overlap between the two strokes (Rüffer and Nultsch [97]; see Figure 1.3). *C. augustae* and *C. reinhardtii* propel themselves with mean swimming speeds of $55 - 63$ μms^{-1} (Hill and Häder [49]) and 130 μms^{-1} (Guasto et al [44]), respectively.

1.3 Bioconvection

Some unicellular bottom−heavy swimming microorganisms are denser than the fluid in which they swim. The green algae *C. augustae*, for example, are 5% denser than the ambient fluid (Pedley and Kessler [87]). The bottom heaviness results in a gravitational torque that orients the cells to swim vertically upwards (negative gravitaxis) on average in the absence of the fluid flow. Hence, swimming cells accumulate at the upper surface of a shallow suspension to form a concentrated layer of cells. When the cell concentration at the upper surface is high enough, the layer overturns to form patterns. This process is called the overturning instability and it is similar to the Rayleigh−Taylor instability of thermal convection (Plesset and Winet [90]; see Figure 1.4).

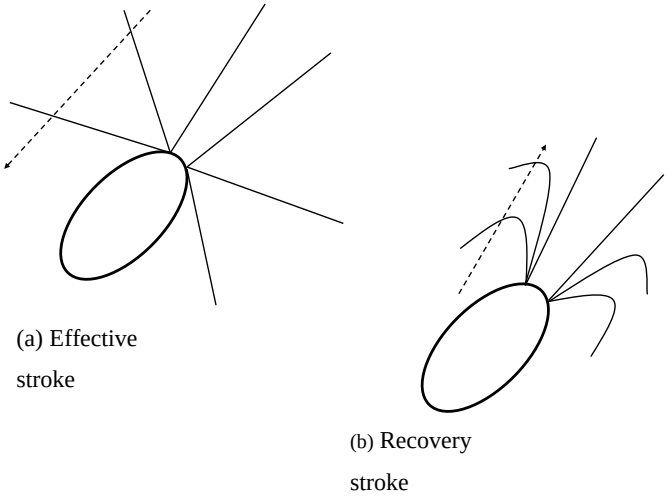

FIGURE 1.3: The swimming stroke of the green algae *Chlamydomonas*. (a) Both flagella point upwards then beat backwards to move the cell forward. (b) The bend passes from the base to the tip to return the flagella to their original position.

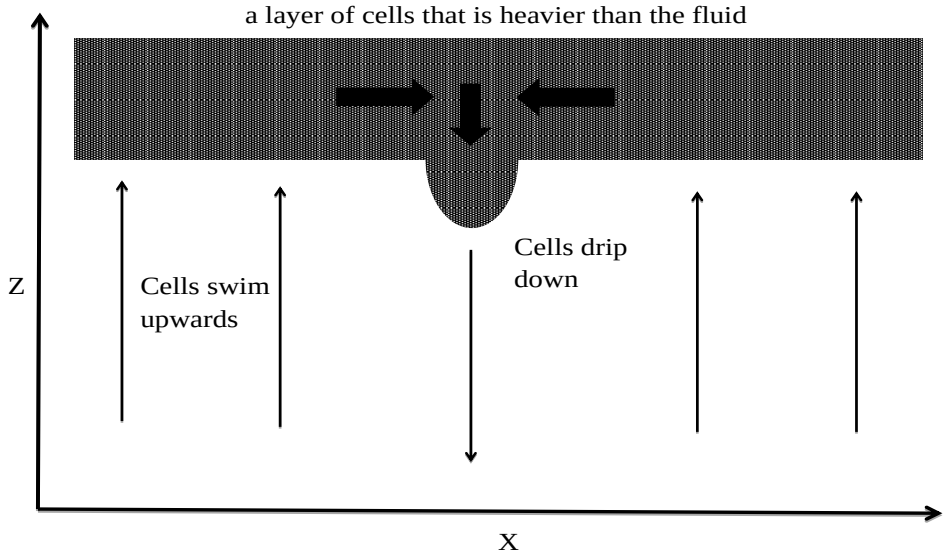

FIGURE 1.4: A diagram that demonstrates the overturning instability when the swimming cells aggregate at the upper surface of the fluid. When the concentration is sufficiently high the layer overturns.

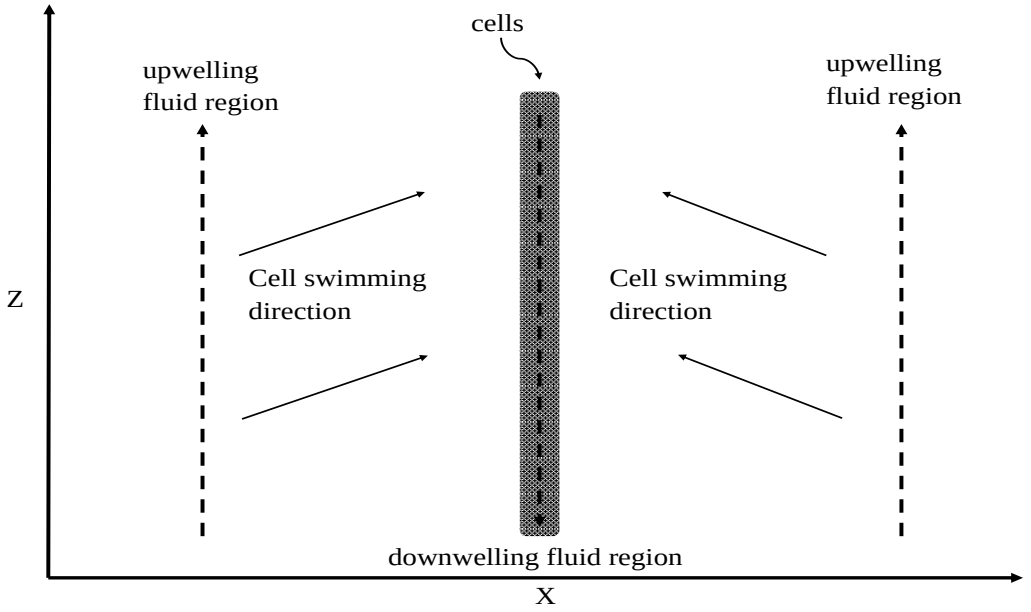

FIGURE 1.5: A diagram of the plumes that form from the gyrotatic instability when the viscous torque is in balance with the gravitational torque. Cells swim towards the downwelling fluid areas.

In the presence of fluid flow, a viscous torque also is exerted on the swimming cells. The balance between the viscous and the gravitational torques determines the mean swimming direction. This is called gyrotaxis (Kessler [62]). Cells, in this case, swim away from upwelling fluid areas towards downwelling fluid areas to form concentrated plumes of cells, that appears as dots when the fluid surface is viewed from above or sometimes as falling sheets of cells; (see Figure 1.7). This is called a gyrotactic instability (see Figure 1.5). The overturning and the gyrotactic instabilities give rise to complex spatial patterns called "bioconvection" (see Figure 1.6).

The name bioconvection was coined by Platt in 1961 [88]. Bioconvection patterns have been observed in species such as *Tetrahymena pyriformis*, bacteria and green algae, such as *Chlamydomonas*, *Dunaliella* and *Volvox*. The nature and the size of the patterns depend on the cell concentration C and the suspension depth H (Wager [114]) as well as on several other parameters.

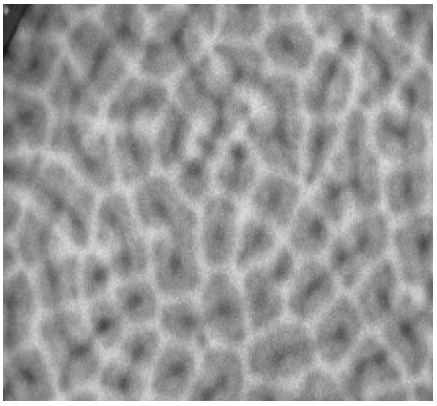

FIGURE 1.6: Bioconvection patterns for a mixed species of *C. augustae* and *C. reinhardtii*. The total concentration is approximately 1.1×10^7 cells per cm^3, with a relative concentration of 50% (matching cell concentration rather than biomass).

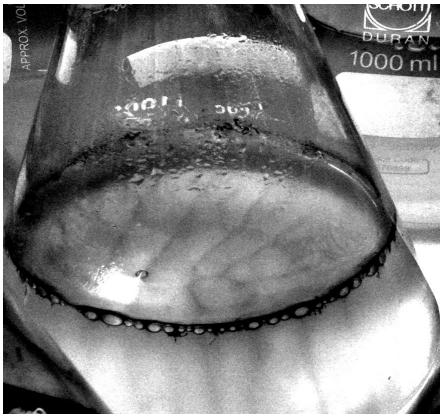

FIGURE 1.7: The gyrotactic instability as it forms falling sheets. When viewed from above one can see a roll structure. The suspension is of the green algae *C. reinhardtii*.

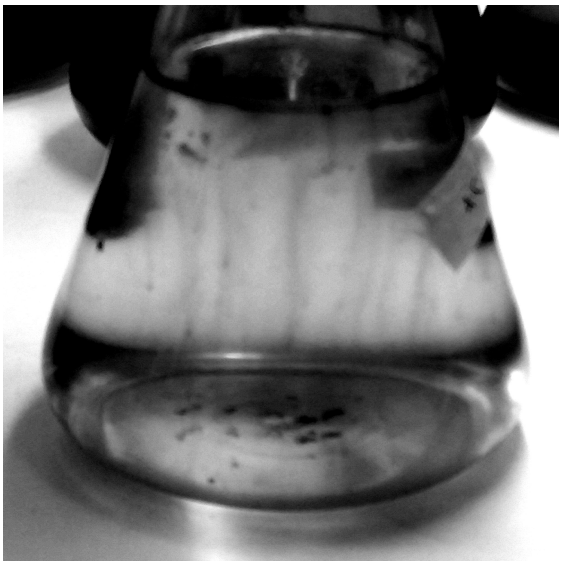

FIGURE 1.8: The gyrotactic instability as it forms plumes. The suspension is of the green algae *C. augustae*.

1.4 Bioconvection modelling

Although bioconvection patterns have been observed for a long time (Wager [114]), the first model was in 1974 by Plesset (Plesset and Winet [90] and Plesset and Whipple [89]). They modelled bioconvection as a Rayleigh−Taylor instability. The microorganism layer was simulated as a homogenous fluid layer of a small depth that is slightly more dense than an underlying layer of uniform fluid. Their investigations resulted in a most unstable disturbance wavelength that agreed with the experimental observations of *Tetrahymena pyriformis*. In their model, diffusion between the two layers was neglected.

A year later, Childress et al. [20] presented the first self−consistent hydrodynamic model. Unlike the study that was conducted by Plesset and Wint [90], negative gravitaxis was considered. Explicitly one of the main assumptions was that the cells swim vertically upward only. They assumed that they have a plane layer of a suspension of swimming microorganisms that was bounded by two infinite horizontal boundaries at $z = -H, 0$, which can be either stress−free or no−slip surfaces. The suspension was taken to be diluted so there were no cell−to−cell interactions. The concentration distribution of the cells was represented by a continuous function $C(\mathbf{x}, t)$. The swimming cells were slightly more dense than the ambient fluid. Thus, the density variation in the suspension

was very small. So, following the Boussinesq approximation, any changes in the fluid density can be neglected except where it is multiplied by acceleration due to gravity $\mathbf{g}$ (Kundu et al. [68]), and as the fluid was taken to be Newtonian, the first two governing equations were

$$\nabla \cdot \mathbf{U} = 0, \tag{1.2}$$

$$\rho \frac{D\mathbf{U}}{Dt} + \nabla p - \mu \nabla^2 \mathbf{U} = -g\rho \left(1 + \alpha C\right) \mathbf{k}, \tag{1.3}$$

where $\mathbf{U}$ is the bulk fluid velocity, p is the pressure, ρ is the fluid density constant, μ is the fluid viscosity constant, $\mathbf{g}$ is the acceleration due to gravity and C is the cell concentration. The density fluctuation of the suspension is given by the term $\alpha C\mathbf{k}$ in equation (1.3), where $0 < \alpha \ll 1$. The final equation in this model was for the evolution of C, given by

$$\frac{dC}{dt} + \nabla \cdot \mathbf{J} = 0, \tag{1.4}$$

where $\mathbf{J}$ is the cell flux, defined as

$$\mathbf{J} = C\mathbf{U}\left(C, z\right) \mathbf{k} - \mathbf{D} \cdot \nabla C. \tag{1.5}$$

Equation (1.5) imposes the negative gravitaxis property in the first term, $C\mathbf{U}\left(C, z\right) \mathbf{k}$, in addition to randomness in cell motion, which was represented by an anisotropic diffusivity tensor $\mathbf{D}$

$$\mathbf{D} = \begin{pmatrix} D_H\left(C, z\right) & 0 & 0 \\ 0 & D_H\left(C, z\right) & 0 \\ 0 & 0 & D_V\left(C, z\right) \end{pmatrix}. \tag{1.6}$$

In contrast with Plesset and Winet [90], the basic state was calculated as a solution of the governing equations and the linear stability was investigated around it. Their results were that the critical Rayleigh number R_c decreases as the depth increases, the

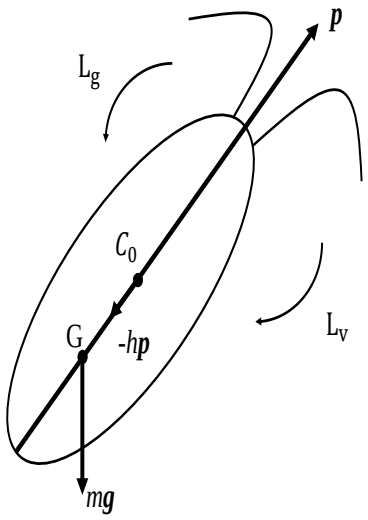

FIGURE 1.9: The torque balance on a bottom−heavy prolate spheroid cell. C_0 is the geometric center, G is the center−of−mass, $-h\mathbf{p}$ is the displacement vector between G and C_0 whereas L_v and L_g are the viscous and the gravitational torques.

critical wavenumber $k_c = 0$ (i.e., infinite wavelength λ_c) and the wavenumber k_m that corresponds to the maximum growth rate time γ is a positive number. Their prediction of k_m to some extent agreed with experimental observations of suspensions of *Tetrahymena pyriformis*. However, extremely large wavelengths were not seen experimentally when the suspension depth is not above the critical value.

Gyrotaxis was modelled in 1987 by Pedley and Kessler [85]. They assumed a spheroidal cell body of mass m and volume v with cell major axis a and minor axis b. The major axis was aligned with the unit vector $\mathbf{p}$, which represents the cell's swimming direction. The cell was assumed to be bottom−heavy. Hence, its centre−of−mass G is displaced from its geometric center C_0 by a distance h, (see Figure 1.9). Since the cell swims at a very small Reynolds number, inertia is absent. The cell's swimming direction $\mathbf{p}$ may be determined by a balance between viscous and gravitational torques, $\mathbf{L}_v$ and $\mathbf{L}_g$, respectively. In other words, the total torque $\mathbf{L}_T$ must vanish:

$$\mathbf{L}_T = \mathbf{L}_g + \mathbf{L}_v = 0. \tag{1.7}$$

The gravitational torque $\mathbf{L}_g$ is

$$\mathbf{L}_g = hmg\,(\mathbf{p} \times \mathbf{k})\,, \tag{1.8}$$

where g is the gravitational constant and $\mathbf{k}$ is the unit vector in the vertical direction. For a rigid prolate spheroid body with zero Reynolds number the viscous torque $\mathbf{L}_v$ can be written in the vector form (Rallison [96] and Batchelor [10])

$$\mathbf{L}_v = \mathbf{Y} \cdot \left[\frac{1}{2}\boldsymbol{\omega} - \boldsymbol{\Omega} + \alpha_0 \mathbf{p} \times (\mathbf{E} \cdot \mathbf{p})\right], \tag{1.9}$$

where

$$\mathbf{Y} = \mu v \left[\alpha_{\parallel}\mathbf{pp} + \alpha_{\perp}\,(\mathbf{I} - \mathbf{pp})\right]. \tag{1.10}$$

Here, α_0, $\alpha_{\parallel}$ and $\alpha_{\perp}$ in equations (1.9)−(1.10) are dimensionless constants, v is the cell volume and μ is the fluid viscousity. The cell eccentricity, α_0 is given by

$$\alpha_0 = \frac{a^2 - b^2}{a^2 + b^2}. \tag{1.11}$$

Also, $\alpha_{\perp}$ is the resistance coefficient for a rotation about an axis perpendicular to $\mathbf{p}$ and $\alpha_{\parallel}$ is the resistance coefficient for rotation about an axis parallel to $\mathbf{p}$. In equation (1.9) $\mathbf{E}$ is the fluid rate−of−strain tensor, $\boldsymbol{\omega}$ is the fluid vorticity and $\boldsymbol{\Omega}$ is the cell's angular velocity, which can be written as (Pedley and Kessler [87])

$$\boldsymbol{\Omega} = \Omega_{\parallel}\mathbf{p} + \mathbf{p} \times \dot{\mathbf{p}}. \tag{1.12}$$

Taking the vector product of $\mathbf{p}$ with the total torque gives

$$\left\{hmg\,(\mathbf{p} \times \mathbf{k}) + \mathbf{Y} \cdot \left[\frac{1}{2}\boldsymbol{\omega} - \boldsymbol{\Omega} + \alpha_0 \mathbf{p} \times (\mathbf{E} \cdot \mathbf{p})\right]\right\} \times \mathbf{p} = 0. \tag{1.13}$$

The tensor $\mathbf{E}$ is symmetric. So, by using tensor identities equation (1.13) can be simplified to

$$hmg\left[\mathbf{k}-(\mathbf{k}\cdot\mathbf{p})\,\mathbf{p}\right]+\mu v\alpha_{\perp}\left[\frac{1}{2}\boldsymbol{\omega}\times\mathbf{p}-\dot{\mathbf{p}}+\alpha_0\mathbf{p}\cdot\mathbf{E}\cdot(\mathbf{I}-\mathbf{pp})\right]=0. \tag{1.14}$$

Hence,

$$\dot{\mathbf{p}}=\frac{1}{2B}\left[\mathbf{k}-(\mathbf{k}\cdot\mathbf{p})\,\mathbf{p}\right]+\frac{1}{2}\boldsymbol{\omega}\times\mathbf{p}+\alpha_0\mathbf{p}\cdot\mathbf{E}\cdot(\mathbf{I}-\mathbf{pp}) \tag{1.15}$$

where

$$B=\frac{\mu\alpha_{\perp}}{2h\rho g}, \tag{1.16}$$

is the gyrotaxis number measured in seconds (Pedley and Kessler [85]). Combining expressions from Leal and Hinch [72] and Hinch and Leal [52] results in equation (1.15).

Gyrotactic bioconvection models were first investigated for a uniform suspension by Pedley et al. [84] and for a layer of a finite depth by Hill et al. [50]. In their model the governing equations were (1.2)− (1.4) as in Childress et al. [20] where the cell flux $\mathbf{J}$ was defined as

$$\mathbf{J}=nV_s\mathbf{p}-\mathbf{D}\cdot\nabla n, \tag{1.17}$$

where $n\,(\mathbf{x},t)$ is the cell concentration, V_s is the constant cell swimming speed and $\mathbf{p}$ is the cell swimming direction that is defined as

$$\mathbf{p}=(\sin\theta\cos\phi,\sin\theta\sin\phi,\cos\theta)\,, \tag{1.18}$$

where θ is the angle measured relative to the $z-$axis and ϕ is the cell orientation angle in the horizontal plane measured relative to the $x-$axis. The cell diffusivity tensor $\mathbf{D}$ was taken to be isotropic, or in other words $D_H=D_V$. This corresponds to assuming that the randomness in the cell motion is strong compared to the gyrotactic effect on the swimming direction, as gyrotaxis would lead to a diffusivity tensor with $D_H\neq D_V$. In contrast with Childress et al. [20], gyrotactic bias results in a non−zero critical

wavenumber in a deep layer suspension (Pedley et al. [84]). In a layer of finite depth Hill et al. [50] predicted the most unstable wavelength of 2 to 3 cm which contradicts with the experimental measurement that gives wavelengths of 0.5 to 1 cm. However, Hill et al. [50] predicted an initial wavelength of 2.9 cm which agrees with the observations of early pattern spacing.

In 1990, Pedley and Kessler [86] explored a new model for gyrotactic cells. The probability density function $f(\mathbf{p})$, defined on a unit sphere was considered. In the absence of all torques, cells swim generally in random directions with probability density function $f = \frac{1}{4\pi}$. However, the present of the viscous and gravitational torques cause the tendency for $\mathbf{p}$ to approach the intrinsic direction to bias the probability density function $f(\mathbf{p})$ and this is completely independent of the instantaneous direction of the cell. Therefore they assumed that f satisfies the Fokker−Planck equation

$$\frac{\partial f}{\partial t} + \nabla \cdot (\dot{\mathbf{p}} f) = D_r \nabla^2 f, \tag{1.19}$$

where $\dot{\mathbf{p}}$ is the rate of change of cell orientation and D_r is the rotational diffusivity. The Fokker−Planck equation allows for a nondeterministic estimate for the mean cell swimming velocity $\mathbf{V}_c$ and the cell diffusivity tensor $\mathbf{D}$. By assuming the time scale for the variation in the fluid flow is large compared with D_r^{-1}, the first term in equation (1.19) was neglected; f was considered a stationary function. $\dot{\mathbf{p}}$ in the second term was calculated from the torque balance equation (1.15), then, substituted in equation (1.19) which can be solved to give $f(\mathbf{p})$.

In their model, they assume that cells swim with different speeds and directions. Also, they assume that the cell swimming speed is stationary and independent of the direction $\mathbf{p}$. Hence, the mean cell swimming velocity $\mathbf{V}_c$ was defined as

$$\mathbf{V}_c = V_s \langle \mathbf{p} \rangle, \tag{1.20}$$

where V_s is the mean cell swimming speed and $\langle\ \rangle$ represents the ensemble average given by

$$\langle \mathbf{p} \rangle = \int_S \int \mathbf{p} f\left(\mathbf{p}\right) d^2\mathbf{p}. \tag{1.21}$$

Moreover, the diffusivity tensor $\mathbf{D}$ was defined as

$$\mathbf{D}\left(t\right) = \int_0^\infty \langle \mathbf{V}_r\left(t\right) \mathbf{V}_r\left(t - t'\right) \rangle dt', \tag{1.22}$$

In equation (1.22), $\mathbf{V}_r$ is the velocity of the cell relative to its mean velocity. They assumed that V_s is constant and it takes a cell τ seconds to settle to a preferred direction. Thus the tensor in equation (1.22) can be expressed as

$$\mathbf{D} \approx \int_0^\tau \left(\mathbf{V}_c - \langle \mathbf{V}_c \rangle\right) \left(\mathbf{V}_c - \langle \mathbf{V}_c \rangle\right) \rangle dt'. \tag{1.23}$$

Leading to

$$\mathbf{D} \approx V_s^2 \tau \langle \left(\mathbf{p} - \langle \mathbf{p} \rangle\right) \left(\mathbf{p} - \langle \mathbf{p} \rangle\right) \rangle. \tag{1.24}$$

The constant τ is called the direction correlation time.

The Pedley and Kessler [86] model consists of the following equations

$$\nabla \cdot \mathbf{U} = 0, \tag{1.25}$$

$$\rho \left(\frac{\partial \mathbf{U}}{\partial t} + \left(\mathbf{U} \cdot \nabla\right) \mathbf{U} \right) = -\nabla p_e + nv\Delta\rho\mathbf{g} + \nabla\mathbf{\Sigma}, \tag{1.26}$$

where $\mathbf{U}$ is the fluid velocity, p_e is the excess pressure above hydrostatic, $n\left(\mathbf{x}, t\right)$ is the local cell concentration, v is the mean cell volume, ρ is the fluid density, $\Delta\rho$ is the difference between the cell density and the fluid density, $\mathbf{g}$ is the acceleration due to gravity and $\mathbf{\Sigma}$ is the fluid stress tensor defined as

$$\mathbf{\Sigma} = 2\mu\mathbf{E} + \mathbf{\Sigma}^d + \mathbf{\Sigma}^s + \mathbf{\Sigma}^p, \tag{1.27}$$

where $\mathbf{E}$ is the fluid rate−of−strain tensor and μ is the fluid viscosity. The term $\mathbf{\Sigma}^d$ tensor represents the stress exerted on the particle due to its rotation caused by the rotary diffusion of $\mathbf{p}$, $\mathbf{\Sigma}^s$ is the stresslet stress tensor due to the cell locomotion, $\mathbf{\Sigma}^p$ is the couplet stress tensor due to the difference in the deformation and rotation of the cell from the fluid if the cells were not present (Batchelor [10], Brenner [19] and Hinch and Leal [51]). The first term in (1.27) is for fluid in the absence of cells.

Finally, the cell concentration equation is given by

$$\frac{\partial n}{\partial t} = -\nabla \cdot \left[n\mathbf{U} + nV_s\langle \mathbf{p} \rangle - \mathbf{D} \cdot \nabla n \right]. \tag{1.28}$$

The first term in on the right hand side of equation (1.28) represents the advection of cells by the fluid velocity while the second term gives the cell movement due to cell swimming and the final term is the diffusion term. The vector $\langle \mathbf{p} \rangle$ is the mean cell swimming direction as defined in equation (1.21) and $\mathbf{D}$ is given in equation (1.24). Pedley and Kessler [86] found that the suspension is always stable in the absence of the gyrotactic bias in deep suspensions. Pedley and Kessler [86] calculated the critical value k_c to be

$$k_c^2 = \frac{\beta \left(J_1 + \alpha_0 J_4 \right)}{D_H \left[\frac{1}{R} + \chi_1 \left(J_2 + \alpha_0 J_5 \right) \right]}, \quad \beta = \frac{n_0 v B g \Delta\rho}{V_s \rho}, \quad R = \frac{\rho V_s^2 B}{\mu}. \tag{1.29}$$

whereas Pedley et al. [84] have calculated this value to be

$$k_c^2 = \frac{R\beta \left(1 - \alpha_0 \right)}{D^*}. \tag{1.30}$$

Hence, for *C. augustae* with $\lambda = 2.2$ and $\alpha_0 = 0.3$, Pedley and Kessler [86] estimated $k_c^2 = 0.65$ for the following values $D_H = 0.10$, $V_s = 63$ μms^{-1}, $R^{-1} = 73$ (cell Reynolds number)and $\beta = 13$ while Pedley et al. [84] estimated this value to be $k_c^2 = 0.17$ for the cell swimming seed $V_s = 100$ μms^{-1} and the dimensionless diffusion value $D^* = 0.74$. Moreover, Pedley and Kessler [86] estimated the most unstable wavelength to be 9 mm at the time 0.017 s^{-1}. while Pedley et al. [84] estimated this value to be 11 mm at the time 0.029 s^{-1}. However, observations of bioconvection patterns give smaller wavelength

of 1 to 3 mm which disagrees with the predictions (Kessler [63]). This could be due to the effect of the non linear factors that were not considered in the linear stability.

The new model of Pedley and Kessler 1990 [86] was used by Bees and Hill [12] to find an equilibrium basic state and investigate its linear stability for a layer of a finite depth with no slip boundaries. They predicted a pattern wavelength of length 1 mm, which differs from the prediction of Hill et al. [50], 2−3 cm in a suspension of depth 1 cm with mean cell concentrations slightly above the critical concentration vale $\bar{n}_c = 5 \times 10^5$ cell per cm^3. However, the experimental results observed patterns with wavelengths of 4 mm to 7 mm.

Bees and Hill [13] have explored the non−linear structure of deep, stochastic gyrotactic bioconvection as proposed by Pedley and Kessler [86] by employing the solutions obtained by Bees et al. [14] from a spheroidal harmonic expansion of the Fokker−Planck equation. A linear analysis considered by Pedley et al. [84] is performed to highlight the scaling for the weak non−linear analysis. Their analysis reveals neutral curves associated with a Hopf bifurcation. In contrast Ghorai et al. [38] investigated the nonlinear numerical simulation of the gyrotactic bioconvection patterns. A fully three−dimension computational model developed in this framework is used to investigate the dependence of bioconvection patterns on the diffusivity of the cells, the mean cell concentration and the depth of the chambers. Their results are that the increase in wavelength with time associated with the formation of isolated nonlinear plumes, is much greater for high values of the diffusivity than for low values. Also, in the numerical experiments, it is observed that the variation in the wavelength with time is not monotonic for smaller values of the cell diffusivity. The wavelength in the experiments also decreased slightly with an increase in the depth of the chamber. Moreover, for small depth and high Rayleigh number, plumes sometimes merge with nearby plumes leading to higher wavelengths. Finally, the well−developed wavelength decreases slightly with increase the mean concentration. They have also observed bottom−standing plumes in deep chambers. In this case, most of the cells are transported to the bottom of the chamber and many plumes at the bottom do not extend to the top of the chamber. In an earlier numerical study, Karimi and Paul [61] claimed that the use of a constant isotropic diffusivity lead

to unrealistic results, but Ghorai et al. [38] showed that this was caused by their use of too high value of the diffusivity. In this and other papers, Ghorai et al. [38] have consistently demonstrated that the use of a constant isotropic diffusion may be regarded as a good first approximation to the dispersion of the swimming cells in bioconvection which provided a good agreement with the experiments.

In this thesis, since there is no previous work of extending the bioconvection model to more than one species, we extend the linear stability analysis in [86] to two species of swimming microorganisms mixed together without any kind of interactions between each other. Unlike Pedley and Kessler [86], the fluid is taken to be Newtonian only without taking into accounts the stress tensors $\mathbf{\Sigma}^d$, $\mathbf{\Sigma}^s$ and $\mathbf{\Sigma}^p$ in equation (1.27). Also, the species are assumed to have different parameters, which introduces an extra term in equation (1.26) as well as an extra cell concentration equation for the second species. Hence, there are two equations of the form of equation (1.28) giving four governing equations rather than three (more details are given in Chapter 3).

Not only do we extend the linear stability analysis to two species, but also we employ the nonnormal stability analysis to study the stability of the system presented by Pedley et al. [84], in the case that the horizontally uniform concentration profile evolves with time, which is new to bioconvection and active fluids (more details are given in Chapter 4).

Moreover, in terms of experiments a new analysis technics using wavelets were developed to provide information about local wavelengths of bioconvection patterns, instead of the global pattern wavelength invested by William and Bees [116]. In general, bioconvection patterns are not spatially uniform and wavelet methods are able to give a measurement of the local variation in the nature and spacing of the patterns. Experimental patterns are to some extent dependent on the initial conditions, and wavelets provide a measure for comparison of the patterns to answer the question " are these two patterns qualitatively similar?" (more details are given in Chapter 2).

1.5 Thesis outline

This thesis consists of:

Chapter 2: we describe experiments on bioconvection of mixed species of *C. augustae* and *C. reinhardtii* to obtain quantitative data on the pattern wavelength. Furthermore, we utilize wavelets to study how pattern wavelengths change as we vary the total concentration and the relative concentration between the two mixed species.

Chapter 3: we generalize the continuum model presented by Pedley and Kessler [86] to consist of two mixed species. Also, we compute the dispersion relationship using Fourier modes and calculate the neutral curve equation as a function of the wavenumbers k and m to compare the instability onset of the suspension of the two mixed species with the instability onset of each species individually.

Chapter 4: we computed the time evolving basic state of the cell concentration. We used the non−normal approach to estimate the energy over a range of wavenumbers. We find the optimal initial perturbation that can be obtained for a given time t as well as a given set of parameters and wavenumber k. Then, we measure the size of the optimal perturbation as it grows with time considering a range of wavenumbers for the same set of parameters to extract the most unstable wavelength in a layer of finite depth.

Chapter 2

A quantitative study of the effects of relative concentration and total concentration of two species on pattern formation

In terms of experiments, the oldest qualitative study of bioconvection was by Wager in 1911 [114]. Since then, many experiments has been conducted to observe bioconvection patterns by scientist such as Rothschild [99], Loefer and Mefferd [75, 76], Platt [88] and recently Kessler [62]. However, the first quantitative systematic experiment was in 1997 by Bees and Hill [11]. In their analysis, the dominant wavelength is presented as a function of cell concentration, suspension depth and time. A Fast Fourier transform is used to analyse bioconvection patterns that are formed by the motile green algae *Chlamydomonas nivalis*, and a non−normalized Gaussian distribution is used as a fitting function to extract the dominant wavelength. Their results are that the initial wavelength increases with increasing the depth. However, when the concentration increases it decreases slightly. For the long-term evolution, the increase of the concentration decreases the wavelength but there is no significant change with the depth. Czirók et al. in 2000 [25] followed the same procedure as Bees and Hill [11] while choosing a

Illumination	Position	Results
red or white light	above or below	the initial wavelength decreases with increasing the concentration.
red light	above or below	equivalent to no light.
white light	above	the initial wavelength increases slightly when 645lx$\leq I <$ 1330lx and decreases when 2020lx$\leq I$.
white light	below	the initial wavelength decreases linearly as the intensity increases to 2020lx, then increases as it reachs 2710lx and remains constant when 2710lx$\leq I$.

TABLE 2.1: Summary of the main results of Williams and Bees [116].

different fitting function to analyse the patterns formed by the bacteria *Bacillus subtilis* and their results were in contrast with Bees and Hill [11]. They found that the initial wavelength decreases with increasing the depth and the concentration. This could be due to the fact that the bacteria *Bacillus subtilis* is aerotaxis. In 2011, Williams and Bees [116] analysed the patterns formed by the motile green algae *Chlamydomonas augustae* to evaluate the wavelength as a function of cell concentration and illumination. The results are shown in Table 2.1

In all these studies, patterns were analysed globally to extract the global dominant wavenumber by using Fourier transform, since the wavenumber is one of the parameters that can be used to characterize these patterns. However, in some cases, patterns can consist of different patches. Even though patterns can look same, the dominant wavenumber changes from one location to another. The purpose of this study is to present a new analysis tool, wavelets, to investigate the local dominant wavenumber as a function of the suspensions total concentration and the relative concentration between the two species.

2.1 Material and Methods

In this framework, species of *Chlamydomonas reinhardtii* and *Chlamydomonas augustae*, strain CCAP 11/32B and CCAP 11/51B, respectively, were used. As the experimental study of bioconvection requires capturing images of clearly defined patterns, fresh and

actively motile cultures of cells need to be bred. Among different types of media that could be used to grow these cultures, such as TAP (Tri Acetate Phosphorous), 3N−BBM was used. Since it does not increase the bacteria's rate of growth, it can easy be prepared in the standard laboratory conditions and it matches with the natural environmental conditions. 3N−BBM medium is the usual BBM (Bold's Basal Medium) (Bees and Hill [11]), with triple the amount of sodium nitrate to enhance the cultures' rate of growth [24]. As in Williams and Bees [116], cultures were stored in 1000 ml and 500 ml flasks, as the long neck is useful for the concentrating process and the light is allowed to pass through the cultures. A cotton wool bung is inserted in the long neck to seal the flasks, and two layers of an aluminium foil were used to cover it. Thus, the oxygen exchange is allowed while avoiding contamination by bacteria or fungi.

Because these motile green algae are photosynthetic, cultures were illuminated from above by lighting them using four florescent tubes with intensity of 1900 lux. The lighting system was set to be 16 hours on to 8 hours off, to capture the cells swimming at a reasonable time of the day. The laboratory temperature was controlled to be $(21\pm2)^{\circ}$C, as the cultures are sensitive to the sudden change in the temperature. Moreover, the laboratory equipments were washed with liquid soap, rinsed with distilled water and sterilized (Williams and Bees [116]).

Following Williams and Bees [116], cultures were subcultured once per calender month to allow cells to be concentrated enough. So that, healthy and motile cells are guaranteed for every experiment. For this reason new media flasks were prepared and sterilized by autoclaving them for 15 minutes at 121°C. Once the new media have cooled enough, one flask of the new media was mixed with an old flask of the cultures over a flame as a part of the sterilization process.

A protocol for concentrating the cells is followed since having enough concentrated suspension is very important to spot well−defined bioconvection patterns. To ensure that the cells are healthy and actively motile, two week old cultures were used. Moreover, the use of younger cells can lead to harvest insufficient amount of concentrated cells from each flask. Because of both *Chlamydomonas reinhardtii* and *Chlamydomonas augustae*

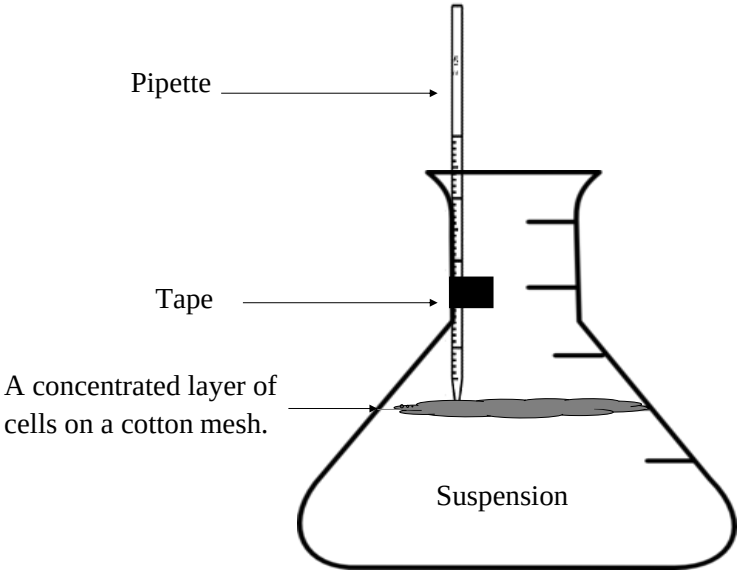

FIGURE 2.1: A diagram to illustrate the concentrating process. The cells swim upwards on average through the cotton wool layer and aggregate on its surface.

are negative gravitactic, they swim upwards on average and accumulate on the fluid surface. Thus, unlike Williams and Bees [116], one can concentrate cells using the following procedure that was newly developed in the laboratory with Dr.Otti Croze to harvest the maximum number of cells. Four thin metal wires are folded and joined together to form a flower shape. Then they are taped onto the upper end of a pipette. The pipette then was inserted inside the flask, which was filled by 800 ml of the culture suspension (400 ml in case of 500 ml flask was used), and stabilized on the long neck using a tape such that the flower shape metal wires was positioned on the upper surface of the fluid. Fine layers of sterilized cotton wool were placed on the metal wires to form a mesh with thickness between $0.5-1$ cm. The flasks were then left for $2-3$ days in the darkness to concentrate; (see Figure 2.1). Leaving the flasks for long time, with cotton wool, could cause cell dehydration. So,concentrated cells older than four days were not used. Then, the cells extraction would take place. Pasteur pipette is used to gently harvest the cells that accumulated on the surface of the cotton mesh. The harvested cells were placed in a clean (washed and rinsed with distilled water) plastic container.

Following Williams and Bees [116], controlling the concentration of the suspension during the experiment is essential. Thus, an electronic spectrophotometer (WPA CO7500 colorimeter, Cambridge, UK, 590 nm), is used to calibrate the number of cells per cm^3 by measuring the amount of light at a wavelength (590 nm) that passes through a sample compared to a reference state. A 2 ml reference of 3N−BBM is placed in a cuvette and measured using the spectrophotometer. Then, 0.5 ml of the concentrated suspension is transferred to another cuvette and is topped by 1.5 ml of the 3N−BBm medium. Next, the suspension is mixed with a pipette to make sure that cells are distributed uniformly. Then, the absorption is measured also using the spectrophotometer. Finally, the absorption is converted to concentration using the following relationships between the cell concentration and the absorption:

$$\begin{aligned} C_a &= (4.935A + 0.4349) \times 10^6, \\ C_r &= (7.183A + 0.833) \times 10^6, \end{aligned} \tag{2.1}$$

where C_a, C_r and A are the cell concentration of the *C. augustae*, *C. reinhardtii* and the absorption, respectively. Hence, the suspension concentration is four times the measured concentration. Equations (2.1) are calibrated manually using a haemocytometer and applying Beer's law to find a linear relationship between the cell concentration and the absorption; (see Figure 2.2). The R^2 values in Figure 2.2 shows that the data are well approximated by a straight line.

Equations (2.1) are applicable because the relationship between the absorption and the cell concentration is linear when the absorption is less than 0.8. The absorption was measured five times and averaged before it was converted to concentration. The cell concentration was measured before the experiment as the patterns formation due to the change in their relative concentration was demonstrated.

The protocol for investigating the pattern wavelength as a function of the relative concentration between the two species *C. augustae* and *C. reinhardtii* is as follow,

1. 11 petri dishes of diameter 5.2 cm are washed with soap and rinsed with distilled water.

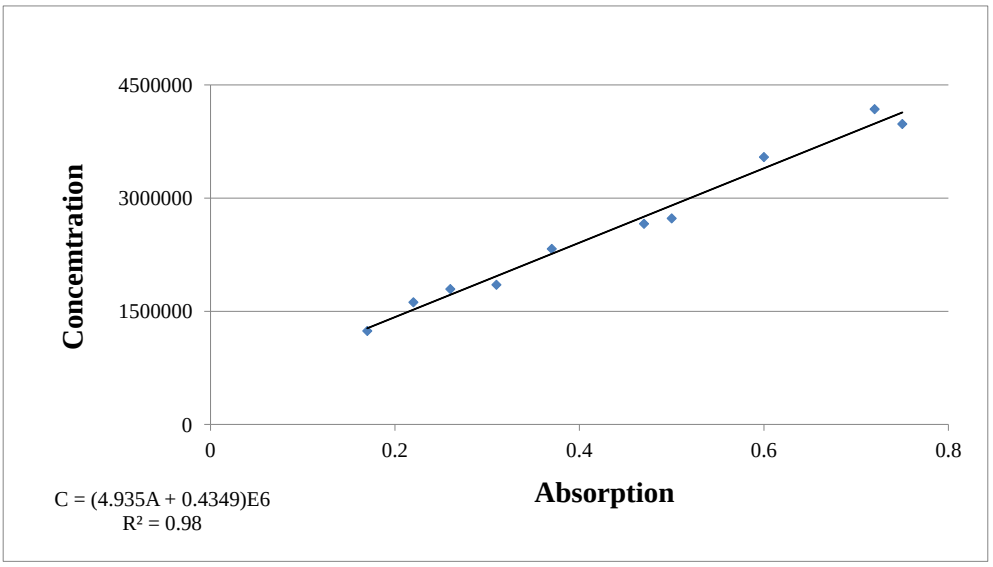

(a) *C. augustae*

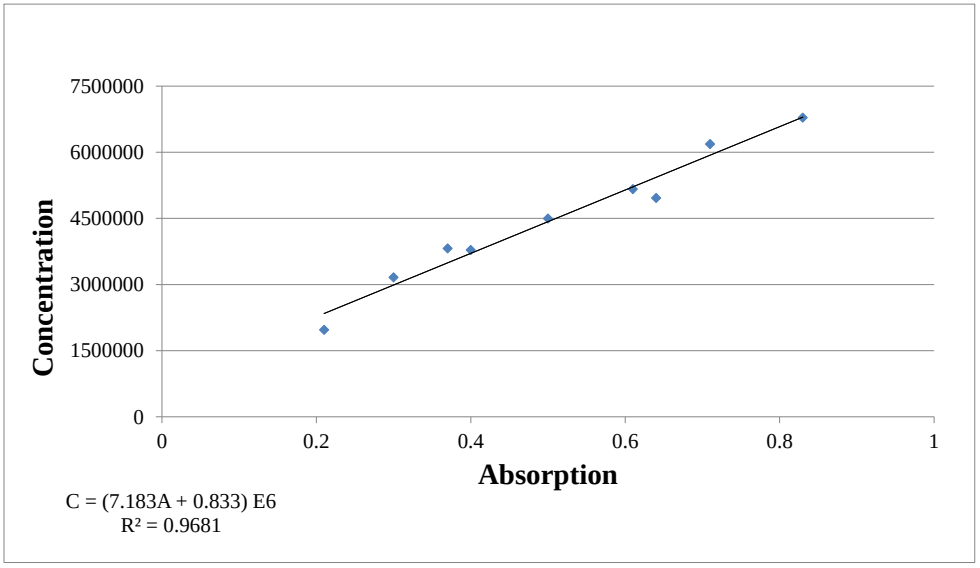

(b) *C. reinhardtii*

FIGURE 2.2: Fitting of the data collected in the biofluid laboratory shows the linear relationship between the cell concentration and the absorption for both species when the absorption is less than 0.8.

2. The 11 petri dishes are labelled by the ratio of the concentration of one species with respect to the other. For example, when the petri dish is labelled by 1a9r, the suspension consists of 10% *C. augustae* and 90% *C. reinhardtii*. In the case that the suspension consists of one species it is labelled by either 10a or 10r, i.e either 100% *C. augustae* or 100% *C. reinhardtii*.

3. A culture volume of 10 ml is placed in all these 11 petri dishes with a relative concentration of a step size of 10%. Thus, pattern formation are recorded as one shifts from 100% *C. augustae* to 100% *C. reinhardtii*.

4. Mixing the two species together takes place after measuring concentration to be certain that they both have the same concentration.

To explore pattern wavelength as the total concentration changes, we use the following protocol:

1. Every suspension in the petri dishes is 20% diluted by removing 2 ml of the suspension and adding 2 ml of the 3N−BBM medium to complete the $10ml$ volume in every dish.

2. Every suspension is diluted three times, so bioconvection patterns are recorded for a suspension that is diluted up to a 60%.

Diluting the suspension more than 60% results in poor patterns as the concentration is not high enough for these patterns to appear.

In every experiment, the petri dish is stabilized on a red light lid to illuminate the patterns from below. Because the experiment takes place in darkness, a light source is required. According to Williams and Bees [116], the cells are not affected by red light illumination, so, the culture are illuminated without affecting their gyrotactic behavior. The light source is positioned on an electrical automated vortex mixing device (Jencons PLS VX100, West Sussex, UK), as illustrated in Figure 2.3, that rotates to create a motion that mixes the culture in a consistent manner every time the experiment is performed. This mixing protocol follows that of Williams and Bees [116], to avoid the

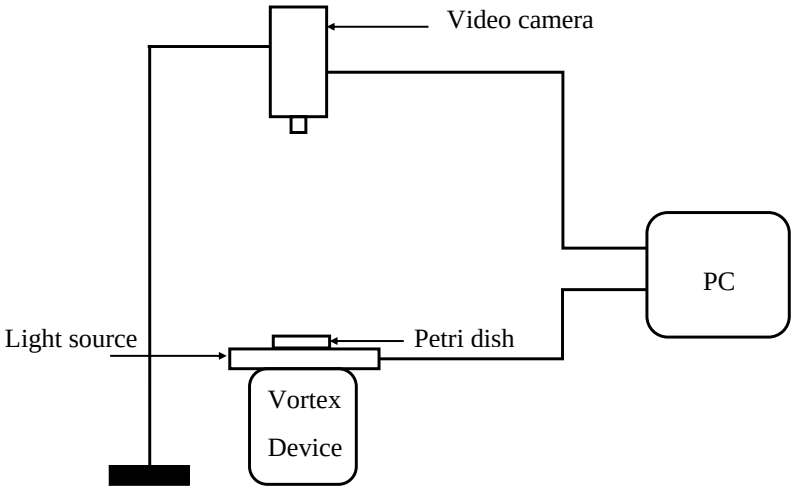

FIGURE 2.3: An illustration of the equipment setting during performing the experiments.

Process	Mix	Stop	Mix	Stop	Mix	Stop	Record
Time	3 sec	2 sec	10 sec	3 sec	2 sec	15 sec	5 min

TABLE 2.2: The mixing protocol table.

variation in the initial wavelength due to the change in initial conditions of the same suspension when mixing by hand as in Bees and Hill [11], and Czirók et al. [25]. As in Williams and Bees [116], a reciprocal mixing and pausing regime for few seconds is used to ensure that the culture is well mixed. This regime is followed by a long pause, of 15 seconds, to allow the residual fluid motion to vanish before the patterns starts to form; see Table 2.2.

A Prosilica video camera (MODEL:GE680C), connected to a computer and controlled via streampix software, is stabilized above the petri dish to record these patterns for five minutes every time the experiment is run.

2.2 Image Analysis

A sequence of 151 images is recorded for every experiment. In other words one image per two seconds. Every image consists of 480×640 pixels of 256 gray scale. The images are not square as this is the best resolution one could get from the camera that is used during the experiment. ImageJ is employed to extract the image frames, to adjust their brightness and contrast and finally to save them in tif format in order to analyse them. The MATLAB software is employed in this analysis due to its ease of use and it has a wavelet package that aid image processing and analysis.

Every image in the sequence contains unwanted information such as the inhomogeneous light from the light source, the walls of the dish, the scratches on the dish and the boundary of the image. A Matlab code is designed to subtract the first image that is captured immediately after 15−25 seconds from ending the mixing regime, i.e. the smooth image with no bioconvection patterns, from all the images in the sequence. So, the inhomogeneous light effect from the light source, the wall of the dish and the scratches at the bottom of the dish are eliminated. To avoid the image edge effect on the analysis, a full size image is analysed, however, the information is extracted from 256×256 frame within the image, see Figure 2.4.

Applying wavelet transform to an image allows us to extract the most dominant wavelength with its associated direction locally. Moreover, it is possible to extract the second dominant one also with its associated direction locally leading to a systematic method to describe the shape of these patterns.

2.2.1 Wavelet Analysis

As images are two−dimensional data, the analysis is presented and performed in two−dimensional space. The notion of representing signals as a linear combination of certain functions was initiated in 1807 (Boggess and Narcowich [18] and Graps [42]), by a French mathematician, Joseph Fourier, who asserted that any 2π periodic function can be expressed as a superposition of the basic sinusoidal functions sine and cosine of different frequencies. This idea is the base of the Fourier transform that is employed in

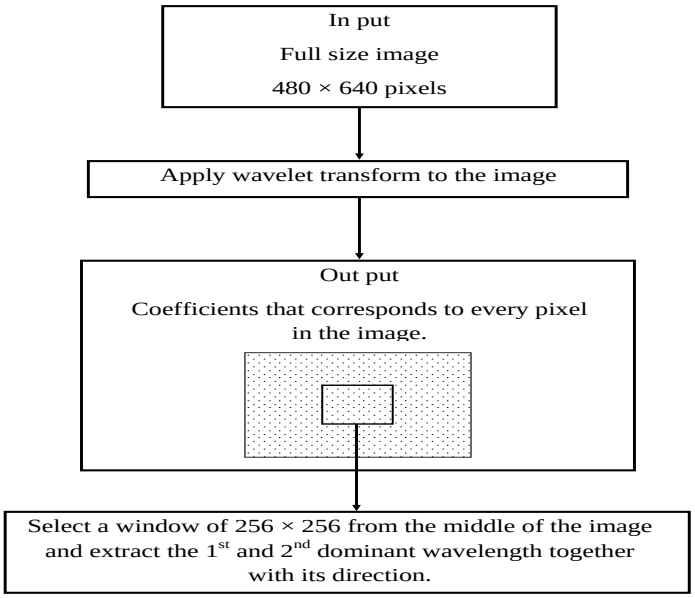

FIGURE 2.4: Protocol for eliminating the image boundary effect on the analysis results.

many scientific fields such as physics and partial differential equations (James [57] and Bahouri et al. [7]).

The basis functions in Fourier transform, sine and cosine, possess a global oscillatory behaviour as they stretch to infinity, which results in a poor localization property in the space domain. As a consequence, Fourier transforms fail, as a tool, for analysing signals that have a very high frequency on short space scale and very low frequency on a long space scale. Signals with these characteristics were a motivation for a French geophysicist named Jean Morlet in 1980s (Sifuzzaman et al. [103]) to construct basis functions that are well localized in space with support that varies as the space scale varies. Even though the concept of the wavelet as an oscillation that decays quickly was introduced by Morlet, the idea of wavelet basis functions was presented in 1909 by Alfred Haar (Gao and Yan [36], Sifuzzaman et al. [103], Boggess and Narcowich [18] and Jaffard et al. [56]). His idea arose based on a question he was trying to answer (Haar [45] and [110]):

"Does there exist another orthonormal system $\psi_0, \psi_1, \cdots, \psi_n, \cdots$ of functions on $[0, 1)$,

such that for any continuous function $f(x)$ defined on $[0,1)$, the series

$$\langle f,\psi_0\rangle\psi_0+\langle f,\psi_1\rangle\psi_1+\cdots+\langle f,\psi_n\rangle\psi_n+\cdots \tag{2.2}$$

converges uniformly to $f(x)$ on $[0,1)$."

The aim was to find basis functions that have local characteristic that are different to the Fourier functions sine and cosine. He succeeded and introduced Haar functions that consist of a short positive pulse followed by a short negative pulse defined on the semi closed interval $[0,1)$. This simple idea opened a wide gate to a new theory, named wavelet theory, that is successfully utilized in many fields (Chui [21]). For example, turbulence (Farge [32]), image and signal analysis and processing (Clonda et al. [22], Merah et al. [81] and He et al.[47]), pattern characterization (Guana [43]).

A mathematical definition equivalent to the above concept in two−dimensional space, due to Antoine et al. [3], is that a two−dimensional wavelet is a complex−valued function $\psi(\mathbf{x})\in L^1\left(\mathbb{R}^2\right)\cap L^2\left(\mathbb{R}^2\right)$, where $L^2\left(\mathbb{R}^2\right)$ is the set of the square integrable functions that satisfies $\int\int_{\mathbb{R}^2}|\psi(\mathbf{x})|^2d\mathbf{x}<\infty$ and $L^1\left(\mathbb{R}^2\right)$ is the set of the integrable functions, i. e. $\int\int_{\mathbb{R}^2}|\psi(\mathbf{x})|d\mathbf{x}<\infty$, that satisfies the following condition

$$C_\psi=(2\pi)^2\int_{\mathbb{R}^2}\frac{|\hat{\psi}(\mathbf{k})|^2}{|\mathbf{k}|^2}d^2\mathbf{k}<\infty, \tag{2.3}$$

where $\hat{\psi}$ is the Fourier transform of the function ψ, i.e.

$$\hat{\psi}(\mathbf{k})=\frac{1}{2\pi}\int_{\mathbb{R}^2}\psi(\mathbf{x})\exp(-i\mathbf{k}\cdot\mathbf{x})\,d\mathbf{x} \tag{2.4}$$

and $\mathbf{k}=(k_x,k_y)\in\mathbb{R}^2$ is the spatial frequency. This agrees with the one−dimensional definition in Sifuzzaman et al. [103] and Daubechies [26]. The condition (2.3) is called the admissibility condition and it indicates that the named function ψ oscillates on a finitely supported area. To illustrate the admissibility condition (2.3), let us consider the one−dimensional Mexican hat wavelet that is given by (Antoine et al. [3])

$$\psi_H(x)=\left(1-x^2\right)\exp\left(-\frac{1}{2}x^2\right). \tag{2.5}$$

The Fourier transform of the above function, on applying the definition in equation (2.4), is given by

$$\hat{\psi}_H(k) = k^2 \exp\left(-\frac{1}{2}k^2\right). \tag{2.6}$$

According to Antoine et al. [3], the admissibility condition in one−dimensional space is

$$C_\psi = 2\pi \int_{\mathbb{R}} \frac{|\hat{\psi}(k)|^2}{|k|} dk < \infty. \tag{2.7}$$

Hence, for the Mexican hat wavelet function in (2.5),

$$C_\psi = 2\pi \int_{\mathbb{R}} \frac{|k^2 \exp\left(-\frac{1}{2}k^2\right)|^2}{|k|} dk = 2\pi \int_{\mathbb{R}} |k^3| \exp\left(-k^2\right) dk. \tag{2.8}$$

Integrating by parts results in $C_\psi = 2\pi$, i. e. $\psi_H(x)$ is admissible.

Wavelet basis functions are the sets of functions, $\psi_{a,\mathbf{b},\theta}(\mathbf{x})$, that are generated by dilation a, translation $\mathbf{b}$, and rotation θ of the the "mother wavelet" ψ as follows

$$\psi_{a,\mathbf{b},\theta}(\mathbf{x}) = a^{-\zeta} \psi\left(a^{-1} r_{-\theta}(\mathbf{x} - \mathbf{b})\right), \tag{2.9}$$

The dilation parameter $a > 0$ in definition (2.9), means either stretching the wavelet function when $a > 1$ or compressing it when $a < 1$, whereas the translation vector $\mathbf{b} \in \mathbb{R}^2$ determines the location of the wavelet basis function. The rotation matrix,

$$r_{-\theta} = \begin{pmatrix} \cos\theta & -\sin\theta \\ \sin\theta & \cos\theta \end{pmatrix}, \tag{2.10}$$

enables us to rotate the wavelet function by an angle θ, where $0 \leq \theta < 2\pi$. Finally, ζ can have the values,

$$\zeta = \begin{cases} 1, & \text{to preserve the } L^2 \text{ norm} \\ 2, & \text{to preserve the } L^1 \text{ norm} \end{cases}. \tag{2.11}$$

Accordingly, a two−dimensional continuous wavelet transform of two−dimensional signal (image), $s(\mathbf{x}) \in L^1(\mathbb{R}^2) \cap L^2(\mathbb{R}^2)$, is

$$S(a, \mathbf{b}, \theta) = a^{-\zeta} \int_{\mathbb{R}^2} s(\mathbf{x}) \overline{\psi(a^{-1} r_{-\theta}(\mathbf{x} - \mathbf{b}))} d^2\mathbf{x}, \tag{2.12}$$

where $\overline{\psi}$ is the complex conjugate, or equivalently, in the frequency domain

$$S(a, \mathbf{b}, \theta) = a^{-\zeta+2} \int_{\mathbb{R}^2} \hat{s}(\mathbf{k}) \overline{\hat{\psi}(a r_{-\theta}(\mathbf{k}))} \exp(i\mathbf{b} \cdot \mathbf{k}) d^2\mathbf{k}. \tag{2.13}$$

Unlike the Fourier transform, the wavelet transform has a wide range of different families (Misiti et al. [82]), each of which has its own mother wavelet function ψ that possesses certain properties. For instance, some of these are orthogonal such as Haar and Daubechies, continuous as Gaussian or have an explicit expression like the Mexican hat. The decision of which wavelet family should be employed depends on the purpose of the analysis. In this study, a wavelet function that has an oscillatory behavior similar to the sinusoidal functions is required, in order to capture the wavenumber associated with the images. Not only that but the ability to control the number of waves in that function is also wanted. Thus, 2D complex Morlet was selected for this work. 2D complex Morlet wavelet is simply a plane wave modulated by Gaussian envelope,

$$\psi_M(\mathbf{x}) = \exp(i\mathbf{k}_\psi \cdot \mathbf{x}) \exp\left(-\frac{1}{2}|\mathbf{x}|^2\right) + \text{correction}. \tag{2.14}$$

The correction term in (2.14) is added to enforce ψ_M to satisfy the condition (2.3). $\mathbf{k}_\psi$ is the wavenumber vector that determines the number of oscillations inside the Gaussian envelope. The correction term can be neglected numerically $O(10^{-4})$ if the $|\mathbf{k}_\psi|$ is large enough. Furthermore, the 2D complex Morlet wavelet is sensitive to the direction which enables us to perform the analysis in different directions, see Figure 2.5.

2.2.2 Pattern Characterization

Bioconvection patterns, even when they appear to be the same across the whole image, can consist of different patches that have different shapes and sizes. However, one of

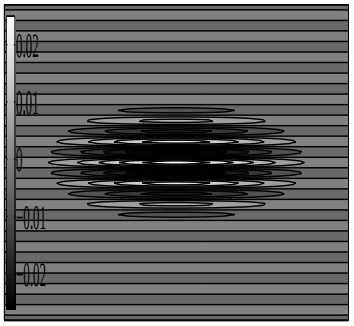

(a) The real part, $\theta = 0°$

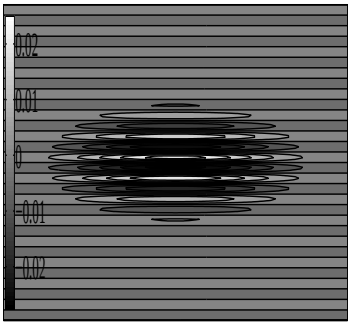

(b) The imaginary part, $\theta = 0°$

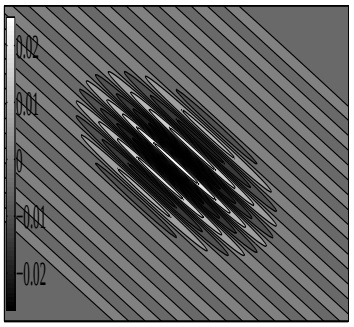

(c) The real part, $\theta = 45°$

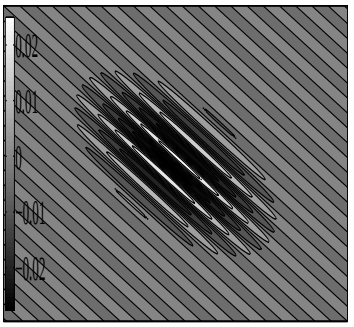

(d) The imaginary part, $\theta = 45°$

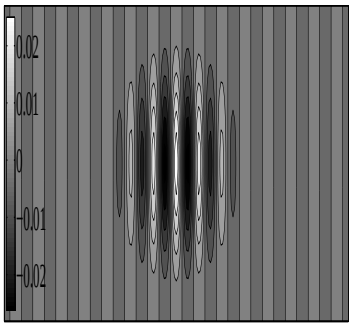

(e) The real part, $\theta = 90°$

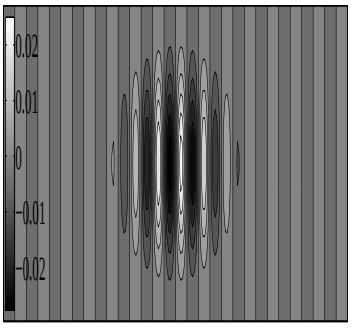

(f) The imaginary part, $\theta = 90°$

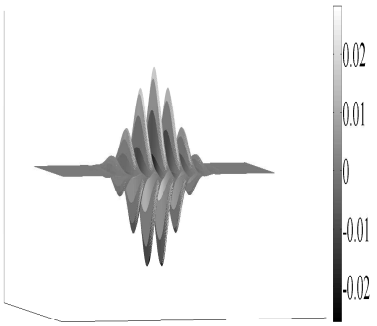

(g) The 3D plot of real part

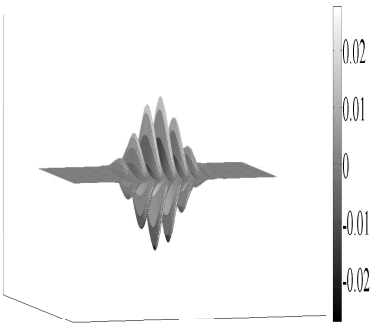

(h) The 3D plot of imaginary part

FIGURE 2.5: 2D complex Morlet wavelet. The scale $a = 20$ and $|k_\psi| = 6$. (a)−(f) show how the real and complex parts orientate with changing the direction θ. (g) and (h) are the real and complex parts 3D plot, respectively.

the measurements that can be used to scale these patterns is the wavenumber. In this investigation, Matlab software was used in order to utilize the two−dimensional complex Morlet wavelet, defined in (2.14), to investigate the pattern's characterization. A code was designed to extract the first and the second local dominant wavelengths associated with their directions as follows (see Appendix A, complex wavelet transform package yawtb is downloaded from the website http://www.fyma.ucl.ac.be/projects/yawtb and used in the code; see Antoine et al. [3])

1. Images were converted into the frequency domain using two dimensional Fast Fourier transform (FFT).

2. The two−dimensional continuous wavelet transform was proceeded for every fast Fourier transformed image, using equation (2.13), according to different scales in different directions. Equation (2.13) was selected since it is easier and faster to perform the two dimensional wavelet transform in the frequency domain than in the spacial domain.

3. As mentioned in Section 2.2.1, the two−dimensional complex Morlet family, (2.14) was selected with $|\mathbf{k}_\psi| = 6$ (Antoine et al. [3]), so that, the correction term can be numerically neglected since the estimated error is $\leq O\left(10^{-4}\right)$.

4. For a window of 256×256, the scale range of a in (2.13) $[1, 128]$ pixels. Thus, the wavelet basis function ψ is stretched to cover half of the window width.

5. The directions are picked to cover the the range $[0, 2\pi]$ with an increment of $\Delta\theta = \frac{\pi}{8}$, so that one revolves a full cycle around each pixel which results in well defined peaks; (see Figure 2.6).

6. Finally, the above transform is chosen to preserve the L^1 norm, in other words, $\zeta = 2$ in (2.9), (2.12) and (2.13). The reason behind that, is when carefully considering the amplitude spectrum

$$|\hat{\psi}_{a,\mathbf{b},\theta}(\mathbf{k})| = a^{-\zeta+2}|\hat{\psi}(ar_{-\theta}\mathbf{k})|, \tag{2.15}$$

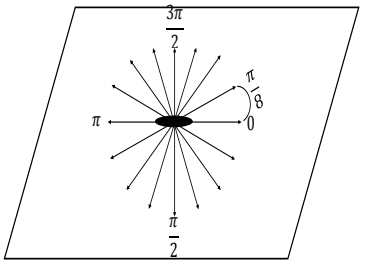

FIGURE 2.6: How the wavelet basis function is rotated at every pixel.

and the energy equation

$$E_{\psi_{a,\mathbf{b},\theta}} = a^{-2\zeta+2} E_{\psi}, \tag{2.16}$$

one can conclude that by preserving the L^2 norm the total energy in (2.16) will be preserved as one stretches or compresses the wavelet mother function. However, according to equation (2.15) this can amplify the low frequency components (a is large and the wavelet is stretched), and decay the high frequency components (a is small and the wavelet is compressed). To overcome this problem, the L^1 norm is selected to give a stable method.

For every location (pixel) $\mathbf{b} = (r, c)$, the output of the wavelet transform is 128×17 complex wavelet coefficients $S_{a,\mathbf{b},\theta}$. As the location is fixed, $S_{a,\mathbf{b},\theta}$ is a function of the scale, a and the direction, θ. Hence, the modulus $|S_{a,\mathbf{b},\theta}|$ is a two−dimensional function of a and θ. The wavelet analysis can not distinguish between the directions θ and $\theta + \pi$ as its unable to detect axial data (Mardia and Jupp [78]). Hence, to avoid the repetition, the peaks of $|S_{a,\mathbf{b},\theta}|$ between the directions $\left[\frac{\pi}{2}, \frac{3\pi}{2}\right)$ were extracted. $|S_{a,\mathbf{b},\theta}|$ reaches its maximum at say the scale, a_1, and the direction, θ_1. The scale, a_1, is converted to a wavelength, λ_1, by

$$\lambda_1 = 2\pi \frac{a_1}{|\mathbf{k}_{\psi}|}, \tag{2.17}$$

where $|\mathbf{k}_\psi| = 6$ (Viswanathan and Krishna [113] and Addison [2] and [1]). Now, λ_1 is the most local dominant wavelength and θ_1 is its associated direction at the location $\mathbf{b}$.

The extraction of the second local dominant wavelength is as follow

- Extract the second maximum of $|S_{a,\mathbf{b},\theta}|$ that is not located in a close angular neighborhood to the angle of the first maximum as it may be a secondary peak inside the main peak. Also, any second maximum that was less than half of the amplitude of the first peak was not be taken into account. Because these peaks may appear due to some noise in the data.
- Take the corresponding scale, a_2, and direction, θ_2.
- The second local dominant wavelength λ_2 can be calculated, using relation (2.17).

The analysis was performed on tested images as well as bioconvection images and the results are presented in the following subsection.

2.2.3 Test of the main and second peak detection

The image in Figure 2.7 was constructed using MATLAB to have a constant wavelength of 19.1 pixels at the directions $\frac{\pi}{4}$ and $\frac{3\pi}{4}$, so that $\lambda_1 = \lambda_2 = 19.1$, see Appendix A. Applying the analysis explained in Section 2.2.2, the results were a constant first and second dominant wavelength $\lambda_1 = \lambda_2 = 18.85$ pixels. The relative error is of order 10^{-2}. Figure 2.8 shows the peaks of $|S_{a,\mathbf{b},\theta}|$ at any location (pixel) in Figure 2.7. Clearly one can identify two peaks, one of which is at the direction $\frac{\pi}{4}$ and the other one is at the direction $\frac{3\pi}{4}$. This means that the image consists of two perpendicular waves both of wavelength 18.85 pixels, which means the pattern has a dot shape. This agrees with the theoretical results. Since the angle between the two directions is $\frac{\pi}{2}$, the scalar product of the first peak direction with the second peak direction is zero.

The image in Figure 2.9 was also constructed in MATLAB to consist of stripes tilted by an angle $\frac{\pi}{4}$ with wavelength of 18.1 pixels, (see Appendix A). The location $\mathbf{b} = (122, 128)$, marked with a green $\bullet$, was selected to perform the analysis. The result was that the

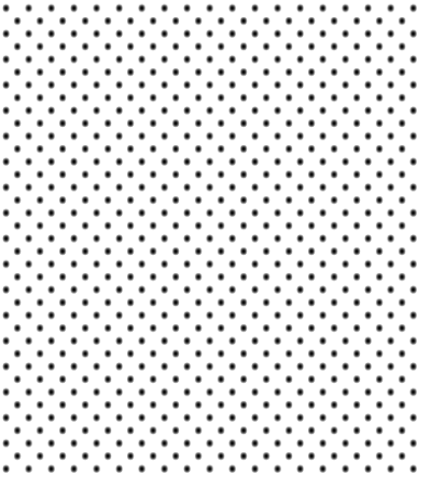

FIGURE 2.7: An image that was constructed using a MATLAB code to be analysed using Wavelet transform. The wavelength $\lambda_1 = \lambda_2 = 19.1$ pixels in either the direction $\frac{\pi}{4}$ or $\frac{3\pi}{4}$

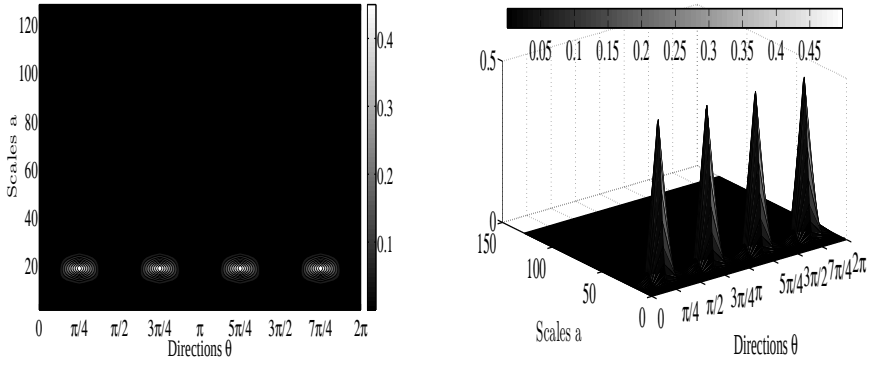

(a) (b)

FIGURE 2.8: (a) Contour plot of the modulus of the wavelet coefficients $S_{a,\mathbf{b},\theta}$, the bright area indicates the peaks. (b) 3D plot of the modulus of the wavelet coefficients $S_{a,\mathbf{b},\theta}$.

local dominant wavelength $\lambda_1 = 17.8$ at the direction $\theta_1 = \frac{\pi}{4}$. The contour plots in Figure 2.10 show that there is only one peak in the direction $\theta_1 = \frac{\pi}{4}$. This means that that the pattern consists of one wave of wavelength 17.8 pixels at the direction $\frac{\pi}{4}$, meaning that the pattern has rolls. The relative error between the theoretical wavelength and the one extracted from the analysis is also of order 10^{-2}.

The wavelet analysis was used to analyse an image of the nested circles that is displayed in Figure 2.11. (The nested circle image was downloaded from

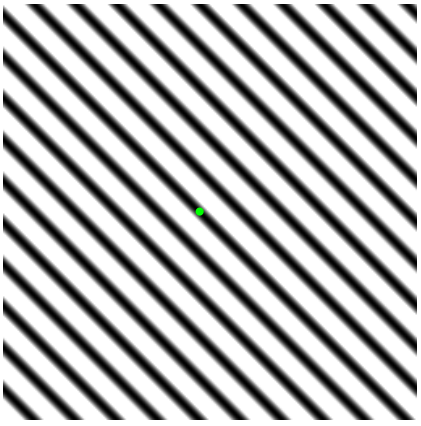

FIGURE 2.9: An image that was constructed using a MATLAB code to be analysed using Wavelet transform. The wavelength $\lambda_1 = 18.1$ pixels in the direction $\frac{\pi}{4}$.

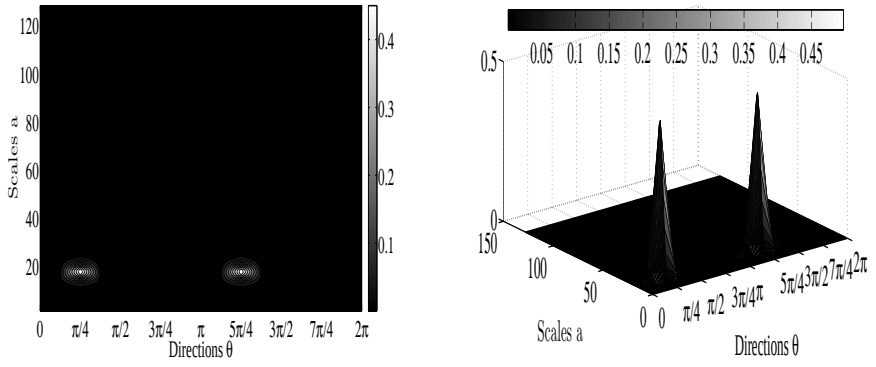

(a) (b)

FIGURE 2.10: (a) Contour plot of the modulus of the wavelet coefficients $S_{a,\mathbf{b},\theta}$, the bright area indicates the peaks. (b) 3D plot of the modulus of the wavelet coefficients $S_{a,\mathbf{b},\theta}$. The peak apears at the direction $\frac{\pi}{4}$

https://upload.wikimedia.org/wikipedia/commons/1/17/Concentric_circles_isotropy.svg.). Two locations were selected to show the wavelet spectrum. Figure 2.12(a) is a 2D contour plot of the complex wavelet coefficients $|S_{a,\mathbf{b},\theta}|$ at the location $\mathbf{b} = (150, 160)$, marked with a green •, whereas Figure 2.12(b) is their 3D plot. Both Figures 2.12(a) and 2.12(b) show that there is one local dominant wavelength $\lambda_1 = 18.85$ in the direction $\frac{3\pi}{4}$, see Figure 2.11. Figures 2.12(c) and 2.12(d) are the 2D and 3D contour plots of $|S_{a,\mathbf{b},\theta}|$ at the location $\mathbf{b} = (114, 113)$ at the centre of the pattern, marked by a red •. As expected

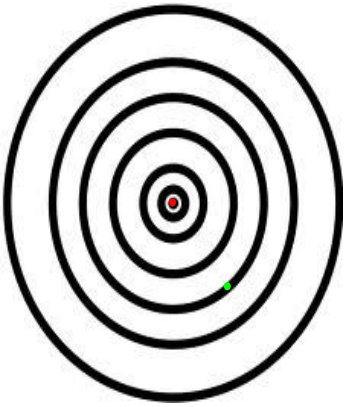

FIGURE 2.11: A nested circles pattern that was analysed by wavelet transform to extract the most local dominant wavelengths with two locations marked as green and red •.

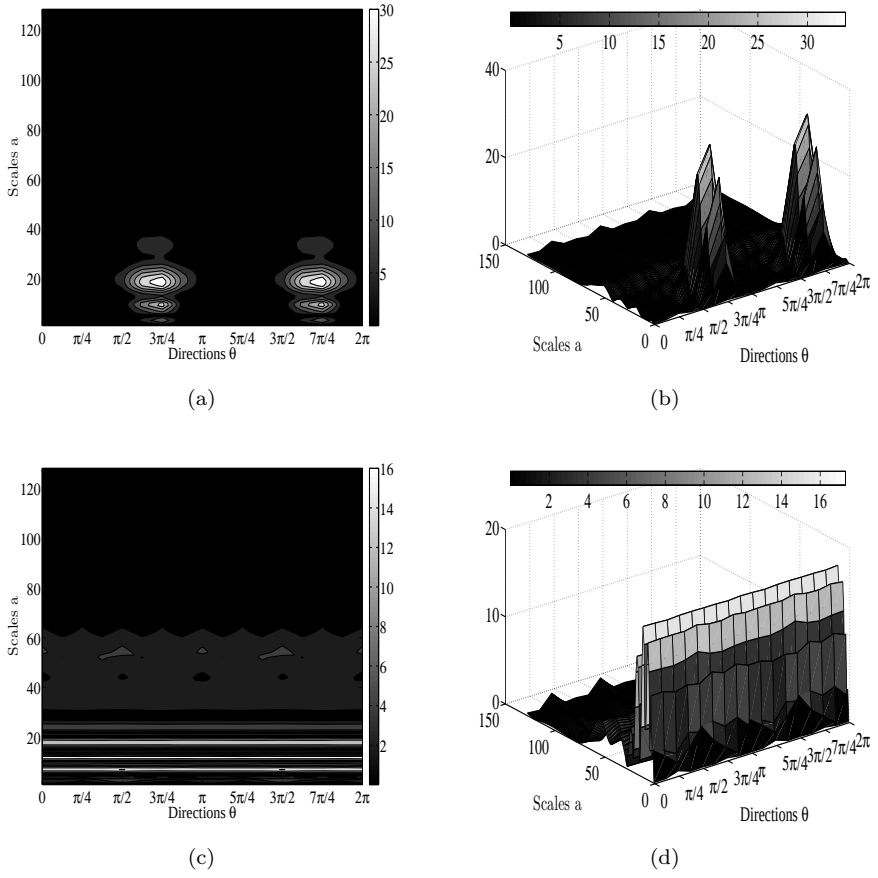

FIGURE 2.12: Analysis results of the two locations marked in Figure 2.11. (a) and (b) results for the green • whereas (c) and (d) are for the red •.

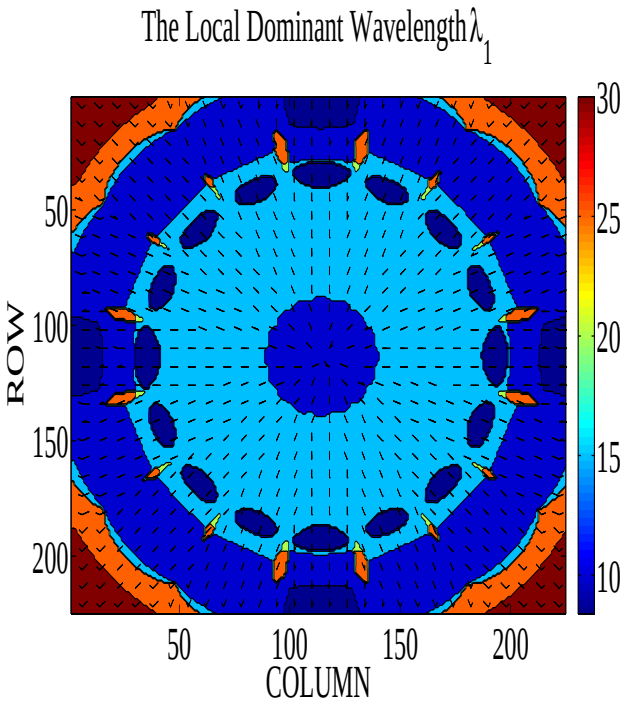

FIGURE 2.13: A contour plot of the most dominant wavelength measured in pixels associated with its direction and the second dominant direction of the nested circles in Figure 2.11.

from the rotational symmetry of the pattern this location has only one dominant wavelength with no preferred direction. The local dominant wavelength is $\lambda_1 = 12.57$ and it is the same in all directions from 0 to 2π. Figure 2.13 displays the contour plot of the most local dominant wavelength λ_1 together with its direction and the second local dominant wavelength direction. The direction of the first local dominant wavelength is always radial. Away from the edge of the image there is no second local dominant wavelength because of the symmetry of the pattern. Near the edges of the pattern the second local dominant wavelength is formed because of the edge effects.

2.3 Results

Bioconvection patterns of the bacteria *Bacillus subtilis* were also analysed, see Figure 2.14(a). The patterns consist of small circles that appear in the upper right of the image and they become larger as we move diagonally to lower left of the image. The

results of the most local dominant wavelength λ_1 were displayed in the contour plot, see figure 2.14(b). This plot shows that the patterns consists of patches of size up to 10 pixels on the upper right then the size of the these patches grows as one moves diagonally to the lower left to be 30 pixels.

Moreover, the code is used to analyse chemoconvection patterns in Figures 2.15(a) and 2.16(a). The results are shown in Figures 2.15(b) and 2.16(b). Figure 2.15(a), clearly shows that the patterns structure changes from approximately dots to lines as one moves cross the image from the top right to the bottom left with some variation in the spacing between the patches. Figure 2.15(b) displays the analysis results of Figure 2.15(a). The contour plot represents the most local dominant wavelength λ_1 and the long lines represents its associated direction whereas the small lines represents the the direction of the second most local dominant wavelength. The contour plot shows that the patterns distance from each others increase from around 15 pixels up to 35 pixels as one moves across the image. While the first and the second most local dominant wavelength directions indicates that the structure of the patches changes from dots on the top right side of the image to lines as one moves to the bottom left side of it.

Figure 2.16(a) shows patterns that are also formed by chemoconvection that consists of dote and lines that seems to be distributed uniformly across the whole image. However, the analysis results in Figure 2.16(b) indicates that there is variation of the spacing between pattern's patches as the wavelength λ_1 changes between 20 to 30 pixels. Also, the direction plot shows that the structure changes from dots to lines at some areas in the image.

2.4 Experimental Results for two−species algal bioconvection

Determining the onset of bioconvection patterns by looking at the images is confusing. So, following Pons et al. [91], the time evolution of the mean of the gray level $\bar{g}$, its standard deviation σ and the standard deviation derivative with respect to time $\dot{\sigma}$ were computed. In Pons et al. [91] the pattern appearance time was estimated by

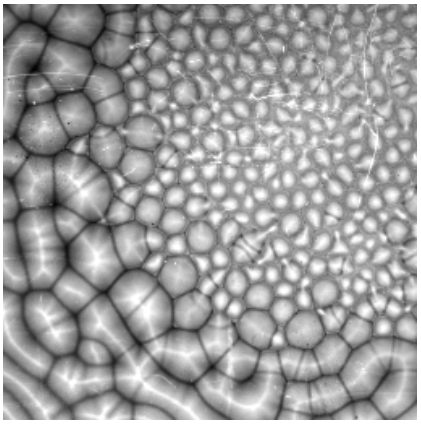

(a)

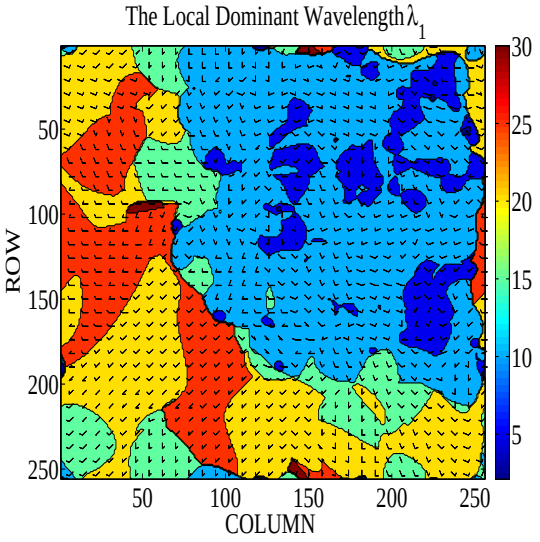

(b)

FIGURE 2.14: (a) Patterns formed by the bacteria *Bacillus subtilis* (M. A. Bees and A. Cooper private communications, 2015). (b) Contour plot of the most local dominant wavelength measured in pixels associated with its direction and the second dominant direction. The direction of the λ_1, presented by the long lines, and the direction of the second local dominant wavelength, presented by the short lines.

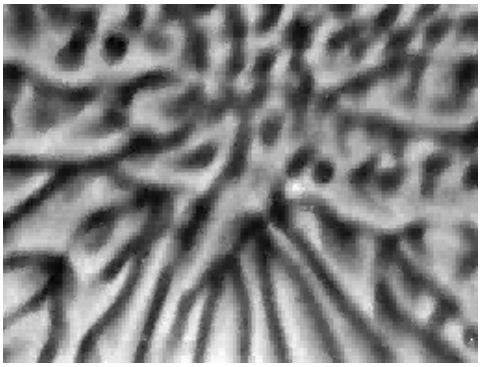

(a)

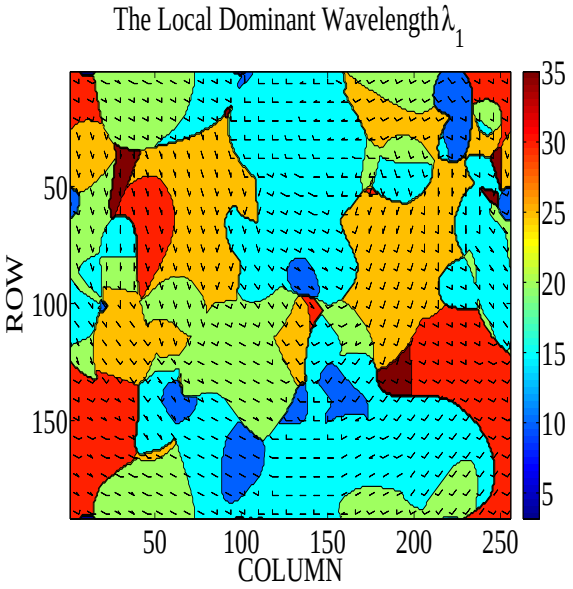

(b)

FIGURE 2.15: (a) Patterns formed by Chemoconvection (M. A. Bees and A. Cooper private communications, 2015). (b) Contour plot of the most local dominant wavelength measured in pixels associated with its direction and the second dominant direction. The direction of the λ_1, presented by the long lines, and the direction of the second local dominant wavelength, presented by the short lines.

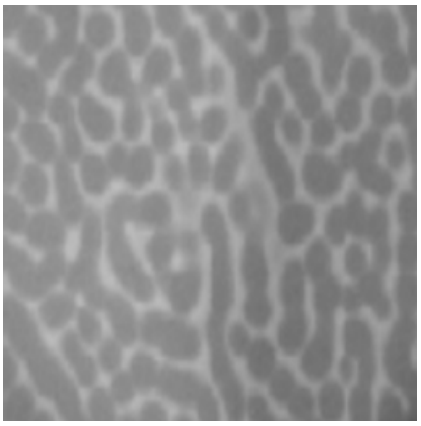

(a)

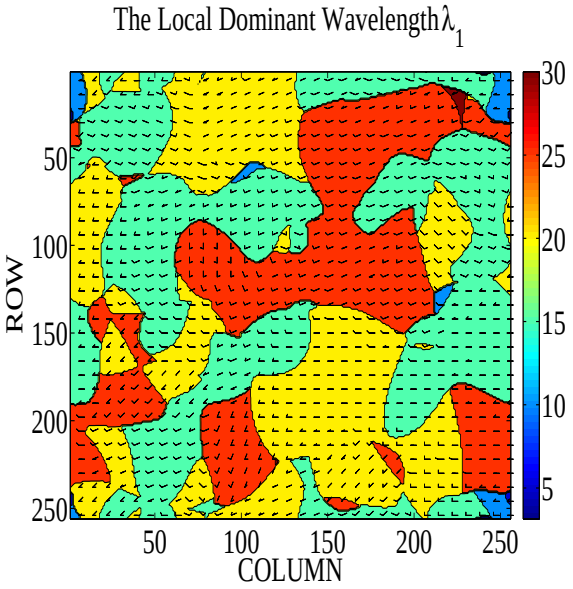

(b)

FIGURE 2.16: (a) Patterns formed by Chemoconvection (M. A. Bees and A. Cooper private communications, 2015). (b) Contour plot of the most local dominant wavelength measured in pixels associated with its direction and the second dominant direction. The direction of the λ_1, presented by the long lines, and the direction of the second local dominant wavelength, presented by the short lines.

picking the time that is associated with the increase in the mean $\bar{g}$ and the standard deviation σ. However, unlike their results, the mean $\bar{g}$ and the standard deviation σ in this investigation do not display a rapid change in their behavior. So, alternatively the standard deviation time derivative $\dot{\sigma}$ was utilized. The patterns appearance time, t_1, was selected as the time that corresponds to $\dot{\sigma} = 20\%$, in order to ensure the existence of a significant change in the cells distributions that might reflect on the patterns.

As mentioned in section 2.1, a suspension volume of 10 ml was placed in a petri dish of diameter 5.2 cm. So, the depth in this case is approximately 0.47 cm. For instance, a cell of *C.reinhardtii* that have a swimming speed of approximately 130 μm will take around 36 seconds to reach the upper surface which agrees to some extent to the estimated time $t_1 = 35$ seconds that coincides with $\dot{\sigma} \approx 20\%$, see Figure 2.19.

Since for every experiment a sequence of 151 images was recorded, it is difficult to display the results of all of these images. Thus, after specifying the time of patterns appearance (initial patterns), t_1, the time when $\dot{\sigma}$ reaches its maxima t_3, t_7 and minimum t_5 were estimated. Furthermore, the time t_2, t_4, and t_6 were evaluated to be the half time between $[t_1, t_3]$, $[t_3, t_5]$ and $[t_5, t_7]$, respectively, i. e. $t_2 = \frac{t_1+t_3}{2}$, $t_4 = \frac{t_3+t_5}{2}$ and $t_6 = \frac{t_5+t_7}{2}$. Then, the corresponding images were analysed. The time t_3 may be associated with the end of the linear growth regime and the patterns then may be driven by the nonlinear regime. The recorded images exhibit a rapid variation in the pattern structure then turns into a slow gradual variation that can hardly be seen by eye. By comparing that to the time evolution of $\dot{\sigma}$; (see Figure 2.19(a)), one can conclude that the sudden change in the pattern formation takes place as the time evolve between the times t_1 and t_5. Then, the change becomes smooth between the times t_5 and t_7. Thus, the above selected times were investigated, in order to cover different stages of patterns formations. Finally, when $\dot{\sigma}$ is steady, the patterns were noticed to be well−developed and a time t_8 were selected in order to analyse the corresponding patterns.

Clearly in the bioconvection images in Figure 2.17 and 2.22, the shape and size of features varies as the total and relative concentration varies. To investigate that, the analysis demonstrated in Section 2.2.1 was used. The results presents a range of wavelengths that has a minimum and a maximum value, see Table 2.3. Figures 2.20(c) and

2.20(d) shows that the initial wavelength $\lambda_{I,\max}$ tends to become smaller as one moves from 100% *C. reinhardtii* to 100% *C. augustae*. Also, it becomes slightly larger when the total concentration is diluted as shown in Figures 2.21(a), 2.21(c) and 2.21(e). For the long−term patterns, $\lambda_{\infty,\min}$ and $\lambda_{\infty,\max}$ are increasing as we dilute the total concentration and decreasing as we change the relative concentration from 100% *C. reinhardtii* to 100% *C. augustae*. However, the range $[\lambda_{\infty,\min}, \lambda_{\infty,\max}]$ does not show any trend to be wider or narrower, see Figures 2.20(a), 2.20(b), 2.21(b), 2.21(d) and 2.21(f). In Figures 2.20(a) and 2.20(b), for the 100% *C. augustae* labelled as 1a, the $\lambda_{\infty,\min}$ is very small. This might be because the spacing between the concentrated areas is very small. The linear regression fittings show that the local dominant wavelengths depend linearly on both the total and the relative concentration of the cells within the experimental accuracy. The linear regression value R^2 varies between the two values 0.7 and 0.9 which means that the data are well approximated by straight lines.

The images of the experimental results in Figures 2.24, 2.26 and 2.28 are presented in the arrangement, see Figure 2.23.

2.5 Discussion

In this chapter an experimental technique was developed to record bioconvection patterns in shallow suspensions as a function of total concentration and relative concentration between two mixed species. Also, a protocol for measuring the cell concentration was established together with a successful culture regime in order to have healthy and motile cells. Moreover, a novel method that employs the wavelet basis functions was developed to investigate the local spatial variation in these bioconvection patterns by extracting the most local dominant wavelength and its direction. The maximum value of the initial dominant wavelength $\lambda_{I,\max}$ and the range of the long term most local dominant wavelengths $[\lambda_{\infty,\min}, \lambda_{\infty,\max}]$ was extracted, as the minimum value $\lambda_{I,\min}$ of the most initial dominant wavelength indicates that the patterns has not been formed yet. It was found that the maximum value of the initial dominant wavelength increases as the total concentration decreases and it decreases as the relative concentration shifts

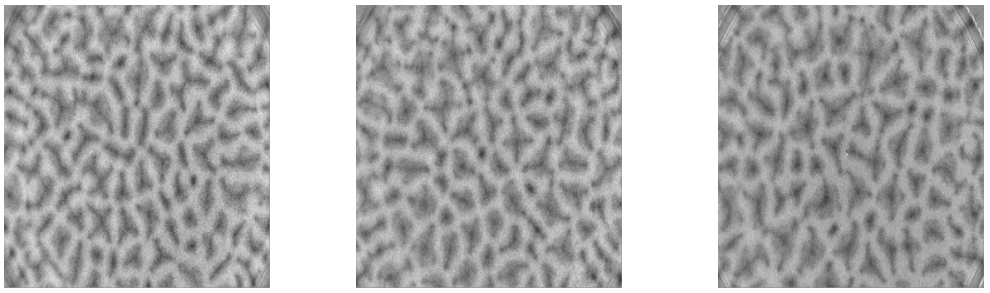

(a) 100% *C.a*

(b) 90%*C.a*:10%*C.r*

(c) 80%*C.a*:20%*C.r*

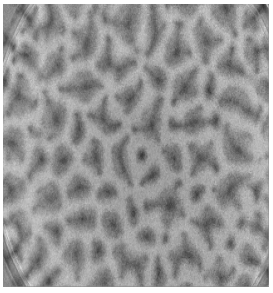

(d) 70%*C.a*:30%*C.r*

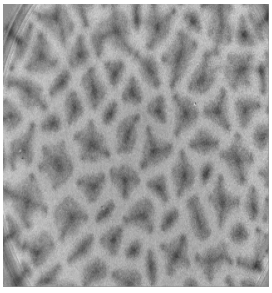

(e) 60%*C.a*:40%*C.r*

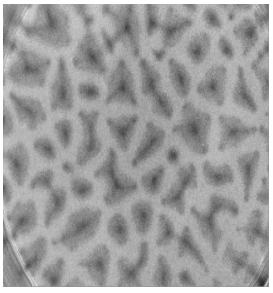

(f) 50%*C.a*:50%*C.r*

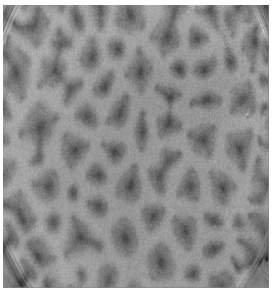

(g) 40%*C.a*:60%*C.r*

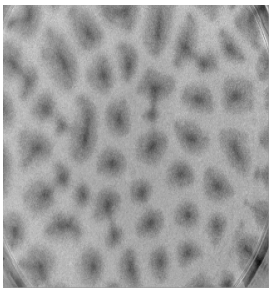

(h) 30%*C.a*:70%*C.r*

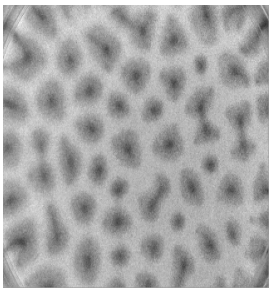

(i) 20%*C.a*:80%*C.r*

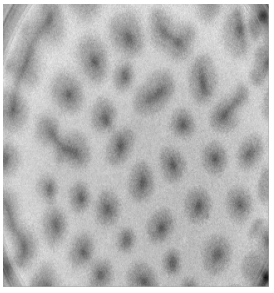

(j) 10%*C.a*:90%*C.r*

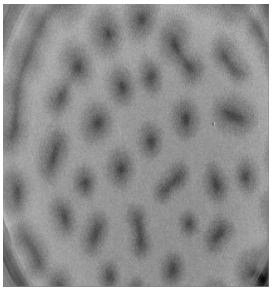

(k) 100% *C.r*

FIGURE 2.17: A smooth transition in the patterns as the relative concentration changes from 100% *C. augustae* in 2.17(a) to 100% *C. reinhardtii* in 2.17(k). The cell concentration is 4.2×10^6 cell per cm^3.

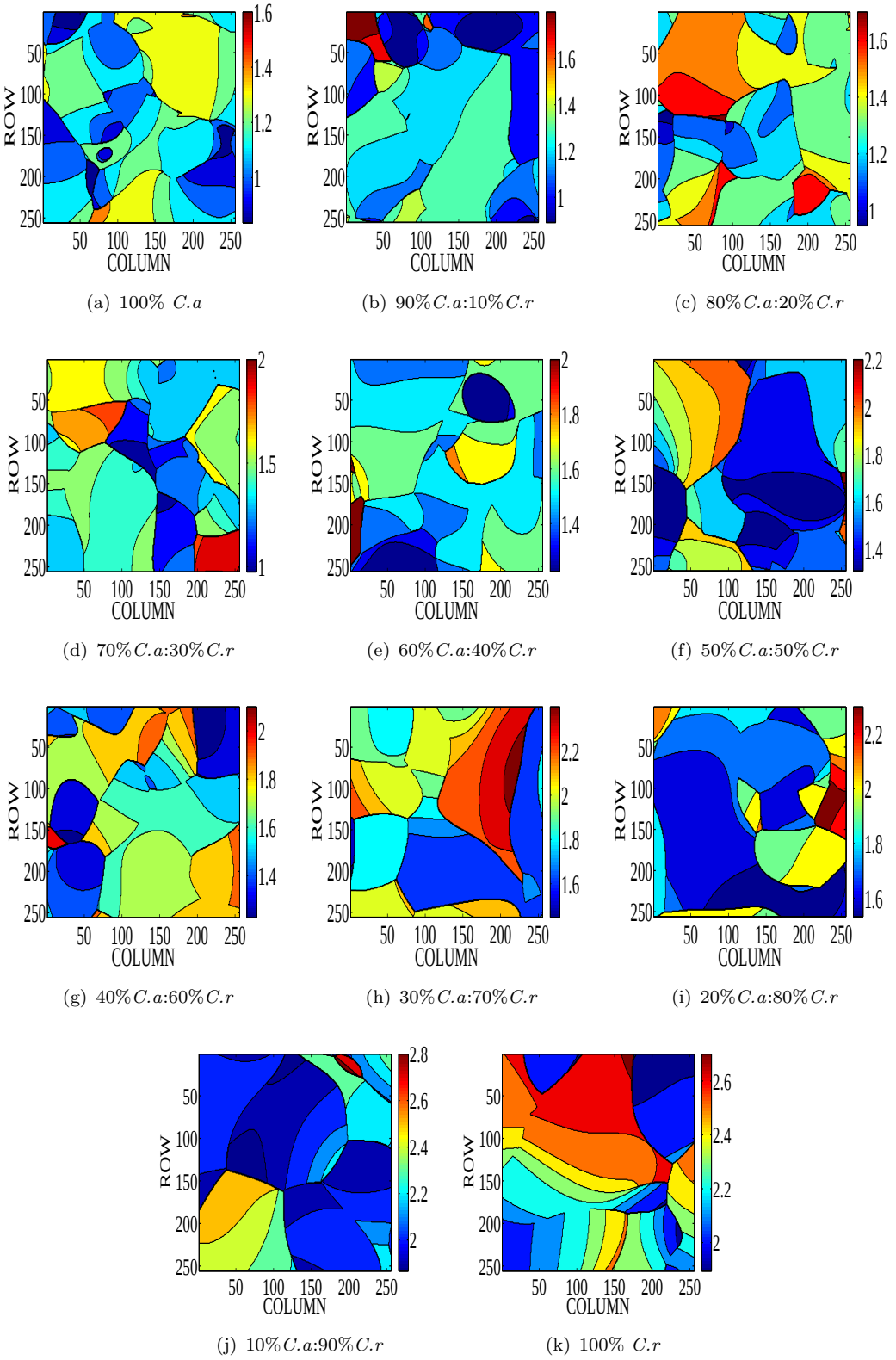

(a) 100% *C.a* (b) 90%*C.a*:10%*C.r* (c) 80%*C.a*:20%*C.r*

(d) 70%*C.a*:30%*C.r* (e) 60%*C.a*:40%*C.r* (f) 50%*C.a*:50%*C.r*

(g) 40%*C.a*:60%*C.r* (h) 30%*C.a*:70%*C.r* (i) 20%*C.a*:80%*C.r*

(j) 10%*C.a*:90%*C.r* (k) 100% *C.r*

FIGURE 2.18: A contour plot that displays how the dominant wavelength changes locally within the pattern. Also, it displays that this local dominant wavelength decreases as the relative concentration moves from 100% *C. reinhardtii* in 2.18(k) to 100% *C. augustae* in 2.18(a).

Exp name	$\lambda_{I,\min} cm$	$\lambda_{I,\max} cm$	$\lambda_{\infty,\min} cm$	$\lambda_{\infty,\max} cm$	Relative conc	Total conc $\frac{\text{cell}}{\text{cm}^{-3}}$
10r1	0.06	1.45	1.14	1.75	$100\% C.r$	1.1×10^7
10r2	0.06	2.23	1.5	2.26	$100\% C.r$	8.8×10^6
10r3	0.06	2.65	1.73	2.65	$100\% C.r$	6.6×10^6
10r4	0.06	2.23	2.06	2.40	$100\% C.r$	4.4×10^6
9r1a1	0.06	1.64	1.39	1.84	$90\% C.r$:$10\% C.a$	10^7
9r1a2	0.06	1.67	1.48	2.28	$90\% C.r$:$10\% C.a$	8×10^6
9r1a3	0.06	3.34	1.98	2.51	$90\% C.r$:$10\% C.a$	6×10^6
9r1a4	0.08	2.42	1.42	2.40	$90\% C.r$:$10\% C.a$	4×10^6
8r2a1	0.06	1.34	1.09	1.61	$80\% C.r$:$20\% C.a$	1.1×10^7
8r2a2	0.06	1.73	1.03	2	$80\% C.r$:$20\% C.a$	8.8×10^6
8r2a3	0.06	2.28	1.42	2.06	$80\% C.r$:$20\% C.a$	6.6×10^6
8r2a4	0.06	1.95	1.53	2.17	$80\% C.r$:$20\% C.a$	4.4×10^6
7r3a1	0.06	1.39	0.89	1.53	$70\% C.r$:$30\% C.a$	1.1×10^7
7r3a2	0.06	1.36	0.97	1.87	$70\% C.r$:$30\% C.a$	8.8×10^6
7r3a3	0.06	1.98	1.33	1.89	$70\% C.r$:$30\% C.a$	6.6×10^6
7r3a4	0.06	2.03	1.23	2.17	$70\% C.r$:$30\% C.a$	4.4×10^6
6r4a1	0.06	1.5	0.78	1.53	$60\% C.r$:$40\% C.a$	1.1×10^7
6r4a2	0.06	1.45	0.89	1.61	$60\% C.r$:$40\% C.a$	8.8×10^6
6r4a3	0.06	1.78	1.18	1.81	$60\% C.r$:$40\% C.a$	6.6×10^6
6r4a4	0.06	2.06	1.03	2.23	$60\% C.r$:$40\% C.a$	4.4×10^6
5r5a1	0.06	1.31	0.75	1.34	$50\% C.r$:$50\% C.a$	1.1×10^7
5r5a2	0.06	1.45	0.72	1.42	$50\% C.r$:$50\% C.a$	8.8×10^6
5r5a3	0.06	1.67	0.92	1.73	$50\% C.r$:$50\% C.a$	6.6×10^6
5r5a4	0.06	1.78	1.03	2.03	$50\% C.r$:$50\% C.a$	4.4×10^6
4r6a1	0.06	1.39	0.72	1.28	$40\% C.r$:$60\% C.a$	1.1×10^7
4r6a2	0.06	1.28	0.86	1.45	$40\% C.r$:$60\% C.a$	8.8×10^6
4r6a3	0.06	1.56	0.97	1.87	$40\% C.r$:$60\% C.a$	6.6×10^6
4r6a4	0.06	1.81	1.31	1.67	$40\% C.r$:$60\% C.a$	4.4×10^6
3r7a1	0.06	0.61	0.67	1.2	$30\% C.r$:$70\% C.a$	10^7
3r7a2	0.06	1.59	0.81	1.34	$30\% C.r$:$70\% C.a$	8×10^6
3r7a3	0.06	1.42	0.72	1.48	$30\% C.r$:$70\% C.a$	6×10^6
3r7a4	0.06	1.67	0.86	1.78	$30\% C.r$:$70\% C.a$	4×10^6
2r8a1	0.06	1.11	0.64	1.03	$20\% C.r$:$80\% C.a$	1.1×10^7
2r8a2	0.06	1.28	0.7	1.14	$20\% C.r$:$80\% C.a$	8.8×10^6
2r8a3	0.06	1.20	0.75	1.53	$20\% C.r$:$80\% C.a$	6.6×10^6
2r8a4	0.06	1.61	0.81	1.53	$20\% C.r$:$80\% C.a$	4.4×10^6
1r9a1	0.06	0.95	0.67	0.95	$10\% C.r$:$90\% C.a$	10^7
1r9a2	0.06	1.31	0.72	1.22	$10\% C.r$:$90\% C.a$	8×10^6
1r9a3	0.06	1.25	0.70	1.31	$10\% C.r$:$90\% C.a$	6×10^6
1r9a4	0.06	1.42	0.78	1.64	$10\% C.r$:$90\% C.a$	4×10^6
10a1	0.06	1	0.11	1.17	$100\% C.a$	6.5×10^6
10a2	0.06	1.18	0.67	1.18	$100\% C.a$	5.2×10^6
10a3	0.06	1.56	0.08	1.28	$100\% C.a$	3.9×10^6

TABLE 2.3: The Experimental results after performing wavelet analysis. λ_I is the initial wavelength at t_1 and λ_∞ is the long term wavelength at t_8. Since the analysis was performed at every location (pixel), the results were a range of wavelengths that have minimum and maximum values.

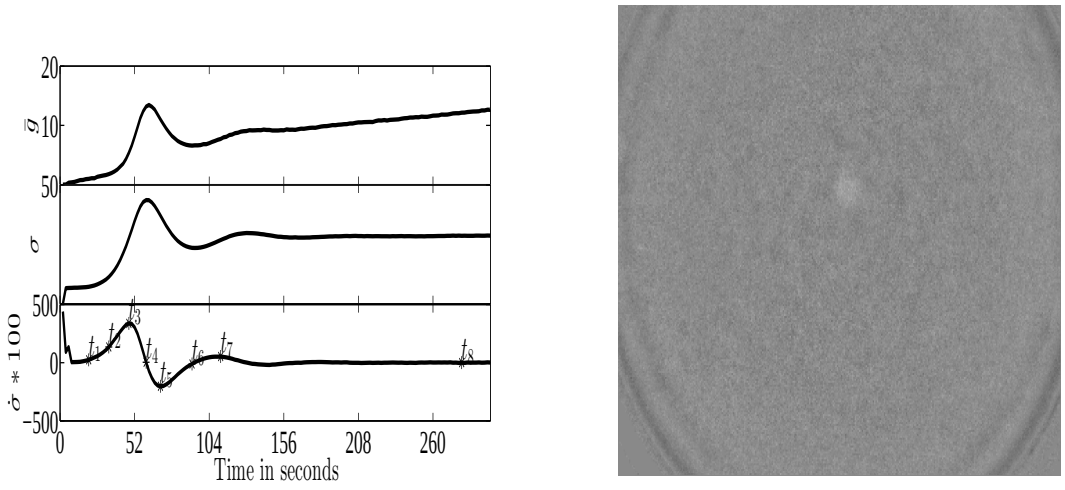

(a) (b)

FIGURE 2.19: (a) The time evolution of the mean of the gray level $\bar{g}$ of the image, the gray level standard deviation σ and $\dot{\sigma}$. (b) The pattern at the onset time t_1, where $\dot{\sigma}(t_1) \approx 20\%$, of the 100% *C. reinhardtii*.

from 100% *C. reinhardtii* to 100% *C. augustae*. It was also found that the range of the long−time local dominant wavelength increases with decreasing total concentration and decreases when shifting the relative concentration from 100% *C. reinhardtii* to 100% *C. augustae*. However, the range $[\lambda_{\infty,\min}, \lambda_{\infty,\max}]$ does not display any tendency to decrease or increase when changing either the total concentration or the relative concentration.

Figure 2.17 displays a sequence of bioconvection images that were recorded during the experiments. Starting from Figure 2.17(a) to Figure 2.17(k), the relative concentration varies from 100% *C. augustae* to 100% *C. reinhardtii* with a step size of 10% the total concentration is 4.2×10^6 cells per cm^3. The images show diversity between the shapes and sizes of the these patterns. In the case of 100% *C. augustae* Figure 2.17(a), the shapes of the concentrated patches diverge between lines, X and Y shape and the spacing between them is very small. On the other hand, Figure 2.17(k) shows that the patches of the 100% *C. reinhardtii* are dots with large spacing between them. Moreover, the existence of the *C. reinhardtii* influences the patterns shape when it occupies 50% of the total concentration while the *C. augustae* effect starts to disappear when it consists 30% of the total concentration. This may be because the *C. augustae* cell is larger in volume than the *C. reinhardtii* cell. Figure 2.18 displays the change in the most

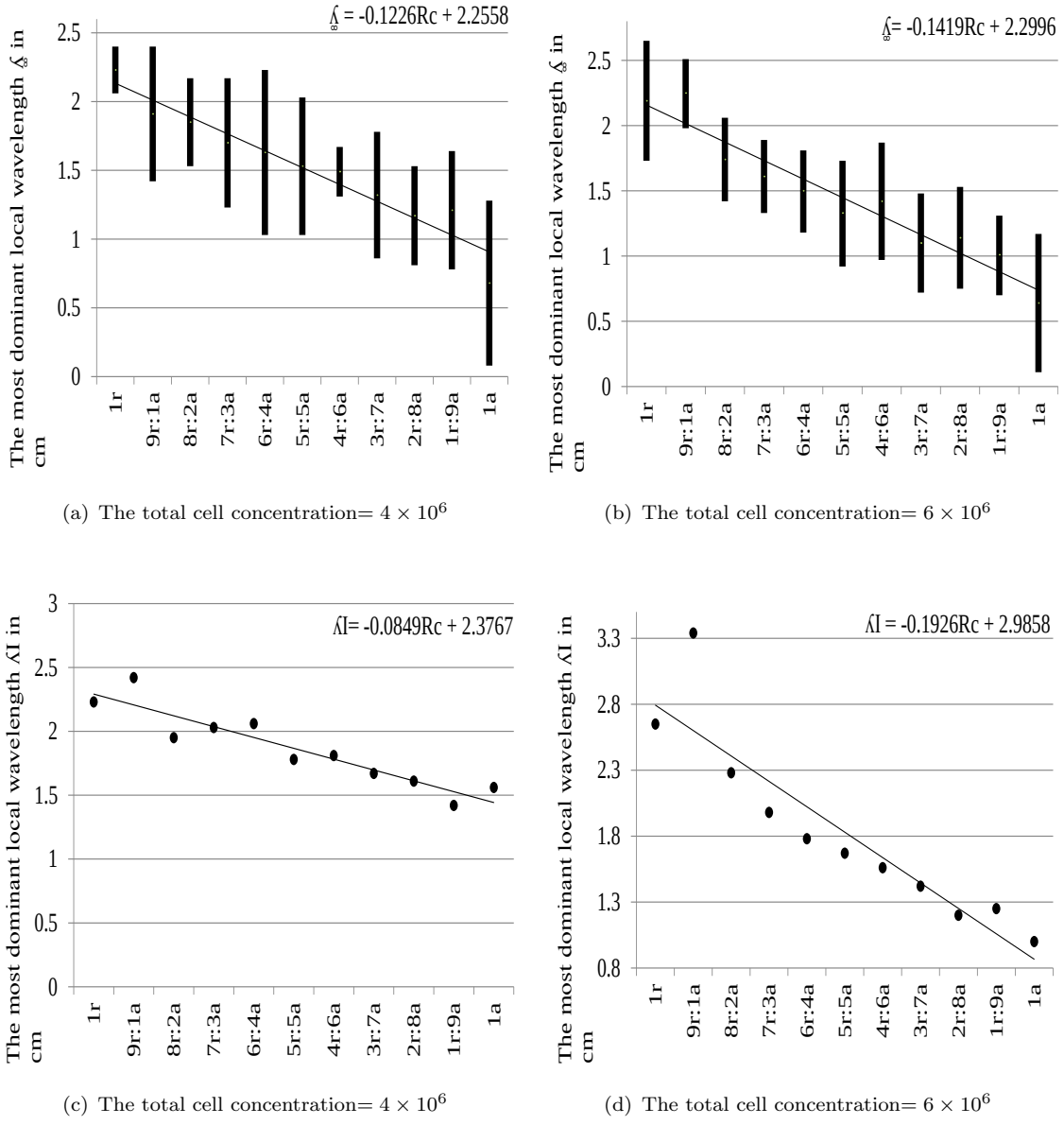

(a) The total cell concentration= 4×10^6

(b) The total cell concentration= 6×10^6

(c) The total cell concentration= 4×10^6

(d) The total cell concentration= 6×10^6

FIGURE 2.20: (a) and (b) are bar plots for the range of the most dominant wavelength for the developed patterns $[\lambda_{\infty,\min}, \lambda_{\infty,\max}]$ versus the relative concentration. The vertical axis represents the wavelength measured in cm while the horizontal axis represents the change in the relative concentration between 100% *C. r* (1r) to 100% *C. a* (1a). (c) and (d) are the scatter plot of the most initial dominant wavelength versus the relative concentration. The vertical axis represents the wavelength measured in cm while the horizontal axis represents the change in the relative concentration between 100% *C. r* (1r) to 100% *C. a* (1a).

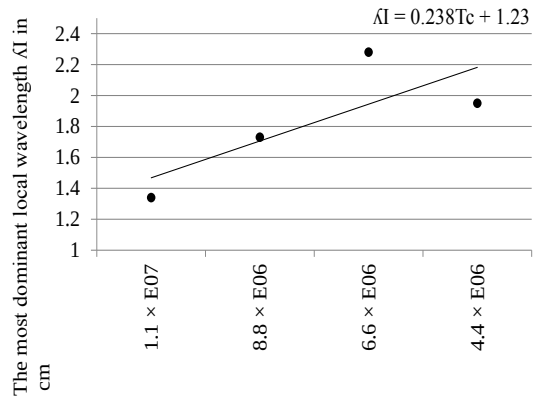

(a) 80% *C. r* : 20% *C. a*

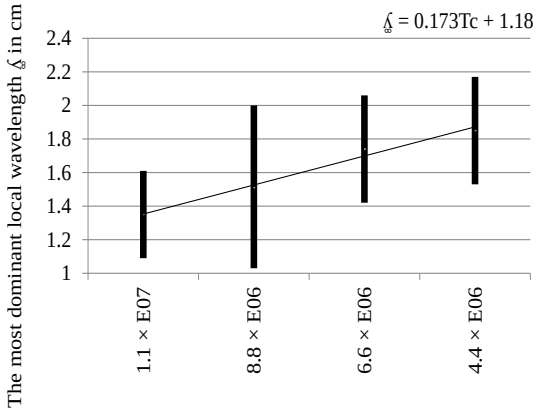

(b) 80% *C. r* : 20% *C. a*

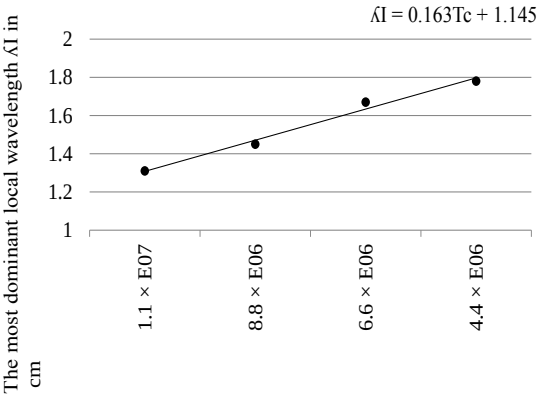

(c) 50% *C. r* : 50% *C. a*

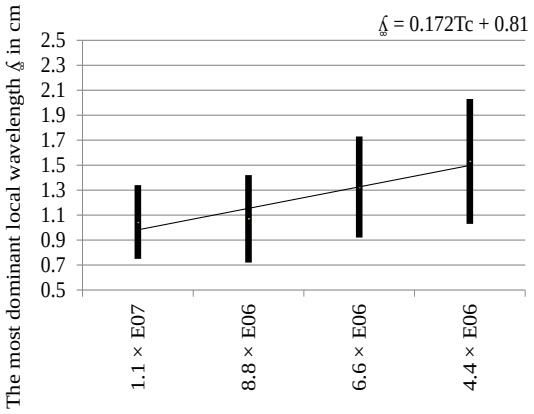

(d) 50% *C. r* : 50% *C. a*

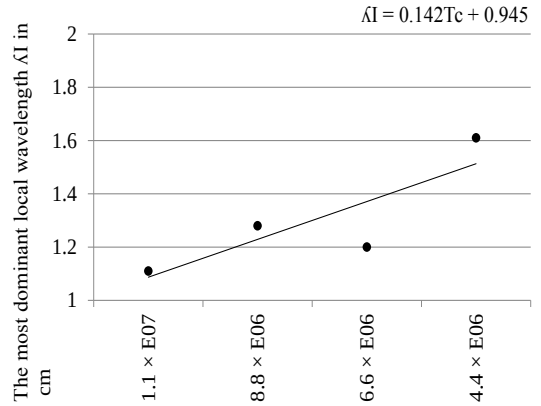

(e) 20% *C. r* : 80% *C. a*

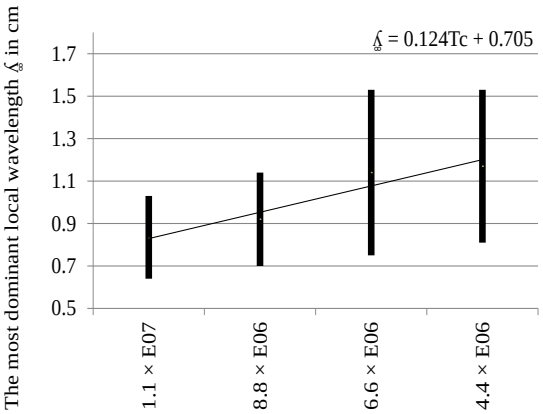

(f) 20% *C. r* : 80% *C. a*

FIGURE 2.21: (a), (c) and (e) are bar plots for the range of the most dominant wavelength for the developed patterns $[\lambda_{\infty,\min}, \lambda_{\infty,\max}]$ versus the total concentration. The vertical axis represents the wavelength measured in cm while the horizontal axis represents the change in the total concentration. (b), (d) and (f) are the scatter plot of the most initial dominant wavelength versus the total concentration. The vertical axis represents the wavelength measured in cm while the horizontal axis represents the change in the total concentration.

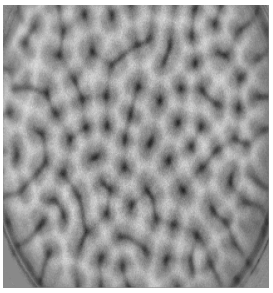

(a) 100% *C. r* of $C_T = 1.1 \times 10^7$

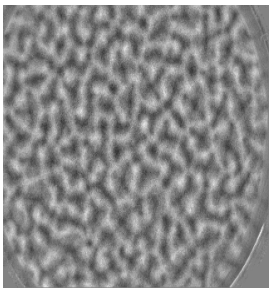

(b) 50% *C. r* : 50% *C. a* of $C_T = 1.1 \times 10^7$

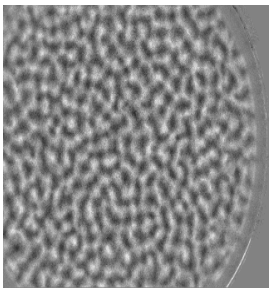

(c) 10% *C. r* : 90% *C. a* of $C_T = 10^7$

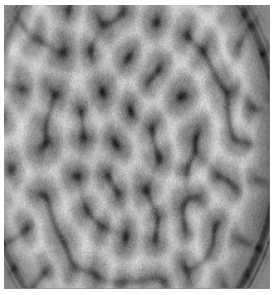

(d) 100% *C. r* of $C_T = 8.8 \times 10^6$

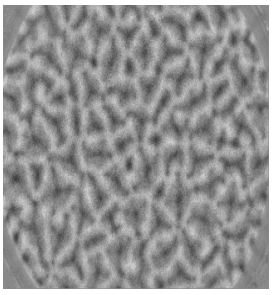

(e) 50% *C. r* : 50% *C. a* of $C_T = 8.8 \times 10^6$

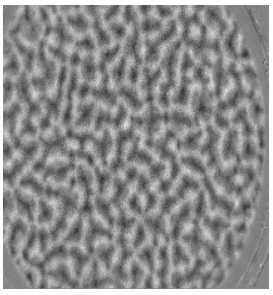

(f) 10% *C. r* : 90% *C. a* of $C_T = 8 \times 10^6$

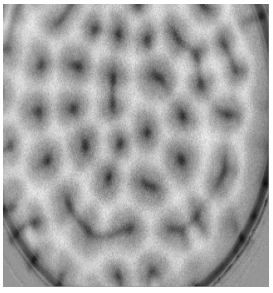

(g) 100% *C. r* of $C_T = 6.6 \times 10^6$

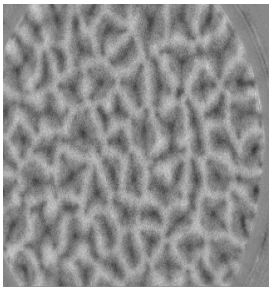

(h) 50% *C. r* : 50% *C. a* of $C_T = 6.6 \times 10^6$

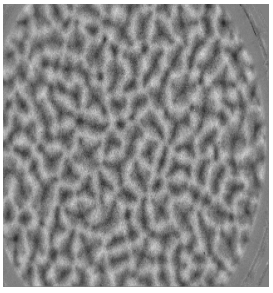

(i) 10% *C. r* : 90% *C. a* of $C_T = 6 \times 10^6$

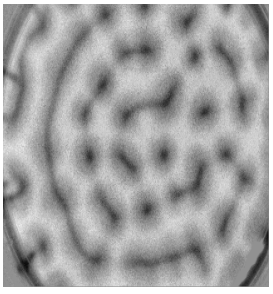

(j) 100% *C. r* of $C_T = 4.4 \times 10^6$

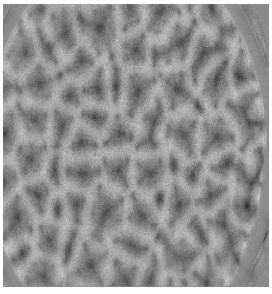

(k) 50% *C. r* : 50% *C. a* of $C_T = 4.4 \times 10^6$

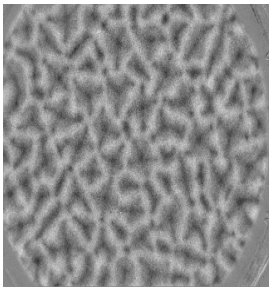

(l) 10% *C. r* : 90% *C. a* of $C_T = 4 \times 10^6$

FIGURE 2.22: The transition in the pattern formation as the total concentration changes. (a), (g), (d) and (i) are patterns formed by 100% *C. r* starting with total concentration 1.1×10^7. (b), (e), (h) and (k) are patterns formed by 50% *C. r* and 50% *C. a* starting with total concentration 1.1×10^7. Finally, (c), (f), (i) and (l) are patterns formed by 10% *C. r* and 90% *C. a* starting with total concentration 10^7.

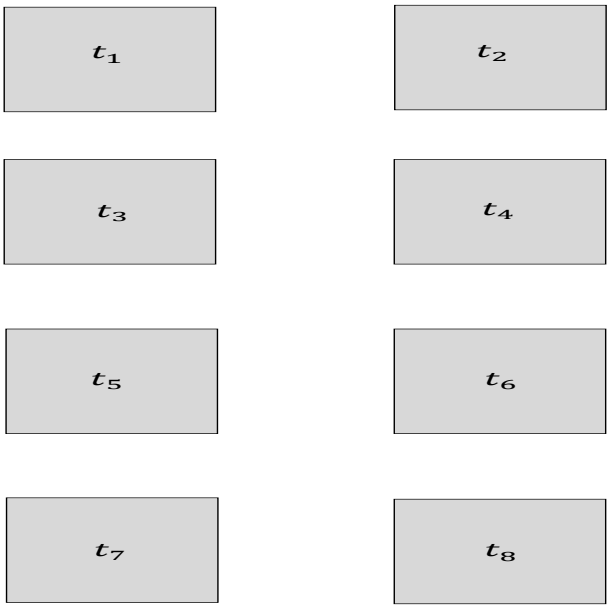

FIGURE 2.23: Image arrangement.

dominant wavelength locally within the pattern. Also, the colourmap bar demonstrates that generally the long term range of the most local dominant wavelength increases as one shifts from 100% *C. augustae* to 100% *C. reinhardtii*.

Figure 2.24, 2.26 and 2.28 are bioconvection images that shows pattern evolution with time of the suspensions that consist of 100% *C. reinhardtii* with total concentration 1.1×10^7, 100% *C. augustae* with total concentration 6.5×10^6 and 50% *C. reinhardtii* and 50% *C. augustae*, respectively. The analysis results of these images are contour plotted in the Figures 2.25, 2.27 and 2.29, respectively. The colourmap bar represents the most dominant local wavelength of these patterns. These figures shows that, the patterns start to form in small areas within the dish then it grows to cover the whole dish. Also, the colourmap bar indicates that the most dominant initial wavelength grows up to a certain time then it falls as the patterns are fully developed. In the case of 100% *C. augustae* with total concentration 6.5×10^6, Figure 2.27 shows that initially the most dominant wavelength is approximately $[0.06, 1]$ cm then it increases to

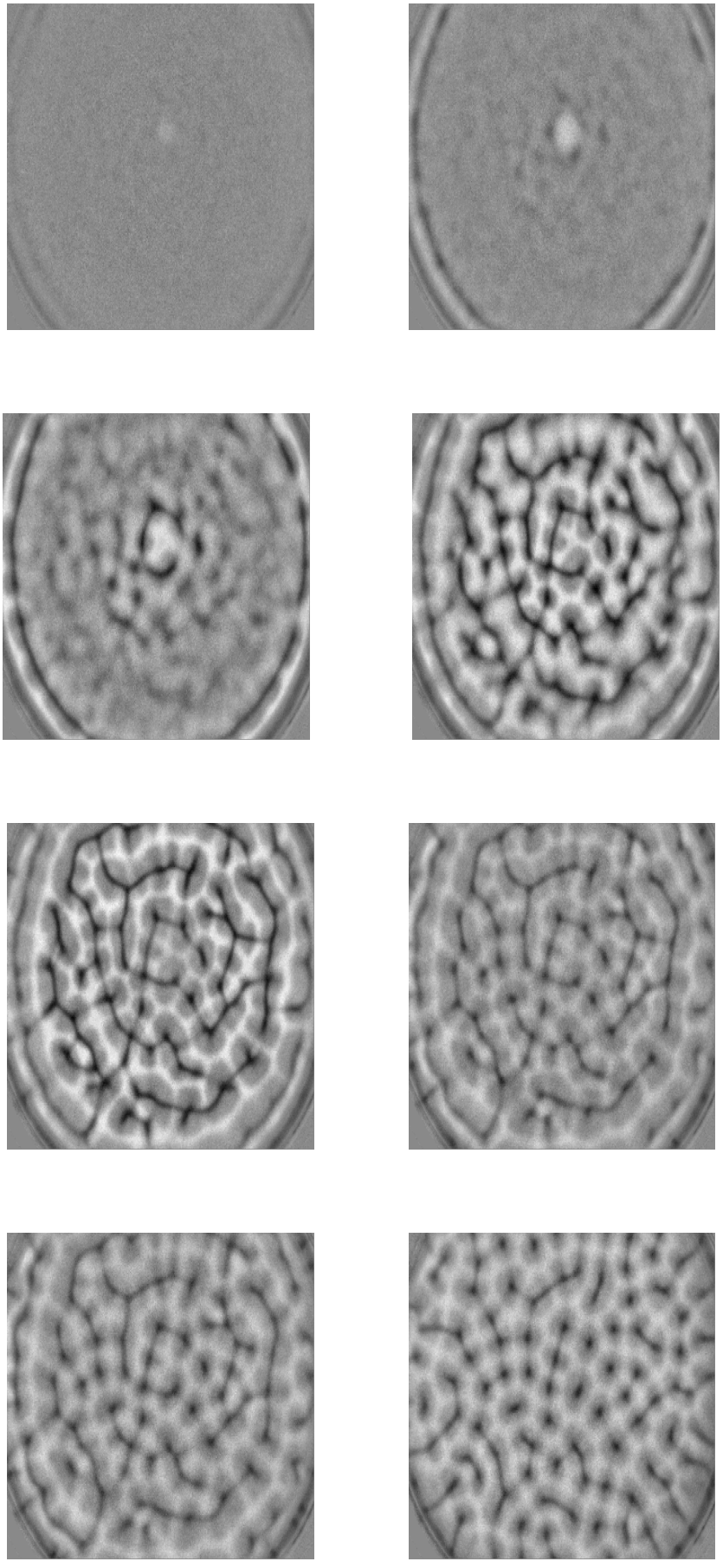

FIGURE 2.24: Experiment 10r1 of 100% *C. r* with total concentration of 1.1×10^7 cell per cm^3. These image show how patterns evolve with time.

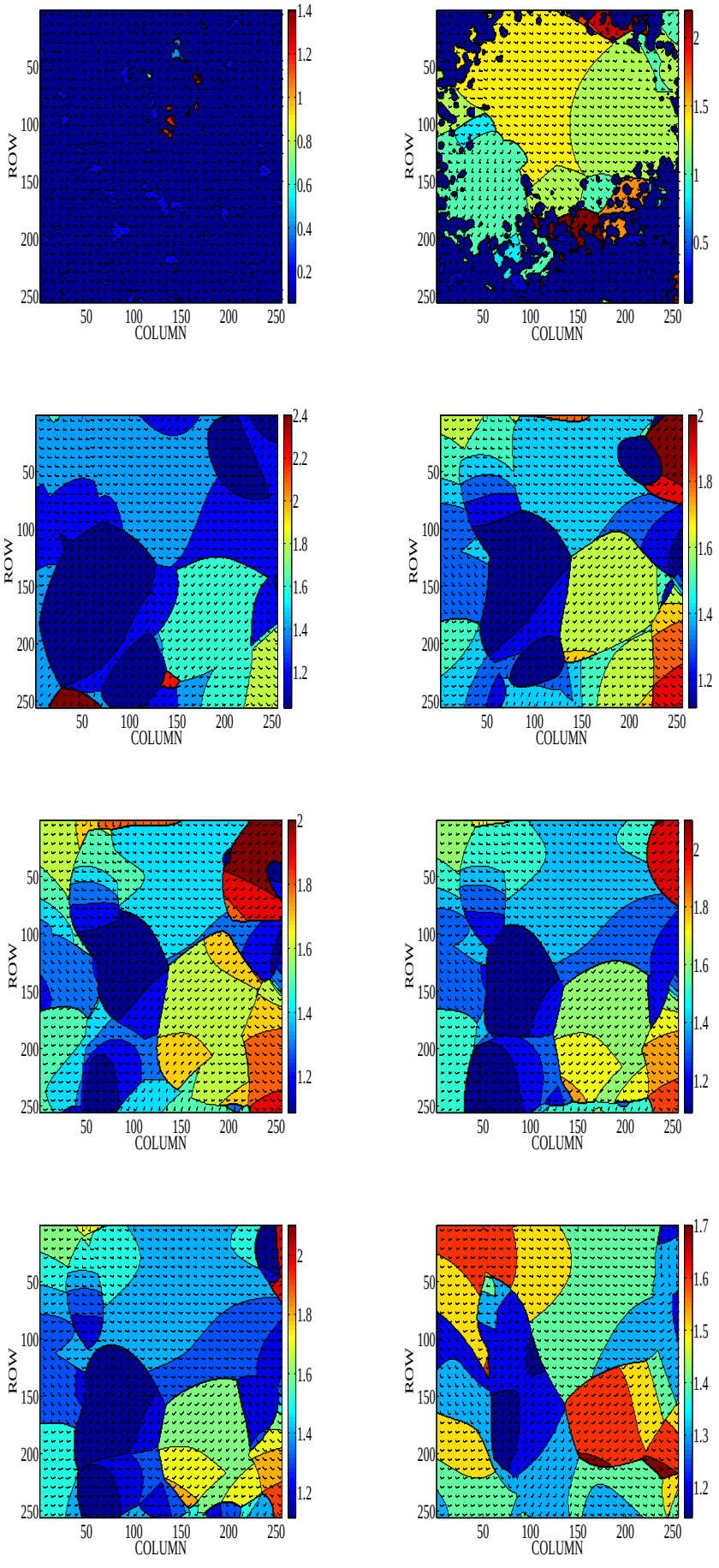

FIGURE 2.25: Contour plot of the experiment 10r1 images of 100% *C. r.*

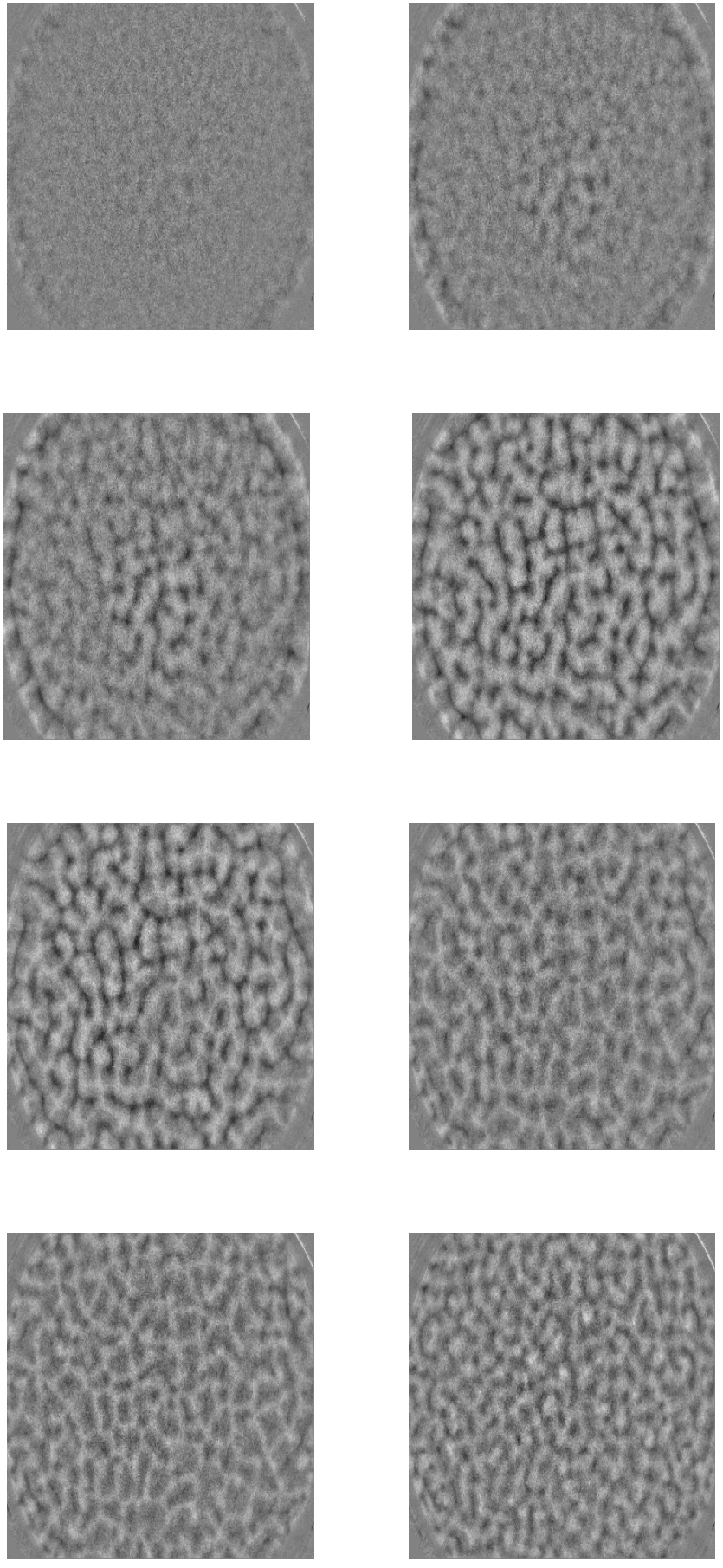

FIGURE 2.26: Experiment 10a1 of 100% *C. a* with total concentration of 6.5×10^6 cell per cm^3. These image show how patterns evolve with time.

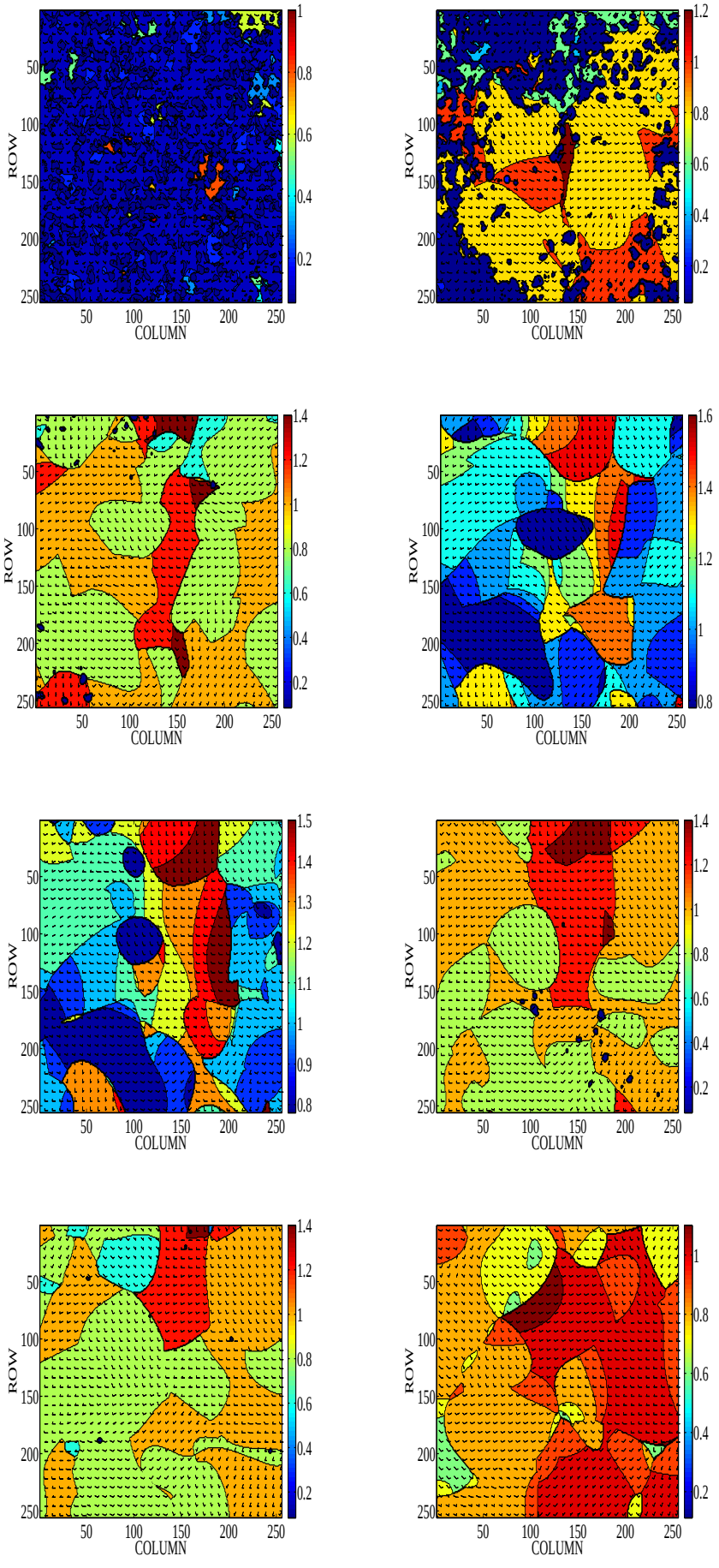

FIGURE 2.27: Contour plot of the experiment 10a1 images of 100% *C. a.*

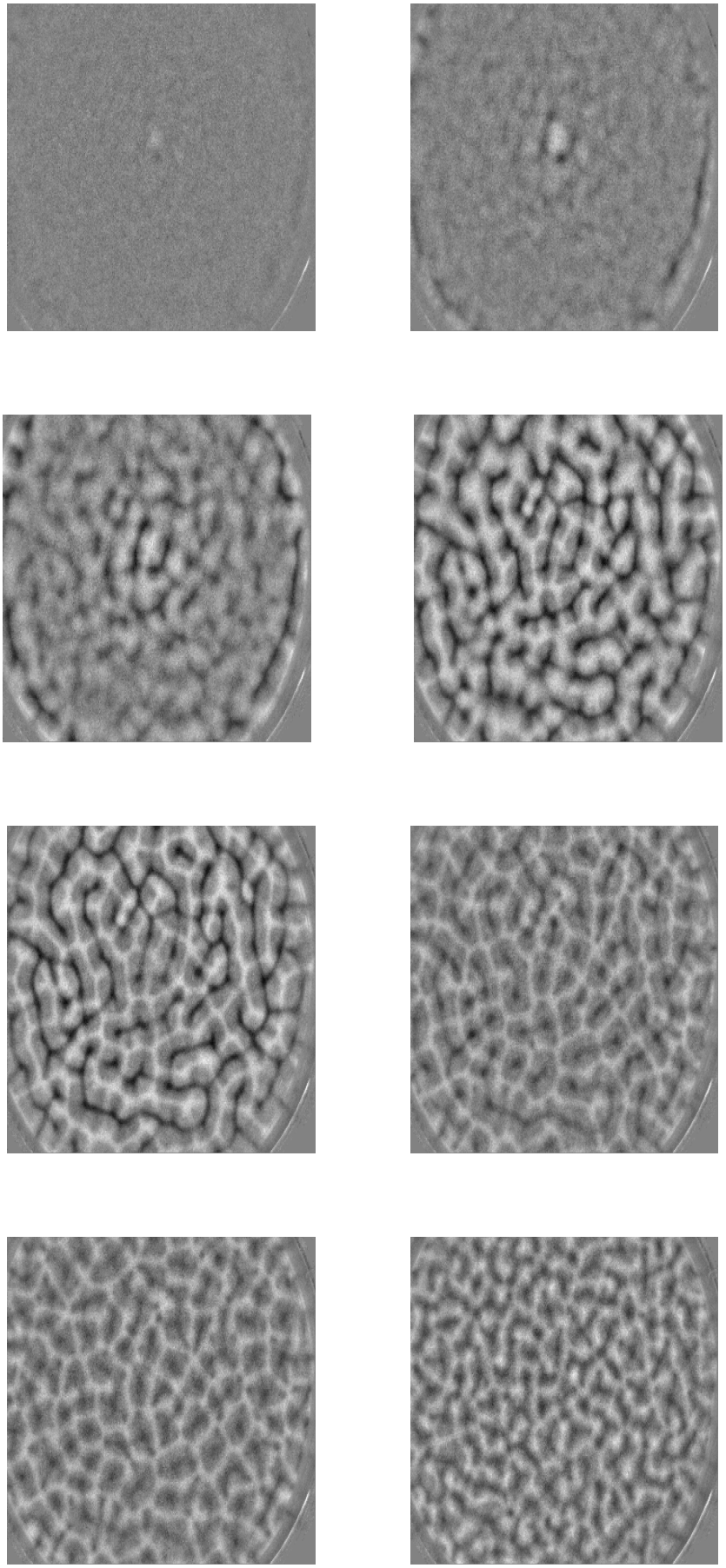

FIGURE 2.28: Experiment 5r5a1 of 50% *C. r* and 50% *C. a* with total concentration of 1.1×10^7 cell per cm^3. These image show how patterns evolve with time.

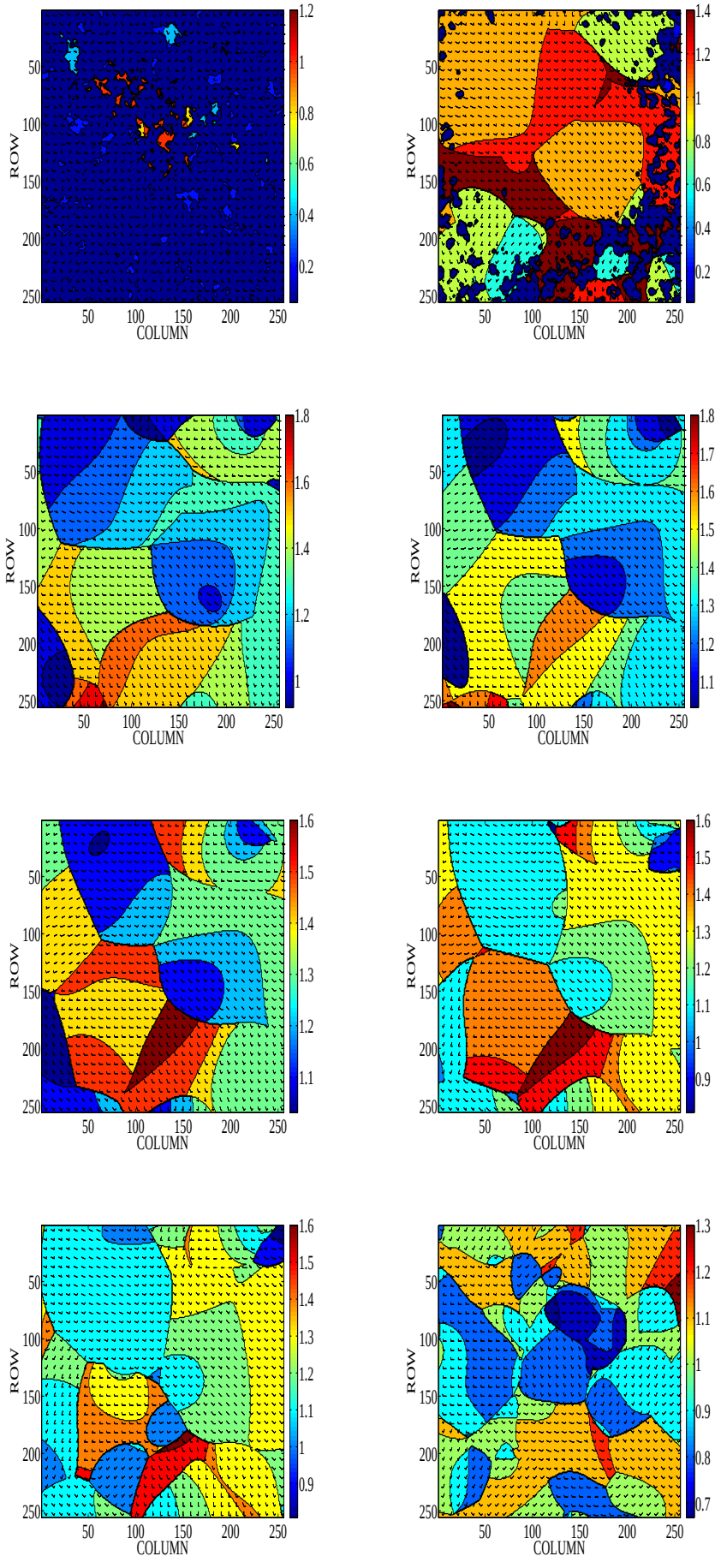

FIGURE 2.29: Contour plot of the experiment 5r5a1 images of 50% $C.$ r and 50% $C.$ $a.$

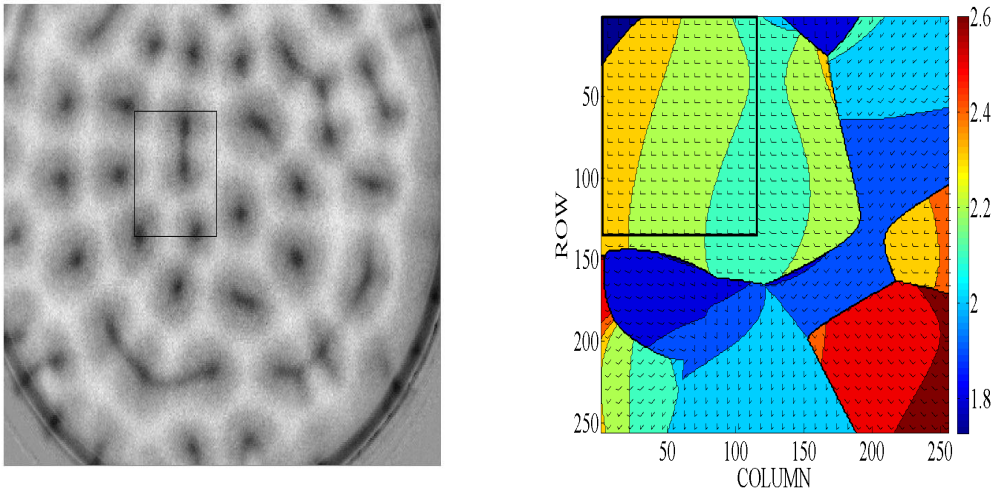

(a) (b)

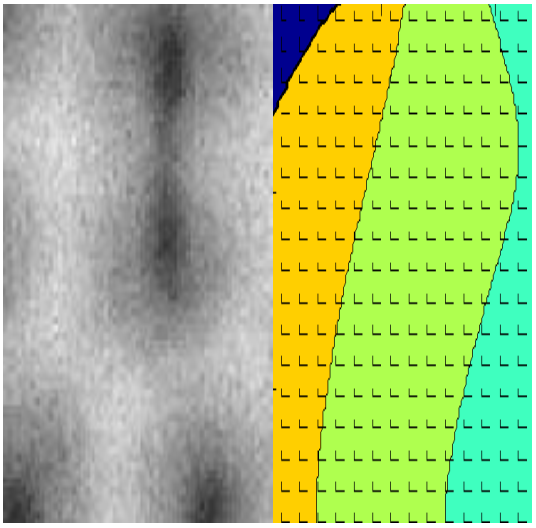

(c)

FIGURE 2.30: (a) Patterns formed by 100% *C. r* with total concentration of 6.6×10^6. (b) Contour plot of the the most local dominant wavelength superimposed with its direction and the direction of the second dominant wavelength. (c) The areas in the boxes are enlarged, the contour on the left side and the bioconvection image on the right side. The first and the second directions are perpendicular to each others which indicated that the patterns have square structure.

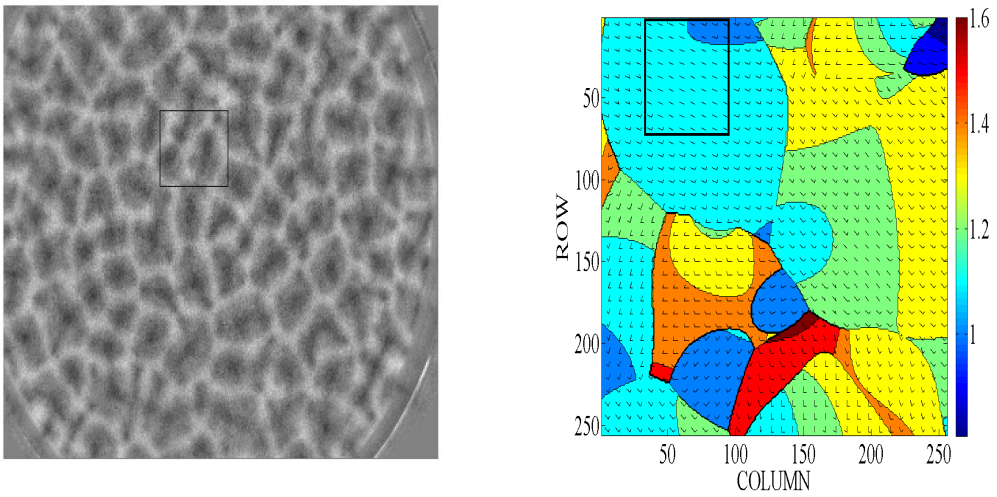

(a) (b)

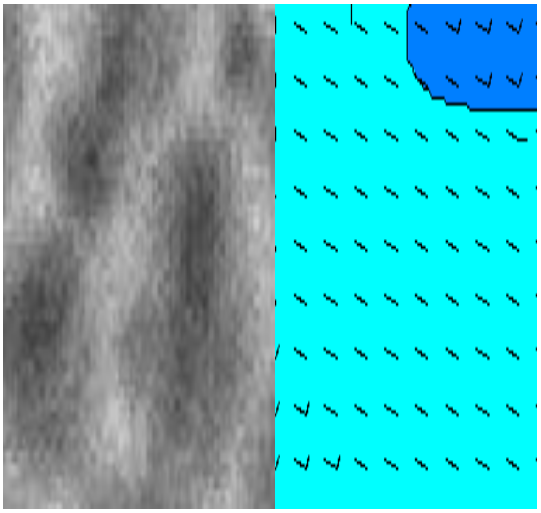

(c)

FIGURE 2.31: (a) Patterns formed by 50% *C. r* and 50% *C. a* with total concentration of 1.1×10^7. (b) Contour plot of the the most local dominant wavelength superimposed with its direction and the direction of the second dominant wavelength. (c) The areas in the boxes are enlarged, the contour on the left side and the bioconvection image on the right side. There is only one direction in this area which conclude that the patterns tend to have roll structure.

approximately$[0.8, 1.6]$ cm. By the time patterns are fully developed the most dominant wavelength will be $[0.8, 1.1]$ cm with a mean value of 0.92 cm.

Figure 2.30(a) is the bioconvection patterns formed by 100% *C. r* with total concentration 6.6×10^6. Figure 2.30(b) is the contour plot of the most dominant local wavelength in the range of $[1.73, 2.65]$ cm superimposed by its associated direction and the direction of the second dominant local wavelength. The area in the box in Figure 2.30(a) corresponds to the result in the box in Figure 2.30(b). These areas are enlarged in Figure 2.30(c). The first and the second directions are perpendicular to each other which indicates that the patterns are square and have the square structure. However, the selected area in Figure 2.31(a) with its results presented in Figure 2.31(c) indicates that the patterns in this location tend to have roll structure as there is only one direction.

To sum up, we used wavelet analysis to discuss the variation of pattern wavelength as a function of total concentration and relative concentration between two mixed species *C. reinhardtii* and *C. augustae*. We found that both the initial and the long term wavelength decrease as we shift from 100% *C. reinhardtii* to 100% *C. augustae*. Also, we found that both the initial and the long term wavelength increase as we decrease the total concentration of the suspension. This result agrees with the results found by Bees and Hill [11] and Williams and Bees [116]. Using wavelets to analyse images is time consuming compared to Fourier. Both analysis wavelet and Fourier succeeded in finding the general trends of the patterns, e.g. investigating the wavelength as a function of cell concentration (Bees and Hill [11] and Williams and Bees [116]). However, the outcome results of wavelet analysis are more realistic than the outcome results of Fourier analysis as wavelet analysis outcome results describe wavelengths at every location in the pattern with the ability to vary the scale (window) around every location. Even when one considers a narrower window to perform Fourier analysis on a small area within the image, the outcome results might not agree with the ones produced by the wavelets. Since the two−dimensional Fourier analysis is performed usually in the $x-$direction (horizontal) and the $y-$direction (vertical) (see Czirók [25], Bees and Hill [11] and William and Bees [116]), while more options of directions can be considered for the scale that corresponds to the size of the selected window. Moreover, changing the

small area within the image requires changing the selected window, which makes Fourier analysis inefficient compared to wavelets.

2.6 Conclusion

Even though wavelet have found applications in many fields (Chui [21], Farge [32], He et al.[47], Guana [43], Barclay et al. [8], Verma and Goel [112] and Huang and Hsien [55]), in this chapter, we developed a new method that utilizes wavelets to analyse images. Experiments were performed to explore how the initial and the long−time most dominant local wavelength varies as a function of the total concentration and relative concentration. The method shows significant results when the patterns consists of different patches with different shapes and sizes. This method might be useful to investigate other stimuli that cause pattern formation such as chemotaxis as local image analysis is required. The code has also been used to analyse some chemoconvection images.

Chapter 3

Linear instability for a suspension of two species

The aim of this theory is to generalize the continuum model of Pedley and Kessler [86] to consist of two species and investigate instability of a uniform suspension of the two mixed species. Unlike Pedley and Kessler [86], we assume a suspension of two different mixed species of swimming microorganisms with no interactions between each other, either biological or chemical. These species have different values of parameters, such as the gyrotactic orientation parameter, the mean cell concentration, the mean cell velocity, etc. Also, the fluid is assumed to be Newtonian only without considering the relation by small stress tensors that are exerted by the cell on the fluid due to its rotation, locomotion and the difference in the deformation of the fluid if the cell were not there. However, assuming that the suspension consists of two different types of swimming microorganisms leads to a cubic dispersion relation, that describes the growth rate of small instability, instead of a quadratic equation as in Pedley and Kessler [86]. The cubic equation results from the terms in the momentum equation where the two species are coupled.

3.1 Mathematical Model

In this model, one assumes a monodisperse cell population. The suspension is assumed to consist of two different types of micro-organisms, each of which has the density ρ_i, $i = 1, 2$. If each type has the concentration, n_i, and mean cell volume v_i, where $i = 1, 2$, then the density of the suspension per unit volume will be $(1 + \alpha_1 n_1 v_1 + \alpha_2 n_2 v_2)\rho$, where $\alpha_i = \frac{\Delta\rho_i}{\rho}$ and, ρ, is the density constant of the media in which they swim. Also, the suspension is assumed to be diluted when $n_1 v_1 + n_2 v_2 \ll 1$ per unit volume, so, the cell−to−cell interactions can be neglected. Finally, the species are assumed not to interact with each other or produce any chemicals that are harmful to each others.

Following the continuum model of Pedley and Kessler in 1990 [86], the suspension is incompressible, so

$$\nabla \cdot \mathbf{U} = 0 \,, \tag{3.1}$$

where $\mathbf{U}(\mathbf{x}, t)$ is the suspension velocity. Assuming Boussinesq approximation that states that any changes in the density of the fluid can be neglected except where the density is multiplied by $\mathbf{g}$, in a unit volume of the suspension the buoyancy force is equal to $(\Delta\rho_1 n_1 v_1 + \Delta\rho_2 n_2 v_2)\mathbf{g}$, and the change in density in the inertia term will be neglected. Also, by considering the fluid to be Newtonian and unlike Pedley and Kessler [86] the stress tensors that are exerted on the cell due to its rotation, locomotion and the difference in the deformation and the rotation of the cell by the fluid if the cell was not there are neglected, the momentum equation in this model is

$$\rho \frac{D\mathbf{U}}{Dt} = -\nabla P_e - (\Delta\rho_1 n_1 v_1 + \Delta\rho_2 n_2 v_2) g\mathbf{k} + \mu\nabla^2\mathbf{U} \,, \tag{3.2}$$

where n_i is the cell concentration and v_i is the mean volume of the cells of each type, μ is the fluid viscosity constant and P_e is the excess pressure above the hydrostatic. Finally, since the total number of cells is conserved, the final governing equation is

$$\frac{\partial n_i}{\partial t} = -\nabla \cdot [n_i(\mathbf{U} + \mathbf{V}_{ic}) - \mathbf{D}_i \cdot \nabla n_i] \;,\; i = 1, 2 \,, \tag{3.3}$$

where $\mathbf{V}_{ic}$ is the mean cell swimming velocity and $\mathbf{D}_i(\mathbf{x}, t)$ is the cell diffusivity tensor for each species i, where $i = 1, 2$.

As there is randomness in the cell swimming velocity, because different cells swim in different directions with different swimming speeds, one defines V_{is} to be the mean of the cell swimming speed, and

$$\mathbf{p}_i = (\sin\theta_i \cos\phi_i \ , \sin\theta_i \sin\phi_i \ , \cos\theta_i) \ , \tag{3.4}$$

to be the unit vector in the direction of the cell axis of symmetry as it is the cell swimming direction. In definition (3.4), θ_i is the angle between the cell axis of symmetry and the z−axis and it represents the swimming direction whereas ϕ_i is the angle between the projection of the cell axis of symmetry on the xy−plane and the x−axis and it represents the cell rotation around the vertical axis, where $i = 1, 2$, see Figure 4.1.

So, the mean swimming velocity $\mathbf{V}_{ic}$ in equation (3.3) is defined as

$$\mathbf{V}_{ic} = V_{is}\langle \mathbf{p}_i \rangle \ , \tag{3.5}$$

where $\langle \ \rangle$ is the ensemble average defined as

$$\langle \mathbf{p}_i \rangle = \int_S \int \mathbf{p}_i f_i(\mathbf{p}_i) \ d^2\mathbf{p}_i \ , \tag{3.6}$$

and $f_i(\mathbf{p}_i)$ is the probability density function defined on a unit sphere.

The tendency to change the swimming direction randomly is assumed to be independent from the instantaneous direction (Hill and Häder [49]). Thus, the probability density function $f_i(\mathbf{p}_i)$ is assumed to satisfy the Fokker-Plank equation

$$\frac{\partial f_i}{\partial t} + \nabla \cdot (\dot{\mathbf{p}}_i f_i) = D_{ir}\nabla^2 f_i \ , i = 1, 2 \ , \tag{3.7}$$

where D_{ir} is the rotational diffusivity that represents the randomness in the cells swimming behaviour and $\dot{\mathbf{p}}_i$ is the rate change of the reorientation defined as (Bees and Hill

[13])

$$\dot{\mathbf{p}}_i = \frac{1}{2B_i}\left[\mathbf{k} - (\mathbf{k}\cdot\mathbf{p}_i)\mathbf{p}_i\right] + \frac{1}{2}\boldsymbol{\omega}\times\mathbf{p}_i + \alpha_{0i}\mathbf{p}_i\cdot\mathbf{E}\cdot(\mathbf{I}-\mathbf{p}_i\mathbf{p}_i)\ , i = 1,2\ . \tag{3.8}$$

Here, $\boldsymbol{\omega}$ is the ambient vorticity, $B_i = \frac{\mu\alpha_{\perp i}}{2h_i\rho g}$ is the gyrotactic orientation parameter, $\alpha_{\perp i}$ is the dimensionless resistance coefficient for rotation about an axis perpendicular to $\mathbf{p}_i$, h_i is the centre−of−mass offset. Finally, $\alpha_{0i} = \frac{ax_i^2 - bx_i^2}{ax_i^2 + bx_i^2}$, where ax_i and bx_i are the major and the minor axes of the cell of each type, respectively. Equation (3.8), means that the rate of change in the cell swimming direction is a linear combination of the effect of the rate−of−strain of the fluid on the cell swimming direction, the effect of the vorticity on that direction and the drift in the direction from being vertical because of the gyrotactic orientation. The Fokker−Plank equation allows a nondeterministic estimation of $\mathbf{V}_{ic}$ and $\mathbf{D}_i$.

The diffusion tensor $\mathbf{D}_i$ in equation (3.3) is given by

$$\mathbf{D}_i(t) = \int_0^\infty \langle \mathbf{V}_{ir}(t)\ \mathbf{V}_{ir}\left(t-t'\right)\rangle dt'\ ,\ i = 1,2\ , \tag{3.9}$$

where $\mathbf{V}_{ir}$ is the velocity of the cell relative to the mean cell velocity, i.e., $\mathbf{V}_{ir} = \mathbf{V}_{ic} - \langle \mathbf{V}_{ic}\rangle$. The definition of $\mathbf{D}_i$ in (3.9) is difficult to be calculated as one has to know all the cells swimming velocities. Thus, an approximation is made by assuming as in Pedley and Kessler [86] that V_{is} is constant for both species as well as the cell settles to a new preferred direction during a constant cell direction correlation time τ_i, the diffusion $\mathbf{D}_i$ can be approximated by

$$\mathbf{D}_i \approx V_{is}^2\tau_i\langle(\mathbf{p}_i - \langle\mathbf{p}_i\rangle)^2\rangle\ , i = 1,2\ , \tag{3.10}$$

Definition (3.10) of the diffusivity tensor was also used by Pedley and Kessler [87], Bees and Hill [12] and Hill and Bees [48].

Parameter	Value	Unit
Fluid density, ρ	1	gm cm^{-3}
Difference between cell and fluid density, $\Delta\rho$	0.05	gm cm^{-3}
Cell volume, v	5×10^{-10}	cm^3
Acceleration due to gravity, g	10^3	cm s^{-2}
Viscosity, μ	10^{-2}	gm cm^{-1} s^{-1}
Mean cell swimming speed, V_s	63	μm s^{-1}
Cell diffusion, D	5×10^{-5}–5×10^{-4}	cm^2 s^{-1}
Gyrotactic parameter, B	3.4	s
Correlation time, τ	1.3	s
Cell rotational diffusivity, D_r	0.067	s^{-1}
Cell eccentricity, α_0	0.2–0.31	
Center–of–mass displacement, h	0–0.5	μm
Deterministic–stochastic parameter, λ	2.2	

TABLE 3.1: Parameters estimated values for the green algae *Chlamydomonas augustae* from Williams and Bees [115]

3.2 Fokker–Plank Equation

To solve the Fokker–Plank equation, we follow Pedley and Kessler [86]. One assumes that the time scale of the variation in the flow is large compared to D_{ir}^{-1} which is the same assumption followed by Pedley and Kessler [87], Bees and Hill [12] and Hill and Bees [48]. Thus, the term $\frac{\partial f_i}{\partial t}$ can be omitted from the Fokker–Plank equation (3.7), i.e. steady state, to be written as

$$D_{ir}\nabla^2 f_i = \frac{1}{2B_i}\left[\mathbf{k}\cdot\nabla f_i - 2\left(\mathbf{k}\cdot\mathbf{p_i}\right)f_i\right] + \frac{1}{2}\boldsymbol{\omega}\cdot\left(\mathbf{p_i}\times\nabla f_i\right) + \alpha_{0i}\left[\mathbf{p_i}\cdot\mathbf{E}\cdot\nabla f_i - 3f_i\mathbf{p_i}\cdot\mathbf{E}\cdot\mathbf{p_i}\right]. \tag{3.11}$$

In the above equation $\boldsymbol{\omega}$ and $\mathbf{E}$ are dimensional constants. Now, one nondimensionlizes the local vorticity and the rate–of–strain tensors by putting

$$\boldsymbol{\omega} = \frac{1}{B}\boldsymbol{\Omega}, \quad \mathbf{E} = \frac{1}{B}\mathbf{e}, \tag{3.12}$$

where $B = \max\left(B_1, B_2\right)$ is the gyrotactic orientation parameter (In this section we nondimesionlized the Fokker–plank equation only. However, the nondimensionlization of the governing equations will be given in detail in Section 3.3). Then, equation (3.11)

becomes

$$\lambda_i^{-1}\nabla^2 f_i = \mathbf{k}\cdot\nabla f_i - 2\left(\mathbf{k}\cdot\mathbf{p}_i\right) f_i + \frac{1}{2}\eta_i \boldsymbol{\Omega}\cdot\left(\mathbf{p_i}\times\nabla f_i\right) + \alpha_{0i}\eta_i\left[\mathbf{p_i}\cdot\mathbf{e}\cdot\nabla f_i - 3 f_i \mathbf{p_i}\cdot\mathbf{e}\cdot\mathbf{p_i}\right], \tag{3.13}$$

where $\lambda_i = \frac{1}{2B_i D_{ir}}$, $\eta_i = \frac{B_i}{B}$, $\boldsymbol{\Omega}$ and $\mathbf{e}$ are the dimensionless fluid local vorticity and rate−of−strain tensors.

3.2.1 No flow solution

Consider the zero flow equilibrium state in which $\mathbf{U}^* = \boldsymbol{\Omega} = \mathbf{e} = 0$ and $f_i = f_i^{(0)}$. Also, $\mathbf{p_i}$ is defined in equation (3.4) and $\mathbf{k} = (0,0,1)$. Using the definitions of the gradient vector and the Laplace operator given in equations (B.1)−(B.5) (Spurk and Aksel [106], see Appendix B.1) and since $\mathbf{p_i}$ is the unit vector in the cell swimming direction, the Fokker−Plank equation (3.13) is

$$\frac{1}{\sin\theta_i}\frac{\partial}{\partial\theta_i}\left(\sin\theta_i \frac{\partial f_i^{(0)}}{\partial\theta_i}\right) + \frac{1}{\sin^2\theta_i}\frac{\partial^2 f^{(0)}}{\partial\phi_i^2} = -\lambda_i\left(\sin\theta_i\frac{\partial f_i^{(0)}}{\partial\theta_i} + 2\cos\theta_i f_i^{(0)}\right). \tag{3.14}$$

For zero flow, one can assume that $f_i^{(0)}$ is independent of ϕ_i, hence, $f_i^{(0)}$ is a function of θ_i only. So, using the substitution $x_i = \cos\theta_i$ in equation (3.14), leads to

$$\left(1-x_i^2\right)\frac{\partial^2 f_i^{(0)}}{\partial {x_i}^2} + \left(-2x_i - \lambda_i\left(1-x_i^2\right)\right)\frac{\partial f_i^{(0)}}{\partial x_i} + 2\lambda_i x_i f_i^{(0)} = 0. \tag{3.15}$$

Integrating with respect to x_i gives

$$\left(1-x_i^2\right)\left(\frac{\partial f_i^{(0)}}{\partial x_i} - \lambda_i f_i^{(0)}\right) = C, \tag{3.16}$$

where C is a constant. Since $f_i^{(0)}$ and its derivative with respect to x_i are both finite, taking $\theta_i = 0$ leads to $C = 0$. Hence,

$$f_i^{(0)} = \varpi_{\lambda_i}\exp\left(\lambda_i\cos\theta_i\right). \tag{3.17}$$

Using the normalization condition imposed on $f_i^{(0)}$,

$$\varpi_{\lambda_i} = \frac{\lambda_i}{4\pi \sinh \lambda_i}. \tag{3.18}$$

Using the definition of $\langle \mathbf{p}_i \rangle$ in (3.6), one can find that

$$\langle \mathbf{p}_i \rangle^{(0)} = \begin{pmatrix} 0 \\ 0 \\ K_{i1} \end{pmatrix}, \tag{3.19}$$

where

$$K_{i1} = \coth \lambda_i - \frac{1}{\lambda_i}. \tag{3.20}$$

Also, the zero−order diffusion is computed from the relation

$$\mathbf{D}_i^{(0)} = V_{is}^2 \tau_i \left(\langle \mathbf{p}_i \mathbf{p}_i \rangle^{(0)} - \langle \mathbf{p}_i \rangle^{(0)} \langle \mathbf{p}_i \rangle^{(0)} \right), \tag{3.21}$$

to be

$$\mathbf{D}_i^{(0)} = V_{is}^2 \tau_i \begin{pmatrix} \frac{K_{i1}}{\lambda_i} & 0 & 0 \\ 0 & \frac{K_{i1}}{\lambda_i} & 0 \\ 0 & 0 & K_{i2} \end{pmatrix}, \tag{3.22}$$

where

$$K_{i2} = 1 - \coth^2 \lambda_i + \frac{1}{\lambda_i^2}. \tag{3.23}$$

3.2.2 Weak ambient flow for spherical cells

One adds a small perturbation to the equilibrium state in Subsection 3.2.1,

$$\mathbf{U}^* = \epsilon \mathbf{U}', \ \mathbf{\Omega} = \epsilon \mathbf{\Omega}^{(1)}, \ \mathbf{e} = \epsilon \mathbf{e}^{(1)}, \ \mathbf{f} = f_i^{(0)} + \epsilon f_i^{(1)}, \tag{3.24}$$

where $0 < \epsilon \ll 1$. Then, for a spherical cell, i.e., $\alpha_{0i} = 0$, $f_i(\mathbf{p}_i)$ is independent of the fluid rate−of−strain. Substitute (3.24) in Fokker−Plank equation (3.13), the $O(\epsilon)$ equation is

$$\frac{1}{\sin\theta_i}\frac{\partial}{\partial\theta_i}\left(\sin\theta_i\frac{\partial f_i^{(1)}}{\partial\theta_i}\right)+\frac{1}{\sin^2\theta_i}\frac{\partial^2 f_i^{(1)}}{\partial{\phi_i}^2}+\frac{\lambda_i}{\sin\theta_i}\frac{\partial}{\partial\theta_i}\left(\sin^2\theta_i f_i^{(1)}\right)= \lambda_i\eta_i\left(\Omega_2^{(1)}\cos\phi_i-\Omega_1^{(1)}\sin\phi_i\right)\frac{\partial f_i^{(0)}}{\partial\theta_i}. \tag{3.25}$$

As in the previous subsection, one uses the substitution $x_i = \cos\theta_i$. The right hand side suggests that

$$f_i^{(1)}(\theta_i,\phi_i) = \varpi_{\lambda_i}\lambda_i\eta_i\left(\Omega_2^{(1)}\cos\phi_i-\Omega_1^{(1)}\sin\phi_i\right)F_{i1}(x_i). \tag{3.26}$$

Then, equation (3.25) becomes

$$\frac{d}{dx_i}\left(\left(1-x_i^2\right)\frac{dF_{i1}}{dx_i}\right)-\frac{F_{i1}}{1-x_i^2}-\lambda_i\frac{d}{dx_i}\left(\left(1-x_i^2\right)F_{i1}\right)= -\lambda_i\left(1-x_i^2\right)^{\frac{1}{2}}\exp(\lambda_i x_i). \tag{3.27}$$

Expand the functions $\exp(\lambda_i x_i)$ and F_{i1} as a power series of λ_i to be

$$\exp(\lambda_i x_i) = \sum_{n=1}^{\infty}\frac{(\lambda_i x_i)^{(n-1)}}{(n-1)!}, \tag{3.28}$$

$$F_{i1}(x_i) = \sum_{n=1}^{\infty}\lambda_i^n\Upsilon_{in}(x_i). \tag{3.29}$$

Substituting equations (3.28) and (3.29) into equation (3.27) leads to

$$\frac{d}{dx_i}\left(\left(1-x_i^2\right)\frac{d\Upsilon_{in}}{dx_i}\right)-\frac{\Upsilon_{in}}{1-x_i^2}=\frac{d}{dx_i}\left(\left(1-x_i^2\right)\Upsilon_{i(n-1)}\right)-\left(1-x_i^2\right)^{\frac{1}{2}}\frac{x_i^{(n-1)}}{(n-1)!}. \tag{3.30}$$

The left hand side of equation (3.30) suggests that one uses the associated Legendre equation (B.6)(Arfken et al. [4]; see Appendix B.2). Hence, equation (3.30) can be

written as

$$n\left(n+1\right)\Upsilon_{in}-2x_i\Upsilon_{i(n-1)}+\left(1-x_i^2\right)\frac{d\Upsilon_{i(n-1)}}{dx_i}=\left(1-x_i^2\right)^{\frac{1}{2}}\frac{x_i^{(n-1)}}{(n-1)!}. \tag{3.31}$$

The solution of this equation can be expressed as a linear combination of the associated Legendre polynomials as follows, let

$$\Upsilon_{in}\left(x_i\right)=\sum_{l=1}^{n}\varsigma_{in,l}P_l^1\left(x_i\right). \tag{3.32}$$

Substitute (3.32) into (3.31)

$$\sum_{l=1}^{n}\varsigma_{in,l}\,l\left(l+1\right)P_l^1\left(x_i\right)+\sum_{l=1}^{n-1}\varsigma_{i(n-1),l}\left[-2x_iP_l^1\left(x_i\right)+\left(1-x_i^2\right)\frac{dP_l^1\left(x_i\right)}{dx_i}\right]=\left(1-x_i^2\right)^{\frac{1}{2}}\frac{x_i^{(n-1)}}{(n-1)!}. \tag{3.33}$$

Putting $m=1$, equations (B.10) and (B.14) in Appendix B.2, become

$$\left(2l+1\right)x_iP_l^1=\left(l+1\right)P_{l-1}^1+lP_{l+1}^1, \tag{3.34}$$

and

$$\left(1-x_i^2\right)\frac{dP_l^1}{dx}=\frac{l\left(l+1\right)}{2l+1}\left[P_{l-1}^1-P_{l+1}^1\right]+x_iP_l^1. \tag{3.35}$$

Substituting equations (3.34) and (3.35) into equation (3.33) gives

$$\sum_{l=1}^{n}\varsigma_{in,l}\,l\left(l+1\right)P_l^1\left(x_i\right)=\sum_{l=1}^{n-1}\varsigma_{i(n-1),l}\left[\frac{l+1}{2l+1}P_{l-1}^1+\frac{l}{2l+1}P_{l+1}^1-\frac{l\left(l+1\right)}{2l+1}\left(P_{l+1}^1-P_{l-1}^1\right)\right]+\left(1-x_i^2\right)^{\frac{1}{2}}\frac{x_i^{(n-1)}}{(n-1)!}. \tag{3.36}$$

Multiplying equation (3.36) by P_q^1 and integrating it with respect to x_i over the convergence interval $(-1,1)$, using equation (B.15) from Appendix B.2 gives

$$\varsigma_{in,l}=-\frac{(l+2)}{(l+1)\left(2l+3\right)}\varsigma_{i(n-1),l+1}+\frac{(l-1)}{l\left(2l-1\right)}\varsigma_{i(n-1),l-1}+\frac{b_{in,l}}{l\left(l+1\right)}, \tag{3.37}$$

where

$$b_{in,l} = \frac{2l+1}{2\,(n-1)!l\,(l+1)} \int_{-1}^{1} \left(1-x_i^2\right)^{\frac{1}{2}} x_i^{(n-1)} P_l^1\left(x_i\right). \tag{3.38}$$

Thus, Gradshteyn and Ryzhik [41] give the formula of the integration (3.38) to be

$$b_{i(n+1),l} = \begin{cases} 0, & n+l \text{ is even} \\ \\ \frac{(2l+1)\Gamma\left(\frac{n+1}{2}\right)\Gamma\left(\frac{n+2}{2}\right)}{4\Gamma(n+1)\Gamma\left(\frac{n-l+3}{2}\right)\Gamma\left(\frac{n+l+4}{2}\right)}, & n+l \text{ is odd.} \end{cases} \tag{3.39}$$

where $n+1 \geq l$. $\varsigma_{in,l}$ are independent of i, since they are defined using the Γ function as a function of n. Hence, $\varsigma_{in,l}$ can be written as $\varsigma_{n,l}$. Pedley and Kessler [86] evaluated these coefficients to be $\varsigma_{n+1,l} = 0$ if $n+l$ is even and the non$-$zero coeffecients are

$$\varsigma_{1,1} = \frac{1}{2},\ \varsigma_{2,2} = \frac{5}{36},\ \varsigma_{3,1} = \frac{1}{120},\ \varsigma_{3,3} = \frac{13}{540}, \cdots \tag{3.40}$$

Now, the first order correction to the mean swimming direction $\langle \mathbf{p}_i \rangle$ can be computed as

$$\begin{aligned} \langle \mathbf{p}_i \rangle^{(1)} &= \int_S \int \mathbf{p}_i f_i^{(1)}(\mathbf{p}_i) d^2\mathbf{p}_i, \\ = \varpi_{\lambda_i} \lambda_i \eta_i \int_0^{2\pi} \int_0^{\pi} &\left(\Omega_2^{(1)} \cos\phi_i - \Omega_1^{(1)} \sin\phi_i\right) \left(\sum_{n=1}^{\infty} \lambda_i^n \sum_{l=1}^{n} \varsigma_{n,l} P_l^1\left(\cos\theta_i\right)\right) \\ &\left(\begin{array}{c} \sin\theta_i \cos\phi_i \\ \sin\theta_i \sin\phi_i \\ \cos\phi_i \end{array}\right) \sin\theta_i \, d\theta_i \, d\phi_i. \end{aligned} \tag{3.41}$$

$\langle \mathbf{p}_i \rangle^{(1)}$ is calculated by Pedley and Kessler [86] and Bees and Hill [12] to be

$$\langle \mathbf{p}_i \rangle^{(1)} = \left(\Omega_2^{(1)}, -\Omega_1^{(1)}, 0\right) \eta_i J_{i1}, \tag{3.42}$$

where

$$J_{i1} = \frac{4}{3} \pi \varpi_{\lambda_i} \lambda_i \sum_{l=0}^{\infty} \lambda_i^{2l+1} \varsigma_{2l+1,1}. \tag{3.43}$$

3.2.3 Weak ambient flow for spheroidal cells

When the cells are spheroidal, $\alpha_{0i} \neq 0$. Thus, the Fokker− Plank equation (3.13) can be written as [86]

$$\frac{1}{\sin\theta_i}\frac{\partial}{\partial\theta_i}\left(\sin\theta_i\frac{\partial f_i^{(1)}}{\partial\theta_i}\right)+\frac{1}{\sin^2\theta_i}\frac{\partial^2 f_i^{(1)}}{\partial{\phi_i}^2}+\frac{\lambda_i}{\sin\theta_i}\frac{\partial}{\partial\theta_i}\left(\sin^2\theta_i f_i^{(1)}\right)= \tag{3.44}$$
$$\lambda_i\eta_i\left(\Omega_2^{(1)}\cos\phi_i-\Omega_1^{(1)}\sin\phi_i\right)\frac{\partial f_i^{(0)}}{\partial\theta_i}+\alpha_{0i}\lambda_i\eta_i\left(\Phi_1\left(\theta_i,\phi_i\right)\frac{df^{(0)}}{d\theta_i}-3\Phi_2\left(\theta_i,\phi_i\right)f^{(0)}\right),$$

where

$$\Phi_1\left(\theta_i,\phi_i\right)=-\frac{3}{4}e_{33}^{(1)}\sin 2\theta_i+\frac{1}{4}\left(e_{11}^{(1)}-e_{22}^{(1)}\right)\sin 2\theta_i\cos 2\phi_i+\frac{1}{2}e_{12}^{(1)}\sin 2\theta_i\sin 2\phi_i$$
$$+e_{13}^{(1)}\cos 2\theta_i\cos\phi_i+e_{23}^{(1)}\cos 2\theta_i\sin\phi_i, \tag{3.45}$$

and

$$\Phi_2\left(\theta_i,\phi_i\right)=\frac{1}{2}e_{33}^{(1)}\left(3\cos^2\theta_i-1\right)+\frac{1}{2}\left(e_{11}^{(1)}-e_{22}^{(1)}\right)\sin^2\theta_i\cos 2\phi_i+e_{12}^{(1)}\sin^2\theta_i\sin 2\phi_i$$
$$+e_{13}^{(1)}\sin 2\theta_i\cos\phi_i+e_{23}^{(1)}\sin 2\theta_i\sin\phi_i, \tag{3.46}$$

Following similar procedure to the one presented in Subsection 3.2.2, Pedley and Kessler [86] and Bees and Hill [12] calculated the contribution of the eccentricity to $\langle\mathbf{p}_i\rangle^{(1)}$ to be

$$-2\alpha_{0i}\eta_i\left(e_{13}^{(1)}J_{i4},e_{23}^{(1)}J_{i4},\frac{3}{2}e_{33}^{(1)}K_{i4}\right)^T, \tag{3.47}$$

where

$$J_{i4}=\frac{4}{3}\pi\varpi_{\lambda_i}\lambda_i\sum_{l=0}^{\infty}\lambda_i^{2l+1}\tilde{\varsigma}_{2l+1,1}, \tag{3.48}$$

and

$$K_{i4}=1-\coth^2\lambda_i-\frac{2K_{i1}}{\lambda_i}, \tag{3.49}$$

λ_i	K_{i1}	K_{i2}	K_{i4}	J_{i1}	J_{i4}
0.3	0.099	0.33	-0.0039	0.015	-4.6×10^{-3}
1.0	0.31	0.28	-0.037	0.14	-0.064
2.2	0.57	0.16	-0.10	0.45	-0.23
3.0	0.67	0.10	-0.12	0.60	-0.41

TABLE 3.2: The values of Ks and Js for different values of λ, from Pedley and Kessler [86], the corrected values of K_{i4} and J_{i4} when $\lambda_i = 0.3$, from Bees and Hill [12] and a corrected value of J_{i4} when $\lambda_i = 2.2$ from Williams and Bees [115]

where the recurrence relation for $\tilde{\varsigma}_{n,1}$ is equation (3.37) with

$$\tilde{b}_{(n+1),l} = -\frac{(2l+1)\,\Gamma\left(\frac{n+1}{2}\right)\Gamma\left(\frac{n+2}{2}\right)\left(n^2+5n+4+l+l^2\right)}{16\Gamma\,(n+1)\,\Gamma\left(\frac{n+5-l}{2}\right)\Gamma\left(\frac{n+6+l}{2}\right)}. \tag{3.50}$$

They calculated the values of the coefficients $\tilde{\varsigma}_{n,1}$ to zero when $n+l$ is odd and

$$\tilde{\varsigma}_{0,2} = -\frac{1}{3},\ \tilde{\varsigma}_{1,1} = -\frac{1}{5},\ \tilde{\varsigma}_{1,3} = -\frac{2}{15},\ \cdots \tag{3.51}$$

3.3 Linear instability

The governing equations (3.1) − (3.3) are nondimensionlized using the time scale $B = \max(B_1, B_2)$, the velocity scale $V_s = \max(V_{1s}, V_{2s})$, BV_s as a length scale, ρV_s^2 as a pressure scale and finally, the concentration is scaled by n_{i0}. So,

$$t = Bt^*,\ \mathbf{U} = V_s\mathbf{U}^*,\ \mathbf{x} = BV_s\mathbf{x}^*,\ P_e = \rho V_s^2 P_e^*,\ n_i = n_{i0}n_i^*. \tag{3.52}$$

Substituting these values in equations (3.1) − (3.3) gives the following nondimensionized governing equations

$$\nabla^* \cdot \mathbf{U}^* = 0; \tag{3.53}$$

$$\frac{D\mathbf{U}^*}{Dt^*} = -\nabla^* P_e^* - \beta\left(\varrho_1\zeta_1\gamma_1 n_1^* + \varrho_2\zeta_2\gamma_2 n_2^*\right) + \frac{1}{Re}\left(\nabla^{*2}\mathbf{U}^*\right), \tag{3.54}$$

$$\frac{\partial n_i^*}{\partial t^*} = -\nabla^* \cdot \left[n_i^*\left(\mathbf{U}^* + a_i\langle\mathbf{p}_i\rangle\right) - \mathbf{D}_i^* \cdot \nabla^* n_i^*\right],\ i = 1, 2, \tag{3.55}$$

In equations (3.54) and (3.55) $Re = \frac{\rho B V_s^2}{\mu}$ is considered the cell Reynolds number and $\beta = \frac{B n_0 v g \triangle \rho}{\rho V_s}$ where

$$\triangle\rho = \max(\triangle\rho_1, \triangle\rho_2),\ v = \max(v_1, v_2),\ n_0 = \max(n_{10}, n_{20}),\ V_s = \max(V_{1s}, V_{2s}), \tag{3.56}$$

$$\varrho_i = \frac{\triangle\rho_i}{\triangle\rho},\ \zeta_i = \frac{v_i}{v},\ \gamma_i = \frac{n_{i0}}{n_0},\ a_i = \frac{V_{is}}{V_s},\ \mathbf{D}_i^* = \frac{\mathbf{D}_i}{BV_s^2}. \tag{3.57}$$

The basic equilibrium situation in this model is when there is no flow, the algae cells of each type are uniformly distributed in the suspension and the swimming direction is vertically upwards. A small perturbation, $0 < \epsilon \ll 1$ is applied to the equilibrium situation so that

$$\mathbf{U}^* = \epsilon\mathbf{U}',\ P_e^* = P_{e0} + \epsilon P_e',\ n_i^* = 1 + \epsilon n_i',\ \langle \mathbf{p}_i \rangle = \langle \mathbf{p}_i \rangle^{(0)} + \epsilon \langle \mathbf{p}_i \rangle^{(1)}. \tag{3.58}$$

Thus, the linearized governing equations are

$$\nabla^* \cdot \mathbf{U}' = 0, \tag{3.59}$$

$$\frac{\partial \mathbf{U}'}{\partial t^*} = -\nabla^* P_e' - \beta \left(\varrho_1 \zeta_1 \gamma_1 n_1' + \varrho_2 \zeta_2 \gamma_2 n_2' \right) \mathbf{k} + \frac{1}{Re} \nabla^{*2} \mathbf{U}', \tag{3.60}$$

$$\frac{\partial n_i'}{\partial t^*} = -\nabla^* \cdot \left[a_i \langle P_i \rangle^{(1)} + a_i \langle P_i \rangle^{(0)} n_i' - \mathbf{D}_i^{*(0)} \cdot \nabla^* n_i' \right],\ i = 1, 2, \tag{3.61}$$

Now, $\langle P_i \rangle^{(0)}$, $\langle P_i \rangle^{(1)}$ and $\mathbf{D}_i^{*(0)}$ in equation (3.61) are defined as follows, (see Section 3.2)

$$\langle \mathbf{p}_i \rangle^{(0)} = \begin{pmatrix} 0 \\ 0 \\ K_{i1} \end{pmatrix}, \quad K_{i1} = \coth \lambda_i - \frac{1}{\lambda_i}. \tag{3.62}$$

$$\langle P_i \rangle^{(1)} = \begin{pmatrix} \Omega_2^{(1)} \eta_i J_{i1} - 2\alpha_{0i} \eta_i e_{13}^{(1)} J_{i4} \\ -\Omega_1^{(1)} \eta_i J_{i1} - 2\alpha_{0i} \eta_i e_{23}^{(1)} J_{i4} \\ 3\alpha_{0i} \eta_i e_{33}^{(1)} K_{i4} \end{pmatrix}, \quad K_{i4} = 1 - \coth^2 \lambda_i - \frac{2K_{i1}}{\lambda_i} \tag{3.63}$$

The dimensionless version of $\mathbf{D}_i^{(0)}$ is:

$$\mathbf{D}_i^{*(0)} = \begin{pmatrix} D_{iH}^{*(0)} & 0 & 0 \\ 0 & D_{iH}^{*(0)} & 0 \\ 0 & 0 & D_{iV}^{*(0)} \end{pmatrix}, \tag{3.64}$$

$$D_{iH}^{*(0)} = a_i^2 \frac{\tau_i K_{i1}}{B\lambda_i},\ D_{iV}^{*(0)} = a_i^2 \frac{\tau_i K_{i2}}{B}, K_{i2} = 1 - \coth^2 \lambda_i + \frac{1}{\lambda_i^2}. \tag{3.65}$$

Substitute from equations (3.62), (3.63) and (3.64) into equation (3.61)

$$\frac{\partial n_i'}{\partial t^*} = -\nabla^* \cdot \Big[a_i \eta_i \left(\Omega_2^{(1)} J_{i1} - 2\alpha_{0i} e_{13}^{(1)} J_{i4}, -\Omega_1^{(1)} J_{i1} - 2\alpha_{0i} e_{23}^{(1)} J_{i4}, -3\alpha_{0i} e_{33}^{(1)} K_{i4} \right) + a_i \left(0, 0, K_{i1}\right) n_i' - \Lambda_i \Big], \tag{3.66}$$

where

$$\Lambda_i = \begin{pmatrix} D_{iH}^{*(0)} & 0 & 0 \\ 0 & D_{iH}^{*(0)} & 0 \\ 0 & 0 & D_{iV}^{*(0)} \end{pmatrix} \cdot \left(\frac{\partial n_i'}{\partial x^*}, \frac{\partial n_i'}{\partial y^*}, \frac{\partial n_i'}{\partial z^*} \right),\ i = 1, 2. \tag{3.67}$$

So, the dimensionless linear governing equations can be simplified as:

$$\nabla^* \cdot \mathbf{U}' = 0, \tag{3.68}$$

$$\frac{\partial \mathbf{U}'}{\partial t^*} = -\nabla^* P_e' - \beta \left(\varrho_1 \zeta_1 \gamma_1 n_1' + \varrho_2 \zeta_2 \gamma_2 n_2' \right) \mathbf{k} + \frac{1}{Re} \nabla^{*2} \mathbf{U}', \tag{3.69}$$

$$\frac{\partial n_i'}{\partial t^*} = a_i J_{i1} \eta_i \left(\frac{\partial \Omega_1^{(1)}}{\partial y^*} - \frac{\partial \Omega_2^{(1)}}{\partial x^*} \right) + 2\alpha_{0i} J_{i4} a_i \eta_i \left(\frac{\partial e_{13}^{(1)}}{\partial x^*} + \frac{\partial e_{23}^{(1)}}{\partial y^*} \right) + 3 a_i \alpha_{0i} \eta_i K_{i4} \frac{e_{33}^{(1)}}{\partial z^*}$$

$$+ D_{iH}^{*(0)} \left(\frac{\partial^2 n_i'}{\partial x^{*2}} + \frac{\partial^2 n_i'}{\partial y^{*2}} \right) + D_{iV}^{*(0)} \frac{\partial^2 n_i'}{\partial z^{*2}} - a_i K_{i1} \frac{\partial n_i'}{\partial z^*}, \; i = 1, 2, \tag{3.70}$$

Using individual Fourier modes to examine the instability:

$$n_i' \left(x^*, y^*, z^*, t^* \right) = N_i \exp \left(\sigma t^* + i \left(k x^* + l y^* + m z^* \right) \right), \tag{3.71}$$

$$\begin{aligned} \mathbf{U}' \left(x^*, y^*, z^*, t^* \right) &= \left(U_1', U_2', U_3' \right) \\ &= \left(U_1, U_2, U_3 \right) \exp \left(\sigma t^* + i \left(k x^* + l y^* + m z^* \right) \right) \end{aligned}, \tag{3.72}$$

$$P_e' \left(x^*, y^*, z^*, t^* \right) = P \exp \left(\sigma t^* + i \left(k x^* + l y^* + m z^* \right) \right), \tag{3.73}$$

where $i = \sqrt{-1}$. Without loss of generality, one can put $l = 0$ as there is no preferable direction for the cell to diffuse in the horizontal plane. Hence, (3.71) – (3.73) can be written as:

$$n_i' \left(x^*, z^*, t^* \right) = N_i \exp \left(\sigma t^* + i \left(k x^* + m z^* \right) \right), \tag{3.74}$$

$$\begin{aligned} \mathbf{U}' \left(x^*, z^*, t^* \right) &= \left(U_1', 0, U_3' \right) \\ &= \left(U_1, 0, U_3 \right) \exp \left(\sigma t^* + i \left(k x^* + m z^* \right) \right) \end{aligned}, \tag{3.75}$$

$$P_e' \left(x^*, z^*, t^* \right) = P \exp \left(\sigma t^* + i \left(k x^* + m z^* \right) \right), \tag{3.76}$$

Substituting equations (3.74), (3.75), (3.76), (B.23), (B.25), (B.27), (B.29) and (B.31) into equations (3.68) – (3.70) gives the incompressibility equation

$$U_1 k + U_3 m = 0, \tag{3.77}$$

while the conservation law of momentum in the x^*- direction is

$$U_1 \left(\sigma + \frac{1}{Re} \left(k^2 + m^2 \right) \right) = -iPk, \tag{3.78}$$

and in the z^*- direction is

$$U_3 \left(\sigma + \frac{1}{Re} \left(k^2 + m^2 \right) \right) = -iPm - \beta \left(\sum_{i=1}^{2} \varrho_i \zeta_i \gamma_i N_i \right), \tag{3.79}$$

and the conservation law for the number of cells is

$$N_i\left(\sigma+ia_iK_{i1}m+D_{iH}^{*(0)}k^2+D_{iV}^{*(0)}m^2\right)=U_1a_i\eta_i\left(J_{i1}-\alpha_{0i}J_{i4}\right)mk$$
$$-U_3a_i\eta_i\left(J_{i1}k^2+\alpha_{0i}J_{i4}k^2+3a_i\alpha_{0i}K_{i4}m^2\right),i=1,2. \tag{3.80}$$

Equation (3.78) gives

$$U_1\left(\sigma+\frac{1}{Re}\left(k^2+m^2\right)\right)/k=-iP, \tag{3.81}$$

Substitute from (3.81) into equation (3.79) leads to

$$U_3\left(\sigma+\frac{1}{Re}\left(k^2+m^2\right)\right)=U_1\left(\sigma+\frac{1}{Re}\left(k^2+m^2\right)\right)\frac{m}{k}-\beta\left(\sum_{i=1}^{2}\varrho_i\zeta_i\gamma_iN_i\right), \tag{3.82}$$

One can get the relationship between U_1 and U_3 from equation (3.77) as follows

$$U_1=-U_3\left(\frac{m}{k}\right), \tag{3.83}$$

Substitute (3.83) into equation (3.82)

$$U_3\left(\sigma+\frac{1}{Re}\left(k^2+m^2\right)\right)=-U_3\left(\frac{m}{k}\right)^2\left(\sigma+\frac{1}{Re}\left(k^2+m^2\right)\right)-\beta\left(\sum_{i=1}^{2}\varrho_i\zeta_i\gamma_iN_i\right), \tag{3.84}$$

From equation (3.80) N_i can be written as a function of U_3 so that

$$N_i=-\frac{a_i\eta_i\left(J_{i1}-\alpha_{0i}J_{i4}\right)m^2+a_i\eta_i\left(J_{i1}k^2+\alpha_{0i}J_{i4}k^2+3\alpha_{0i}K_{i4}m^2\right)}{\sigma+ia_iK_{i1}m+D_{iH}^{*(0)}k^2+D_{iV}^{*(0)}m^2}U_3. \tag{3.85}$$

Substitute the value of N_i in equation (3.85) into equation (3.84) gives

$$\left(\sigma+\frac{1}{Re}\left(k^2+m^2\right)\right)+\left(\frac{m}{k}\right)^2\left(\sigma+\frac{1}{Re}\left(k^2+m^2\right)\right)=$$

$$\beta\left(\sum_{i=1}^{2}\varrho_i\zeta_i\gamma_i\frac{a_i\eta_i\left(J_{i1}-\alpha_{0i}J_{i4}\right)m^2+a_i\eta_i\left(J_{i1}k^2+\alpha_{0i}J_{i4}k^2+3\alpha_{0i}K_{i4}m^2\right)}{\sigma+ia_iK_{i1}m+D_{iH}^{*(0)}k^2+D_{iV}^{*(0)}m^2}\right), \tag{3.86}$$

Hence, the dispersion relation is

$$\left(\sigma+\left(\frac{k^2+m^2}{Re}\right)\right)=\left(\frac{k^2}{k^2+m^2}\right)\beta\left(\sum_{i=1}^{2}\varrho_i\eta_i\zeta_i\gamma_i a_i\times \frac{\left[\left(J_{i1}+\alpha_{0i}J_{i4}\right)k^2+\left(J_{i1}-\alpha_{0i}J_{i4}+3\alpha_{0i}K_{i4}\right)m^2\right]}{\sigma+ia_iK_{i1}m+D_{iH}^{*(0)}k^2+D_{iV}^{*(0)}m^2}\right). \tag{3.87}$$

To simplify the above equation, one sets the following parameters to be

$$A_1=\frac{k^2+m^2}{Re}, \tag{3.88}$$

$$A_2=\left(\frac{k^2}{k^2+m^2}\right)\beta, \tag{3.89}$$

$$B_{i1}=S_i\left(S_{1i}k^2+S_{2i}m^2\right),\quad i=1,2, \tag{3.90}$$

$$B_{i2}=ia_iK_{i1}m+D_{iH}^{*(0)}k^2+D_{iV}^{*(0)}m^2,\quad i=1,2, \tag{3.91}$$

where

$$S_i=\varrho_i\eta_i\zeta_i\gamma_i a_i,\quad i=1,2, \tag{3.92}$$

$$S_{1i}=J_{i1}+\alpha_{0i}J_{i4},\quad i=1,2, \tag{3.93}$$

$$S_{2i}=J_{i1}-\alpha_{0i}J_{i4}+3\alpha_{0i}K_{i4},\quad i=1,2, \tag{3.94}$$

The dispersion relationship (3.87) is

$$\sigma+A_1=A_2\left[\frac{B_{11}}{\sigma+B_{12}}+\frac{B_{21}}{\sigma+B_{22}}\right], \tag{3.95}$$

which simplifies to

$$\sigma^3+F_1\sigma^2+F_2\sigma+F_3=0, \tag{3.96}$$

where F_1, F_2, $F_3\in\mathbb{C}$ and

$$F_1=F_{1R}+iF_{1I}=A_1+B_{12}+B_{22}, \tag{3.97}$$

$$F_1=\left(\frac{1}{Re}+D_{1H}^{*(0)}+D_{2H}^{*(0)}\right)k^2+\left(\frac{1}{Re}+D_{1V}^{*(0)}+D_{2V}^{*(0)}\right)m^2+i\left(a_1K_{11}+a_2K_{21}\right)m, \tag{3.98}$$

$$\begin{aligned} F_2 &= F_{2R} + iF_{2I}, \\ &= A_1 \left(B_{12} + B_{22}\right) - A_2 \left(B_{11} + B_{21}\right) + B_{12}B_{22}, \end{aligned} \tag{3.99}$$

$$\begin{aligned} &= \left(\tfrac{k^2+m^2}{Re}\right)\left[\left(D_{1H}^{*(0)} + D_{2H}^{*(0)}\right)k^2 + \left(D_{1V}^{*(0)} + D_{2V}^{*(0)}\right)m^2\right] \\ &- \left(\tfrac{k^2}{k^2+m^2}\right)\beta\left[\left(S_1S_{11} + S_2S_{12}\right)k^2 + \left(S_1S_{21} + S_2S_{22}\right)m^2\right] \\ &+ \left(D_{1H}^{*(0)}k^2 + D_{1V}^{*(0)}m^2\right)\left(D_{2H}^{*(0)}k^2 + D_{2V}^{*(0)}m^2\right) - a_1a_2K_{11}K_{21}m^2 \end{aligned} \tag{3.100}$$

$$\begin{aligned} &+i\Bigg[\left(\tfrac{k^2+m^2}{Re}\right)\left(a_1K_{11} + a_2K_{21}\right)m + a_1K_{11}m\left(D_{2H}^{*(0)}k^2 + D_{2V}^{*(0)}m^2\right) \\ &+a_2K_{21}m\left(D_{1H}^{*(0)}k^2 + D_{1V}^{*(0)}m^2\right)\Bigg], \end{aligned}$$

$$\begin{aligned} F_3 &= F_{3R} + iF_{3I}, \\ &= A_1B_{12}B_{22} - A_2\left(B_{11}B_{22} + B_{21}B_{12}\right), \end{aligned} \tag{3.101}$$

$$\begin{aligned} &= \left(\tfrac{k^2+m^2}{Re}\right)\left[\left(D_{1H}^{*(0)}k^2 + D_{1V}^{*(0)}m^2\right)\left(D_{2H}^{*(0)}k^2 + D_{2V}^{*(0)}m^2\right) - a_1a_2K_{11}K_{21}m^2\right] \\ &- \left(\tfrac{k^2}{k^2+m^2}\right)\beta\Bigg[S_1\left(S_{11}k^2 + S_{21}m^2\right)\left(D_{2H}^{*(0)}k^2 + D_{2V}^{*(0)}m^2\right) \\ &+S_2\left(S_{12}k^2 + S_{22}m^2\right)\left(D_{1H}^{*(0)}k^2 + D_{1V}^{*(0)}m^2\right)\Bigg] \\ &+i\Bigg[\left(\tfrac{k^2+m^2}{Re}\right)\left[a_1K_{11}m\left(D_{2H}^{*(0)}k^2 + D_{2V}^{*(0)}m^2\right) + a_2K_{21}m\left(D_{1H}^{*(0)}k^2 + D_{1V}^{*(0)}m^2\right)\right] \\ &- \left(\tfrac{k^2}{k^2+m^2}\right)\beta\left[a_2K_{21}S_1m\left(S_{11}k^2 + S_{21}m^2\right) + a_1K_{11}S_2m\left(S_{12}k^2 + S_{22}m^2\right)\right]\Bigg]. \end{aligned} \tag{3.102}$$

The dispersion relationship in equation (3.96) is a cubic equation. Let $\sigma = \sigma_R + i\sigma_I$, then, the dispersion relation (3.96) yields

$$(\sigma_R + i\sigma_I)^3 + (F_{1R} + iF_{1I})(\sigma_R + i\sigma_I)^2 + (F_{2R} + iF_{2I})(\sigma_R + i\sigma_I) + F_{3R} + iF_{3I} = 0, \tag{3.103}$$

So, when $\sigma_R = 0$ equation (3.103) gives:

$$(i\sigma_I)^3 + (F_{1R} + iF_{1I})(i\sigma_I)^2 + (F_{2R} + iF_{2I})(i\sigma_I) + F_{3R} + iF_{3I} = 0, \tag{3.104}$$

$$\iff \left(-F_{1R}\sigma_I^2 - F_{2I}\sigma_I + F_{3R}\right) + i\left(-\sigma_I^3 - F_{1I}\sigma_I^2 + F_{2R}\sigma_I + F_{3I}\right) = 0, \tag{3.105}$$

The real part of the dispersion equation is

$$-F_{1R}\sigma_I^2 - F_{2I}\sigma_I + F_{3R} = 0, \tag{3.106}$$

and the imaginary part is

$$-\sigma_I^3 - F_{1I}\sigma_I^2 + F_{2R}\sigma_I + F_{3I} = 0, \tag{3.107}$$

Equation (3.106), gives the key parameter $Re\beta$ as a function of σ_I and the other parameters as follows:

$$F_{3R} = F_{1R}\sigma_I^2 + F_{2I}\sigma_I, \tag{3.108}$$

Using equation (3.102) leads to

$$\begin{aligned}
&\left(\tfrac{k^2+m^2}{Re}\right)\left[\left(D_{1H}^{*(0)}k^2 + D_{1V}^{*(0)}m^2\right)\left(D_{2H}^{*(0)}k^2 + D_{2V}^{*(0)}m^2\right) - a_1a_2K_{11}K_{21}m^2\right] \\
&- \left(\tfrac{k^2}{k^2+m^2}\right)\beta\Big[S_1\left(S_{11}k^2 + S_{21}m^2\right)\left(D_{2H}^{*(0)}k^2 + D_{2V}^{*(0)}m^2\right) \\
&+S_2\left(S_{12}k^2 + S_{22}m^2\right)\left(D_{1H}^{*(0)}k^2 + D_{1V}^{*(0)}m^2\right)\Big] \\
&= F_{1R}\sigma_I^2 + F_{2I}\sigma_I,
\end{aligned} \tag{3.109}$$

Multiplying equation (3.109) by Re yields

$$Re\beta = \frac{-E_1\sigma_I^2 - E_2\sigma_I + E_3}{E_4}, \tag{3.110}$$

where

$$E_1 = Re\left[\left(\tfrac{1}{Re} + D_{1H}^{*(0)} + D_{2H}^{*(0)}\right)k^2 + \left(\tfrac{1}{Re} + D_{1V}^{*(0)} + D_{2V}^{*(0)}\right)m^2\right], \tag{3.111}$$

$$\begin{aligned} E_2 = Re\Bigg[&\left(\tfrac{k^2+m^2}{Re}\right)(a_1K_{11} + a_2K_{21})\,m + a_1K_{11}m\left(D_{2H}^{*(0)}k^2 + D_{2V}^{*(0)}m^2\right) \\ +\;& a_2K_{21}m\left(D_{1H}^{*(0)}k^2 + D_{1V}^{*(0)}m^2\right)\Bigg], \end{aligned} \tag{3.112}$$

$$E_3 = (k^2+m^2)\left[\left(D_{1H}^{*(0)}k^2 + D_{1V}^{*(0)}m^2\right)\left(D_{2H}^{*(0)}k^2 + D_{2V}^{*(0)}m^2\right) - a_1a_2K_{11}K_{21}m^2\right], \tag{3.113}$$

$$E_4 = \left(\tfrac{k^2}{k^2+m^2}\right)\Bigg[S_1\left(S_{11}k^2 + S_{21}m^2\right)\left(D_{2H}^{*(0)}k^2 + D_{2V}^{*(0)}m^2\right) \tag{3.114}$$

$$+S_2\left(S_{12}k^2 + S_{22}m^2\right)\left(D_{1H}^{*(0)}k^2 + D_{1V}^{*(0)}m^2\right)\Bigg],$$

Equation (3.110) gives the neutral curve as a function of the wavenumbers k and m. The neutral curves are the curves where $\sigma_R = 0$.

Substituting the expression of F_{2R} and F_{3I} given in equations (3.100) and (3.102) into equation (3.107) and multiplying it by Re leads to

$$Re\sigma_I^3 + ReF_{1I}\sigma_I^2 - [E_6 - Re\beta E_7 + E_8]\,\sigma_I - [E_9 - Re\beta E_{10}] = 0, \tag{3.115}$$

Substituting from (3.110) into (3.115) gives

$$\begin{aligned} &Re\sigma_I^3 + ReF_{1I}\sigma_I^2 - \left[E_6 - \left(\tfrac{-E_1\sigma_I^2 - E_2\sigma_I + E_3}{E_4}\right)E_7 + E_8\right]\sigma_I \\ &- \left[E_9 - \left(\tfrac{-E_1\sigma_I^2 - E_2\sigma_I + E_3}{E_4}\right)E_{10}\right] = 0, \end{aligned} \tag{3.116}$$

Equation (3.116) can be reorganized as

$$\sigma_I^3 + G_1\sigma_I^2 + G_2\sigma_I + G_3 = 0, \tag{3.117}$$

where

$$G_1 = \frac{E_5E_4 - E_2E_7 - E_1E_{10}}{ReE_4 - E_1E_7}, \tag{3.118}$$

$$G_2 = \frac{E_3E_7 - E_2E_{10} - E_6E_4 - E_8E_4}{ReE_4 - E_1E_7}, \tag{3.119}$$

$$G_3 = \frac{E_3E_{10} - E_9E_4}{ReE_4 - E_1E_7}, \tag{3.120}$$

and E_1, E_2, E_3 and E_4 are given in equations (3.111)−(3.114) and E_5, E_6, E_7, E_8, E_9, E_{10} and the expressions of G_1, G_2 and G_3 are given in Appendix B.5.

By calculating the real root of the imaginary part of the dispersion equation (3.117) and substitute it into the equation (3.110), one can plot the neutral curves and extracted the critical values $Re\beta_c$ and k_c that gives the instability onset.

3.4 Results

3.4.1 No vertical variation

When there is no vertical variation in the disturbance, i.e. $m = 0$, the coefficients G_1, G_2 and G_3 in relations (3.118)−(3.120) become

$$G_1 = 0,\ G_3 = 0, \tag{3.121}$$

$$G_2 = \frac{k^4\left\{\left(S_1S_{11}D_{2H}^{*(0)2} + S_2S_{12}D_{1H}^{*(0)2}\right) + Re\left(S_1S_{11}D_{2H}^{*(0)} + S_2S_{12}D_{1H}^{*(0)}\right)\left(D_{1H}^{*(0)}D_{2H}^{*(0)}\right)\right\}}{Re\left[\left(\frac{S_1S_{11}+S_2S_{12}}{Re}\right) + S_1S_{11}D_{1H}^{*(0)} + S_2S_{12}D_{2H}^{*(0)}\right]}. \tag{3.122}$$

Hence, equation (3.117) takes the form

$$\sigma_I^3 + G_2\sigma_I = 0, \tag{3.123}$$

Since G_2 is positive, the above equation (3.123) has only one real root

$$\sigma_I = 0, \tag{3.124}$$

Substituting (3.124) into the relation (3.110) gives

$$Re\beta = \frac{D_{1H}^{*(0)} D_{2H}^{*(0)}}{S_1 S_{11} D_{2H}^{*(0)} + S_2 S_{12} D_{1H}^{*(0)}} \, k^2. \tag{3.125}$$

The above relation (3.125) shows that there is a linear relationship between the $Re\beta$ and k^2 for the neutral curves that reaches its minimum at $k_c = k = 0$.

3.4.2 Non−zero vertical variation

In case of $m \neq 0$, a Matlab program is used to solve the imaginary part of the dispersion relation given by equation (3.117). Since this equation is cubic, it has three roots, with at least one real root and two complex conjugates. Then, one substitutes the real root into equation (3.110) to calculate and plot the neutral curves (the Matlab codes are given in the Appendix B.6). The coefficients G_1, G_2 and G_3 in equation (3.117) and the neutral curves equation (3.110) depend on the following parameters; the horizontal and vertical diffusion of each species $D_{iH}^{*(0)}$ and $D_{iV}^{*(0)}$ that are given by equations (3.64) and (3.65), the value of K_{i1} that represents the magnitude of $\langle \mathbf{P}_i \rangle^{(0)}$ in the vertical direction, the values of S_{1i} and S_{2i} that are given in equations (3.93) and (3.94), the values of S_i that are given by equation (3.92) and finally the value of Re. Typical values of the parameters used in this investigation are summarized in Tables 3.3 and 3.4, taking into account that the total mean concentration of the mixed suspension should be 6.5×10^6 cells cm^{-3}.

The results are presented in Figure 3.1, that displays the neutral curve when $m = 1$ and $m = 0$, and Figure 3.2 that shows the neutral curves of each species individually as well as the neutral curve that results from the mixing for the value of $m = 1$. Figure 3.2 displays the difference between the neutral curves that are plotted for every species individually and the one when mixing them together. Mixing them may results in neutral curve that

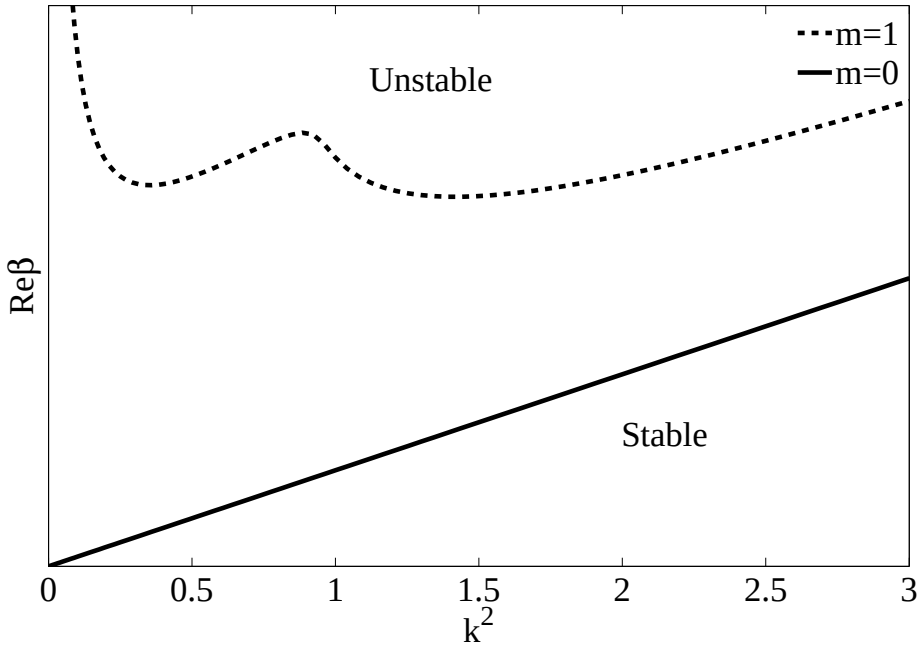

FIGURE 3.1: The neutral curves for the set of parameters given in Tables 3.3 and 3.4. The case of $m = 0$ is plotted as the solid line, the growth rate on this line is zero. The case of $m = 1$ is plotted as a dashed line and $\sigma_R = 0$ along that dashed line. The mean cell swimming speed of the green algae *Chlamydomonas reinhardtii* is assumed to be 40% less than the mean cell swimming speed of the green algae *Chlamydomonas augustae*, i.e.$V_{2s} = 0.6V_{1s}$.

has a bump in the area between the wavenumbers $k^2 = 0.5$ and $k^2 = 1.25$ while on the other hand considering one species results in a Hopf bifurcation neutral curve.

Given that the maximum value of the gyrotactic orientation parameter is $B = 3.4$ s and the maximum mean cell swimming speed is $V_s = 9 \times 10^{-3}$ cm s^{-1}, the value $m = 1$ corresponds to a suspension depth of 0.19 cm. For these values to be realistic we take a small value of m, for example $m = 10^{-2}$, corresponding to a suspension of depth of 19 cm which can be considered a sufficiently deep suspension that the effect of the top and bottom boundaries does not need to be taken into account. The neutral curve in this case for the values of parameters given in Tables 3.3 and 3.4 is plotted in Figure 3.3. Figure 3.3 shows that when $m = 10^{-2}$, the neutral curves arise from Hopf bifurcation whether they are mixed or not. Moreover, the neutral curve of the two species mixed together lies above the neutral curve of *C. augustae*, the one with the minimum mean cell swimming speed, and slightly above the neutral curve of *C. reinhardtii*, the one with the maximum mean cell swimming speed. The instability of *C.*

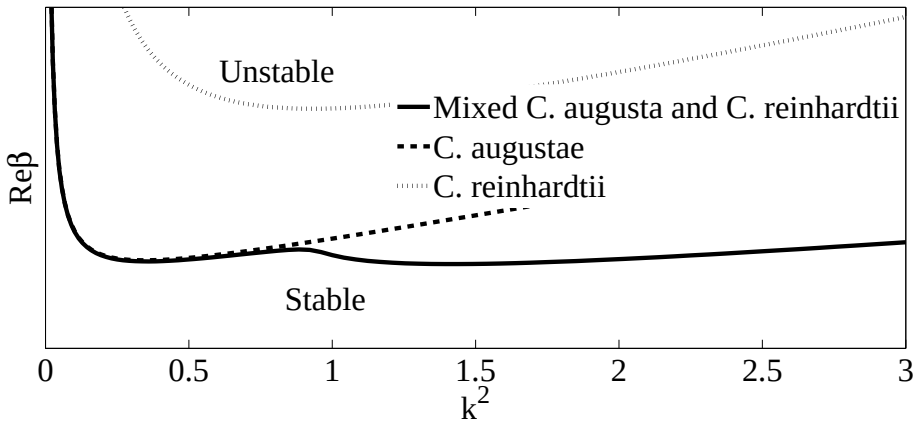

FIGURE 3.2: The neutral curves for the set of parameters given in Tables 3.3 and 3.4 when $m = 1$. The solid line represents the mixed species, the dashed line represents species 1 and the dotted line represents species 2. $\sigma_R = 0$ along these lines.The mean cell swimming speed of the green algae *Chlamydomonas reinhardtii* is assumed to be 40% less than the mean cell swimming speed of the green algae *Chlamydomonas augustae*, i.e.$V_{2s} = 0.6V_{1s}$.

Parameter	Value	Reference
τ_1	1.3 s	[115]
λ_1	2.2	[115]
B_1	3.4 s	[115]
K_{11}	0.57	[86]
K_{12}	0.16	[86]
α_{01}	0.2	[115]
$\Delta\rho_1$	0.05 gm cm^{-3}	[115]
J_{11}	0.45	[86]
J_{14}	-0.23	[115]
K_{14}	-0.10	[86]
v_1	5×10^{-10} cm^3	[115]
V_{1s}	6.3×10^{-3} cm s^{-1}	[115]
n_{10}	6.5×10^6	
Re	5.2×10^{-5}	[13]
S_{11}	0.404	calculated
S_{21}	0.436	calculated
S_1	1	calculated

TABLE 3.3: Estimated values of the parameters for the green algae *Chlamydomonas augustae*.

Parameter	Value	Reference
τ_2	2 s	assumed
λ_2	1	[86]
B_2	3.4 s	
K_{21}	0.31	[86]
K_{22}	0.28	[86]
α_{02}	0.3	assumed
$\Delta\rho_2$	0.05 gm cm^{-3}	assumed
J_{21}	0.14	[86]
J_{24}	-0.064	[86]
K_{24}	-0.037	[86]
v_2	5×10^{-10} cm^3	assumed
V_{2s}	9×10^{-3} cm s^{-1}	[79]
n_{20}	6.5×10^6	
S_{12}	0.1208	calculated
S_{22}	0.1259	calculated
S_2	0.6	calculated

TABLE 3.4: Estimated values of the parameters assumed for the green algae *Chlamydomonas reinhardtii*.

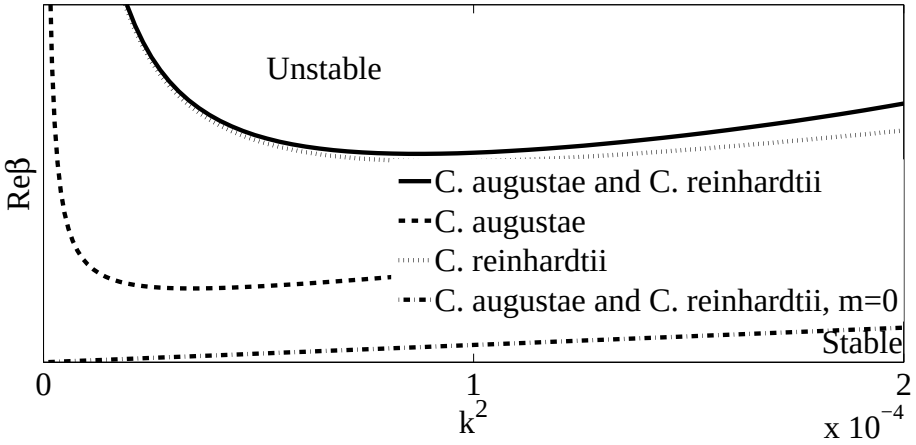

FIGURE 3.3: The neutral curves when the mean swimming speed of *C. augustae*, V_{1s}, is 40% less than the mean swimming speed of the *C. reinhardtii*, i.e.$V_{1s} = 0.6V_{2s}$, for two species of the same mean cell concentration with a total concentration of 6.5×10^6. The case of $m = 10^{-2}$ is plotted as the solid line for the mixed species. The growth rate $\sigma_R = 0$ on these lines.

augustae, the one with the minimum mean cell swimming speed (see Table 3.3), starts at $Re\beta_c = 2.065 \times 10^{-4}$ at a critical wavenumber of $k_c = 0.0059$. The instability of the *C. reinhardtii*, with 40% increase in the mean cell swimming speed (see Table 3.4), occurs at $Re\beta_c = 5.63 \times 10^{-4}$ at $k_c = 0.0096$. However, the instability onset when mixing them together is at $Re\beta_c = 5.85 \times 10^{-4}$ at $k_c = 0.0167$.

Neutral curves do not depend only on the relative mean cell swimming speed but also depend on the ratio of the mean cell concentrations, the mean cell volume, the difference in density and the gyrotactic orientation parameters between the two species. Assuming that both species have the same gyrotactic orientation parameter, the same mean cell volume and the same density difference $\Delta\rho_i$, we will discuss the changing of mean cell concentration of one species with respect to the other. So, instead of the species have different mean swimming speed, one assumes that $V_{1s} = V_{2s} = 6.3 \times 10^{-3}$ cm s^{-1} in Tables 3.3 and 3.4 and that $n_{20} = 3.9 \times 10^6$ cells cm^{-3}, i.e. $n_{20} = 0.6n_{10}$. The neutral curves in this case are plotted in Figure 3.4 for $m = 10^{-2}$. Figure 3.4 shows that when the suspension consists of two species mixed together with different concentration, the neutral curve is located above the neutral curves of *C. augustae* and *C. reinhardtii* with $Re\beta_c = 9.4 \times 10^{-3}$ and $k_c = 0.0069$, since decreasing the concentration of one species causes the suspension to be diluted. $Re\beta_c$ in this case is larger than $Re\beta_c$ for both *C.*

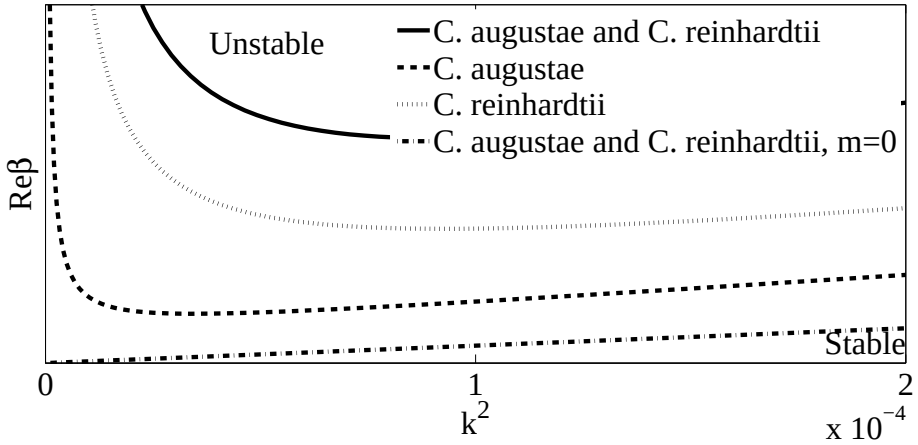

FIGURE 3.4: The neutral curves when the mean cell concentration of *C. reinhardtii*, n_{20}, is 60% of the the mean cell concentration of *C. augustae*, n_{10}, i.e.$n_{20} = 0.6n_{10}$, for two species with same mean swimming speed $V_{1s} = V_{2s} = 6.3 \times 10^{-3}$ cm s^{-1}. The case $m = 10^{-2}$ is plotted as the solid line for the mixed species. The growth rate $\sigma_R = 0$ on these lines.

	$Re\beta_c$	k_c	Notes
C. augustae	2.065×10^{-4}	0.0058	
C. reinhardtii	5.63×10^{-4}	0.0096	
C. augustae and *C. reinhardtii*	2.25×10^{-4}	0.0096	$V_{2s} = 0.4V_{1s}$ same concentration
C. augustae and *C. reinhardtii*	3.37×10^{-4}	0.0096	$V_{2s} = 0.6V_{1s}$ same concentration
C. augustae and *C. reinhardtii*	4.5×10^{-4}	0.0096	$V_{2s} = 0.8V_{1s}$ same concentration
C. augustae and *C. reinhardtii*	5.63×10^{-4}	0.0096	$V_{2s} = V_{1s}$ same concentration
C. augustae and *C. reinhardtii*	9.92×10^{-4}	0.027	$n_{20} = 0.4n_{10}$ same swimming speed
C. augustae and *C. reinhardtii*	9.4×10^{-4}	0.0096	$n_{20} = 0.6n_{10}$ same swimming speed
C. augustae and *C. reinhardtii*	7.04×10^{-4}	0.0096	$n_{20} = 0.8n_{10}$ same swimming speed

TABLE 3.5: The critical values $Re\beta_c$ and k_c that results from this analysis when using the parameters in Tabes 3.3 and 3.4, for the maximum speed $V_{1s} = V_{2s} = 6.3 \times 10^{-3}$.

augustae and *C. reinhardtii*, however, the critical wavenumber k_c equals to the critical wavenumber of *C. reinhardtii*, i.e. $k_c = 0.0096$.

Moreover, Figures 3.5 and 3.6 show the effect of the relative mean cell concentration and mean cell swimming speed on the instability, respectively. Clearly one can see in Figure 3.5 that when we decrease the mean cell concentration of the green algae *C. reinhardtii*, n_{20}, the neutral curves are raised and the instability occurs for larger values of $Re\beta_c$ because the suspension is becoming diluted. The critical value $Re\beta_c$ as the mean cell concentration, n_{20} decreases, see Figures 3.7(b), however, the value of k_c is 0.0096

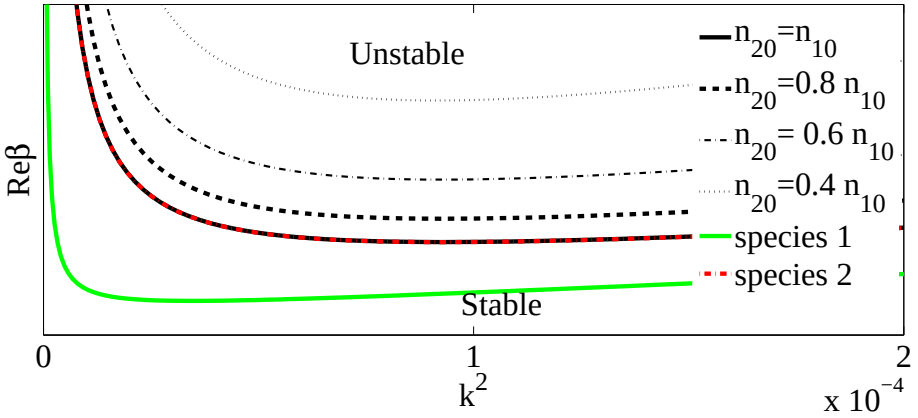

FIGURE 3.5: Neutral curves for $m = 10^{-2}$. The mean cell swimming speed is taken to be the same for both species, i.e. $V_{1s} = V_{2s} = 6.3 \times 10^{-3}$, whereas the concentration of the *C. reinhardtii*, n_{20} is taken to be less than the concentration of *C. augustae* n_{10} with different ratios.

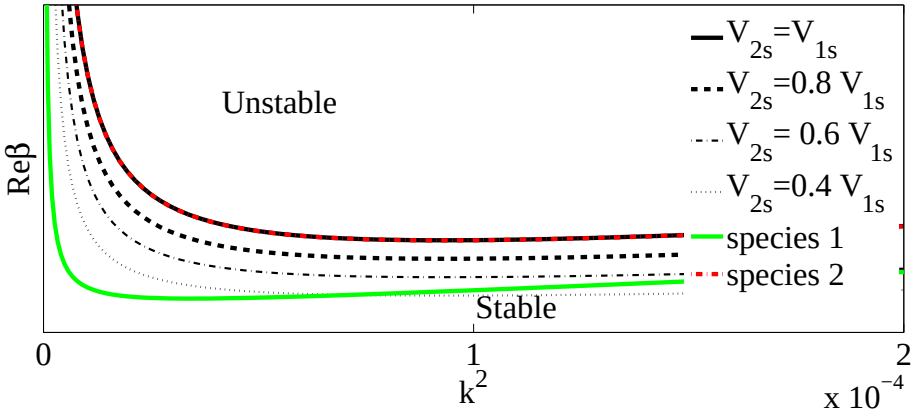

FIGURE 3.6: Neutral curves for $m = 10^{-2}$. The mean cell concentration is taken to be the same for both species, i.e. $n_{10} = n_{20} = 6.5 \times 10^{6}$, whereas the mean cell swimming speed of the *C. reinhardtii*, V_{2s} is taken to be less than the swimming speed of *C. augustae* V_{1s} with different ratios.

and it becomes 0.027, three times larger, when the cell concentration n_{20} is 60% less than n_{10} because the suspension is becoming very diluted. While decreasing the mean cell swimming speed of species 2, *C. reinhardtii*, V_{2s}, the neutral curves are lowered and the instability occurs for smaller values of $Re\beta_c$. The critical value $Re\beta_c$ decreases linearly as the mean cell swimming speed V_{2s} decreases with the value $k_c = 0.0096$ at all cases, see Figures 3.7(a). Decreasing the cell volume of the second species *C. reinhardtii*, v_2, gives similar results to the one we get from decreasing the cell concentration, since the smaller cell volume leads to the less biomass, Figures 3.7(c).

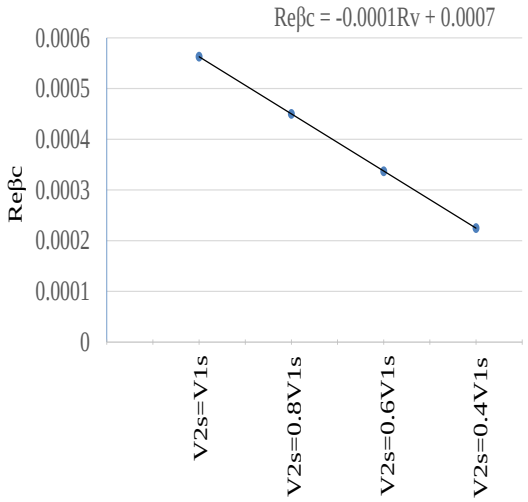

(a) $n_{10} = n_{20} = 6.5 \times 10^6$ cell cm^{-3} and $v_1 = v_2 = 5 \times 10^{-10}$ cm^3

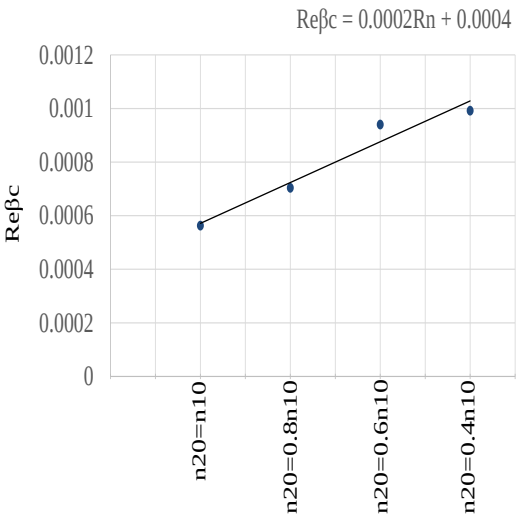

(b) $V_{1s} = V_{2s} = 6.3 \times 10^{-3}$ cm s^{-1} and $v_1 = v_2 = 5 \times 10^{-10}$ cm^3

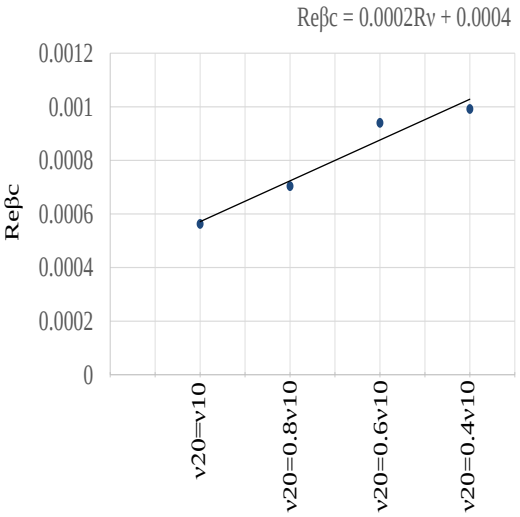

(c) $n_{10} = n_{20} = 6.5 \times 10^6$ cell cm^{-3} and $V_{1s} = V_{2s} = 6.3 \times 10^{-3}$ cm s^{-1}

FIGURE 3.7: The critical value $Re\beta_c$ of the mixed species of *C. augustae*(species1) and *C.reinhardtii*(species2) versus (a) the relative mean cell swimming speed for the same cell volume and total cell concentration, Rv stands for the relative speed, (b) the relative concentration for the same cell volume and swimming speed, Rn stands for the relative concentration and (c) the relative cell volume for the same swimming speed and cell concentration, $R\nu$ stands for the relative cell volume.

3.5 Discussion

In this chapter, we investigated the instability of a uniform suspension that consists of two species mixed together. Moreover, a comparison of the instability onset between the suspension that consists of the two mixed species and the suspension that consists of each species individually is performed. As a results of this analysis, a finite critical wavenumber k_c is predicted when $m \neq 0$ and $k_c = 0$ when $m = 0$.

When $m = 1$, using the parameters in Tables 3.3 and 3.4, produces a neutral curve for the suspension of the two mixed species that has a local maximum between the wavenumbers $k^2 = 0.5$ and 1.25, (see Figure 3.2). This bump appears to be as a result of a competition between two instabilities. Figure 3.6 shows this competition clearly when m is chosen to be 10^{-2} because the situation is more realistic with the suspension depth 19 cm in that case. One can see that the instability onset of the suspension of the mixed species together lies between the instability onset of species 1 and 2. The reason is that species have different stochastic parameters $\lambda_1 \neq \lambda_2$ as well as different mean cell swimming velocities $V_{1s} > V_{2s}$. These values contribute in defining the diffusivity tensor, hence $D_{1H}^{*(0)} \neq D_{2H}^{*(0)}$ and $D_{1V}^{*(0)} \neq D_{2V}^{*(0)}$. The diffusivity tensor of each species affects the mean of the cell swimming direction $\langle \mathbf{p}_i \rangle$ of the other species, via the expressions of E_4 in equations (3.114) which causes the neutral curves to lie between the individual neutral curves. However, decreasing the mean cell swimming speed of the second species V_{2s}, causes the instability onset to be closer to the instability onset of species 1, the one with the maximum speed, since the diffusion effect on $\langle \mathbf{p}_1 \rangle$ is becoming less. Moreover, the effect of the relative concentration is found to be that decreasing the cell concentration of species 2 n_{20}, causes the the critical value $Re\beta_c$ to increase as the suspension is becoming less concentrated.

The assumption that the suspension consists of two different species appeared in the buoyancy term of the momentum equation (3.69). Hence, the dispersion relation in equation (3.95) has an extra term, $\frac{B_{21}}{\sigma + B_{22}}$ that raises its degree to the third power (cubic equation). This is a major difference between this model and the continuum model presented by Pedley and Kessler [86]. However, when considering one species only, the

dispersion relationship in equation (3.95) reduces to the following quadratic equation

$$\sigma^2 + (A_1 + B_{12})\,\sigma + A_1 B_{12} - A_2 B_{11} = 0. \tag{3.126}$$

The neutral curve equation in this case is given by

$$Re\beta = \frac{\left(k^2+m^2\right)^2\left(D_{1H}^{*(0)}k^2 + D_{1V}^{*(0)}m^2\right)}{B_{11}k^2}\left[1 + \frac{K_{11}^2 m^2}{\left(\frac{k^2+m^2}{Re} + D_{1H}^{*(0)}k^2 + D_{1V}^{*(0)}m^2\right)^2}\right] \tag{3.127}$$

When $m = 0$

$$Re\beta = \frac{D_{1H}^{*(0)}}{J_{11} + \alpha_{01}J_{14}}k^2. \tag{3.128}$$

The difference between this equation and the one derived by Pedley and Kessler [86] is the extra term $\chi_1\left(J_2 + \alpha_2 J_5\right)$ that results from the terms $\Sigma^{(d)} + \Sigma^{(s)} + \Sigma^{(p)}$ that are considered in the conservation of momentum equation. Using the parameter values estimated for *C. augustae* given in Table 3.3 for the value of $\lambda_1 = 2.2$, α_{01} and $\beta = 13$, we calculate that $D_{1H}^{*(0)} = 0.09$, $J_{11} + \alpha_{01}J_{14} = 0.404$. Hence, using equation (3.128), $k_c^2 = 3.303 \times 10^{-3}$. This value disagrees with the values predicted by Pedley and Kessler [86], $k_c^2 = 0.67$, and Pedley et al. [84], $k_c^2 = 0.17$. This difference is due to the following; the value of $D_{1H}^{*(0)}$ is estimated to be 0.09 in our analysis while Pedley and Kessler [86] estimated this value to be 0.10 and Pedley et al. [84] evaluated D^* to be 0.74 (Pedley et al. [84] took the diffusion to be 10^{-4} cm s^{-1} and the mean cell swimming speed to be 10^{-2} cm s^{-1}). So, our evaluation of the diffusion is less than theirs. Furthermore, the value of $\alpha_{01} = 0.2$ in our investigation makes $J_{11} + \alpha_{01}J_{14} = 0.404$, whereas Pedley and Kessler [86] selected this value to be 0.31 giving $J_{11} + \alpha_{01}J_{14} = 0.37$. Moreover, the value $J_{11} + \alpha_{01}J_{14}$ was replaced by $1 - \alpha_{01}$ in Pedley et al. [84] leading to the value 0.69 when $\alpha_{01} = 0.31$. Finally, Pedley and Kessler [86] found $k_c^2 = \frac{\beta(J_{11}+\alpha_{01}J_{14})}{D_H\left[\frac{1}{Re}+\chi_1(J_{12}+\alpha_{01}J_{15})\right]}$ with estimating $J_{12} + \alpha_{01}J_{15} = 0.12$ and $\chi_1 Re = 0.11$, and Pedley et al. [84] evaluated k_c^2 to be $k_c^2 = \frac{Re\beta(1-\alpha_0)}{D^*}$.

To compare our predictions with the experiments, we assume that we have a suspension of two mixed species of the green algae *C. augustae* and *C. reinhardtii* with relative

mean cell concentration 50% *C. augustae* to 50% *C. reinhardtii*, i.e. both have the same mean cell concentration, and the total cell concentration to be 1.3×10^7 cell cm^{-3}. The green algae *C. augustae* has the estimated parameters given in Table 3.3. However, we assumed that the deterministic−stochastic parameter of the *C. reinhardtii* is $\lambda_2 = 1$, $\alpha_{02} = 0.3$, $\tau_2 = 2$ s and the mean cell swimming speed is measured to be 90 μm s^{-1} (Guasto et al [44]). Also, we assume that $B_1 = B_2 = 3.4$ s. Using the above analysis, we predicted an initial critical wavenumber $k_c = 0.0167$, i.e. $\lambda_c^d = \frac{2\pi B V_s}{k_c} \approx 0.66$ cm, which does not agree with the experimental results given in Chapter 2, as for this ratio the initial wavelength is estimated to be 1.31 cm. This disagreement could be due to many reasons. One of them is that the experiment is performed for a suspension in a layer of finite depth of 0.47 cm with considering boundary conditions, the no−slip boundary condition at the rigid boundary together with the stress−free boundary condition at the free surface, whereas this analysis is conducted for a deep suspension where the layer is deep enough to neglect the boundary conditions. Another reason is that there is some nonlinear effect on the bioconvection pattern formation that was not considered in this investigation. The final reason is the lack of the accurate parameter estimation for the *C. reinhardtii*. The above reasons combined together results in uncertain estimation of the initial critical wavenumber k_c.

Chapter 4

Time evolving bioconvection patterns in a layer of finite depth: non−normal stability analysis

The most unstable wavelength was predicted in a layer of a finite depth by Hill et al. [50] and Bees and Hill [12]. In their analysis, the concentration profile in the equilibrium solution was assumed to reach its steady state at the time $t = 0$; before the instability started, and this does not change as the time grows but this contradicts the experiments. It was observed that the cells are uniformly distributed across the whole suspension at the time $t = 0$, and as the time evolves, the cell concentration profile changes, due to the cells upswimming behaviour, to form an exponential profile as a function of the suspension depth z. For example, in a suspension of 0.5 cm depth of the green algae *C. augustae* that swim with a speed of 63 μms^{-1}, the instability may start at the time $t = 30$ s and the steady basic state will be reached at the time $t = 80$ s. Hence, the investigation can be more realistic by considering a time evolving basic state for the concentration profile in the equilibrium solution instead of the steady state.

In this chapter, we follow the non−normal stability analysis that was presented by Doumenc et al. [27] for the unsteady Bénard−Marangoni problem. To start with, we consider an equilibrium solution that has a time dependent concentration profile n^*_{bs}

as a basic state. Unlike the linear stability analysis presented by Hill et al. [50] and Bees and Hill [12], the time evolving basic state changes the size of initial perturbation, $\varsigma(z^*, t^*)$, at every time step. Next, we measure the size of the initial perturbation $\varsigma(z^*, t_1^*)$ at a given time t_1 for a given set of parameters over a range of wavenumbers k by evaluating $E(\varsigma(t_1^*)) = \int_a^b \varsigma(z^*, t_1^*)\,\bar{\varsigma}(z^*, t_1^*)\ dz^*$, where $^-$ is the complex conjugate. Then, we extract the most unstable wavelength of the bioconvection patterns by specifying the wavenumber that corresponds to the maximum energy amplified over a range of wavenumbers.

4.1 Mathematical Model

In this analysis and for the sake of simplicity we follow the model presented by Hill et al. [50]. A monoculture of swimming microorganisms is considered. All of the cells are assumed to have the same body volume, v, with cell density, $\rho + \Delta\rho$, where ρ is the density constant of the ambient fluid and $\Delta\rho \ll \rho$. In a unit volume, that is centered at the location $\mathbf{x}$ at the time t, the cell concentration is $n(\mathbf{x}, t)$. The suspension is also assumed to be diluted so that $nv \ll 1$ per unit volume. Since the suspension is diluted, the distance between the cells is large enough, compared to the cell size, to neglect the cell−to−cell interaction.

The suspension is assumed to be incompressible

$$\nabla \cdot \mathbf{U} = 0, \tag{4.1}$$

where $\mathbf{U}(\mathbf{x}, t)$ is the suspension velocity at location $\mathbf{x}$ and time t.

Since the swimming cells increase the density of the fluid slightly, according to the Boussinesq approximation, any changes in the fluid density can be neglected except where it is multiplied by the acceleration due to gravity $\mathbf{g}$ (Kundu and Dowling [68]). In a unit volume of the suspension, the buoyancy force equals to $nv\mathbf{g}\Delta\rho$. Following Hill et al. [50], $\mathbf{U}$ is assumed to be governed by Navier−Stokes equation with added buoyancy

term, such that

$$\rho\frac{D\mathbf{U}}{Dt} = -\nabla P_e + nv\mathbf{g}\Delta\rho + \mu\nabla^2\mathbf{U}, \tag{4.2}$$

where μ is the dynamic constant viscosity of the fluid, $P_e(\mathbf{x},t)$ is the excess pressure above the hydrostatic and $\frac{D}{Dt} = \frac{\partial}{\partial t} + \mathbf{U}\cdot\nabla$ is the material derivative.

Conservation of the number of cells gives the final governing equation, which is

$$\frac{\partial n}{\partial t} = -\nabla\cdot\left[n\mathbf{U} + nV_s\mathbf{p} - D\nabla n\right]. \tag{4.3}$$

The randomness in the cell swimming velocity is presented by the term $D\nabla n$ in equation (4.3). The cells diffuse from regions of high cell concentration to regions of low cell concentration. For simplicity, cell diffusion is assumed to be isotropic, and the diffusivity D is constant, and independent of all the other parameters in this analysis.

The term $nV_s\mathbf{p}$ in (4.3) represents the cell flux due to directed swimming. The quantity $V_s\mathbf{p}$ is the average swimming velocity relative to the fluid, where V_s is the cell swimming speed, assumed to be constant and the same for all swimming cells. The unit vector $\mathbf{p}(\mathbf{x},t)$ is the direction in which the cells swim. Consider,

$$\mathbf{p} = (\sin\theta\cos\phi, \sin\theta\sin\phi, \cos\theta), \tag{4.4}$$

where θ is the angle between the cell's axis of symmetry that is aligned with $\mathbf{p}$, the swimming direction, since the cell is spheroidal, and the $z-$axis, while ϕ is the angle between the projection of $\mathbf{p}$ on the $xy-$plane and the $x-$axis, as illustrated in Figure 4.1.

Gyrotaxis is the dominant mechanism. As a consequence, the orientation $\mathbf{p}(\mathbf{x},t)$ can be determined by balancing the viscous torque, which is exerted by the fluid on the cell, and the gravitational torque due to gravity. Pedley and Kessler [85] calculated θ and ϕ using equation (1.14). They multiplied equation (1.14) by 2, divided it by $\mu v\alpha_\perp$ and defining $\dot{\mathbf{p}} = \boldsymbol{\Omega}\times\mathbf{p}$ to obtain the following equation

$$\frac{2hmg}{\mu v\alpha_\perp}\left[\mathbf{k} - (\mathbf{k}\cdot\mathbf{p})\,\mathbf{p}\right] + 2\left[\frac{1}{2}\boldsymbol{\omega}\times\mathbf{p} - \boldsymbol{\Omega}\times\mathbf{p} + \alpha_0\mathbf{p}\cdot\mathbf{e}\cdot(\mathbf{I} - \mathbf{pp})\right] = \tilde{\mathbf{L}} = 0. \tag{4.5}$$

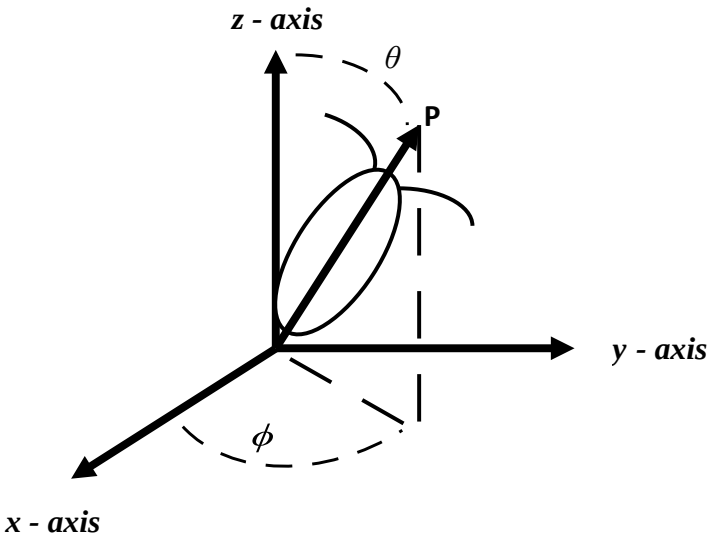

FIGURE 4.1: The angles θ and ϕ that determines the cell's swimming direction in equations (4.11)−(4.12) visualized in the cartesian coordinates xyz.

Then, they calculated the scalar product of the resultant equation (4.5) with the vectors $\mathbf{p}$ that is given by equation (4.4), $\mathbf{q}$ and $\mathbf{r}$ that are given by

$$\mathbf{q} = (\cos\theta\cos\phi, \cos\theta\sin\phi, -\sin\theta)\,, \tag{4.6}$$

and

$$\mathbf{r} = (-\sin\phi, \cos\phi, 0)\,, \tag{4.7}$$

where $\mathbf{p}$, $\mathbf{q}$ and $\mathbf{r}$ are a set of right handed unit vectors to obtain the following equations

$$\tilde{\mathbf{L}}\cdot\mathbf{p} = \left(\frac{\alpha_{\parallel}}{\alpha_{\perp}}\right)\left(\acute{\boldsymbol{\omega}}\cdot\mathbf{p} - 2\acute{\Omega}\right) = 0, \tag{4.8}$$

$$\tilde{\mathbf{L}}\cdot\mathbf{q} = \acute{\boldsymbol{\omega}}\cdot\mathbf{q} - B^{-1}r_3 - 2\alpha_0 p_j r_k e_{jk} = 0, \tag{4.9}$$

and

$$\tilde{\mathbf{L}} \cdot \mathbf{r} = \acute{\boldsymbol{\omega}} \cdot \mathbf{r} + B^{-1} q_3 + 2\alpha_0 p_j q_k e_{jk} = 0, \tag{4.10}$$

where $\acute{\boldsymbol{\omega}} = \boldsymbol{\omega} - 2\boldsymbol{\Omega}_c$, $\boldsymbol{\Omega} - \boldsymbol{\Omega}_c = \acute{\Omega}\mathbf{p}$ and $\boldsymbol{\Omega}_c$ represents the local equilibrium cell angular velocity. Hence, substituting the above definitions of $\mathbf{p}$, $\mathbf{q}$ and $\mathbf{r}$ in equations (4.9) and (4.10) as well as, for the sake of simplicity, considering a two−dimensional flow in the vertical plane that contains the unit vectors $\mathbf{p}$ and $\mathbf{q}$ so that $\boldsymbol{\Omega}_c = 0$, θ and ϕ are given by the equations

$$\begin{aligned} B^{-1} \sin\theta = \omega_2 \cos\phi - \omega_1 \sin\phi + \alpha_0 \{ & \sin 2\theta \left(e_{11} \cos^2\phi + 2e_{12} \sin\phi \cos\phi \right. \\ & \left. + e_{22} \sin^2\phi - e_{33} \right) + 2\cos 2\theta \left(e_{13} \cos\phi + e_{23} \sin\phi \right) \}, \end{aligned} \tag{4.11}$$

and

$$\begin{aligned} 0 = -\omega_1 \cos\theta \cos\phi - \omega_2 \cos\theta \sin\phi + \omega_3 \sin\theta + \alpha_0 \{ & \sin\theta \left(-e_{11} \sin 2\phi \right. \\ & \left. + 2e_{12} \cos 2\phi + e_{22} \sin 2\phi \right) + 2\cos\theta \left(-e_{13} \sin\phi + e_{23} \cos\phi \right) \}, \end{aligned} \tag{4.12}$$

where

$$\alpha_0 = \frac{a^2 - b^2}{a^2 + b^2}, \tag{4.13}$$

in equations (4.11) and (4.12) is called the cell eccentricity, a is the major axis and b is the minor axis of the spheroidal cell. The gyrotactic orientation parameter B in (4.11) is defined as $B = \frac{\mu\alpha_\perp}{2h\rho g}$, where $\alpha_\perp$ is the dimensionless resistance coefficient for the rotation about an axis perpendicular to $\mathbf{p}$, h is the center−of−mass offset, $\boldsymbol{\omega}$ is the fluid vorticity and $\mathbf{e}$ is the rate−of−strain tensor.

The fluid layer is assumed to be of depth H with boundaries at $z = -H$ and $z = 0$, (see Figure 4.2). Thus, the governing equations are complemented by the boundary conditions

$$\mathbf{U} \cdot \mathbf{k} = 0, \qquad \text{at} \quad z = -H, 0. \tag{4.14}$$

i.e. the vertical component of the velocity vanishes at the boundary, and

$$[\mathbf{U}n + nV_s\mathbf{p} - D\nabla n] \cdot \mathbf{k} = 0, \quad \text{at} \quad z = -H, 0. \tag{4.15}$$

i.e. no cell flux at the boundaries. Since the boundaries could be no−slip or stress−free, two types of boundary conditions are investigated. The no−slip boundary condition requires

$$\mathbf{U} \times \mathbf{k} = \mathbf{0} \quad \text{at} \quad z = -H, \tag{4.16}$$

whereas the stress−free boundary condition is

$$\frac{\partial \mathbf{U}}{\partial z} = 0 \quad \text{at} \quad z = 0. \tag{4.17}$$

Each theoretical situation is assumed to start from a uniform well−mixed state. Hence, the initial condition

$$n\,(z, 0) = n_0, \qquad -H \leq z \leq 0, \tag{4.18}$$

is imposed.

Equations (4.1)−(4.3), (4.11), (4.12) and (4.14)−(4.18) are non−dimensionlized as in Table 4.1.

The nondimensionlized governing equations are

$$\nabla^* \cdot \mathbf{U}^* = 0. \tag{4.19}$$

$$S_c^{-1} \frac{D\mathbf{U}^*}{Dt^*} = -\nabla^* P_e^* - Ra\; n^* \mathbf{k} + {\nabla^*}^2 \mathbf{U}^*, \tag{4.20}$$

where $S_c = \frac{\nu}{D}$ is the Schmidt number and $Ra = \frac{H^3 n_0 v g \Delta\rho}{D\rho\nu}$ is the Rayleigh number, and

$$\frac{\partial n^*}{\partial t^*} = -\nabla^* \cdot \left[n^* \mathbf{U}^* + \kappa n^* \mathbf{p} - \nabla^* n^*\right], \tag{4.21}$$

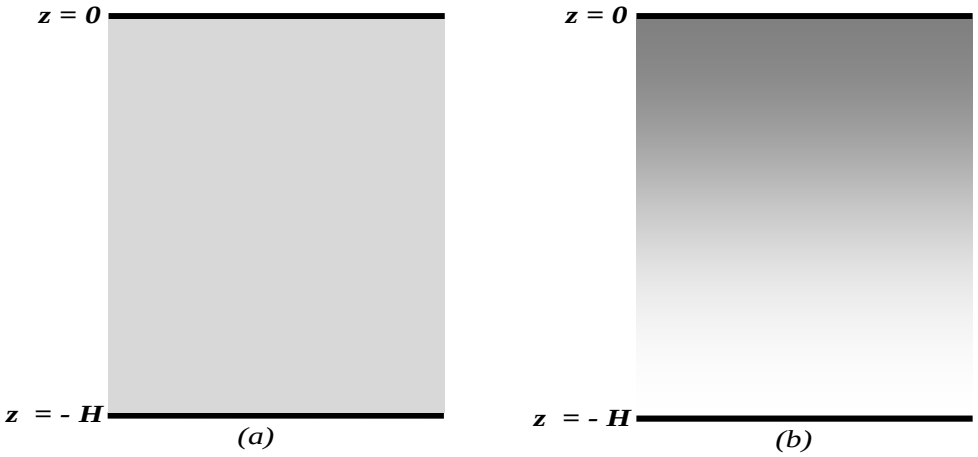

FIGURE 4.2: Visualization of the suspension in layer that lies between two horizontal boundaries at $z = 0$ and $z = -H$. (a) The suspension is distributed uniformly to start with at the time $t = 0$. (b) The cells distribution after a time $t = t_1$, the dark area indicates a higher cell concentration.

Variables	Non−dimensionlization
Length	$x = Hx^*$
Time	$t = \frac{H^2}{D}t^*$
Bulk velocity	$\mathbf{U} = \frac{D}{H}\mathbf{U}^*$
Pressure excess	$P_e = \frac{D\rho\nu}{H^2}P_e^*$
Concentration	$n = n_0 n^*$
Vorticity	$\boldsymbol{\omega} = \frac{D}{H^2}\boldsymbol{\omega}^*$
Rate−of−strain	$\mathbf{e} = \frac{D}{H^2}\mathbf{e}^*$

TABLE 4.1: The new non−dimensional variables $x^*, t^*, \mathbf{U}^*, P_e^*$, n^*, $\boldsymbol{\omega}^*$ and $\mathbf{e}^*$, and their relation to the dimensional variables.

where $\kappa = \frac{V_s H}{D}$. The equations for the swimming direction become

$$G^{-1}\sin\theta = \omega_2^*\cos\phi - \omega_1^*\sin\phi + \alpha_0\left\{\sin 2\theta\left(e_{11}^*\cos^2\phi + 2e_{12}^*\sin\phi\cos\phi\right.\right.$$
$$\left.\left.+e_{22}^*\sin^2\phi - e_{33}^*\right) + 2\cos 2\theta\left(e_{13}^*\cos\phi + e_{23}^*\sin\phi\right)\right\}, \tag{4.22}$$

and

$$0 = -\omega_1^*\cos\theta\cos\phi - \omega_2^*\cos\theta\sin\phi + \omega_3^*\sin\theta + \alpha_0\left\{\sin\theta\left(-e_{11}^*\sin 2\phi\right.\right.$$
$$\left.\left.+2e_{12}^*\cos 2\phi + e_{22}^*\sin 2\phi\right) + 2\cos\theta\left(-e_{13}^*\sin\phi + e_{23}^*\cos\phi\right)\right\}, \tag{4.23}$$

where $G = \frac{BD}{H^2}$ is the dimensionless gyrotactic reorientation parameter. The boundary conditions are

$$\mathbf{U}^*\cdot\mathbf{k} = 0, \quad \text{at} \quad z^* = -1, 0, \tag{4.24}$$

and

$$\left[\mathbf{U}^* n^* + \kappa n^*\mathbf{p} - \nabla^* n^*\right]\cdot\mathbf{k} = 0, \quad \text{at} \quad z^* = -1, 0, \tag{4.25}$$

and either the no−slip boundary condition

$$\mathbf{U}^*\times\mathbf{k} = 0, \tag{4.26}$$

or the stress−free boundary condition

$$\frac{\partial\mathbf{U}^*}{\partial z^*} = 0. \tag{4.27}$$

applied at $z^* = 0, -1$ Finally, the initial condition is

$$n^*\left(z^*, 0\right) = 1, \quad -1 \le z^* \le 0. \tag{4.28}$$

Parameter	Value	Reference
Cell volume v	$5{\times}10^{-10}$ cm^3	[115]
Cell density ratio $\frac{\Delta\rho}{\rho}$	$5{\times}10^{-2}$	[115]
Cell diffusivity D	$5{\times}10^{-4}$ cm^{2}s^{-1}	[50]
Gyrotactic number G	$\frac{0.5}{\kappa^2}$	[50]
Cell eccentricity α_0	0.2	[115]
Swimming speed V_s	6.3×10^{-3} cm s^{-1}	[115]
Mean cell concentration n	6.5×10^6 cm^{-3}	
Schmidt number S_c	20	[50]

TABLE 4.2: Typical parameters values for a suspension of the green algae *Chlamydomonas augustae*

4.2 The concentration as it evolves with time

In the absence of fluid flow (i.e., when $\mathbf{U}^* = 0$), the vorticity vector $\boldsymbol{\omega}^*$ and the rate−of−strain tensor $\mathbf{e}^*$ vanish. Hence, the swimming direction equation (4.22) will be

$$\sin\theta = 0, \tag{4.29}$$

which indicates that the swimming direction is vertically upwards (i.e., $\mathbf{p} = \mathbf{k}$). Hence, equation (4.21) can be written as

$$\frac{\partial n^*}{\partial t^*} = -\kappa\frac{\partial n^*}{\partial z^*} + \frac{\partial^2 n^*}{\partial {z^*}^2}. \tag{4.30}$$

Equation (4.30) is solved by using the method of separation of variables (Articolo [6]). Consider

$$n^*\left(z^*, t^*\right) = n_s^*\left(z^*\right) + H^*\left(z^*, t^*\right). \tag{4.31}$$

The solution $n^*\left(z^*, t^*\right)$ satisfies the boundary conditions

$$\left[\kappa n^*\mathbf{k} - \nabla^* n^*\right]\cdot\mathbf{k} = 0, \qquad \text{at} \qquad z^* = -1, 0, \tag{4.32}$$

and the initial condition

$$n^*\left(z^*, 0\right) = 1. \tag{4.33}$$

4.2.1 The steady state solution

The steady state solution is obtained by solving the equation

$$-\kappa\frac{\partial n^*}{\partial z^*}+\frac{\partial^2 n^*}{\partial {z^*}^2}=0, \tag{4.34}$$

subject to the conditions (4.32) and (4.33). The general solution is

$$n_s^*\left(z^*\right)=Ae^{\kappa z^*}+B. \tag{4.35}$$

Applying the boundary condition at $z^*=0$ gives $B=0$. Also, $\int_{-1}^{0} n_s^*\,dz^*=1$ implies that

$$A=\frac{\kappa}{1-e^{-\kappa}}. \tag{4.36}$$

where $\kappa=\frac{V_s H}{D}$.

4.2.2 Time−dependent solution

Consider solution of the form $F^*\left(t^*\right)G^*\left(z^*\right)$. Substituting into (4.30) yields

$$F^{*\prime}\left(t^*\right)G^*\left(z^*\right)=-\kappa F^*\left(t^*\right)G^{*\prime}\left(z^*\right)+F^*\left(t^*\right)G^{*\prime\prime}\left(z^*\right). \tag{4.37}$$

Divide by $F^*\left(t^*\right)G^*\left(z^*\right)$ to give

$$\frac{F^{\prime *}\left(t^*\right)}{F^*\left(t^*\right)}=-\kappa\frac{G^{\prime *}\left(z^*\right)}{G^*\left(z^*\right)}+\frac{G^{\prime\prime *}\left(z^*\right)}{G^*\left(z^*\right)}=\sigma, \tag{4.38}$$

where σ is a non−zero constant. Hence,

$$F^*\left(t^*\right)=e^{\sigma t^*}, \tag{4.39}$$

and

$$G^*\left(z^*\right)=C_1e^{m_+z^*}+C_2e^{m_-z^*}, \tag{4.40}$$

where

$$m_{\pm} = \frac{\kappa \pm \sqrt{\kappa^2 + 4\sigma}}{2}, \tag{4.41}$$

and C_1 and C_2 are functions of σ. Applying the boundary condition

$$[\kappa n^* \mathbf{k} - \nabla^* n^*] \cdot \mathbf{k} = 0, \quad \text{at} \quad z = -1, 0, \tag{4.42}$$

yields

$$(\kappa - m_+) C_1 = -(\kappa - m_-) C_2, \tag{4.43}$$

and

$$(\kappa - m_+) C_1 e^{-m_+} + (\kappa - m_-) C_2 e^{-m_-} = 0. \tag{4.44}$$

These relationships between C_1 and C_2 imply that

$$(\kappa - m_-) C_2 \left[e^{-m_-} - e^{-m_+}\right] = 0. \tag{4.45}$$

As $\sigma \neq 0$, when $\kappa \neq m_-$. Therefore, for a non−trivial solution

$$e^{-m_-} - e^{-m_+} = 0 \Longrightarrow e^{m_+ - m_-} = 1. \tag{4.46}$$

This implies

$$m_+ - m_- = 2k\pi i, \quad k = 0, 1, 2, \ldots \tag{4.47}$$

Hence, from equation (4.41) the growth rate σ is a function of k given by

$$\sigma = \sigma_k = -\frac{1}{4}\left(4k^2\pi^2 + \kappa^2\right), \quad k = 0, 1, 2, \ldots \tag{4.48}$$

As a consequence, m_+ and m_- are functions of k such that

$$m_\pm = m_{\pm k} = \frac{\kappa \pm 2k\pi i}{2}, \quad k = 0, 1, 2, \ldots \tag{4.49}$$

Also, equation (4.44) with $C_1 = C_{1k}$ and $C_2 = C_{2k}$ can be written as

$$C_{1k} = -\left(\frac{\kappa - m_{-k}}{\kappa - m_{+k}}\right) C_{2k}, \quad k = 0, 1, 2, \ldots \tag{4.50}$$

Thus,

$$H^*(z^*, t^*) = \sum_{k=0}^{\infty} e^{-\frac{1}{4}\left(4k^2\pi^2+\kappa^2\right)t^*} \left[-\left(\frac{\kappa - m_{-k}}{\kappa - m_{+k}}\right) C_{2k} e^{\left(\frac{\kappa+2k\pi i}{2} z^*\right)} + C_{2k} e^{\left(\frac{\kappa-2k\pi i}{2} z^*\right)}\right], \tag{4.51}$$

since equation (4.30) is linear, its solution is a linear combination of linearly independent solutions. Equation (4.51) can be simplified as

$$H^*(z^*, t^*) = e^{\frac{\kappa}{2} z^*} \sum_{k=0}^{\infty} e^{-\frac{1}{4}\left(4k^2\pi^2+\kappa^2\right)t^*} \left(\frac{C_{2k}}{m_{-k}}\right) \left[-m_{+k} e^{k\pi z^* i} + m_{-k} e^{-k\pi z^* i}\right]. \tag{4.52}$$

So that

$$H^*(z^*, t^*) = -e^{\frac{\kappa}{2} z^*} \sum_{k=0}^{\infty} e^{-\frac{1}{4}\left(4k^2\pi^2+\kappa^2\right)t^*} \left(\frac{4C_{2k} i}{\kappa - 2k\pi i}\right) \left[\frac{\kappa}{2} \sin(k\pi z^*) + k\pi \cos(k\pi z^*)\right] \tag{4.53}$$

The coefficients $\frac{4C_{2k}}{\kappa - 2k\pi i}$ in (4.53) must be purely imaginary to ensure that $H^*(z^*, t^*)$ is a real function. Hence,

$$\frac{4C_{2k}}{\kappa - 2k\pi i} = iX_k, \quad \text{where} \quad X_k \in \mathbb{R} \quad \text{and} \quad C_{2k} = a_k + b_k i. \tag{4.54}$$

Equation (4.54) leads to a system of two linear equations

$$\begin{aligned} \kappa a_k - 2\pi k b_k &= 0, \\ 2k\pi a_k + \kappa b_k &= \left(\frac{\kappa^2 + 4k^2\pi^2}{4}\right) X_k. \end{aligned} \tag{4.55}$$

The solution to the above system is

$$a_k = \frac{k\pi}{2} X_k, \quad b_k = \frac{\kappa}{4} X_k. \tag{4.56}$$

Now,

$$H^*\left(z^*,t^*\right)=e^{\frac{\kappa}{2}z^*}\sum_{k=0}^{\infty}e^{-\frac{1}{4}\left(4k^2\pi^2+\kappa^2\right)t^*}\left[\eta_k\cos\left(k\pi z^*\right)+\xi_k\sin\left(k\pi z^*\right)\right], \tag{4.57}$$

where $\eta_k = k\pi X_k$ and $\xi = \frac{\kappa}{2}X_k$.

The values of the coefficients η_k and ξ_k are calculated be imposing the initial condition on the function $H^*\left(z^*,t^*\right)$, such that

$$e^{\frac{\kappa}{2}z^*}\sum_{k=0}^{\infty}\left[\eta_k\cos\left(k\pi z^*\right)+\xi_k\sin\left(k\pi z^*\right)\right]=1-n_s^*\left(z^*\right), \tag{4.58}$$

and

$$n_s^*\left(z^*\right)=\left(\frac{\kappa}{1-e^{-\kappa}}\right)e^{\kappa z^*}. \tag{4.59}$$

$$\sum_{k=0}^{\infty}\left[\eta_k\cos\left(k\pi z^*\right)+\xi_k\sin\left(k\pi z^*\right)\right]=e^{-\frac{\kappa}{2}z^*}-\left(\frac{\kappa}{1-e^{-\kappa}}\right)e^{\frac{\kappa}{2}z^*}. \tag{4.60}$$

Here, η_0, η_k and ξ_k are defined as, (see Appendix C.1),

$$\eta_0=\frac{1}{2}\int_{-1}^{0}\left[e^{-\frac{\kappa}{2}z^*}-\left(\frac{\kappa}{1-e^{-\kappa}}\right)e^{\frac{\kappa}{2}z^*}\right]dz^*, \tag{4.61}$$

$$\eta_k=\int_{-1}^{0}\left[e^{-\frac{\kappa}{2}z^*}-\left(\frac{\kappa}{1-e^{-\kappa}}\right)e^{\frac{\kappa}{2}z^*}\right]\cos\left(k\pi z^*\right)dz^*, \tag{4.62}$$

and

$$\xi_k=\int_{-1}^{0}\left[e^{-\frac{\kappa}{2}z^*}-\left(\frac{\kappa}{1-e^{-\kappa}}\right)e^{\frac{\kappa}{2}z^*}\right]\sin\left(k\pi z^*\right)dz^*. \tag{4.63}$$

Using the integrals in Appendix C.2, η_0, η_k and ξ_k are calculated to be

$$\eta_0=-\frac{1}{\kappa}\left[\left(1-e^{\frac{\kappa}{2}}\right)+\left(\frac{\kappa}{1-e^{-\kappa}}\right)\left(1-e^{-\frac{\kappa}{2}}\right)\right], \tag{4.64}$$

$$\eta_k = -\left[\frac{\kappa}{2\left(\frac{\kappa^2}{4}+k^2\pi^2\right)}\right]\left[\left(1-(-1)^k\, e^{\frac{\kappa}{2}}\right)+\left(\frac{\kappa}{1-e^{-\kappa}}\right)\left(1-(-1)^k\, e^{-\frac{\kappa}{2}}\right)\right], \quad (4.65)$$

$$\xi_k = -\left[\frac{k\pi}{2\left(\frac{\kappa^2}{4}+k^2\pi^2\right)}\right]\left[\left(1-(-1)^k\, e^{\frac{\kappa}{2}}\right)-\left(\frac{\kappa}{1-e^{-\kappa}}\right)\left(1-(-1)^k\, e^{-\frac{\kappa}{2}}\right)\right]. \quad (4.66)$$

Finally, the concentration as a function of time and depth is

$$n^*_{bs}\left(z^*,t^*\right) = \frac{\kappa e^{\kappa z^*}}{1-e^{-\kappa}} + e^{\frac{\kappa}{2}z^*}\sum_{k=0}^{\infty} e^{-\frac{1}{4}\left(4k^2\pi^2+\kappa^2\right)t^*}\left[\eta_k\cos\left(k\pi z^*\right)+\xi_k\sin\left(k\pi z^*\right)\right], \quad (4.67)$$

where the subscript bs stands for the basic state. The function n^*_{bs} states that if initially the suspension is well mixed and the cell distribution is uniform,then, the concentration evolves to reach a top−heavy exponential profile due to the upswimming behavior of the cells (see Figure 4.2).

Figure 4.3 displays the basic state profile of the cell concentration as a function of time t^* and depth z^*. Figure 4.3(a) shows a three−dimensional plot of the concentration profile that results from solving equation (4.30) numerically for $\kappa = 0.1$, whereas Figure 4.3(b) shows the analytical concentration profile that is given by equation (4.67) for the value of $\kappa = 0.1$ and $k = 1000$. The relative error between the analytical and numerical solution is less than 2.5%. The relative error reaches its maximum value 2.5% at time $t^* = 0$ for the value of $z^* = -1$ and 0 since the analytical solution requires approximating the infinite summation over k in equation (4.67) by a finite one; in this case $k = 0, 1, \cdots, 1000$. Hence, the oscillatory behavior will affect the value of n^*_{bs} at the above values of t^* and z^* which makes the numerical solution more accurate. Figures 4.3(c) and 4.3(d) present the numerical solution of the concentration profile at $t^* = 0.01$ and 0.05, respectively, for different values of κ, while Figure 4.3(e) presents the steady state solution given by equation (4.59). The graphs in Figure 4.3 show that cell concentration profile evolves with time to reach the steady state.

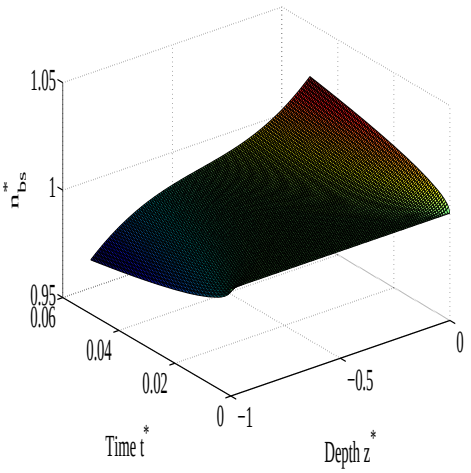

(a) Numerical solution

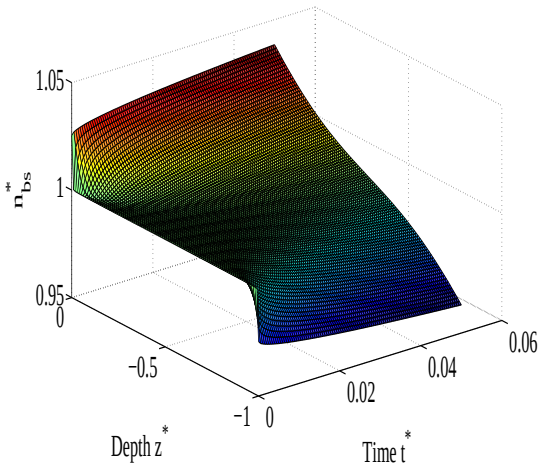

(b) Analytical solution

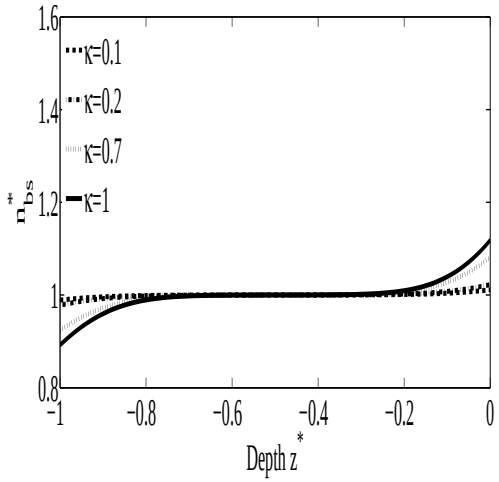

(c) $t^* = 0.01$

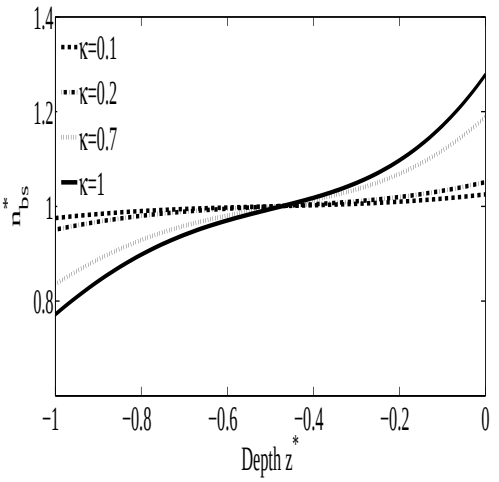

(d) $t^* = 0.05$

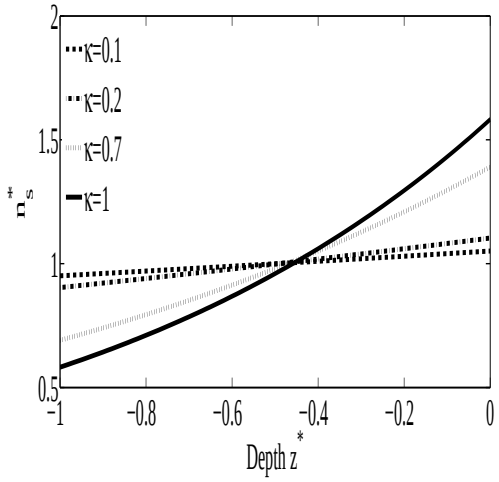

(e) Steady state solution

FIGURE 4.3: The basic state concentration profile. (a) The numerical solution for the value of $\kappa = 0.1$ (b) The analytical solution for the value of $\kappa = 0.1$ (c),(d) Concentration profile as a function of depth z^* at the times $t^* = 0.01$ and 0.05 respectively, for different values of $\kappa = 0.1, 0.2.0.7$ and 1 and (e) The steady state profile for $\kappa = 0.1, 0.2, 0.7$ and 1.

4.3 Linearization

A small perturbation of order ϵ is added to the basic field and substituted in equations (4.19)−(4.28), so that

$$\begin{aligned}
&\mathbf{U}^*(\mathbf{x}^*,t^*) = \epsilon\mathbf{U}_p(\mathbf{x}^*,t^*), \quad P_e^*(\mathbf{x}^*,t^*) = P_{ebs}^*(\mathbf{x}^*,t^*) + \epsilon P_{ep}(\mathbf{x}^*,t^*),\\
&n^*(\mathbf{x}^*,t^*) = n_{bs}^*(\mathbf{z}^*,t^*) + \epsilon n_p(\mathbf{x}^*,t^*), \quad \mathbf{p}(\mathbf{x}^*,t^*) = \mathbf{k} + \epsilon\mathbf{p}_p(\mathbf{x}^*,t^*),
\end{aligned} \tag{4.68}$$

where $0 \leq \epsilon \ll 1$.

For the basic state, the swimming direction is vertically upwards. Hence, if the perturbation plane is the $zx-$plane, (i.e., $\phi = 0$), the swimming direction in (4.68) is

$$\begin{aligned}
\mathbf{p} &= (\sin\epsilon\theta_p, \cos\epsilon\theta_p, 1)\\
&= (\epsilon\theta_p, 0, 1) + O\left(\epsilon^2\right).
\end{aligned} \tag{4.69}$$

with $\mathbf{p}_p$ given by

$$\mathbf{p}_p = (\theta_p, 0, 0). \tag{4.70}$$

Consequently, the linearized governing system is,

$$\nabla^* \cdot \mathbf{U}_p = 0, \tag{4.71}$$

$$S_c^{-1}\frac{\partial \mathbf{U}_p}{\partial t^*} = -\nabla^* P_{ep} - Ra\, n_p\mathbf{k} + \nabla^{*^2}\mathbf{U}_p, \tag{4.72}$$

$$\frac{\partial n_p}{\partial t^*} = -\nabla^* \cdot \left[n_{bs}^*\mathbf{U}_p + \kappa\left(n_{bs}^*\mathbf{p}_p + n_p\mathbf{k}\right) - \nabla^* n_p\right], \tag{4.73}$$

and

$$G^{-1}\theta_p - (1+\alpha_0)\frac{\partial u_p}{\partial z^*} - (\alpha_0 - 1)\frac{\partial w_p}{\partial x^*} = 0. \tag{4.74}$$

with the boundary conditions

$$\mathbf{U}_p \cdot \mathbf{k} = 0, \quad \text{at} \quad z^* = -1, 0, \tag{4.75}$$

$$[n^*_{bs}\mathbf{U}_p + \kappa\,(n^*_{bs}\mathbf{p}_p + n_p\mathbf{k}) - \nabla^* n_p] \cdot \mathbf{k} = 0, \quad \text{at} \quad z^* = -1, 0, \tag{4.76}$$

for the no−slip boundary

$$\mathbf{U}_p \times \mathbf{k} = 0, \tag{4.77}$$

whereas at the stress−free boundary

$$\frac{\partial \mathbf{U}_p}{\partial z^*} = 0, \tag{4.78}$$

applied at $z^* = -1$ and 0.

Without loss of generality consider $\mathbf{U}_p = (u_p, 0, w_p)$. The linearized equations (4.71)−(4.78) can be written in the component form as

$$\frac{\partial u_p}{\partial x^*} + \frac{\partial w_p}{\partial z^*} = 0, \tag{4.79}$$

$$S_c^{-1}\frac{\partial u_p}{\partial t^*} + \frac{\partial P_{ep}}{\partial x^*} - \left(\frac{\partial^2}{\partial x^{*2}} + \frac{\partial^2}{\partial z^{*2}}\right) u_p = 0, \tag{4.80}$$

$$S_c^{-1}\frac{\partial w_p}{\partial t^*} + \frac{\partial P_{ep}}{\partial z^*} + Ra\; n_p - \left(\frac{\partial^2}{\partial x^{*2}} + \frac{\partial^2}{\partial z^{*2}}\right) w_p = 0, \tag{4.81}$$

$$\frac{\partial n_p}{\partial t^*} + \frac{\partial n^*_{bs}}{\partial z^*} w_p + \kappa\left(n^*_{bs}\frac{\partial \theta_p}{\partial x^*} + \frac{\partial n_p}{\partial z^*}\right) - \left(\frac{\partial^2}{\partial x^{*2}} + \frac{\partial^2}{\partial z^{*2}}\right) n_p = 0, \tag{4.82}$$

and

$$G^{-1}\theta_p - (1+\alpha_0)\frac{\partial u_p}{\partial z^*} - (\alpha_0 - 1)\frac{\partial w_p}{\partial x^*} = 0, \tag{4.83}$$

with the following set of boundary conditions:

$$w_p\left(z^*,t^*\right)=0,\quad \text{at}\quad z^*=-1,0, \tag{4.84}$$

$$\kappa n_p\left(z^*,t^*\right)-\frac{\partial n_p}{\partial z^*}\left(z^*,t^*\right)=0,\quad \text{at}\quad z^*=-1,0, \tag{4.85}$$

$$u_p\left(z^*,t^*\right)=0,\quad \text{at the no−slip boundary}, \tag{4.86}$$

$$\frac{\partial u_p}{\partial z^*}\left(z^*,t^*\right)=0,\quad \text{at the stress−free boundary}, \tag{4.87}$$

applied at $z^*=-1$ and 0.

4.4 Non−normal analysis

To investigate the stability using non−normal modes, one may assume without loss of generality, as in Doumenc et al. [27], that all the perturbed quantities in (4.79)−(4.87) are independent of y^* and are expressed as

$$\begin{aligned}
\mathbf{U}_p\left(x^*,z^*,t^*\right)&=\left(\tilde{u}_p\left(z^*,t^*\right),0,\tilde{w}_p\left(z^*,t^*\right)\right)e^{ikx^*},\\
n_p\left(x^*,z^*,t^*\right)&=\tilde{n}_p\left(z^*,t^*\right)e^{ikx^*},\\
\theta_p\left(x^*,z^*,t^*\right)&=\tilde{\theta}_p\left(z^*,t^*\right)e^{ikx^*},\\
P_{ep}\left(x^*,z^*,t^*\right)&=\tilde{P}_{ep}\left(z^*,t^*\right)e^{ikx^*},
\end{aligned} \tag{4.88}$$

where k is the dimensionless wavenumber in the x^*−direction. Hence, the governing equations (4.79)−(4.87) become

$$ik\tilde{u}_p+\frac{\partial\tilde{w}_p}{\partial z^*}=0, \tag{4.89}$$

$$S_c^{-1}\frac{\partial\tilde{u}_p}{\partial t^*}+ik\tilde{P}_{ep}-\left(\frac{\partial^2}{\partial z^{*2}}-k^2\right)\tilde{u}_p=0, \tag{4.90}$$

$$S_c^{-1}\frac{\partial \tilde{w}_p}{\partial t^*}+\frac{\partial \tilde{P}_{ep}}{\partial z^*}+Ra\;\tilde{n}_p-\left(\frac{\partial^2}{\partial z^{*^2}}-k^2\right)\tilde{w}_p=0, \tag{4.91}$$

$$\frac{\partial \tilde{n}_p}{\partial t^*}+\frac{\partial n^*_{bs}}{\partial z^*}\tilde{w}_p+\kappa\left(ikn^*_{bs}\tilde{\theta}_p+\frac{\partial \tilde{n}_p}{\partial z^*}\right)-\left(\frac{\partial^2}{\partial z^{*^2}}-k^2\right)\tilde{n}_p=0, \tag{4.92}$$

and

$$G^{-1}\tilde{\theta}_p-(1+\alpha_0)\frac{\partial \tilde{u}_p}{\partial z^*}-(\alpha_0-1)\,ik\tilde{w}_p=0, \tag{4.93}$$

with the boundary conditions

$$\tilde{w}_p=0,\quad \text{at}\quad z^*=-1,0, \tag{4.94}$$

$$\kappa\tilde{n}_p-\frac{\partial \tilde{n}_p}{\partial z^*}=0,\quad \text{at}\quad z^*=-1,0, \tag{4.95}$$

$$\tilde{u}_p=0,\quad \text{at the no−slip boundary}, \tag{4.96}$$

$$\frac{\partial \tilde{u}_p}{\partial z^*}=0,\quad \text{at the stress−free boundary}, \tag{4.97}$$

applied at $z^*=-1$ and 0.

Assume that $\mathbf{Q}\left(z^*,t^*\right)$ is the vector field defined as

$$\mathbf{Q}\left(z^*,t^*\right)=\left(\tilde{u}_p\left(z^*,t^*\right),\tilde{w}_p\left(z^*,t^*\right),\tilde{n}_p\left(z^*,t^*\right),\tilde{P}_{ep}\left(z^*,t^*\right),\tilde{\theta}_p\left(z^*,t^*\right)\right). \tag{4.98}$$

The perturbation energy at a given time t_1^* may be defined as (Doumenc et al. [27])

$$E\left(\mathbf{Q}\left(t_1^*\right)\right)=\sum_{j=1}^{3}\vartheta_j\int_{-1}^{0}Q_j\left(z^*,t_1^*\right)\bar{Q}_j\left(z^*,t_1^*\right)dz^*, \tag{4.99}$$

where the ($^-$) stands for the complex conjugates and ϑ_j, $j=1,2,3$, are the weight coefficients to put emphasis on the velocity or the concentration according to the case

considered. In other words, when analyzing the initial perturbation in the velocity, the kinetic energy norm E_V is used and one takes $\vartheta_{1,2} = 1$ and $\vartheta_3 = 0$. Whereas the concentration norm E_N is used to analyze the initial perturbation in the concentration with $\vartheta_{1,2} = 0$ and $\vartheta_3 = 1$. $\tilde{P}_{ep}$ and $\tilde{\theta}_p$ are not considered in the definition of the energy given by equation (4.99) because they will be eliminated later in this chapter.

The purpose of the non−normal analysis is to quantify (Doumenc et al. [27] and Schmid and Henningson [100])

$$GE\left(t_1^*; k^*, S_c, Ra, \kappa\right) = \max\left[\frac{E\left(\mathbf{Q}\left(t_1^*\right)\right)}{E\left(\mathbf{Q}\left(0\right)\right)}\right], \tag{4.100}$$

where GE stands for the gained energy at a given set of parameters and a given time and it differs from the scalar G that gives the dimensionless gyrotactic number. GE is the upper bound for the energy amplification that a disturbance with wavenumber k can reach at time t_1^*, restricted to the following constraints:

- The initial perturbation energy is normalized, i.e. $E\left(\mathbf{Q}\left(0\right)\right) = 1$.
- The vector field components satisfy the governing equations (4.89)−(4.93) together with boundary conditions (4.94)−(4.97).

The form of the optimization problem (4.100) suggests using Lagrange multipliers (Vanderbei [111] and Doumenc et al. [27]). Hence, the Lagrange function L is given by

$$\begin{aligned} L\left(\mathbf{Q}, \boldsymbol{\lambda}, t_1^*\right) &= E\left(\mathbf{Q}\left(t_1^*\right)\right) - s\left(E\left(\mathbf{Q}\left(0\right)\right) - 1\right) \\ &- \sum_{j=1}^{5} \int_0^{t_1^*} \int_{-1}^{0} \left[F_j\left(\mathbf{Q}\left(z^*, t^*\right)\right) \lambda_j\left(z^*, t^*\right) + c.c.\right] dz^* dt^*. \end{aligned} \tag{4.101}$$

where $\boldsymbol{\lambda} = \left(\lambda_1\left(z^*, t^*\right), \lambda_2\left(z^*, t^*\right), \lambda_3\left(z^*, t^*\right), \lambda_4\left(z^*, t^*\right), \lambda_5\left(z^*, t^*\right)\right)$ are Lagrange multipliers, $F_j\left(Q\left(z^*, t^*\right)\right)$ are the governing equations (4.89)−(4.93) and s is a normalization scalar. The first term of equation (4.101) is the function that we want to maximize, i. e. the numerator of equation (4.100), whereas the second term is a restriction that is added to the denominator of equation (4.100) to normalize the energy of the initial

perturbation for the sake of simplicity in computing the function GE. The final terms in (4.101) are the governing equations that the field variables must satisfy integrated across the suspension depth and time from 0 to t_1^*.

Equation (4.101) can be written in terms of the inner product

$$L\left(\mathbf{Q},\boldsymbol{\lambda},t_1^*\right)=E\left(\mathbf{Q}\left(t_1^*\right)\right)-s\left(E\left(\mathbf{Q}\left(0\right)\right)-1\right)$$
$$-\sum_{j=1}^{5}\int_0^{t_1^*}\left[\left\langle F_j\left(\mathbf{Q}\left(z^*,t^*\right)\right),\bar{\lambda}_j\left(z^*,t^*\right)\right\rangle+c.c.\right]dt^*. \tag{4.102}$$

The method of Lagrange multipliers requires computing the variation δL of the function L in (4.102) (Dym and Shames [29], see Appendix C.3). This variation equals

$$\delta L\left(\mathbf{Q},\boldsymbol{\lambda},t_1^*\right)=\sum_{j=1}^{3}\vartheta_j\int_{-1}^{0}\delta Q_j\left(z^*,t_1^*\right)\bar{Q}_j\left(z^*,t_1^*\right)dz^*$$
$$-s\sum_{j=1}^{3}\vartheta_j\int_{-1}^{0}\delta Q_j\left(z^*,0\right)\bar{Q}_j\left(z^*,0\right)dz^*-\sum_{j=1}^{5}\int_0^{t_1^*}\left[\left\langle\delta F_j\left(\mathbf{Q}\left(z^*,t^*\right)\right),\bar{\lambda}_j\left(z^*,t^*\right)\right\rangle\right. \tag{4.103}$$
$$\left.+\left\langle F_j\left(\mathbf{Q}\left(z^*,t^*\right)\right),\delta\bar{\lambda}_j\left(z^*,t^*\right)\right\rangle\right]dt^*+c.c.$$

The expression $\left\langle F_j\left(\mathbf{Q}\left(z^*,t^*\right)\right),\delta\bar{\lambda}_j\left(z^*,t^*\right)\right\rangle$ in (4.103) equals zero when $F_j\left(\mathbf{Q}\left(z^*,t^*\right)\right)=0$ during the time interval $[0,t_1^*]$. The main idea is to rewrite the quantity $\left\langle\delta F_j\left(\mathbf{Q}\left(z^*,t^*\right)\right),\bar{\lambda}_j\left(z^*,t^*\right)\right\rangle$ to be of the form $\left\langle\delta Q_j\left(z^*,t^*\right),\breve{F}_j\left(\bar{\lambda}_j\left(z^*,t^*\right)\right)\right\rangle$. So,

$$\delta L\left(\mathbf{Q},\boldsymbol{\lambda},t_1^*\right)=\left\{\sum_{j=1}^{3}\vartheta_j\int_{-1}^{0}\delta Q_j\left(z^*,t_1^*\right)\bar{Q}_j\left(z^*,t_1^*\right)dz^*-s\sum_{j=1}^{3}\vartheta_j\int_{-1}^{0}\delta Q_j\left(z^*,0\right)\bar{Q}_j\left(z^*,0\right)dz^*\right\} \tag{4.104}$$

$$-\int_0^{t_1^*}\int_{-1}^{0}\left[\begin{pmatrix} ik & \frac{\partial}{\partial z^*} & 0 & 0 & 0\\ A_D & 0 & ik & 0 & 0\\ 0 & A_D & \frac{\partial}{\partial z^*} & Ra & 0\\ 0 & \frac{\partial n_{bs}^*}{\partial z^*} & 0 & B_D & \kappa ikn_{bs}^*\\ -\left(1+\alpha_0\right)\frac{\partial}{\partial z^*} & -\left(\alpha_0-1\right)ik & 0 & 0 & G^{-1}\end{pmatrix}\begin{pmatrix}\delta\tilde{u}_p\\ \delta\tilde{w}_p\\ \delta\tilde{P}_{ep}\\ \delta\tilde{n}_p\\ \delta\tilde{\theta}_p\end{pmatrix}\right]\cdot\begin{pmatrix}\lambda_1\\ \lambda_2\\ \lambda_3\\ \lambda_4\\ \lambda_5\end{pmatrix}dz^*dt^*,$$

where

$$A_D = S_c^{-1}\frac{\partial}{\partial t^*} - \left(\frac{\partial^2}{\partial z^{*2}} - k^2\right), \tag{4.105}$$

$$B_D = \frac{\partial}{\partial t^*} - \left(\frac{\partial^2}{\partial z^{*2}} - k^2\right) + \kappa\frac{\partial}{\partial z^*}. \tag{4.106}$$

Integrating all the partial derivatives by parts leads to

$$\delta L\left(\mathbf{Q},\boldsymbol{\lambda},t_1^*\right) = \left\{\sum_{j=1}^{3}\vartheta_j\int_{-1}^{0}\delta Q_j\left(z^*,t_1^*\right)\bar{Q}_j\left(z^*,t_1^*\right)dz^* - s\sum_{j=1}^{3}\vartheta_j\int_{-1}^{0}\delta Q_j\left(z^*,0\right)\bar{Q}_j\left(z^*,0\right)dz^*\right\}$$

$$-\int_0^{t_1^*}\int_{-1}^{0}\left[\begin{pmatrix} ik & A_J & 0 & 0 & (1+\alpha_0)\frac{\partial}{\partial z^*} \\ -\frac{\partial}{\partial z^*} & 0 & A_J & \frac{\partial n_{bs}^*}{\partial z^*} & -(\alpha_0-1)ik \\ 0 & 0 & Ra & B_J & 0 \\ 0 & ik & -\frac{\partial}{\partial z^*} & 0 & 0 \\ 0 & 0 & 0 & \kappa ikn_{bs}^* & G^{-1} \end{pmatrix}\begin{pmatrix}\lambda_1\\ \lambda_2\\ \lambda_3\\ \lambda_4\\ \lambda_5\end{pmatrix}\right]\cdot\begin{pmatrix}\delta\tilde{u}_p\\ \delta\tilde{w}_p\\ \delta\tilde{P}_{ep}\\ \delta\tilde{n}_p\\ \delta\tilde{\theta}_p\end{pmatrix}dz^*dt^*$$

$$-\int_{-1}^{0}\left\{S_c^{-1}\left[\left(\delta\tilde{u}_p\right)\lambda_2\right]_0^{t_1^*} + S_c^{-1}\left[\left(\delta\tilde{w}_p\right)\lambda_3\right]_0^{t_1^*} + \left[\left(\delta\tilde{n}_p\right)\lambda_4\right]_0^{t_1^*}\right\}dz^* \tag{4.107}$$

$$-\int_0^{t_1^*}\left\{\left[\left(\delta\tilde{w}_p\right)\lambda_1\right]_{-1}^{0} + \left[\left(\delta\tilde{P}_{ep}\right)\lambda_3\right]_{-1}^{0} + \kappa\left[\left(\delta\tilde{n}_p\right)\lambda_4\right]_{-1}^{0} - (1+\alpha_0)\left[\left(\delta\tilde{u}_p\right)\lambda_5\right]_{-1}^{0} - \left[\frac{\partial\left(\delta\tilde{u}_p\right)}{\partial z^*}\lambda_2\right]_{-1}^{0}\right.$$

$$\left. + \left[\frac{\partial\lambda_2}{\partial z^*}\left(\delta\tilde{u}_p\right)\right]_{-1}^{0} - \left[\frac{\partial\left(\delta\tilde{w}_p\right)}{\partial z^*}\lambda_3\right]_{-1}^{0} + \left[\frac{\partial\lambda_3}{\partial z^*}\left(\delta\tilde{w}_p\right)\right]_{-1}^{0} - \left[\frac{\partial\left(\delta\tilde{n}_p\right)}{\partial z^*}\lambda_4\right]_{-1}^{0} + \left[\frac{\partial\lambda_4}{\partial z^*}\left(\delta\tilde{n}_p\right)\right]_{-1}^{0}\right\}dt^*,$$

where

$$A_J = -S_c^{-1}\frac{\partial}{\partial t^*} - \left(\frac{\partial^2}{\partial z^{*2}} - k^2\right), \tag{4.108}$$

$$B_J = -\frac{\partial}{\partial t^*} - \left(\frac{\partial^2}{\partial z^{*2}} - k^2\right) - \kappa\frac{\partial}{\partial z^*}. \tag{4.109}$$

Following the definition of the adjoint differential operator in Gitman et al. [39], (see Appendix C.4), one concludes that the Lagrange multipliers are the adjoint field variables.

Thus, equation (4.107) suggests renaming the variables as follow

$$\begin{aligned}\bar{\lambda}_1 &= \tilde{P}_{ep}^j,\\ \bar{\lambda}_2 &= \tilde{u}_p^j,\\ \bar{\lambda}_3 &= \tilde{w}_p^j,\\ \bar{\lambda}_4 &= \tilde{n}_p^j,\\ \bar{\lambda}_5 &= \tilde{\theta}_p^j.\end{aligned} \tag{4.110}$$

Then, the second and forth terms in equation (4.107) give the following adjoint problem

$$ik\tilde{u}_p^j + \frac{\partial \tilde{w}_p^j}{\partial z^*} = 0, \tag{4.111}$$

$$\left[S_c^{-1}\frac{\partial}{\partial \tau^*} - \left(\frac{\partial^2}{\partial z^{*2}} - k^2\right)\right]\tilde{u}_p^j - ik\tilde{P}_{ep}^j + (1+\alpha_0)\frac{\partial \tilde{\theta}_p^j}{\partial z^*} = 0, \tag{4.112}$$

$$\left[S_c^{-1}\frac{\partial}{\partial \tau^*} - \left(\frac{\partial^2}{\partial z^{*2}} - k^2\right)\right]\tilde{w}_p^j - \frac{\partial \tilde{P}_{ep}^j}{\partial z^*} + \frac{\partial n_{bs}^*}{\partial z^*}\tilde{n}_p^j + (\alpha_0 - 1)\, ik\tilde{\theta}_p^j = 0, \tag{4.113}$$

$$\left[\frac{\partial}{\partial \tau^*} - \left(\frac{\partial^2}{\partial z^{*2}} - k^2\right) - \kappa\frac{\partial}{\partial z^*}\right]\tilde{n}_p^j + Ra\tilde{w}_p^j = 0, \tag{4.114}$$

$$-\kappa ikn_{bs}^*\tilde{n}_p^j + G^{-1}\tilde{\theta}_p^j = 0, \tag{4.115}$$

where $\tau^* = -t^*$. The adjoint problem has the boundary conditions

$$\tilde{w}_p^j = 0, \quad \text{at} \quad z^* = 0, -1, \tag{4.116}$$

$$\frac{\partial \tilde{n}_p^j}{\partial z^*} = 0, \quad \text{at} \quad z^* = 0, -1, \tag{4.117}$$

$$-(1+\alpha_0)\,\tilde{\theta}_p^j + \frac{\partial \tilde{u}_p^j}{\partial z^*} = 0, \quad \text{at the stress−free surface}, \tag{4.118}$$

$$\tilde{u}_p^j = 0, \quad \text{at the no−slip surface,} \tag{4.119}$$

applied at $z^* = -1$ and 0.

Whereas the first and third terms in equation (4.107) suggests the conversion relationship between the direct and the adjoint problem as follow: when one is considering the initial perturbation in the velocity field only, the conversion from the direct to the adjoint problem at $t^* = t_1^*$, for finite Schmidt number S_c, is

$$\tilde{u}_p^j\left(z^*, t_1^*\right) = S_c \tilde{u}_p\left(z^*, t_1^*\right), \tag{4.120}$$

$$\tilde{w}_p^j\left(z^*, t_1^*\right) = S_c \tilde{w}_p\left(z^*, t_1^*\right), \tag{4.121}$$

and

$$\tilde{n}_p^j\left(z^*, t_1^*\right) = 0. \tag{4.122}$$

Whereas from the adjoint to the direct problem at $t^* = 0$

$$\tilde{u}_p\left(z^*, 0\right) = s^{-1} S_c^{-1} \tilde{u}_p^j\left(z^*, 0\right), \tag{4.123}$$

$$\tilde{w}_p\left(z^*, 0\right) = s^{-1} S_c^{-1} \tilde{w}_p^j\left(z^*, 0\right), \tag{4.124}$$

$$\tilde{n}_p^j\left(z^*, 0\right) = 0, \tag{4.125}$$

However, when the perturbation is considered to be in the concentration field, we get the following relationships to convert the direct to the adjoint problem at $t^* = t_1^*$,

$$\tilde{n}_p^j\left(z^*, t_1^*\right) = \tilde{n}_p\left(z^*, t_1^*\right), \tag{4.126}$$

$$\tilde{u}_p^j\left(z^*, t_1^*\right) = \tilde{w}_p^j\left(z^*, t_1^*\right) = 0, \tag{4.127}$$

and from the adjoint to the direct at $t^* = 0$

$$\tilde{n}_p\left(z^*, 0\right) = s^{-1}\tilde{n}_p^j\left(z^*, 0\right), \tag{4.128}$$

$$\tilde{u}_p^j\left(z^*, 0\right) = \tilde{w}_p^j\left(z^*, 0\right) = 0. \tag{4.129}$$

4.5 Numerical solution

The numerical solution algorithm works as follows, the maximum energy amplification is gained at the optimal initial perturbation. The optimal initial perturbation is achieved when $\delta L = 0$. This condition is obtained by solving the governing equations of the direct problem (4.89)−(4.93) together with the boundary conditions (4.94)−(4.97) forward in time for an imposed initial condition that satisfies the boundary conditions. Then, using the relationships between the field variables $Q\left(z^*, t^*\right)$ and the adjoint field variables $Q^j\left(z^*, t^*\right)$ given in either equations (4.120)−(4.122) or (4.126)−(4.127), one gets the initial conditions of the adjoint problem given by equations (4.111)−(4.115) with the boundary conditions (4.116)−(4.119). The adjoint problem is then solved backward in time and we use conversion relationships given by either equations (4.123)−(4.125) or (4.128)−(4.129) to get the initial condition of the direct problem again. One can perform a forward−backward scheme until the initial perturbation of the direct problem does not change appreciably. Hence, once the convergence is reached, the optimal initial perturbation will be obtained.

For the sake of simplicity in obtaining the numerical solution, one reduces the number of variables in the governing equations of the direct problem given by equations (4.89)−(4.97) by eliminating the perturbed pressure, horizontal velocity and swimming

direction by following the procedure in Bees & Hill [12]. Applying the divergence operator to equation (4.72) yields

$$-\nabla^{*^2} P_{ep} = Ra \frac{\partial n_p}{\partial z^*}. \tag{4.130}$$

Also, applying the Laplacian operator to the third component of (4.72) leads to

$$S_c^{-1} \frac{\partial f_p}{\partial t^*} = Ra \frac{\partial^2 n_p}{\partial z^{*^2}} - Ra \nabla^{*^2} n_p + \nabla^{*^2} f_p, \tag{4.131}$$

where

$$f_p = \nabla^{*^2} w_p, \tag{4.132}$$

and w_p is the third component of the velocity.

The direction equation (4.74) states

$$\frac{\partial \theta_p}{\partial x^*} = G \left[(1 + \alpha_0) \frac{\partial^2 u_p}{\partial x^* \partial z^*} + (\alpha_0 - 1) \frac{\partial^2 w_p}{\partial x^{*^2}} \right]. \tag{4.133}$$

where $G = \frac{BD}{H^2}$.

The incompressibility equation (4.71) results in

$$\frac{\partial^2 u_p}{\partial x^* \partial z^*} = -\frac{\partial^2 w_p}{\partial z^{*^2}}. \tag{4.134}$$

Combining (4.133) and (4.134) together defines θ_p as a function of the vertical velocity w_p, such that

$$\frac{\partial \theta_p}{\partial x^*} = G \left[-(1 + \alpha_0) \frac{\partial^2 w_p}{\partial z^{*^2}} + (\alpha_0 - 1) \frac{\partial^2 w_p}{\partial x^{*^2}} \right]. \tag{4.135}$$

Using (4.135), equation (4.73) can be written as

$$\begin{aligned} \frac{\partial n_p}{\partial t^*} = &-w_p \frac{\partial n_{bs}^*}{\partial z^*} - \kappa \left[-G (1 + \alpha_0) n_{bs}^* \frac{\partial^2 w_p}{\partial z^{*^2}} + G (\alpha_0 - 1) n_{bs}^* \frac{\partial^2 w_p}{\partial x^{*^2}} + \frac{\partial n_p}{\partial z^*} \right] \\ &+ \frac{\partial^2 n_p}{\partial x^{*^2}} + \frac{\partial^2 n_p}{\partial z^{*^2}}. \end{aligned} \tag{4.136}$$

Eliminating the perturbed pressure P_{ep}, horizontal velocity u_p and swimming direction θ_p from equations (4.71)−(4.74) results in two governing equations with two variables: the perturbed concentration n_p and the perturbed vertical velocity w_p. Hence, the perturbed governing system becomes

$$\tilde{f}_p\left(z^*,t^*\right)=\left[\frac{\partial^2}{\partial z^{*2}}-k^2\right]\tilde{w}_p\left(z^*,t^*\right), \tag{4.137}$$

$$S_c^{-1}\frac{\partial\tilde{f}_p\left(z^*,t^*\right)}{\partial t^*}=Rak^2\tilde{n}_p\left(z^*,t^*\right)+\left[\frac{\partial^2}{\partial z^{*2}}-k^2\right]\tilde{f}_p\left(z^*,t^*\right), \tag{4.138}$$

$$\begin{aligned}\frac{\partial\tilde{n}_p\left(z^*,t^*\right)}{\partial t^*}&=-\tilde{w}_p\left(z^*,t^*\right)\frac{\partial n_{bs}^*}{\partial z^*}+\left\{\beta\left(1+\alpha_0\right)n_{bs}^*\frac{\partial^2\tilde{w}_p\left(z^*,t^*\right)}{\partial z^{*2}}\right.\\&\left.+\beta\left(\alpha_0-1\right)k^2n_{bs}^*\tilde{w}_p\left(z^*,t^*\right)-\kappa\frac{\partial\tilde{n}_p\left(z^*,t^*\right)}{\partial z^*}\right\}+\left[\frac{\partial^2}{\partial z^{*2}}-k^2\right]\tilde{n}_p\left(z^*,t^*\right),\end{aligned} \tag{4.139}$$

where $\beta=\kappa G$. The boundary conditions are

$$\tilde{w}_p=0,\qquad\text{at}\quad z^*=-1,0, \tag{4.140}$$

$$\kappa\tilde{n}_p-\frac{\partial\tilde{n}_p}{\partial z^*}=0,\qquad\text{at}\quad z^*=-1,0, \tag{4.141}$$

with no−slip boundary condition

$$\frac{\partial\tilde{w}_p}{\partial z^*}=0 \tag{4.142}$$

or the stress−free boundary condition

$$\frac{\partial^2\tilde{w}_p}{\partial z^{*2}}=0, \tag{4.143}$$

applied at $z^*=-1$ and 0. Similarly, we eliminate the perturbed pressure, the horizontal velocity and the swimming direction from the adjoint problem as follows, adding $ik\frac{\partial}{\partial z^*}$

multiplied by equation (4.112) to k^2 multiplied by equation (4.113) gives

$$\tilde{f}_p^j\left(z^*,t^*\right)=\left(\frac{\partial^2}{\partial z^{*^2}}-k^2\right)\tilde{w}_p^j\left(z^*,t^*\right), \tag{4.144}$$

$$\begin{aligned}\left[S_c^{-1}\frac{\partial}{\partial\tau^*}-\left(\frac{\partial^2}{\partial z^{*^2}}-k^2\right)\right]\tilde{f}_p^j\left(z^*,t^*\right)=k^2\left(\frac{\partial n_{bs}^*}{\partial z^*}\tilde{n}_p^j\right)\left(z^*,t^*\right)\\ -k^4\left(\alpha_0-1\right)\beta\left(n_{bs}^*\tilde{n}_p^j\right)\left(z^*,t^*\right)-k^2\left(\alpha_0+1\right)\beta\frac{\partial^2\left(n_{bs}^*\tilde{n}_p^j\right)}{\partial z^{*^2}}\left(z^*,t^*\right),\end{aligned} \tag{4.145}$$

$$\left[\frac{\partial}{\partial\tau^*}-\left(\frac{\partial^2}{\partial z^{*^2}}-k^2\right)-\kappa\frac{\partial}{\partial z^*}\right]\tilde{n}_p^j\left(z^*,t^*\right)=-Ra\tilde{w}_p^j\left(z^*,t^*\right). \tag{4.146}$$

The boundary conditions are

$$\tilde{w}_p^j\left(z^*,t^*\right)=0,\quad \text{at}\quad z^*=0,-1, \tag{4.147}$$

$$\frac{\partial\tilde{n}_p^j}{\partial z^*}\left(z^*,t^*\right)=0,\quad \text{at}\quad z^*=0,-1, \tag{4.148}$$

$$\left(1+\alpha_0\right)\beta k^2 n_{bs}^*\tilde{n}_p^j\left(z^*,t^*\right)-\frac{\partial^2\tilde{w}_p^j}{\partial z^{*^2}}\left(z^*,t^*\right)=0,\quad \text{at a stress−free surface} \tag{4.149}$$

$$\frac{\partial\tilde{w}_p^j}{\partial z^*}\left(z^*,t^*\right)=0,\quad \text{at a no−slip surface} \tag{4.150}$$

applied at $z^*=-1$ and 0.

The time derivative is discretised using the backward Euler method (Gautschi [37]). The terms with the basic profile are treated using the explicit Euler method. Hence, the perturbed system (4.137)−(4.139) will be

$$\begin{aligned}\left[\frac{d^2}{dz^{*^2}}-\kappa\frac{d}{dz^*}-k^2-\frac{1}{\Delta t^*}\right]\tilde{n}_p^{(n+1)}=-\frac{\tilde{n}_p^{(n)}}{\Delta t^*}+\tilde{w}_p^{(n)}\frac{dn_{bs}^{*(n)}}{dz^*}\\ -\beta n_{bs}^{*(n)}\left\{-\left(1+\alpha_0\right)\frac{d^2\tilde{w}_p^{(n)}}{dz^{*^2}}+\left(\alpha_0-1\right)k^2\tilde{w}_p^{(n)}\right\},\end{aligned} \tag{4.151}$$

$$\left[\frac{d^2}{dz^{*2}} - k^2 - S_c^{-1}\frac{1}{\Delta t^*}\right]\tilde{f}_p^{(n+1)} = -S_c^{-1}\frac{\tilde{f}_p^{(n)}}{\Delta t^*} - Rak^2\tilde{n}_p^{(n+1)}, \tag{4.152}$$

and

$$\left[\frac{d^2}{dz^{*2}} - k^2\right]\tilde{w}_p^{(n+1)} = \tilde{f}_p^{(n+1)}, \tag{4.153}$$

subject to the boundary conditions

$$\tilde{w}_p^{(n+1)} = 0, \quad \text{at} \quad z^* = -1, 0, \tag{4.154}$$

$$\kappa\tilde{n}_p^{(n+1)} - \frac{d\tilde{n}_p^{(n+1)}}{dz^*} = 0, \quad \text{at} \quad z^* = -1, 0, \tag{4.155}$$

$$\frac{d\tilde{w}_p^{(n+1)}}{dz^*} = 0, \quad \text{no−slip boundary}, \tag{4.156}$$

$$\frac{d^2\tilde{w}_p^{(n+1)}}{dz^{*^2}} = 0, \quad \text{stress−free boundary}, \tag{4.157}$$

applied at $z^* = -1$ and 0, and the adjoint system (4.144)−(4.146) will be

$$\begin{aligned}\left[\frac{d^2}{dz^{*2}} - k^2 - S_c^{-1}\frac{1}{\Delta\tau^*}\right]\tilde{f}_p^{j(n+1)} &= -S_c^{-1}\frac{\tilde{f}_p^{j(n)}}{\Delta\tau^*} - k^2\frac{\partial n_{bs}^{*(n)}}{\partial z^*}\tilde{n}_p^{j(n)} \\ &+\beta\left\{k^4\left(\alpha_0 - 1\right)n_{bs}^{*(n)}\tilde{n}_p^{j(n)} + k^2\left(\alpha_0 + 1\right)\frac{\partial^2\left(n_{bs}^{*(n)}\tilde{n}_p^{j(n)}\right)}{\partial z^{*2}}\right\},\end{aligned} \tag{4.158}$$

$$\left[\frac{d^2}{dz^{*2}} - k^2\right]\tilde{w}_p^{j(n+1)} = \tilde{f}_p^{j(n+1)}, \tag{4.159}$$

$$\left[\frac{d^2}{dz^{*2}} + \kappa\frac{d}{dz^*} - k^2 - \frac{1}{\Delta\tau^*}\right]\tilde{n}_p^{j(n+1)} = -\frac{\tilde{n}_p^{j(n)}}{\Delta\tau^*} + Ra\tilde{w}_p^{j(n+1)}, \tag{4.160}$$

subject to the boundary conditions

$$\tilde{w}_p^{j(n+1)} = 0, \quad \text{at} \quad z^* = -1, 0, \tag{4.161}$$

$$\frac{\partial \tilde{n}_p^{j(n+1)}}{\partial z^*} = 0, \quad \text{at} \quad z^* = -1, 0, \tag{4.162}$$

$$\frac{\partial \tilde{w}_p^{j(n+1)}}{\partial z^*} = 0, \quad \text{no−slip boundary}, \tag{4.163}$$

$$(1+\alpha_0)\,\beta n_{bs}^{*(n)} \tilde{n}_p^{j(n)} - \frac{\partial^2 \tilde{w}_p^{(n+1)}}{\partial z^{*2}} = 0, \quad \text{stress−free boundary}, \tag{4.164}$$

applied at $z^* = -1$ and 0.

The boundary conditions for $\tilde{f}_p$ are given in terms of $\tilde{w}_p$. To satisfy them at the no−slip boundary, both $\tilde{f}_p$ and $\tilde{w}_p$ are represented by the linear combination

$$\tilde{f}_p^{(n+1)} = \tilde{f}_P + \lambda \tilde{f}_1 + \mu \tilde{f}_2, \tag{4.165}$$

$$\tilde{w}_p^{(n+1)} = \tilde{w}_P + \lambda \tilde{w}_1 + \mu \tilde{w}_2, \tag{4.166}$$

where the subscript P is the particular solution of the $\tilde{f}_p$ in (4.152) with

$$\tilde{f}_P = 0, \quad \text{at} \quad z^* = -1, 0, \tag{4.167}$$

The functions with the subscript 1 and 2 are the homogeneous solutions of (4.152) with the two linearly independent boundary conditions,

$$\begin{aligned} \tilde{f}_1(-1) &= \tilde{f}_1(0) = 1, \\ \tilde{f}_2(-1) &= -\tilde{f}_2(0) = 1. \end{aligned} \tag{4.168}$$

The boundary conditions (4.156)−(4.157) determine the coefficients λ and μ in (4.165)

and (4.166). The functions $\tilde{w}_P$, $\tilde{w}_1$ and $\tilde{w}_2$ satisfy zero boundary conditions at $z = -1, 0$. We use a similar procedure for the boundary conditions of $\tilde{f}_p^j$.

4.6 Results

A solution to the optimization problem given in equations (4.100), (4.151)−(4.157) and (4.158)−(4.164) is calculated using the Matlab boundary problem solver bvp4c that solves an ordinary differential equation with a tolerance error of $O\left(10^{-3}\right)$.

4.6.1 Algorithm

A Matlab program was written to calculate the maximum energy amplification gained at a given time t_1^* for a given values of the parameters κ, $\beta = \kappa G$, α_0 and Ra over a range of wavenumbers k, (see Appendix C.6), as follows:

1. The values of the following parameters t_1^*, κ, $\beta = \kappa G$, α_0, Ra and k are inserted in the code.

2. The code computes the basic state profile using equations (4.30), (4.32) and (4.33) as follows: discretise the time derivative using the Euler backward method, (see Appendix C.5), and solve an ordinary differential equation with respect to the depth z^* for every time step. Record the results to save time at later stages.

3. For every wavenumber, initial conditions are imposed. This initial condition should satisfy the boundary conditions that are given for the direct problem (4.154)−(4.157). The initial conditions used in the code are

$$\tilde{n}_p^{(0)} = \frac{1}{||\tilde{n}_p^{(0)}||} \sin^2\left(\pi z^*\right), \tag{4.169}$$

$$\tilde{w}_p^{(0)} = 0, \tag{4.170}$$

$$\tilde{f}_p^{(0)} = 0. \tag{4.171}$$

The initial condition in equation (4.169) is multiplied by $\frac{1}{||\tilde{n}_p^{(0)}||}$ to ensure that the initial energy is normalized, i. e. $E\left(\mathbf{Q}\left(0\right)\right) = 1$.

4. The homogenous solutions $\tilde{f}_1$, $\tilde{f}_2$, $\tilde{w}_1$ and $\tilde{w}_2$ of the equations (4.152)−(4.153) are solved as these equations are independent of time. Similarly, the adjoint equations (4.158)−(4.159) are solved.

5. Next, for every time step, the direct problem is solved in the following order: the concentration equation (4.151) subject to the boundary conditions (4.155); the particular solutions of the functions $\tilde{f}_P$ and $\tilde{w}_P$ using equations (4.152) and (4.153) subject the following boundary conditions

$$\tilde{f}_P = 0, \qquad \tilde{w}_P = 0 \quad \text{at } z^* = -1, 0. \tag{4.172}$$

6. The boundary conditions at the no−slip and the stress−free boundaries (4.156) and (4.157) are used to find the values of λ and μ.

7. The solutions $\tilde{f}_p$ and $\tilde{w}_p$ are computed using relations (4.165) and (4.166).

8. After solving the direct problem at every time step, the conversion relations either equations (4.120)−(4.122) or (4.126)−(4.127) are used to impose initial conditions on the adjoint problem.

9. The adjoint problem in equations (4.158)−(4.160) is then solved backward in time in a similar way to the direct problem.

10. Either equations (4.123)−(4.125) or (4.128)−(4.129) are used to convert the initial condition to the initial conditions of the direct problem again. The forward and backward scheme is used until the optimal initial perturbation is obtained (when the initial perturbation of the direct problem does not change appreciably from one iteration to the next). The convergence condition is that the absolute error is less than $O\left(10^{-3}\right)$.

11. Finally, the maximum energy gained at the given time t_1^* for the given parameters is computed using equation (4.99) and (4.100).

4.6.2 Test and accuracy

The code is tested on the unsteady Bénard−Marangoni problem, as investigated by Doumenc et al. [27], for the following set of the parameters: $Ra = 0$, $Bi = 1$, $Ma = 300$ and $Pr = \infty$. The number of points in both time and space domains is 151. The results agree very well with the results of Doumenc et al. [27], (see Figure 4.4(a)).

To reduce the computation time, one needs to determine the minimum number of points in the time and the space domain that gives the solution within the set of tolerance. Hence, the code was executed for the unsteady Bénard−Marangoni problem with the parameters $Ra = 0$, $Bi = 1$, $Ma = 300$ and $Pr = \infty$, considering different time and space resolutions over the time $t^* = 0.43$. Figure 4.4(b) shows the energy gained with time resolution fixed at 101 points and three different space resolutions, 101, 151 and 201 over the range of wavenumbers between 1 and 3, and Figure 4.4(d) shows the relative error with respect to the solution that corresponds to the maximum space resolution 201. The two figures indicate that increasing the number of points in the space domain does not have a large impact on the accuracy of the results. The energy gained at the time $t^* = 0.43$ is plotted in Figure 4.4(c) fixing the space resolution to be 101 points with five different time resolutions, 101, 151, 201, 251 and 301. Figure 4.4(c) shows that there are variations in the energy amplifications profile when we change the time resolution. The relative error with respect to the solution that corresponds to the maximum time resolution, 301, is plotted in Figure 4.4(e). Figures 4.4(d) and 4.4(e) show that increasing the time resolution has more effect on the accuracy of the solution than increasing the domain resolution. However, since the target is to extract the wavenumber that corresponds to the maximum energy amplification, $k_{\max}$ that corresponds to the maximum energy amplification GE gained for every resolution is given in Table 4.3. The relative error of these wavenumbers with respect to the most accurate wavenumber 2.2841 that corresponds to the time resolution 301 is shown in Figure 4.4(f). The maximum value of the relative error is 0.0057, i.e. approximately 0.6% when the time resolution is 101 points.

The code was executed for the bioconvection problem and the energy amplification GE profile is plotted with considering the following values of the parameters $\beta = 0.1$,

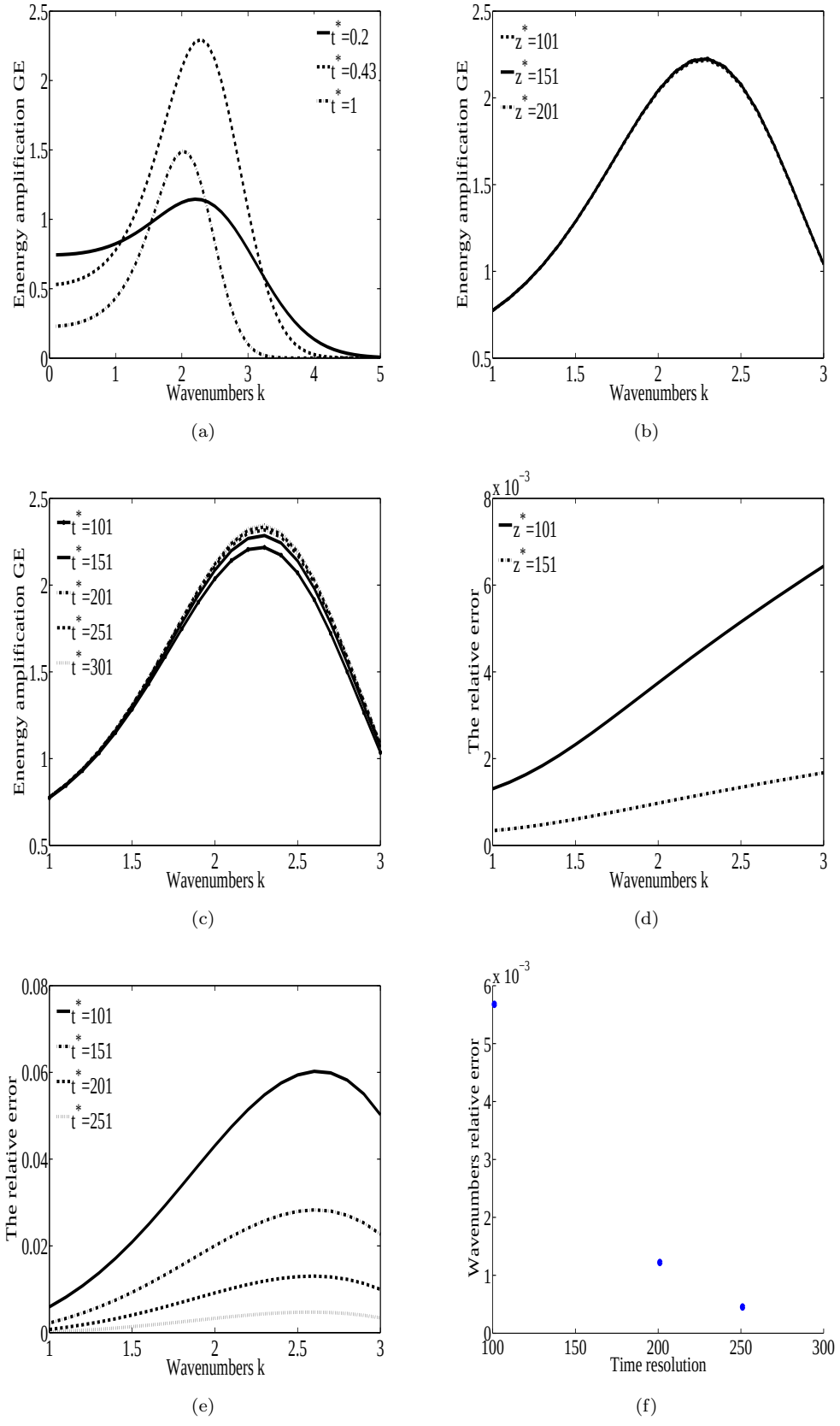

FIGURE 4.4: (a) The energy amplification GE profile plotted for the unsteady Bénard−Marangoni problem with $Ra = 0$, $Bi = 1$, $Ma = 300$ and $Pr = \infty$ for total times $t^* = 0.2$, 0.43 and 1. (b) and (c) GE at $t^* = 0.43$ for different domain and time resolutions, respectively. (d) and (e) The relative error of the GE profile that corresponds to the space and time resolution, respectively. (f) The relative error of the wavenumber that gives the maximum energy gained at that time.

Time resolution	101	201	251	301
Wavenumber $k_{\max}$	2.2711	2.2813	2.2830	2.2841

TABLE 4.3: The wavenumber that corresponds to the maximum energy gained at the time $t^* = 0.43$ for the time resolutions 101, 201, 251 and 301.

Time resolution	101	201	251	301
Wavenumber $k_{\max}$	3.8945	3.9090	3.9116	3.9132

TABLE 4.4: The wavenumber that corresponds to the maximum energy gained at the time $t^* = 0.05$ for the time resolutions 101, 201, 251 and 301 when testing the code on the bioconvection for the following parameters $\beta = 0.1$, $Ra = 725$, $\kappa = 0.1$, $Sc = 20$ and $\alpha_0 = 0.2$.

$Ra = 725$, $\kappa = 0.1$, $Sc = 20$ and $\alpha_0 = 0.2$ at the time $t^* = 0.05$ for three space resolutions 101, 151 and 201 over a range of wavenumbers between 3.5 and 4.3 (see Figure 4.5(a)) with fixing the time resolution to be 101. Figure 4.5(c) shows the relative error with respect to the solution that corresponds to the maximum space resolution 201. The results shows that increasing the number of points in the space domain does not have a large impact on the accuracy of the results. On the other hand, the space resolution is fixed to be 101 points and the time resolution is changed to take the values 101, 151, 201, 251 and 301 (see Figure 4.5(b)) for the same values of the parameters. The relative error with respect to the solution that corresponds to the maximum time resolution, 301, is plotted in Figure 4.5(d). As mentioned earlier, the aim is to extract the wavenumber, $k_{\max}$ that correspond to the maximum energy gained over a range of wavenumbers at a given time t^*, thus, $k_{\max}$ that corresponds to the maximum energy amplification GE gained for every resolution is given in Table 4.4. The relative error of these wavenumbers with respect to the most accurate wavenumber 3.9132 that corresponds to the time resolution 301 is shown in Figure 4.5(e). The maximum value of the relative error is 0.0048, i.e. approximately less than 0.5% when the time resolution is 101 points. To sum up, the resolution in the time and space domain is chosen to be 101 points with an expected accuracy of 99.5%.

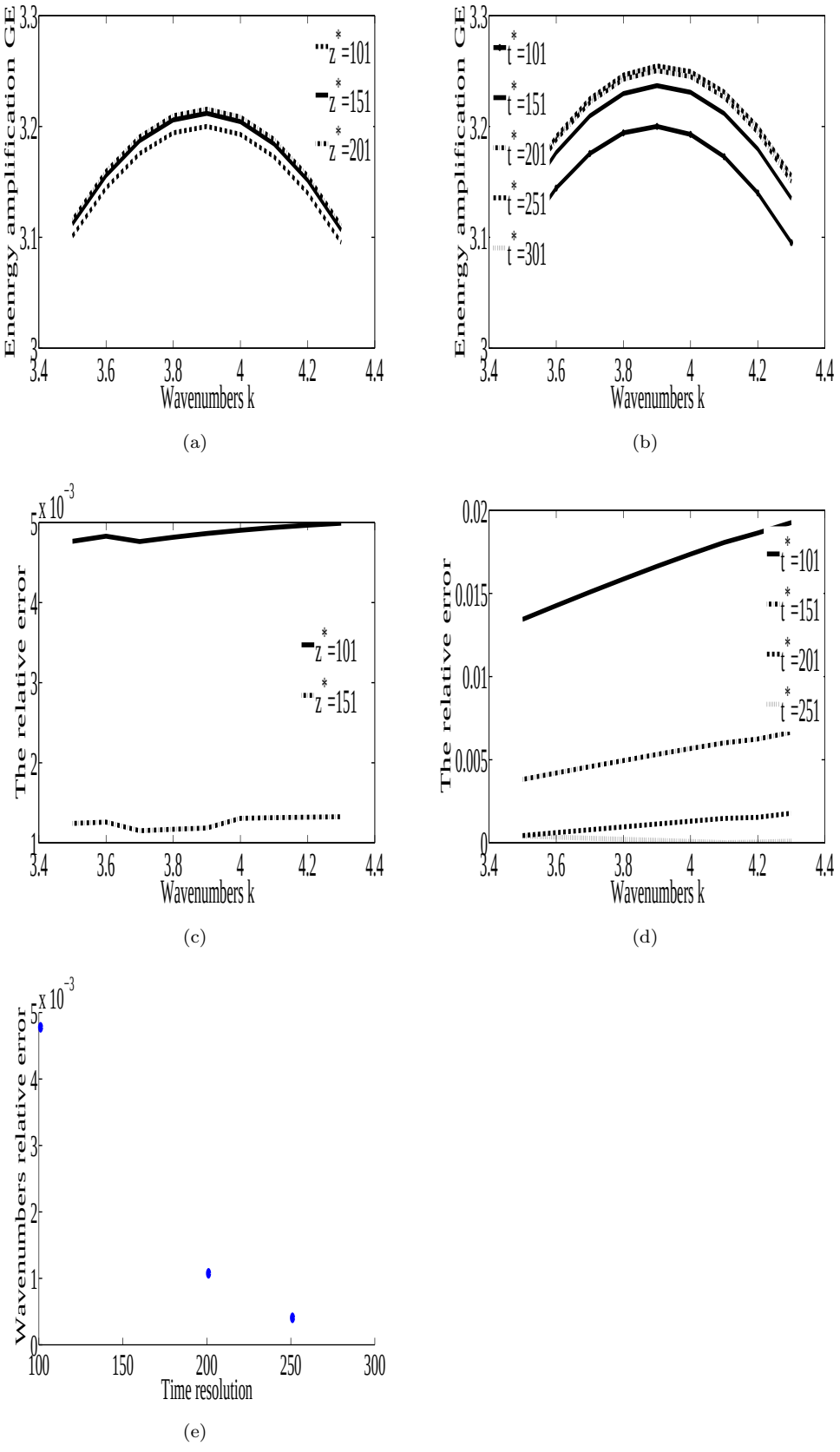

FIGURE 4.5: The energy amplification GE profile plotted for the bioconvection problem with $\beta = 0.1$, $Ra = 725$, $\kappa = 0.1$, $Sc = 20$ and $\alpha_0 = 0.2$ for $t^* = 0.05$ (a) and (b) GE at $t^* = 0.05$ for different domain and time resolutions, respectively. (c) and (d) The relative error of the GE profile that corresponds to the space and time resolution, respectively. (e) The relative error of the wavenumber that gives the maximum energy gained at that time.

4.6.3 Bioconvection results

The code is excuted for the bioconvection problem during the dimensionless time interval $t^* = [0, 0.05]$ as it corresponds to the dimensional time $[0, 100]$ seconds which is long enough for these upswimming microorganisms to approach the steady state profile. If we consider a uniform suspension of depth 0.5 cm to begin with and the cells swim with a speed of 63 μms^{-1}, the basic state will be reached at $t = 80$ s. Also, we consider the Schmidt number to be the typical value estimated for the upswimming gyrotactic microorganisms *Chlamydomonas augustae*, which is $S_c = 20$ as in Hill et al. [50]. An earlier work from Williams and Bees [115] estimated S_c to be 19 for the *C. augustae*. The cell eccentricity is taken to be $\alpha_0 = 0.2$ (Hill et al. [50]). Two values are selected of the scaled depth κ and two values of the Rayleigh number Ra. These values are

- In the first set of the numerical parameters, a small value of κ is assumed, $\kappa = 0.1$. The value of Ra is set to be 725, which is slightly above the critical value, $Ra_c = 720$ that was calculated for gyrotacic microorganisms in a layer of finite depth by Hill et al. [50]. The gyrotactic number G is taken to be 1, hence, $\beta = \kappa G = 0.1$. The wavenumbers range is between $[0.1, 6]$ with a stepsize of 0.2.

- In the second set of the numerical parameters, κ is assumed to be 1 and Ra is taken to be 500 which is close to the critical value, (see Hill et al. [50]). G is taken to be 0.5, so, $\beta = \kappa G = 0.5$. The range of wavenumbers is $[3, 9]$ with a stepsize of 0.2.

The results are as follows:

The initial conditions given in equations (4.169)−(4.171) are used for the two sets of parameters. The optimal initial perturbation at the time $t^* = 0$ for the first set of these parameters is plotted for the following wavenumbers $k = 4.0945$ and 5.5 in Figure 4.6(a). The optimal initial perturbation at the time $t^* = 0$ for the second set of parameters for the following wavenumbers $k = 1.567$, 3.5 and 6.254 is shown in Figure 4.6(b). Both figures indicate that the optimal initial perturbations are independent of the imposed initial condition, depending on all the parameters used in the problem but mainly on

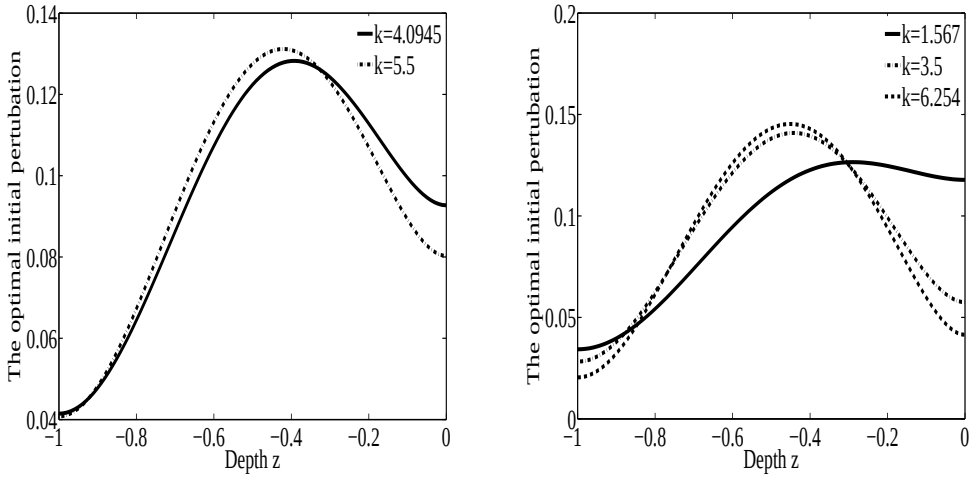

(a) $\kappa = 0.1$ (b) $\kappa = 1$

FIGURE 4.6: The optimal initial perturbation at the time $t^* = 0$ for the two cases: (a) $\kappa = 0.1$, $G = 1$, $Ra = 725$, $S_c = 20$ and $\alpha_0 = 0.2$ at the wavenumbers $k = 4.0945$ and 5.5; and (b) $\kappa = 1$, $G = 0.5$, $Ra = 500$, $S_c = 20$ and $\alpha_0 = 0.2$ at the wavenumbers $k = 1.567$, 3.5 and 6.254.

the wavenumber. For example, Figure 4.6(b) displays a plot of these optimal initial perturbations for the same set of parameters for different wavenumbers. One can see clearly the difference between these curves.

The maximum energy amplification was calculated using equation (4.100) for the above sets of parameters with the initial conditions (4.169)−(4.171). It was found that when $\kappa = 0.1$, $Ra = 725$ and $G = 1$ the maximum energy gained is at the wavenumber $k_{\max} = 3.8945$ whereas when $\kappa = 1$, $Ra = 500$ and $G = 1$ the energy reaches its maximum value at the wavenumber $k_{\max} = 8.0154$ which is almost twice the wavenumber when κ is 10 times larger.

The effect of the variation of the parameters κ, Ra, and G on the maximum energy amplified at the specified time $t^* = 0.05$ is also investigated and the results are shown in Figures 4.7 and 4.8, and Tables 4.5, to 4.10. The results in these tables are plotted in Figure 4.9 and show that $k_{\max}$ increases monotonically as the values of these parameters increase. However, the increasing rates differ. For instance, Tables 4.9 and 4.10 show that even there is an increase in the value of $k_{\max}$ as κ increases. This variation seems to be small of $O\left(10^{-4}\right)$ compared to the variation due to the gyrotactic effect in Tables 4.5

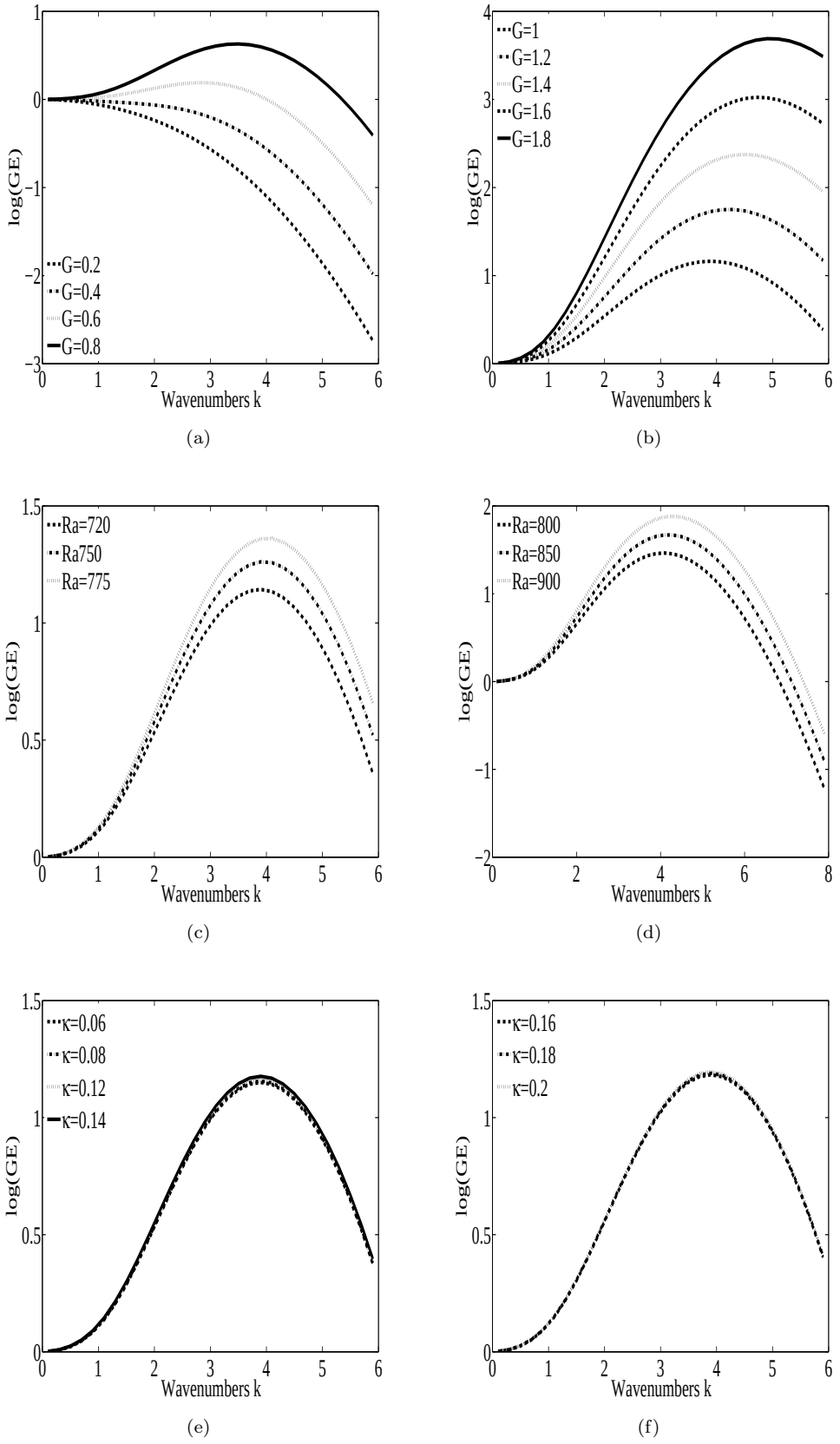

FIGURE 4.7: A logarithm plot of the energy amplification profile GE over the total time $t^* = 0.05$. Here, $\kappa = 0.1$, $\alpha_0 = 0.2$, $Ra = 725$ and $G = 1$. The plots of $\log(GE)$ show the effect of the gyrotactic number G in (a) and (b), the Rayleigh number Ra in (c) and (d) and, finally, the scaled layer depth κ in (e) and (f).

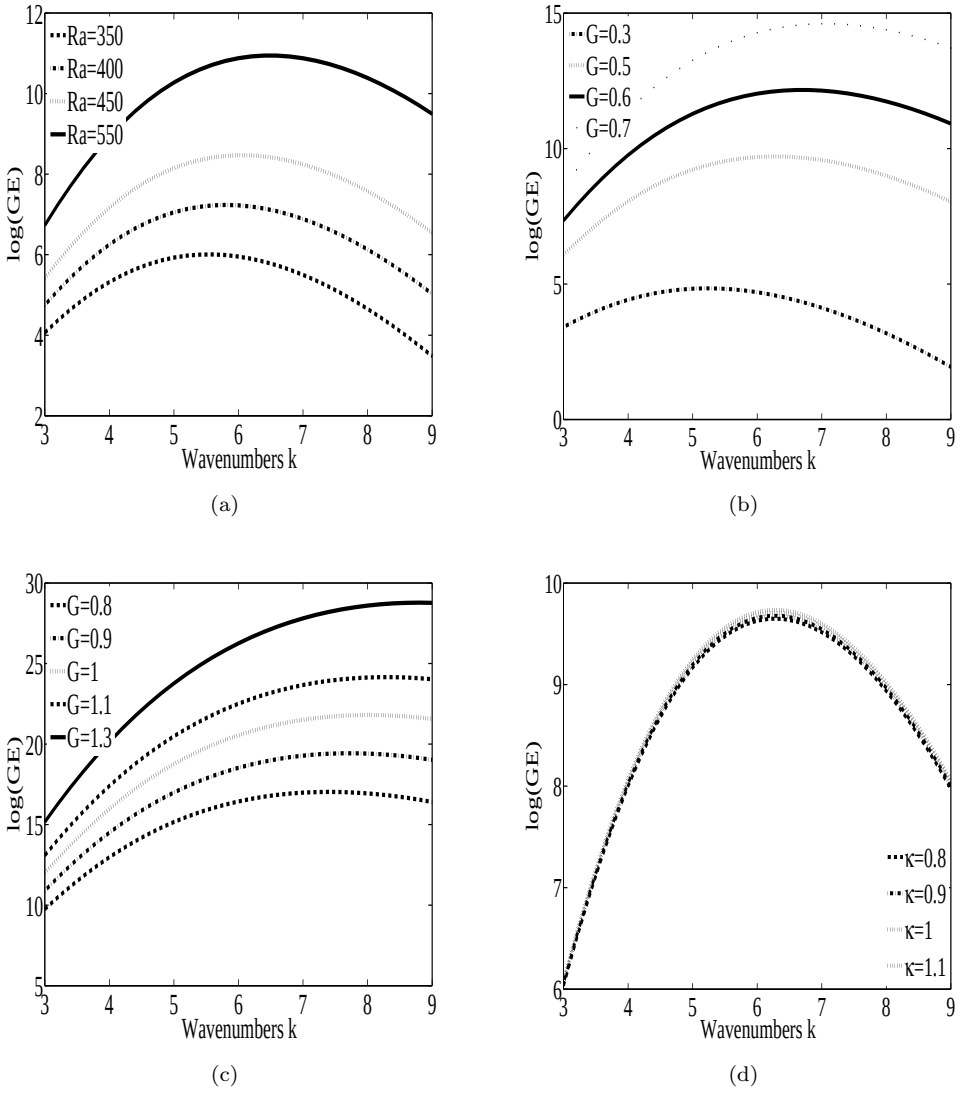

FIGURE 4.8: A logarithm plot of the energy amplification profile GE over the total the time $t^* = 0.05$. Here, $\kappa = 1$, $\alpha_0 = 0.2$, $Ra = 500$ and $G = 0.5$. The plots of $\log(GE)$ show the effect of the Rayleigh number Ra in (a), the gyrotactic number G in (b) and (c) and, finally, the scaled layer depth κ in (d).

and 4.6. Table 4.5 shows that when G is small 0.2 and 0.4, $k_{\max} = 0.1$. This suggests that the suspension is stable.

4.7 Discussion

In this chapter, a time evolving basic state is calculated. The stability around that basic state is investigated using non−normal modes in order to evaluate the maximum energy gained at a given time over a range of wavenumbers by using Lagrange multipliers; the

G	$k_{\max}$	$\lambda_{\max}$
0.2	0.1	62.8319
0.4	0.1	62.8319
0.6	2.8393	2.2130
0.8	3.4709	1.8102
1	3.8945	1.6134
1.2	4.2268	1.4865
1.4	4.5069	1.3942
1.6	4.7509	1.3225
1.8	4.9696	1.2643

TABLE 4.5: The dimensionless values of $k_{\max}$ and $\lambda_{\max}$ that correspond to the maximum energy gained at the time $t^* = 0.05$ when $\kappa = 0.1$, $\alpha_0 = 0.2$ and $Ra = 725$ for different values of G.

G	$k_{\max}$	$\lambda_{\max}$
0.3	5.2330	1.2007
0.5	6.2782	1.0008
0.6	6.6922	0.9389
0.7	7.0646	0.8894
0.8	7.4056	0.8484
0.9	7.7197	0.8139
1	8.0154	0.7839
1.1	8.2916	0.7578
1.3	8.8022	0.7138

TABLE 4.6: The dimensionless values of $k_{\max}$ and $\lambda_{\max}$ that correspond to the maximum energy gained at the time $t^* = 0.05$ when $\kappa = 1$, $\alpha_0 = 0.2$ and $Ra = 500$ for different values of G.

Ra	$k_{\max}$	$\lambda_{\max}$
720	3.8817	1.6187
750	3.9565	1.5880
775	4.0157	1.5656
800	4.0742	1.5422
850	4.1843	1.5016
900	4.2882	1.4652

TABLE 4.7: The dimensionless values of $k_{\max}$ and $\lambda_{\max}$ that correspond to the maximum energy gained at the time $t^* = 0.05$ when $\kappa = 0.1$, $\alpha_0 = 0.2$ and $G = 1$ for different values of Ra.

Ra	$k_{\max}$	$\lambda_{\max}$
350	5.5405	1.1341
400	5.8091	1.0816
450	6.0528	1.0381
550	6.4893	0.9682

TABLE 4.8: The dimensionless values of $k_{\max}$ and $\lambda_{\max}$ that correspond to the maximum energy gained at the time $t^* = 0.05$ when $\kappa = 1$, $\alpha_0 = 0.2$ and $G = 0.5$ for different values of Ra.

κ	$k_{\max}$	$\lambda_{\max}$
0.06	3.8939	1.6136
0.08	3.8942	1.6135
0.12	3.8947	1.6133
0.14	3.8950	1.6132
0.16	3.8952	1.6130
0.18	3.8955	1.6129
0.2	3.8958	1.6128

TABLE 4.9: The dimensionless values of $k_{\max}$ and $\lambda_{\max}$ that correspond to the maximum energy gained at the time $t^* = 0.05$ when $Ra = 725$, $\alpha_0 = 0.2$ and $G = 1$ for different values of κ.

κ	$k_{\max}$	$\lambda_{\max}$
0.8	6.2771	1.0010
0.9	6.2776	1.0009
1	6.2782	1.0008
1.1	6.2790	1.0007

TABLE 4.10: The dimensionless values of $k_{\max}$ and $\lambda_{\max}$ that correspond to the maximum energy gained at the time $t^* = 0.05$ when $Ra = 500$, $\alpha_0 = 0.2$ and $G = 0.5$ for different values of κ.

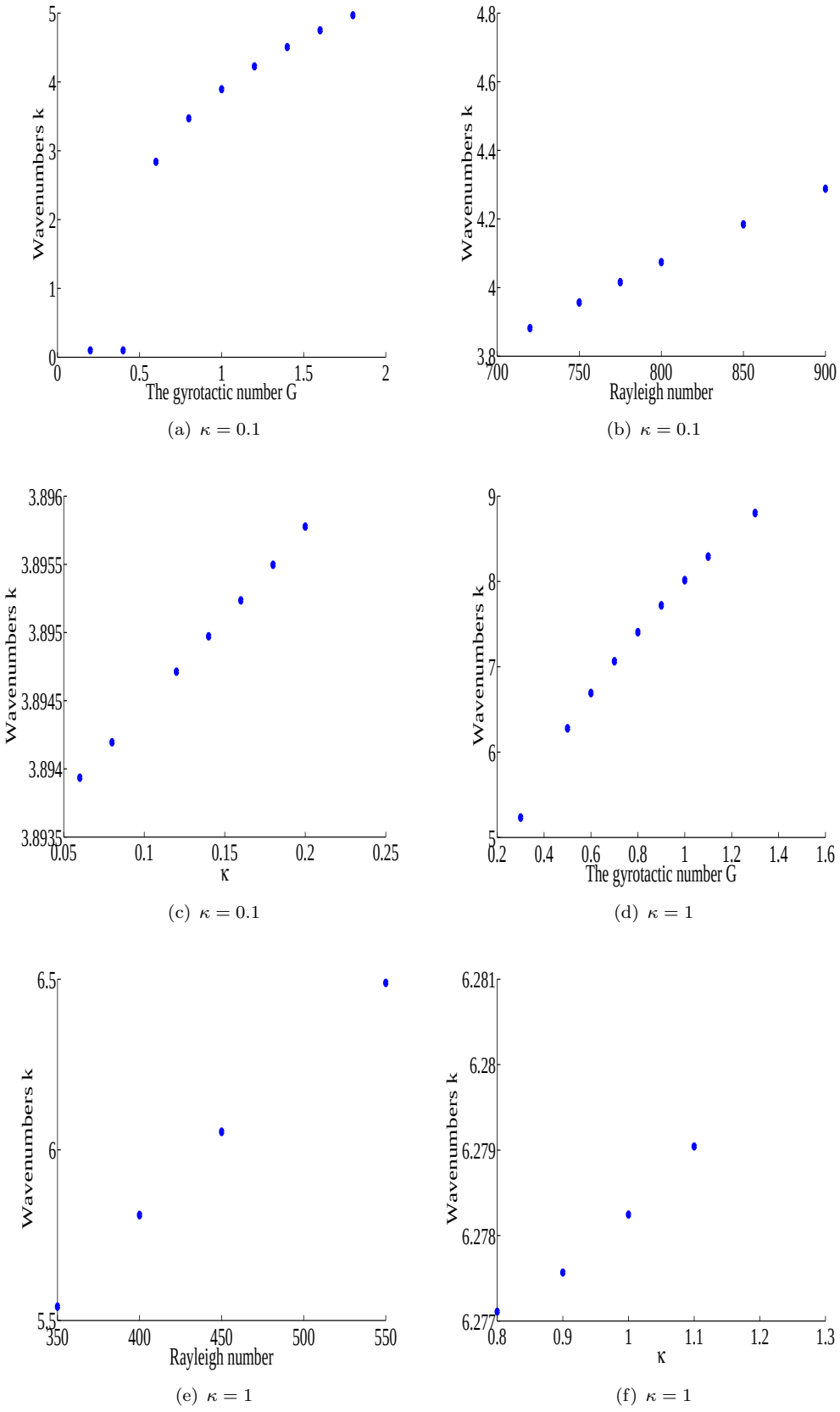

(a) $\kappa = 0.1$ (b) $\kappa = 0.1$

(c) $\kappa = 0.1$ (d) $\kappa = 1$

(e) $\kappa = 1$ (f) $\kappa = 1$

FIGURE 4.9: The relationship between $k_{\max}$ and the Gyrotacyic number G (a) and (d), the Rayleigh number Ra (b) and (e) and the layer depth scale κ (c) and (f).

Mean cell concentration (cells cm^{-3})	$\lambda^d_{\max}$ (cm)
1.1×10^5	0.97
10^5	1
8×10^4	1.04
7×10^4	1.13

TABLE 4.11: The mast unstable wavelength of a suspension of *C. augustae* for the given concentrations. $S_c = 20$, $D = 5 \times 10^{-4}$ and the suspension depth $H = 1$ cm.

variation of a Lagrange function was computed, and adjoint equations to the governing equations were imposed. A Matlab code was designed to solve the problem forward and backward in time to find the optimal initial perturbation and evaluate the energy. It is found that, the optimal initial perturbation is independent from the imposed initial conditions and depends on the layer depth scale κ, Ra, G, and significantly on k. Also, it is found that $k_{\max}$ increases as we increase κ, Ra and G.

To compare these results with the experimental results in Chapter 2, we can consider a suspension of the green algae *Chlamydomonas augustae*. The relationship between the cell concentration and Ra is given by $Ra = \frac{H^3 n_0 v g \Delta\rho}{D\rho\nu}$. Since the suspension depth in our experiments is approximately 0.5 cm and for the values given in Table 4.2, the mean cell concentration that corresponds to $Ra = 550$ is 8.8×10^5. Experiment 10a3 in Table 2.3 gives the results of *C. augustae* of concentration 3.9×10^6 which is closest among the experiments to the concentration 8.8×10^5. The mean value of the local dominant wavelength in the experiment 10a3 is calculated to be $\lambda = 0.9583$ cm. The Table 4.8 gives the corresponding dimensional value of $\lambda^d_{\max} = \frac{2\pi}{k_{\max}} H \approx 0.5$ cm which does not seem to agree very well with the experimental results. Since the pattern displays spacing between 0.8 to 1.1 cm.

Table 4.11 shows the predicted values of $\lambda^d_{\max}$ for a suspension of the green algae *C. augustae* of depth 1 cm. These predicted values are smaller than the most unstable wavelengths predicted by Hill et al. [50], 2 to 3 cm for mean cell concentrations that are slightly larger than 5×10^5. However, our predictions are closer their experimental observation of *C. augustae* that shows patterns with spacing between 0.5 to 1 cm.

Running the program to produce the results takes long time. However, it predicts typical wavelengths of less than 1 cm when the suspension depth is 1 cm which agrees with the typical experiment measurements that give wavelengths less than 1 cm in Bees and Hill [12] and Hill et al. [50].

Chapter 5

Conclusions

Bioconvection usually arise due to the upswimming behaviour of micro−organisms that are slightly more dense than the surrounding fluid. In this thesis, we have performed controlled experiments on bioconvection of mixed species of algae *C. reinhardtii* and *C. augustae*. Also, we have investigated the instability onset of bioconvection in a uniform suspension of mixed species. Moreover, we have used the non−normal modes to investigate the stability around a time evolving cell concentration basic state.

In Chapter 2, we described controlled experiments, measured the local dominant patterns wavelength as a function of the relative concentration between two species of the green algae *C. reinhardtii* and *C. augustae* and the total concentration. Wavelet analysis was employed for the first time in the bioconvection to extract the local dominant wavelength with its direction. Moreover, the second local dominant wavelength was extracted with its direction to examine the patterns structure in a systematic way. We found the following general results.

- The dominant wavelength varies from one location to another across the whole pattern. Hence, the analysis provides a range of local dominant wavelengths for every analysed pattern, unlike Fourier analysis (Bees & Hill [11] and Williams & Bees [116]) that results in one global dominant wavelength across the whole pattern.

- The initial wavelength decreases as the relative concentration shifts from 100% *C. reinhardtii* to 100% *C. augustae* and increases as the total cell concentration decreases.

- The long−term wavelength range also decreases as the relative concentration shifts from 100% *C. reinhardtii* to 100% *C. augustae* and increases as the total cell concentration decreases. However, the range of the long−term wavelength does not show tendency to be wider or narrower as the relative and total concentration changes.

- The instability arose in the middle of the dish. Then, as the time evolves it propagates to cover the whole dish.

- Calculating the first dominant local wavelength direction and the second local dominant wavelength provides a quantitative measurements of the change in patterns from rolls to squares and dots across the pattern.

Increasing the wavelength as the total concentration decrease agrees with the investigations performed be Bees and Hill [11] and Williams and Bees [116].

In Chapter 3, the continuum model by Pedley and Kessler [86] was generalized to consist of two species. Also, we completed the linear stability analysis about a uniform basic state in an infinite layer depth which gives the following results.

- A zero most unstable wavenumber is predicted for a disturbance with no vertical variation as in Pedley & Kessler [86] and Pedley et al. [84].

- For a disturbance with a vertical variation, we found the following

  – When both species have the same gyrotactic parameters, same mean cell concentration and different mean cell swimming speed, the neutral curve (instability onset) will be located in the middle, i.e. above the neutral curve of the species with the maximum mean cell swimming speed and below the neutral curve of the species with the minimum mean cell swimming speed, due to the two compatible instability modes in the suspension that result from the

difference in the cell swimming speed. The swimming speed of each species affects its diffusion that has its influence on the mean cell swimming direction of the other one which causes this competition between the instabilities. As a consequence, decreasing the mean cell swimming speed of one species cause the neutral curve of the mixed species to converge to the neutral curve of the species with the maximum mean cell swimming speed since the influence of the diffusion on the mean cell swimming direction will decrease. However, when both species have the same mean cell swimming speed, the neutral curve of the mixed species converges to the neutral curve of the species with the smaller value of the deterministic−stochastic parameter.

- When both species have the same gyrotactic parameters and mean cell swimming speed, decreasing the mean cell concentration of one species with respect to the other makes the suspension of the mixed species to be diluted. Hence, the neutral curve of the mixed species will be above the neutral of species 1 and 2.
- Considering a suspension of two mixed species of *C. augustae* and *C. reinhardtii* with total mean cell concentration of 1.3×10^7 cells cm^{-3}, the analysis predicted an initial wavelength of approximately 0.87 cm which disagree with the experimental results. The experimental results give an initial wavelength of 1.31 cm.

In Chapter 4, we completed the non−normal analysis for the gyrotactic bioconvection model by Hill et al. [50] in a layer of finite depth. We found the general results below.

- The optimal initial disturbance is independent of the imposed initial disturbance and it depends on all the parameters in the problem but significantly on wavenumber.
- The most unstable wavelength decreases with increasing the gyrotactic and Rayleigh number. However, it decreases slightly, $O\left(10^{-4}\right)$, when increasing the value of κ.
- Considering a suspension of the green algae *C. augustae* with a total concentration of 8.8×10^6 cells cm^{-3} and depth of 0.5 cm, the analysis predicted the most unstable

wavelength to be 0.5 cm. The value does not agree with the experimental results in chapter 2 as the experimental observation shows patterns with spacing between 0.8 to 1 cm for a suspension with a mean cell concentration 3.9×10^6.

- Although our prediction does not agree very well with experimental observations, we predicted most unstable wavelength of less than 1 cm for a suspension of depth 1 cm which gives better predictions than Hill et al. [50], 2 to 3 cm, and Bees & Hill [12], 1 mm. These predictions are closer to their experimental observations of a suspension of depth 1 cm as their experiments shows patterns of wavelengths between 0.5 to 1 cm for a suspension of *C. agustae* of depth 1 cm.

5.1 Future developments and applications

- Wavelet techniques developed in the thesis can be applied to a wide range of convection patterns. For example, it can be used to analyse chemoconvection patterns to study the local variation of the wavelength as a function of the chemical gradients or to provide quantitative measure of patterns structure.

- The experimental protocol and techniques developed in this thesis are first step towards understanding bioconvection in communities of micro−organisms. Future experiments could be performed on mixed suspension of two species swimmers and non−swimmers to investigate how each one of them influences the other. Also, it could be used to perform experiments on mixed suspension of two species that interact with each others such as algae and bacteria to investigate how they affect each others or to explore the effect of phototaxis.

- Investigating the linear stability of a uniform suspension of the two mixed species theoretically can lead to better understanding to how one species can motivate the other which can be utilized in the industrial field. For example, it could give ideas to enhance the growth of algae used biofuel industry to increase the production.

- Non−normal analysis has been used to study the onset of bioconvection to bring the theory closer to the initial conditions in experiments. An interesting challenge will be to account for the residual bulk fluid motion that results from the mixing

for the suspension at the start of experiments and this explain the observation of the early onset of patterns.

- It would be instructive to compare the results of the non−normal analysis with carefully chosen and controlled full numerical simulation of bioconvection to ascertain how robust the non−normal analysis is in predicting initial growth of instabilities and to validate numerical results.

- It will also be important to design quantitative experiments of the formation of bioconvection patterns in deep layers to determine if the non−normal theory is applicable to the real system and over what range of time scales.

- Finally, a future application of the non−normal method will be to investigate the onset of bioconvection in deep layer of suspensions of more than one species to better understanding competing effects and parametric dependence.

Appendix A

Image_Subtraction.m

```
function Im1=Image_Subtraction;

% ========================================================================
% This programed is designed to subtract the first frame from the rest
% images in the series, after transforming the images into integers.
% ========================================================================

% """""""""""""""""""""""""""""""""""
% Calling the 1st sequence of images.
% """""""""""""""""""""""""""""""""""
MyFolder1='F:\Experiment\Image Analysis\10r\1';
% MyFolder1='C:\Reem\Experiment\Image Analysis\1A9R\full Conc\1';
% MyFolder1='C:\Reem\TEMP\NEW';
FilePattern1=fullfile(MyFolder1,'*.tif');
tifFiles1=dir(FilePattern1);

% """""""""""""""""""""""
% Reading the 1st image.
% """""""""""""""""""""""
im11=imread(tifFiles1(1).name);

% """""""""""""""""""""""""""""""""""
% Specifying the size of the image.
% """""""""""""""""""""""""""""""""""
[ROW1,COLUMN1]=size(im11);

% """""""""""""""""""""""""""
% Building the output cell.
% """""""""""""""""""""""""""
Im1=zeros(ROW1,COLUMN1,length(tifFiles1));

% """""""""""""""""""""""""""""""""""""""
```

```
% Converting the 1st image into integers.
% """""""""""""""""""""""""""""""""""""""""
A1=double(im11);

% """""""""""""""""""""""""
% The subtraction process.
% """""""""""""""""""""""""
for k=1:length(tifFiles1)
    k
    im21=imread(tifFiles1(k).name);
    B1=double(im21);
    C1=B1-A1;
    Im1(:,:,k)=C1;
end
```

```
Pattern_appearance_New.m
% This program has been designed to compute the mean value, the standard
% deviation and the time derivative of the standard deviation of the gray
% level of an image ( seequence of images). Also, plot them as a function
% of time, after subtracting the 1st frame using the program
% Image_Subtraction.m.
% ========================================================================
function [G,SD,SDD]=Pattern_appearance_New(IM1);

% """""""""""""""""""""""""""""""""""""
% Specifying the size of the 1st input.
% """""""""""""""""""""""""""""""""""""
[r1,c1,d1]=size(IM1);

% """""""""""""""""""""""""""""""""""""""""""""
% Specifying a 256*256 window in the image.
% """""""""""""""""""""""""""""""""""""""""""""
  x10=(c1/2)-128;
  x1F=x10+255;
  y10=(r1/2)-128;
  y1F=y10+255;
% ============================================
for k=1:d1
  k
  t(k)=2*k;
  Im2=IM1(y10:y1F,x10:x1F,k);
  A=reshape(Im2,1,65536);
  g1(k)=mean(A);
  sd1(k)=std(double(A),0);
end
```

```
yy1 = smooth(transpose(sd1));
sdd1 = diff(yy1);
sdd1(k)=0;

G1=g1;
SD1=sd1;
SDD1=sdd1;
% ========================================================================
G=G1;

SD=SD1;

SDD=SDD1;

% ========================================================================
% Plotting the Mean of the gray values, the Standard deviation and the time
% derivative of the standad deviation versus the time.
% ========================================================================

% ==================
% Plotting the mean.
% ==================

subplot(3,1,1)
plot(t,G,'LineWidth',4,'color','k')

% ======================
% The title of the graph.
% ======================

% ============================
set(gca,'XTick',0:52:310)
set(gca,'XTickLabel',{''},'fontsize',30,'FontName','Times New Roman')
ylabel('$$\bar{g}$$', 'interpreter', 'latex','fontsize',30,'FontName','Times New Roman')

% ================================
% Plotiing the standard deviation.
% ================================
subplot(3,1,2)
plot(t,SD,'LineWidth',4,'color','k')
set(gca,'XTick',0:52:310)
set(gca,'XTickLabel',{''},'fontsize',30,'FontName','Times New Roman')
ylabel('$$\sigma$$','interpreter', 'latex','fontsize',30,'FontName','Times New Roman')
```

```
% ================================================
% Plotting the standard deviation time derivativ.
% ================================================
subplot(3,1,3)
plot(t,SDD*100,'LineWidth',4,'color','k')
set(gca,'XTick',0:52:310)
set(gca,'XTickLabel',{'0','52','104','156','208','260','302'},...
'fontsize',30,'FontName','Times New Roman')
xlabel('Time in seconds','fontsize',30)
ylabel('$$\dot{\sigma} * 100$$','interpreter', 'latex',...
'fontsize',30,'FontName','Times New Roman')
hold on
```

```
Peak_2nd.m
% This program is written to plot the amplitude at one location as a
% function of the natural logarithm of the wavenumber and the direction
% together with computing the 1st and the 2nd peak information.
% ========================================================================
function [WAVL1,WAVL2,DIR1,DIR2]=Peak_2nd(cir);
% ***************************************************
% *(I)- Setting the image up for the wavelet analysis.*
% ***************************************************

% ==================
% Reading the image.
% ==================
%    cir=imread('cconv3n.tif');
%    cir=bioimage4;
%    cir=IM3;

% ==============================
% Specify the size of the image.
% ==============================
[mrow,mcolumn]=size(cir);

% ********************************************************************
% * Choose a window of size 256*256 pixels inside the image.          *
% * These values have been chosen to ensure that the window is centred *
% * within the petri dish and fare from the edge.                      *
% ********************************************************************

x0=(mcolumn/2)-128;
xF=x0+255;
y0=(mrow/2)-128;
yF=y0+255;
```

```
% ========================================================================
% Taking FFT of the image since the definition of the wavelet transform has
% been used is the one that depends on FFT.
% ========================================================================
fimg=fft2(cir);

% ============================
% Setting up the scales (scl).
% ============================
scl=1:128;
ss=size(scl);

% ================================
% Setting up the directions (ang).
% ================================
inc=pi/8;
ang=0:inc:2*pi;
h=size(ang);

% ***********************************
% *(II)- Performing Wavelet Analysis.*
% ***********************************

% ===================================================================
% Applying the Wavelet Transform (Computing the CWT coefficients).
% ===================================================================
out = cwt2d(fimg, 'morlet2d', scl, ang,'export','norm','l1');

% ************************************************************************
% *(III) Computing the 1st dominant wavelength, wavenumber, direction and *
% *the 2nd dominant wavelength, wavenumber, direction for each lacation.  *
% ************************************************************************
 t=tic;
 for r=y0:yF
    for c=x0:xF
        r
        c
        locationCOEFFs(:,:)=out(r,c,:,:);
        locationAMPs=abs(locationCOEFFs);
        [zmax,smax,zmin,smin]=extrema2(locationAMPs);
        siz1=size(locationAMPs);
        [I,J]=ind2sub(siz1,smax);
```

```
        IND=1;
        for INDZ=1:length(zmax)
            if (J(INDZ)>=5) && (J(INDZ)<13)
                Lmax(IND)=zmax(INDZ);
                Imax(IND)=I(INDZ);
                Jmax(IND)=J(INDZ);
                IND=IND+1;
            end
        end
            % =========================
            % (D) Extracting the peaks.
            % =========================

% The peaks are at the scale I and the direction ang(J).

            % =================
            % (a) The 1st peak.
            % =================

            kpsi=6;
            WAVL1(r,c)=2*pi*Imax(1)/kpsi;

            if (Jmax(1)>=9)
            DIR1(r,c)=ang(Jmax(1)-8);
            else
            DIR1(r,c)=ang(Jmax(1));
            end
            Magnitude1(r,c)=Lmax(1);


            % =================
            % (B) The 2nd Peak.
            % =================

           if (abs(Jmax(1)-Jmax(2))<=2)
               z=3;
           else
               z=2;
           end

            if (Lmax(z)<=(5*Lmax(1)/10))
                WAVL2(r,c)=NaN;
                DIR2(r,c)=NaN;
                Magnitude2(r,c)=Lmax(z);
```

```
            else
               WAVL2(r,c)=2*pi*Imax(z)/kpsi;
               if (Jmax(z)>=9)
               DIR2(r,c)=ang(Jmax(z)-8);
               else
               DIR2(r,c)=ang(Jmax(z));
               end
               Magnitude2(r,c)=Lmax(z);
            end
    end
 end
 toc(t)
 time=toc(t);
% ======================================
% plotting the location amplitude figure.
% ======================================
%IN=1;
%figure (IN)
%imshow(cir)
%imagesc(S1)
%colormap(gray)
% hold on;
% for rk=168            % y0+165
%      for ck=146       % x0+50
% plot(ck,rk,'*','color','g')
% hold on
%      end
% end
%
% figure(IN+1)
% [A,S]=meshgrid(ang,scl);
% contour(A,S,locationAMPs)
```

```
CONTOURDIRPLOT.m
%
% Contour plot of the the most local dominant wavelength superimposed by
% the 1st and the 2nd peaks directions.
% ========================================================================

x=1:256;    %COLUMNS
y=1:256;    %ROWS

% ================================================
% Plotting the contour of the 1st dominant wavelength.
% ================================================
```

```
figure
[X,Y]=meshgrid(x,y);
contourf(X,Y,WAVL1);
colorbar
set(gca,'Ydir','reverse','fontsize',30,'FontName','Times New Roman')
title('The Local Dominant Wavelength \lambda_{1}','fontsize',30,'FontName','Times New Roman')
xlabel('COLUMN','fontsize',30,'FontName','Times New Roman')
ylabel('ROW','fontsize',30,'FontName','Times New Roman')
hold on

% ====================================
% averaging the 1st and 2nd directions.
% ====================================
npix=8;
krow=256/npix;
kcolumn=256/npix;
for i=1:krow
for j=1:kcolumn
for s=i*npix-(npix-1):i*npix
for t=j*npix-(npix-1):j*npix
SubDF1(s-(i-1)*npix,t-(j-1)*npix)=DIR1(s,t);
SubDF2(s-(i-1)*npix,t-(j-1)*npix)=DIR2(s,t);
end
end
mode11=mode(SubDF1,2);
mode21=mode(SubDF2,2);
mode12=mode(mode11);
mode22=mode(mode21);
FinalD1(i,j)=mode12;
FinalD2(i,j)=mode22;
end
end

% ========================================
% plotting the 1st and 2nd peak directions.
% ========================================
npix=8;
krow=256/npix;
kcolumn=256/npix;
for j=1:krow
for l=1:kcolumn
    arrow([l*npix-2 j*npix-2],[l*npix-2+(3.5)*cos(-FinalD1(j,l))...
     j*npix-2+(3.5)*sin(-FinalD1(j,l))],'length',0,'tipangle',0)
if isnan(FinalD2(j,l))
```

```
    arrow([l*npix-2 j*npix-2],[l*npix-2 j*npix-2],'length',0,'tipangle',0)
    else
    arrow([l*npix-2 j*npix-2],...
    [l*npix-2+(2)*cos(-FinalD2(j,l)) j*npix-2+(2)*sin(-FinalD2(j,l))],'length',0,'tipangle',0)
    end
end
end

% ====================================================
% Plotting the contour of the 2nd dominant wavelength.
% ====================================================
figure
[X,Y]=meshgrid(x,y);
contourf(X,Y,WAVL2);
colorbar
set(gca,'Ydir','reverse','fontsize',30,'FontName','Times New Roman')
title('The Local Dominant Wavelength \lambda_{2}','fontsize',30,'FontName','Times New Roman')
xlabel('COLUMN','fontsize',30,'FontName','Times New Roman')
ylabel('ROW','fontsize',30,'FontName','Times New Roman')
```

Image constructed in Figure 2.7

```
for i=1:500
    for j=1:500
        IM3(i,j)=2+ (1)*sin(2*pi*(i+j)/27)-(1)*cos(2*pi*(i-j)/27);
    end
end
IM=imshow(IM3);
```

Image constructed in Figure 2.9

```
for i=1:500
    for j=1:500
        IM4(i,j)=1+(1)*sin(2*pi*(-i+j)/25.6);
    end
end
IM=imshow(IM4);
```

Appendix B

B.1

In the spherical coordinates, the gradient vector and the Laplace operator are given by (Spurk and Aksel [106])

$$\nabla = \frac{\partial}{\partial r}\mathbf{e}_r + \frac{1}{r}\frac{\partial}{\partial \theta}\mathbf{e}_\theta + \frac{1}{r\sin(\theta)}\frac{\partial}{\partial \phi}\mathbf{e}_\phi, \tag{B.1}$$

$$\nabla^2 = \frac{1}{r^2}\frac{\partial}{\partial r}\left[r^2\frac{\partial}{\partial r}\right] + \frac{1}{r^2\sin(\theta)}\frac{\partial}{\partial \theta}\left[\sin(\theta)\frac{\partial}{\partial \theta}\right] + \frac{1}{r^2\sin^2(\theta)}\frac{\partial^2}{\partial \phi^2}, \tag{B.2}$$

where $\mathbf{e}_r$, $\mathbf{e}_\theta$ and $\mathbf{e}_\phi$ are the unit vectors such that

$$\mathbf{e}_r = \sin(\theta)\cos(\phi)\,\mathbf{i} + \sin(\theta)\sin(\phi)\,\mathbf{j} + \cos(\theta)\,\mathbf{k}, \tag{B.3}$$

$$\mathbf{e}_\theta = \cos(\theta)\cos(\phi)\,\mathbf{i} + \cos(\theta)\sin(\phi)\,\mathbf{j} - \sin(\theta)\,\mathbf{k}, \tag{B.4}$$

$$\mathbf{e}_\phi = -\sin(\phi)\,\mathbf{i} + \cos(\phi)\,\mathbf{j}, \tag{B.5}$$

where $\mathbf{i}$, $\mathbf{j}$ and $\mathbf{k}$ are the set of mutually orthogonal unit vectors in the cartesian coordinates.

B.2

The associated Legendre equation has the form (Arfken et. al. [4])

$$\left(1-x^2\right)Y''(x)-2xY'(x)-\frac{1}{(1-x^2)}Y(x)+n(n+1)Y(x)=0, \tag{B.6}$$

where $|x|<1$ and $m\in\mathbb{Z}$. Associated Legendre equation has regular singular points at $x=-1,1$ and $x=\infty$. Its solution takes the form

$$Y(x)=\sum_{l=1}^{\infty}\varsigma_l P_l^m(x), \tag{B.7}$$

with

$$P_l^m(x)=(-1)^m\left(1-x^2\right)^{\frac{m}{2}}\frac{d^m}{dx^m}P_l(x). \tag{B.8}$$

P_l^m and P_l are the associated Legendre polynomial and Legendre polynomial, respectively.

Rodrigues formula of P_l^m is

$$P_l^m(x)=\frac{(-1)^m}{2^l l!}\left(1-x^2\right)^{\frac{m}{2}}\frac{d^{l+m}}{dx^{l+m}}\left(x^2-1\right)^l. \tag{B.9}$$

The associated Legendre polynomials have the following recurrence relations:

$$(2l+1)xP_l^m=(l+m)P_{l-1}^m+(l-m+1)P_{l+1}^m, \tag{B.10}$$

$$P_l^{m+1}+\frac{2mx}{(1-x^2)^{\frac{1}{2}}}P_l^m+(l+m)(l-m+1)P_l^{m-1}=0, \tag{B.11}$$

$$\left(1-x^2\right)^{\frac{1}{2}}\frac{dP_l^m}{dx}=\frac{1}{2}(l+m)(l-m+1)P_l^{m-1}-\frac{1}{2}P_l^{m+1}, \tag{B.12}$$

$$(2l+1)\left(1-x^2\right)^{\frac{1}{2}}P_l^m=P_{l-1}^{m+1}-P_{l+1}^{m+1}, \tag{B.13}$$

Combining equations (B.11) to (B.13) together gives

$$\left(1-x^2\right)\frac{dP_l^m}{dx}=\frac{(l+m)\,(l-m+1)}{2l+1}\left[P_{l-1}^m-P_{l+1}^m\right]+mxP_l^m. \tag{B.14}$$

P_l^m are also orthogonal in the lower index

$$\int_{-1}^{1}P_l^mP_q^m=\delta_l^q\frac{1}{q}\frac{(l+m)!}{(l-m)!}, \tag{B.15}$$

where $0\leq m\leq l,q$.

B.3

Gamma function is (Berg and McGregor [17])

$$\Gamma\left(\kappa\right)=\int_0^\infty\exp\left(t\right)t^{\kappa-1}dt,\ \kappa>0. \tag{B.16}$$

For integers

$$\Gamma\left(n\right)=n!. \tag{B.17}$$

and

$$\Gamma\left(\frac{1}{2}\right)=\sqrt{\pi}. \tag{B.18}$$

B.4

The vorticity components in equation (3.70) is defined as

$$\begin{aligned}\Omega_1^{(1)} &= \frac{\partial\mathbf{U}_3'}{\partial y^*}-\frac{\partial\mathbf{U}_2'}{\partial z^*}\\ &\qquad\qquad ,\\ \Omega_2^{(1)} &= \frac{\partial\mathbf{U}_1'}{\partial z^*}-\frac{\partial\mathbf{U}_3'}{\partial x^*}\end{aligned} \tag{B.19}$$

Hence,

$$\begin{aligned} \frac{\partial \Omega_1^{(1)}}{\partial y^*} &= \frac{\partial^2 \mathbf{U}_3'}{\partial y^{*2}} - \frac{\partial^2 \mathbf{U}_2'}{\partial y^* \partial z^*} \\ &, \\ \frac{\partial \Omega_2^{(1)}}{\partial x^*} &= \frac{\partial^2 \mathbf{U}_1'}{\partial x^* \partial z^*} - \frac{\partial^2 \mathbf{U}_3'}{\partial x^{*2}} \end{aligned} \tag{B.20}$$

The rate-of-strain in equation (3.70) is defined by:

$$\begin{aligned} e_{13}^{(1)} &= \frac{1}{2}\left[\frac{\partial \mathbf{U}_1'}{\partial z^*} + \frac{\partial \mathbf{U}_3'}{\partial x^*}\right] \\ e_{23}^{(1)} &= \frac{1}{2}\left[\frac{\partial \mathbf{U}_2'}{\partial z^*} + \frac{\partial \mathbf{U}_3'}{\partial y^*}\right] , \\ e_{33}^{(1)} &= \frac{\partial \mathbf{U}_3'}{\partial z^*} \end{aligned} \tag{B.21}$$

Hence,

$$\begin{aligned} \frac{\partial e_{13}^{(1)}}{\partial x^*} &= \frac{1}{2}\left[\frac{\partial^2 \mathbf{U}_1'}{\partial x^* \partial z^*} + \frac{\partial^2 \mathbf{U}_3'}{\partial x^{*2}}\right] \\ \frac{\partial e_{23}^{(1)}}{\partial y^*} &= \frac{1}{2}\left[\frac{\partial^2 \mathbf{U}_2'}{\partial y^* \partial z^*} + \frac{\partial^2 \mathbf{U}_3'}{\partial y^{*2}}\right] , \\ \frac{e_{33}^{(1)}}{\partial z^*} &= \frac{\partial^2 \mathbf{U}_3'}{\partial z^{*2}} \end{aligned} \tag{B.22}$$

Using (3.75) to compute the space derivatives of the vorticity and the rate-of-strain components as follows

$$\frac{\partial \Omega_1^{(1)}}{\partial y^*} = \frac{\partial^2 U_3'}{\partial y^{*2}} - \frac{\partial^2 U_2'}{\partial y^* \partial z^*} = 0, \tag{B.23}$$

$$\begin{aligned} \frac{\partial \Omega_2^{(1)}}{\partial x^*} &= \frac{\partial^2 U_1'}{\partial x^* \partial z^*} - \frac{\partial^2 U_3'}{\partial x^{*2}} \\ &= \frac{\partial}{\partial x^*}\left(U_1 (im) \exp\left(\sigma t^* + i\left(kx^* + mz^*\right)\right)\right) - \frac{\partial}{\partial x^*}\left(U_3 (ik) \exp\left(\sigma t^* + i\left(kx^* + mz^*\right)\right)\right) , \\ &= U_1 (im)(ik) \exp\left(\sigma t^* + i\left(kx^* + mz^*\right)\right) - U_3 (ik)^2 \exp\left(\sigma t^* + i\left(kx^* + mz^*\right)\right) \end{aligned} \tag{B.24}$$

$$\implies \quad \frac{\partial \Omega_2^{(1)}}{\partial x^*} = \left(-U_1 mk + U_3 k^2\right) \exp\left(\sigma t^* + i\left(kx^* + mz^*\right)\right), \tag{B.25}$$

$$\begin{aligned}
\tfrac{\partial e_{13}^{(1)}}{\partial x^*} &= \tfrac{1}{2}\left[\tfrac{\partial^2 U_1'}{\partial x^* \partial z^*} + \tfrac{\partial^2 U_3'}{\partial x^{*2}}\right] \\
&= \tfrac{1}{2}\left[\tfrac{\partial}{\partial x^*}\left(U_1 (im) \exp\left(\sigma t^* + i\left(kx^* + mz^*\right)\right)\right) - \tfrac{\partial}{\partial x^*}\left(U_3 (ik) \exp\left(\sigma t^* + i\left(kx^* + mz^*\right)\right)\right)\right], \\
&= \tfrac{1}{2}\left[U_1 (im)(ik) \exp\left(\sigma t^* + i\left(kx^* + mz^*\right)\right) - U_3 (ik)^2 \exp\left(\sigma t^* + i\left(kx^* + mz^*\right)\right)\right]
\end{aligned} \tag{B.26}$$

$$\implies \quad \frac{\partial e_{13}^{(1)}}{\partial x^*} = -\frac{1}{2}\left(U_1 mk + U_3 k^2\right) \exp\left(\sigma t^* + i\left(kx^* + mz^*\right)\right), \tag{B.27}$$

$$\frac{\partial e_{23}^{(1)}}{\partial y^*} = \frac{1}{2}\left[\frac{\partial^2 U_2'}{\partial y^* \partial z^*} - \frac{\partial^2 U_3'}{\partial y^{*2}}\right], \tag{B.28}$$

$$\implies \quad \frac{\partial e_{23}^{(1)}}{\partial y^*} = 0, \tag{B.29}$$

$$\begin{aligned}
\tfrac{\partial e_{33}^{(1)}}{\partial z^*} &= \tfrac{\partial^2 U_3'}{\partial z^{*2}} \\
&= \tfrac{\partial}{\partial z^*}\left(U_3 (im) \exp\left(\sigma t^* + i\left(kx^* + mz^*\right)\right)\right), \\
&= U_3 (im)^2 \exp\left(\sigma t^* + i\left(kx^* + mz^*\right)\right)
\end{aligned} \tag{B.30}$$

$$\implies \quad \frac{\partial e_{33}^{(1)}}{\partial z^*} = -U_3 m^2 \exp\left(\sigma t^* + i\left(kx^* + mz^*\right)\right), \tag{B.31}$$

B.5

$$\begin{aligned} E_5 &= ReF_{1I}, \\ &= Re\left(a_1K_{11}+a_2K_{21}\right)m, \end{aligned} \tag{B.32}$$

$$E_6 = \left(k^2+m^2\right)\left[\left(D_{1H}^{*(0)}+D_{2H}^{*(0)}\right)k^2+\left(D_{1V}^{*(0)}+D_{2V}^{*(0)}\right)m^2\right], \tag{B.33}$$

$$E_7 = \left(\frac{k^2}{k^2+m^2}\right)\left[\left(S_1S_{11}+S_2S_{12}\right)k^2+\left(S_1S_{21}+S_2S_{22}\right)m^2\right], \tag{B.34}$$

$$E_8 = Re\left[\left(D_{1H}^{*(0)}k^2+D_{1V}^{*(0)}m^2\right)\left(D_{2H}^{*(0)}k^2+D_{2V}^{*(0)}m^2\right)-a_1a_2K_{11}K_{21}m^2\right], \tag{B.35}$$

$$E_9 = \left(k^2+m^2\right)\left[a_1K_{11}m\left(D_{2H}^{*(0)}k^2+D_{2V}^{*(0)}m^2\right)+a_2K_{21}m\left(D_{1H}^{*(0)}k^2+D_{1V}^{*(0)}m^2\right)\right], \tag{B.36}$$

$$E_{10} = \left(\frac{k^2}{k^2+m^2}\right)\left[a_2K_{21}S_1m\left(S_{11}k^2+S_{21}m^2\right)+a_1K_{11}S_2m\left(S_{12}k^2+S_{22}m^2\right)\right], \tag{B.37}$$

To solve equation (3.117) above the sign of the the coefficients need to be known. The denominator of the coefficients G_1, G_2 and G_3 is:

$$\begin{aligned} ReE_4-E_1E_7 &= -Re\left(\tfrac{k^2}{k^2+m^2}\right)\Bigg\{\Bigg[\left(\tfrac{S_1S_{11}+S_2S_{12}}{Re}\right)+S_1S_{11}D_{1H}^{*(0)}+S_2S_{12}D_{2H}^{*(0)}\Bigg]k^4 \\ &+ \Bigg[\left(\tfrac{S_1S_{21}+S_2S_{22}}{Re}\right)+S_1S_{21}D_{1H}^{*(0)}+S_2S_{22}D_{2H}^{*(0)}+\left(\tfrac{S_1S_{11}+S_2S_{12}}{Re}\right)+S_1S_{11}D_{1V}^{*(0)} \\ &+ S_2S_{12}D_{2V}^{*(0)}\Bigg]m^2k^2+\Bigg[\left(\tfrac{S_1S_{21}+S_2S_{22}}{Re}\right)+S_1S_{21}D_{1V}^{*(0)}+S_2S_{22}D_{2V}^{*(0)}\Bigg]m^4\Bigg\}, \end{aligned} \tag{B.38}$$

Now, the numerator of G_1 can be calculated as follow,

$$\begin{aligned} E_4E_5 - E_2E_7 - E_1E_{10} &= -Re\left(\tfrac{k^2}{k^2+m^2}\right)\Bigg\{\left(\tfrac{k^2+m^2}{Re}\right)(a_1K_{11}+a_2K_{21})\,m\Bigg[(S_1S_{11}+S_2S_{12})\,k^2 \\ &+ (S_1S_{21}+S_2S_{22})\,m^2\Bigg] + \left(a_1K_{11}S_2S_{12}mk^2\right)\left(D_{2H}^{*(0)}k^2 + D_{2V}^{*(0)}m^2\right) \\ &+ \left(a_1K_{11}S_2S_{22}m^3\right)\left(D_{2H}^{*(0)}k^2 + D_{2V}^{*(0)}m^2\right) + \left(a_2K_{21}S_1S_{11}mk^2\right) \\ &\quad \left(D_{1H}^{*(0)}k^2 + D_{1V}^{*(0)}m^2\right) + \left(a_2K_{21}S_1S_{21}m^3\right)\left(D_{1H}^{*(0)}k^2 + D_{1V}^{*(0)}m^2\right) \\ &+ \left(\tfrac{k^2+m^2}{Re}\right)\Bigg[a_2K_{21}m\left(S_1S_{11}k^2 + S_1S_{21}m^2\right) + a_1K_{11}m\big(S_2S_{12}k^2 \\ &+ S_2S_{22}m^2\big)\Bigg] + \left(D_{2H}^{*(0)}k^2 + D_{2V}^{*(0)}m^2\right)\Bigg[a_1K_{11}m\left(S_2S_{12}k^2 + S_2S_{22}m^2\right)\Bigg] \\ &+ \left(D_{1H}^{*(0)}k^2 + D_{1V}^{*(0)}m^2\right)\Bigg[a_2K_{21}m\left(S_1S_{11}k^2 + S_1S_{21}m^2\right)\Bigg]\Bigg\}, \end{aligned} \tag{B.39}$$

Next, the numerator of G_2 can be calculated as follow,

$$\begin{aligned}
E_3E_7 - E_4E_6 - E_4E_8 - E_2E_{10} &= -k^2\Bigg\{ \left(a_1a_2K_{11}K_{21}m^2\right)\Bigg[\left(S_1S_{11} + S_2S_{12}\right)k^2 \\
&+ \left(S_1S_{21} + S_2S_{22}\right)m^2\Bigg] + \left(D_{2H}^{*(0)}k^2 + D_{2V}^{*(0)}m^2\right)^2 \\
&\left(S_1S_{11}k^2 + S_1S_{21}m^2\right) + \left(D_{1H}^{*(0)}k^2 + D_{1V}^{*(0)}m^2\right)^2 \\
&\left(S_2S_{12}k^2 + S_2S_{22}m^2\right)\Bigg\} - Re\left(\tfrac{k^2}{k^2+m^2}\right)\Bigg\{\Bigg[S_1\left(S_{11}k^2 + S_{21}m^2\right) \\
&\left(D_{2H}^{*(0)}k^2 + D_{2V}^{*(0)}m^2\right) + S_2\left(S_{12}k^2 + S_{22}m^2\right) \\
&\left(D_{1H}^{*(0)}k^2 + D_{1V}^{*(0)}m^2\right)\Bigg]\Bigg[\left(D_{1H}^{*(0)}k^2 + D_{1V}^{*(0)}m^2\right) \\
&\left(D_{2H}^{*(0)}k^2 + D_{2V}^{*(0)}m^2\right) - a_1a_2K_{11}K_{21}m^2\Bigg] \\
&+ \Bigg[\left(\tfrac{k^2+m^2}{Re}\right)\left(a_1K_{11} + a_2K_{21}\right)m + a_1K_{11}m\left(D_{2H}^{*(0)}k^2 + D_{2V}^{*(0)}\right) \\
&+ a_2K_{21}m\left(D_{1H}^{*(0)}k^2 + D_{1V}^{*(0)}\right)\Bigg]\Bigg[a_2K_{21}S_1\left(S_{11}k^2 + S_{21}m^2\right)m \\
&+ a_1K_{11}S_2\left(S_{12}k^2 + S_{22}m^2\right)m\Bigg]\Bigg\},
\end{aligned} \tag{B.40}$$

Finally, the numerator of G_3 can be calculated as follows,

$$\begin{aligned} E_3E_{10} - E_4E_9 &= -k^2\Big[a_1a_2^2K_{11}K_{21}^2\left(S_1S_{11}m^3k^2 + S_1S_{21}m^5\right) + a_1^2a_2K_{11}K_{21}\Big(S_2S_{12}m^3k^2 \\ &+ S_2S_{22}m^5\Big) + a_1K_{11}S_1S_{11}\left(D_{2H}^{*(0)2}mk^2 + 2D_{2H}^{*(0)}D_{2V}^{*(0)}m^3k^4 + D_{2V}^{*(0)2}m^5k^2\right) \\ &+ a_1K_{11}S_1S_{21}\left(D_{2H}^{*(0)2}m^3k^4 + 2D_{2V}^{*(0)}D_{2H}^{*(0)}m^5k^2 + D_{2V}^{*(0)2}m^7\right) \\ &+ a_2K_{21}S_2S_{12}\left(D_{1H}^{*(0)2}mk^2 + 2D_{1V}^{*(0)}D_{1H}^{*(0)}m^3k^4 + D_{1V}^{*(0)2}m^5k^2\right) \\ &+ a_2K_{21}S_2S_{22}\left(D_{1H}^{*(0)2}m^3k^4 + 2D_{1H}^{*(0)}D_{1V}^{*(0)}m^5k^2 + D_{1V}^{*(0)2}m^7\right)\Big], \end{aligned} \tag{B.41}$$

B.6

```
% This program has been designed to plot the key parameter vs k^2.
% ================================================================
function [Kc,ReRic,ReRI1,k,ReRI2,ReRI3]=KEY_PARAMETER_PLOT(m0)
%
for m=m0
[ReRI1,ReRI2,ReRI3,sigmaI1,sigmaI2,sigmaI3,k]=KEY_PARAMETER(m);
%
x=k.^2;
y=length(x);
[ReRic,0]=min(ReRI1);
Kc=x(0);
plot(x,ReRI1)
 axis([0 5 0 50])
 hold on
end
%
xlabel('k^2','fontsize',10)
ylabel('Re\beta','fontsize',10)
```

```
% This program is desgined to compute the real roots of the cubic equation
% in sigma_I.
% ========================================================================
```

```
function [ReRI1,ReRI2,ReRI3,sigmaI1,sigmaI2,sigmaI3,k]=KEY_PARAMETER(m);
k=0.001:0.02:4;
%
% ====================
% The relative speed.
% ====================
% spd1=0.0063;   % cm s^(-1)
% spd2=0.013;    % cm s^(-1)
% spd=max(spd1,spd2);
a1=1;  %spd1/spd;          % non_dim
a2=1; %spd2/spd;          % non_dim
%
% ============
% Ki1 and Ki2.
% ============
lambda1=2.2;
lambda2=1;
K11=0.57;
K12=0.31;
K41=-0.10;
K42=-0.037;
K21=0.16;
K22=0.28;
TUE=1.3;
%
% ==============
% The diffusion.
%===============
% B1=3.4;        % s
% B2=3.4;        % s
B= 3.4; %max(B1,B2);
eta1=1;%B1/B;
eta2=1;%B2/B;

D1Hn=((a1)^2*TUE*K11)/B*lambda1;
D2Hn=((a2)^2*TUE*K12)/B*lambda2;
D1Vn=((a1)^2*TUE*K21)/B;
D2Vn=((a2)^2*TUE*K22)/B;  % non_dim
%
% ============================
% Set up the other parameters.
% ============================
alpha10=0.2;
alpha20=0.5;
```

```
J11=0.45;
J12=0.14;
J41=-0.23;
J42=-0.064;
S11=J11+alpha10*J41;
S12=J12+alpha20*J42;
S21=J11-alpha10*J41+3*alpha10*K41;
S22=J12-alpha20*J42+3*alpha20*K42;
%
% ============================
% The relative concentration.
% ============================
% n1=10^7;        % cells cm^(-3)
% n2=10^7;        % cells cm^(-3)
% n=max(n1,n2);
gama1=1; %n1/n;    % non_dim
gama2=1; %n2/n;    % non_dim
% ====================
% The relative volume.
% ====================
% vol1=5*10^(-10);   % cm^3
% vol2=3.5*10^(-10);   % cm^3
% vol=max(vol1,vol2);
pitta1=1; %vol1/vol;   % non_dim
pitta2=1; %vol2/vol;   % non_dim
%
% ==================================
% The relative difference in density.
% ==================================
% rho=1;                      % g cm^(-3)
% cellrho1=1.05;              % g cm^(-3)
% cellrho2=1.05;              % g cm^(-3)
% delrho1=cellrho1-rho;
% delrho2=cellrho2-rho;
% delrho=max(delrho1,delrho2);
delta1=1;  %delrho1/delrho;     % non_dim
delta2=1;  %delrho2/delrho;    % non_dim
%
% The relation.
S1=delta1*pitta1*a1*gama1*eta1;
S2=delta2*pitta2*a2*gama2*eta2;
%
Re=10^(-2);
% ======================
```

```
% Solving the equation.
% =====================
for I=1:length(k)
E1(I)=Re*((Re^(-1)+D1Hn+D2Hn)*k(I)^2+(Re^(-1)+D1Vn+D2Vn)*m^2);
E2(I)=Re*(((k(I)^2+m^2)/Re)*(a1*K11+a2*K12)*m+a1*K11*(D2Hn*k(I)^2+D2Vn*m^2)*m+...
a2*K12*(D1Hn*k(I)^2+D1Vn*m^2)*m);
E3(I)=(k(I)^2+m^2)*((D1Hn*k(I)^2+D1Vn*m^2)*(D2Hn*k(I)^2+D2Vn*m^2)-a1*a2*K11*K12*m^2);
E4(I)=(k(I)^2/(k(I)^2+m^2))*(S1*(S11*k(I)^2+S21*m^2)*(D2Hn*k(I)^2+D2Vn*m^2)+...
S2*(S12*k(I)^2+S22*m^2)*(D1Hn*k(I)^2+D1Vn*m^2));
E5(I)=Re*(a1*K11+a2*K12)*m;
E6(I)=(k(I)^2+m^2)*((D1Hn+D2Hn)*k(I)^2+(D1Vn+D2Vn)*m^2);
E7(I)=(k(I)^2/(k(I)^2+m^2))*((S1*S11+S2*S12)*k(I)^2+(S1*S21+S2*S22)*m^2);
E8(I)=Re*((D1Hn*k(I)^2+D1Vn*m^2)*(D2Hn*k(I)^2+D2Vn*m^2)-a1*a2*K11*K12*m^2);
E9(I)=(k(I)^2+m^2)*(a1*K11*(D2Hn*k(I)^2+D2Vn*m^2)*m+a2*K12*(D1Hn*k(I)^2+D1Vn*m^2)*m);
E10(I)=(k(I)^2/(k(I)^2+m^2))*(a2*K12*S1*(S11*k(I)^2+S21*m^2)*m+..
a1*K11*S2*(S12*k(I)^2+S22*m^2)*m);
EE(I)=Re*E4(I)-E1(I)*E7(I);
EE1(I)=E4(I)*E5(I)-E2(I)*E7(I)-E1(I)*E10(I);
EE2(I)=E3(I)*E7(I)-E4(I)*E6(I)-E4(I)*E8(I)-E2(I)*E10(I);
EE3(I)=E3(I)*E10(I)-E4(I)*E9(I);
G1(I)=EE1(I)/EE(I);
G2(I)=EE2(I)/EE(I);
G3(I)=EE3(I)/EE(I);
d=1000;
digits(d)
syms X
solve(X^3+G1(I)*X^2+G2(I)*X+G3(I));
sigmaI1(I)=double(ans(1,1));
sigmaI2(I)=double(ans(2,1));
sigmaI3(I)=double(ans(3,1));
end

for J=1:length(k)
    ReRI1(J)=(-E1(J)*sigmaI1(J)^2-E2(J)*sigmaI1(J)+E3(J))/E4(J);
    ReRI2(J)=(-E1(J)*sigmaI2(J)^2-E2(J)*sigmaI2(J)+E3(J))/E4(J);
    ReRI3(J)=(-E1(J)*sigmaI3(J)^2-E2(J)*sigmaI3(J)+E3(J))/E4(J);
end
```

```
% Plotting the neutral curves to investigate the linear instability of
% mixed species.
% ============================================================================
%
% ====================
% Loading the results.
% ====================
```

```
load('a1.mat')
load('a02.mat')
load('a04.mat')
load('a06.mat')
load('a08.mat')
load('b02.mat')
load('b04.mat')
load('b06.mat')
load('b08.mat')
load('e03.mat')
load('e04.mat')
load('e05.mat')
load('g02.mat')
load('g04.mat')
load('g06.mat')
load('g08.mat')
load('p04.mat')
load('p06.mat')
load('p08.mat')
%
% ====================
% Plotting the graphs.
% ====================
x=k.^2;
%
% ====================
% 1 - Relative speed.
% ====================
figure
plot(x,a1,'LineWidth',4,'color','k');
hold on
plot(x,a08,'--','LineWidth',4,'color','k');
hold on
plot(x,a06,'-.','LineWidth',4,'color','k');
hold on
plot(x,a04,':','LineWidth',4,'color','k');
hold on
plot(x,a02,'-*','LineWidth',4,'color','k');
axis([0 4 0 3])
legend('V_{2s}=V_{1s}','V_{2s}=0.8V_{1s}','V_{2s}=0.6V_{1s}',...
'V_{2s}=0.4V_{1s}','V_{2s}=0.2V_{1s}')
set(gca,'FontSize',30,'FontName','Times New Roman')
xlabel('k^{2}_{c}','FontSize',30)
ylabel('Re\beta_{c}','FontSize',30)
```

```
%
% ================================
% Critical values: Re\beta and Kc.
% ================================
AC=[a1c a08c a06c a04c a02c];
KAC1=[Ka1 Ka08 Ka06 Ka04 Ka02];
kac1=sqrt(KAC1);
figure
for i=1:5
    x1=kac1(1,i);
    y=AC(1,i);
    plot(i,y,'.','color','r','MarkerSize',20,'LineWidth',6)
    hold on
    plot(i,x1,'o','MarkerSize',5,'LineWidth',4)
    hold on
    axis([0.5 5.5 0.2 2.4])
    legend('Re\beta_{c}','k_{c}')
    set(gca,'FontSize',30,'FontName','Times New Roman')
    [hx,hy] = format_ticks(gca,{'V_{2s}=V_{1s}','V_{2s}=0.8V_{1s}',...
    'V_{2s}=0.6V_{1s}','V_{2s}=0.4V_{1s}','V_{2s}=0.2V_{1s}'},[],[1,2,3,4,5]);
end
% ========================
% Small relative velocity.
% ========================
% figure
% plot(x,a01,'LineWidth',2,'color','k');
% hold on
% plot(x,a001,'--','LineWidth',2,'color','k');
% hold on
% plot(x,a0001,'-.','LineWidth',2,'color','k');
% axis([0 4 0 0.5])
% legend('V_{2s}=0.1V_{1s}','V_{2s}=0.0.01V_{1s}','V_{2s}=0.001V_{1s}')
% xlabel('k^{2}','FontSize',24)
% ylabel('Re\beta','FontSize',24)
%
% ================================
% 2 - Relative cell concentration.
% ================================
figure
plot(x,a1,'LineWidth',4,'color','k');
hold on
plot(x,g08,'--','LineWidth',4,'color','k');
hold on
plot(x,g06,'-.','LineWidth',4,'color','k');
```

```
hold on
plot(x,g04,':','LineWidth',4,'color','k');
hold on
plot(x,g02,'-*','LineWidth',4,'color','k');
axis([0 4 1 3])
legend('n_{2}=n_{1}','n_{2}=0.8n_{1}','n_{2}=0.6n_{1}',...
'n_{2}=0.4n_{1}','n_{2}=0.2n_{1}')
set(gca,'FontSize',30,'FontName','Times New Roman')
xlabel('k^{2}','FontSize',30)
ylabel('Re\beta','FontSize',30)
%
% ================================
% Critical values: Re\beta and Kc.
% ================================
GC=[a1c g08c g06c g04c g02c];
KGC1=[Ka1 Kg08 Kg06 Kg04 Kg02];
kgc1=sqrt(KGC1);
figure
for i=1:5
    x1=kgc1(1,i);
    y=GC(1,i);
    plot(i,y,'.','color','r','MarkerSize',20,'LineWidth',6)
    hold on
    plot(i,x1,'o','MarkerSize',5,'LineWidth',4)
    hold on
    axis([0.5 5.5 0.2 2.4])
    legend('Re\beta_{c}','k_{c}')
    set(gca,'FontSize',30,'FontName','Times New Roman')
    [hx,hy] = format_ticks(gca,{'n_{2}=n_{1}','n_{2}=0.8n_{1}',...
    'n_{2}=0.6n_{1}','n_{2}=0.4n_{1}','n_{2}=0.2n_{1}'},[],[1,2,3,4,5]);
end
% =========================
% 3 - Relative cell volume.
% =========================
figure
plot(x,a1,'LineWidth',4,'color','k');
hold on
plot(x,p08,'--','LineWidth',4,'color','k');
hold on
plot(x,p06,'-.','LineWidth',4,'color','k');
hold on
plot(x,p04,':','LineWidth',4,'color','k');
axis([0 4 1 3])
legend('v_{2}=v_{1}','v_{2}=0.8v_{1}','v_{2}=0.6v_{1}',...
```

```
'v_{2}=0.4v_{1}','v_{2}=0.2v_{1}')
set(gca,'FontSize',30,'FontName','Times New Roman')
xlabel('k^{2}','FontSize',30)
ylabel('Re\beta','FontSize',30)
%
% ================================
% Critical values: Re\beta and Kc.
% ================================
PC=[a1c p08c p06c p04c];
KPC1=[Ka1 Kp08 Kp06 Kp04];
kpc1=sqrt(KPC1);
figure
for i=1:4
    x1=kpc1(1,i);
    y=PC(1,i);
    plot(i,y,'.','color','r','MarkerSize',20,'LineWidth',6)
    hold on
    plot(i,x1,'o','MarkerSize',5,'LineWidth',4)
    hold on
    axis([0.5 4.5 0.2 2.4])
    legend('Re\beta_{c}','k_{c}')
    set(gca,'FontSize',30,'FontName','Times New Roman')
    [hx,hy] = format_ticks(gca,{'v_{2}=v_{1}','v_{2}=0.8v_{1}',...
    'v_{2}=0.6v_{1}','v_{2}=0.4v_{1}','v_{2}=0.2v_{1}'},[],[1,2,3,4]);
end
% ============================================
% 4 - Relative gyrotactic orientation parameter.
% ============================================
figure
plot(x,a1,'LineWidth',4,'color','k');
hold on
plot(x,b08,'--','LineWidth',4,'color','k');
hold on
plot(x,b06,'-.','LineWidth',4,'color','k');
hold on
plot(x,b04,':','LineWidth',4,'color','k');
hold on
plot(x,b02,'-*','LineWidth',4,'color','k');
axis([0 4 1 3])
legend('B_{2}=B_{1}','B_{2}=0.8B_{1}','B_{2}=0.6B_{1}',...
'B_{2}=0.4B_{1}','B_{2}=0.2B_{1}')
set(gca,'FontSize',30,'FontName','Times New Roman')
xlabel('k^{2}','FontSize',30)
ylabel('Re\beta','FontSize',30)
```

```
%
% ================================
% Critical values: Re\beta and Kc.
% ================================
BC=[a1c b08c b06c b04c b02c];
KBC1=[Ka1 Kb08 Kb06 Kb04 Kb02];
kbc1=sqrt(KBC1);
figure
for i=1:5
    x1=kbc1(1,i);
    y=BC(1,i);
    plot(i,y,'.','color','r','MarkerSize',20,'LineWidth',6)
    hold on
    plot(i,x1,'o','MarkerSize',5,'LineWidth',4)
    hold on
    axis([0.5 5.5 0.2 2.4])
    legend('Re\beta_{c}','k_{c}')
    set(gca,'FontSize',30,'FontName','Times New Roman')
    [hx,hy] = format_ticks(gca,{'B_{2}=B_{1}','B_{2}=0.8B_{1}',...
    'B_{2}=0.6B_{1}','B_{2}=0.4B_{1}','B_{2}=0.2B_{1}'},[],[1,2,3,4,5]);
end
% =================
% 5 - Eccentricity.
% =================
figure
plot(x,a1,'LineWidth',4,'color','k');
hold on
plot(x,e03,'--','LineWidth',4,'color','k');
hold on
plot(x,e04,'-.','LineWidth',4,'color','k');
hold on
plot(x,e05,':','LineWidth',4,'color','k');
axis([0 4 1 3])
legend('\alpha_{10}=\alpha_{20}=0.2','\alpha_{10}=0.2,\alpha_{20}=0.3',...
'\alpha_{10}=0.2,\alpha_{20}=0.4','\alpha_{10}=0.2,\alpha_{20}=0.5')
set(gca,'FontSize',30,'FontName','Times New Roman')
xlabel('k^{2}','FontSize',30)
ylabel('Re\beta','FontSize',30)
```

Appendix C

C.1

Fourier series for a function defined on an interval of length $2a$ (Boggess and Narcowich [18]),

Theorem C.1. *If* $f(x) = a_0 + \sum_{k=1}^{\infty} \left[a_k \cos \frac{k\pi x}{a} + b_k \sin \frac{k\pi x}{a}\right]$ *on the interval* $-a \leq x \leq a$, *then*

$$a_0 = \frac{1}{2a} \int_{-a}^{a} f(t)\, dt, \tag{C.1}$$

$$a_n = \frac{1}{a} \int_{-a}^{a} f(t) \cos \frac{k\pi t}{a} dt, \tag{C.2}$$

$$b_n = \frac{1}{a} \int_{-a}^{a} f(t) \sin \frac{k\pi t}{a} dt. \tag{C.3}$$

C.2

(Thomas and Finney [109])

$$\int e^{ax} \sin bx \; dx = \frac{e^{ax}}{a^2 + b^2} (a \sin bx - b \cos bx) + C. \tag{C.4}$$

$$\int e^{ax} \cos bx \, dx = \frac{e^{ax}}{a^2 + b^2} (a \cos bx + b \sin bx) + C. \tag{C.5}$$

C.3

Let I be (Dym and Shames [29])

$$I = \int_a^b F\left(x, y, y'\right). \tag{C.6}$$

Then, the variation of the function I is

$$\delta I = \int_a^b \left(\frac{\partial F}{\partial y} \delta y + \frac{\partial F}{\partial y'} \delta y' \right) dx. \tag{C.7}$$

C.4

(Gitman et al. [39]) Let f be a linear differential operation given by

$$f = f_n(x) \, d^n x + f_{n-1}(x) \, d^{n-1} x + \cdots + f_1(x) \, d^1 x + f_0(x), \tag{C.8}$$

where the functions $f_k(x)$, $k = 0, 1, \cdots, n$, defined on (a, b), are called the coefficient functions of f with $f_n(x) \neq 0$. Also, assume that the function ψ is of class C^n. Let $\phi, \psi, f\psi \in L^2(a, b)$, then,

$$\langle \phi, f\psi \rangle = \int_a^b \bar{\phi} \left(\sum_{k=0}^{n} f_k \psi^{(k)} \right) dx, \tag{C.9}$$

where

$$\psi^{(k)} = d^k x \psi. \tag{C.10}$$

Integrating each term in relationship (C.9) by parts k times and letting the integrated terms vanish at the boundaries, one obtains the following

$$\langle \phi, f\psi \rangle = \langle \breve{f}\phi, \psi \rangle, \tag{C.11}$$

where $\breve{f}$ is called the adjoint differential operation.

C.5

(Gautschi [37]) In Euler backward method, the step is defined as

$$y_{n+1} - y_n = hf\left(x_{n+1}, y_{n+1}\right). \tag{C.12}$$

C.6

```
function [WN,TENERGY]=Energy_amplification

% ------------------------------------------------------------------------
% Setting the parameters.
% The parameters used here are kappa-length scale, Sc-Schmidt number,
% beta-Gyrotaxis number and Ra-Rayleigh number/kappa.
% These parameters are set by the M-files:
% kappa_number
% Schmidt_number
% beta_number
% Ra_number
% To avoid the intensive use of the global command. The parameters values
% are inserted in these files and will be called when they are needed.

global k rd rb Ld Nb N W F FP dNdz dNdz2 NJ WJ FJ FJP dNdzJ dNdzJ2 Tmax alpha0
global dNbdz delt

alpha0=0.2; % Cell eccentricity.
WN=0.1:0.5:10;

kappa=kappa_number;
beta=beta_number;
Ra=Ra_number;
% ------------------------------------------------------------------------
% Setting the domain.
% Setting the initial values in z direction. In the M-file Domain.

 [z,solinit,t]=Domain;
 tend=length(t);
 zend=length(z);
```

```
% ------------------------------------------------------------------------
% (I)- Solving the basic state.
Concentrationbasicstate_New(z,solinit,t);

% ------------------------------------------------------------------------
% (II)- Solving the direct problem.

% ------------------------------------------------------------------------
% Assume the initial perturbation so that they satisfy the boundary
% conditions at each boundary. Also, they are normalized.To normalise the
% initial perturbation, we divide it by its norm
% ||f||=(int_{a}^{b} abs(f(z)*f^{+}(z))dz)^{1/2}, where + means complex
% conjugate.
% This step has been done to make sure that the first condition is satisfied
% in lagrange function. Equation (B2), page:16.
% TN, WN and FN are the norms of the initial perturbations T, W and F
% respectively.
% ------------------------------------------------------------------------
for i=1:length(WN)
    i
    K=WN(i);
    k=K;
NY=(sin(pi*z)).^2;
NYS=NY.^2;      % Square the function.
NYI=trapz(NYS); % Integrate the square using trapasoidal method.
NN=sqrt(NYI);   % Taking the square root wich represents the the norm.

Nin=(1/NN)*NY;  % The initial perturbation of the concentration is normalized.
Win=zeros(1,length(z));
Fin=zeros(1,length(z));


% ************************************************************************
% PS: The initial perturbation of the velocity is assigned to be zero, as
% the conversion between the direct and the adjoint field is not satisfied.
% ************************************************************************

% ------------------------------------------------------------------------
% Solving the homogeneous ODE of f1 and f2 at the beginning as they do
% not depend on the previous time step.
% See the M-files fhomogeneous1_New and fhomogeneous2_New.

f1=fhomogeneous1_New(z,solinit);
```

```
f2=fhomogeneous2_New(z,solinit);

A21=f1(zend);
A22=f2(zend);

% ------------------------------------------------------------------------
% Solving the ODE equations of w1 and w2. These equations do not depend on
% the previous time step.
% See the M-files WH1_New and WH2_New.

[W1,DW1]=WH1_New(z,solinit);
[W2,DW2]=WH2_New(z,solinit);
A11=DW1(1);
A12=DW2(1);
A=[A11 A12; A21 A22];

Tmax=1;
for count=1:10
    count
    N=zeros(length(t),length(z));
    W=zeros(length(t),length(z));
    F=zeros(length(t),length(z));

    N(1,:)=Nin;
    W(1,:)=Win;
    F(1,:)=Fin;

% ------------------------------------------------------------------------
% The particular solution of f.

FP(1,:)=F(1,:);

% ------------------------------------------------------------------------
% Solving the governing equations at every time step. The variable rd here
% is the time step, i.e, each row represents a time step.
% ------------------------------------------------------------------------
Ld=1;
for rd=2:length(t)
    rb=rd;
    % --------------------------------------------------------------------
    % Solving the concentration ODE.
    % See the M-file NNode and NNbc.
    % --------------------------------------------------------------------
    solN=bvp4c(@NNode,@NNbc,solinit);
```

```
    uN=deval(solN,z);
    N(rd,:)=uN(1,:);
    dNdz(rd,:)=uN(2,:);
    dNdz2(rd,:)=kappa*dNdz(rd,:)+((k^2)+(1/delt))*N(rd,:)-...
    (1/delt)*N(rd-1,:)+W(rd-1,:).*dNbdz(rd-1,:)-...
    beta*Nb(rd-1,:).*((1+alpha0)*F(rd-1,:)+2*alpha0*(k^2)*W(rd-1,:));
    Ld=Ld+1;
    % ---------------------------------------------------------------------
    % Solving the fp.
    % See the M-files FPNode and FPNbc.
    % ---------------------------------------------------------------------
    solFP=bvp4c(@FPNode,@FPNbc,solinit);
    uFP=deval(solFP,z);
    FP(rd,:)=uFP(1,:);
    C1=FP(rd,zend);
    % ---------------------------------------------------------------------
    % Solving the equation of wp.
    % See M-files WPNode and WPNbc.
    % ---------------------------------------------------------------------
    solWP=bvp4c(@WPNode,@WPNbc,solinit);
    uWP=deval(solWP,z);
    WPS=uWP(1,:);
    WP(rd,:)=WPS;
    DWP(rd,:)=uWP(2,:);
    B1=-DWP(rd,1);
    B2=-C1;
    B=[B1; B2];
    % ---------------------------------------------------------------------
    % Solving the linear system to find the vallues of lambda and mu that
    % satisfy the boundary conditions.
    % ---------------------------------------------------------------------
    X = linsolve(A,B);
    lambda=X(1);
    mu=X(2);
    W(rd,:)=WP(rd,:)+lambda*W1+mu*W2;
    F(rd,:)=FP(rd,:)+lambda*f1+mu*f2;
end

if (Tmax<=2*10^(-3))
    break
end
% -------------------------------------------------------------------------
% (II)- Adjoint problem.
```

```
% ------------------------------------------------------------------------
% Temperature conversion to the adjoint problem Condition (B11), page:18.
% ------------------------------------------------------------------------
NJ=zeros(length(t),length(z));
WJ=zeros(length(t),length(z));
FJ=zeros(length(t),length(z));

NJ(1,:)=N(tend,:);
dNdzJ(1,:)=dNdz(tend,:);
dNdzJ2(1,:)=dNdz2(tend,:);
WJ(1,:)=0;
FJ(1,:)=0;

% ------------------------------------------------------------------------
% The particular solution of fj.
% ------------------------------------------------------------------------

FJP(1,:)=FJ(1,:);
Ld=1;
for rj=2:length(t)
    % --------------------------------------------------------------------
    % Finding the particular solution of fjp.
    % See M-files FJPNode and FJPNbc.
    % --------------------------------------------------------------------
    solFJP=bvp4c(@FJPNode,@FJPNbc,solinit);
    uFJP=deval(solFJP,z);
    FJP(rj,:)=uFJP(1,:);
    % --------------------------------------------------------------------
    % Finding the particular solution of wj.
    % See M-files WJPNode and WJPNbc.
    % --------------------------------------------------------------------
    solWJP=bvp4c(@WJPNode,@WJPNbc,solinit);
    uWJP=deval(solWJP,z);
    WJP(rj,:)=uWJP(1,:);
    DWJP(rj,:)=uWJP(2,:);
    BJ1=-DWJP(rj,1);
    BJ2=-FJP(rj,zend)+(1+alpha0)*beta*(k^2)*NJ(rj,zend)*Nb(rj,zend);
    BJ=[BJ1; BJ2];
    % --------------------------------------------------------------------
    % Solving the linear system to find the vallues of lambdaj and muj that
    % satisfy the boundary conditions.
    % --------------------------------------------------------------------
    X = linsolve(A,BJ);
    lambdaJ=X(1);
```

```
    muJ=X(2);
    WJ(rj,:)=WJP(rj,:)+lambdaJ*W1+muJ*W2;
    FJ(rj,:)=FJP(rj,:)+lambdaJ*f1+muJ*f2;
    % -------------------------------------------------------------------
    % Solving the adjoint concentration equation.
    % See M-files NJNode and NJNbc.
    % -------------------------------------------------------------------
    solNJ=bvp4c(@NJNode,@NJNbc,solinit);
    uNJ=deval(solNJ,z);
    NJ(rj,:)=uNJ(1,:);
    dNdzJ(rj,:)=uNJ(2,:);
    dNdzJ2(rj,:)=-kappa*dNdzJ(rj,:)+((k^2)+(1/delt))*NJ(rj,:)-...
    (1/delt)*NJ(rj-1,:)+Ra*WJ(rj,:);
    Ld=Ld+1;
end
%
% -------------------------------------------------------------------------
% Testing the convergence by computing the relative error.

TYJ=NJ(tend,:);
TYSJ=TYJ.^2;
TYIJ=trapz(TYSJ);
TNJ=sqrt(TYIJ);
CT=(1/TNJ)*NJ(tend,:);

Tdiff=abs(N(1,:)-CT);

Tmax=max(Tdiff);
Nin=CT;
Win=zeros(1,length(z));
Fin=zeros(1,length(z));
end

TY1=N(tend,:);
    TYS1=TY1.^2;
    TENERGY(i)=trapz(TYS1);
end
```

```
% M-file-setting the gyrotactic number.
function beta=beta_number
beta=0.5;

% M-file-setting the length scale.
function kappa=kappa_number
kappa=1;
```

```
% M-file-setting the Ra number.
function Ra=Ra_number
Ra=500;

% M-file-Setting Schmidt number.
function Sc=Schmidt_number
Sc=20;

% M-file- The use of Schmidt number in the ODEs.

function con=Sc_times_delt
global delt
Sc=Schmidt_number;
if Sc==inf
    con=0;
else
    con=1/(Sc*delt);
end
```

```
% Setting the boundary conditions of the concentration basic state equation.
% The conditions of the concentration basic state equation are:
% kappa*Nb-d/dz(Nb)=0 at both boundaries z=-1,0.
% Since the substitution d/dz(Nb)^(n+1) = NBS(2),
% Nb^(n+1)=NBS(1) was used, the boundary condition are written
% as:
% kappa*NBS(1)-NBS(2) at z=-1,0.
% See the bvp4c M-file.

function NbcBS=BSNbc(NBSa,NBSb)
kappa=kappa_number;
NbcBS=[ kappa*NBSa(1)-NBSa(2)
        kappa*NBSb(1)-NBSb(2)];
```

```
% Setting the basic state ode that gives the values of Nb.
% The basic state equation is given by d/dt(Nb)=d^2/dz^2(Nb)-kappa*d/dz(Nb).
% The above PDE is discretized with respect to time, using Eular backward,
% which results in the following ODE at each time step:
% d^2/dz^2(Nb)^(n+1) = kappa*d/dz(Nb)^(n+1) + (1/delt)*Nb^(n+1) -
% (1/delt)*Nb^(n).
% To solve it using bvp4c solver, the above ODE is rewritten as a system of
% ODEs as follow:
% d/dz(Nb)^(n+1) = NBS(2), Nb^(n+1)=NBS(1).
% d/dz(NBS(2))= kappa*NBS(2)+(1/delt)*NBS(1)-(1/delt)*Nbs(z).
% Where Nbs(z) is the interpolated concentration basic state at the previous
```

```
% time step.
% See the M-file Nbs.

function dNdzbs=BSNode(z,NBS)
global delt
kappa=kappa_number;
dNdzbs=[NBS(2)
        kappa*NBS(2)+(1/delt)*NBS(1)-(1/delt)*Nbs(z)];
```

```
% M-file to plot the 3D-graph of the concentration basic profile N_{b} for
% a value of kappa.
% The parameters here are for the bioconvection due to gyrotactic effect.
% See M-files BSNode and BSNbc.
% ------------------------------------------------------------------------

function Concentrationbasicstate_New(z,solinit,t)
global rb Nb dNbdz dNbdz2 delt
% ------------------------------------------------------------------------
% Solve the basic state Nb. The rows are the time domain t, while the
% colunms are the space z.
Nb(1,:)=ones(1,length(z)); % As we start initially with a uniform suspension.
dNbdz(1,:)=zeros(1,length(z)); %(To be used in solving the governing equations)
dNbdz2(1,:)=zeros(1,length(z)); %(To be used in solving the governing equations)

% ------------------------------------------------------------------------
% Solving the ODE for every time step.
kappa=kappa_number;
for rb=2:length(t)
    sol0=bvp4c(@BSNode,@BSNbc,solinit);
    BSN=deval(sol0,z);
    Nb(rb,:)=BSN(1,:);
    dNbdz(rb,:)=BSN(2,:);
    dNbdz2(rb,:)=kappa*dNbdz(rb,:)+(1/delt)*Nb(rb,:)-(1/delt)*Nb(rb-1,:);
end

% ------------------------------------------------------------------------
% 3D-plot of thet basic state profile.

% figure
% [T,Z]=meshgrid(z,t);
% surf(T,Z,Nb);
% set(gca,'FontSize',30,'FontName','Times New Roman');
% xlabel('Depth z^{*}','fontsize',30,'FontName','Times New Roman');
% ylabel('Time t^{*}','fontsize',30,'FontName','Times New Roman');
% % zlim([0.99 1.01])
```

```
% zlabel('N_{bs}','fontsize',30,'FontName','Times New Roman');
%
% figure
% [T,Z]=meshgrid(z,t);
% surf(T,Z,dNbdz);
% set(gca,'FontSize',30,'FontName','Times New Roman');
% xlabel('Depth z^{*}','fontsize',30,'FontName','Times New Roman');
% ylabel('Time t^{*}','fontsize',30,'FontName','Times New Roman');
% % zlim([0.99 1.01])
% zlabel('N_{bs} 1st derivative','fontsize',30,'FontName','Times New Roman');
%
% figure
% [T,Z]=meshgrid(z,t);
% surf(T,Z,dNbdz2);
% set(gca,'FontSize',30,'FontName','Times New Roman');
% xlabel('Depth z^{*}','fontsize',30,'FontName','Times New Roman');
% ylabel('Time t^{*}','fontsize',30,'FontName','Times New Roman');
% % zlim([0.99 1.01])
% zlabel('N_{bs} 2st derivative','fontsize',30,'FontName','Times New Roman');
```

```
% Interpolating the function dNbdz2 in order to be used in setting the ODE
% of N.
% ------------------------------------------------------------------------
function value=dNbdz2I(zz)
z=Domain;
global dNbdz2 Ld
BS=dNbdz2(Ld,:);
value=interp1(z,BS,zz);
```

```
% Interpolating the function dNbdz in order to be used in setting the ODE
% of N.
% ------------------------------------------------------------------------
function value=dNbdzI(zz)
z=Domain;
global dNbdz Ld
BS=dNbdz(Ld,:);
value=interp1(z,BS,zz);
```

```
% Interpolating the function dNdzJ2 in order to be used in setting the ODE
% of N.
% ------------------------------------------------------------------------
function value=dNdzJ2I(zz)
z=Domain;
global dNdzJ2 Ld
BS=dNdzJ2(Ld,:);
```

```
value=interp1(z,BS,zz);
```

```
% Interpolating the function dNdzJ in order to be used in setting the ODE
% of N.
% ------------------------------------------------------------------------
function value=dNdzJI(zz)
z=Domain;
global dNdzJ Ld
BS=dNdzJ(Ld,:);
value=interp1(z,BS,zz);
```

```
% M-file-setting the time and space domain.
% Also, setting the initial guesse in the z direction.

function [z,solinit,t]=Domain

global delt
t0=0; t1=0.05; npt=101;
z0=-1; z1=0; npz=101;
z=linspace(z0,z1,npz);
t=linspace(t0,t1,npt);
delt= (t1-t0)/(npt-1);

solinit=bvpinit(linspace(z0,z1,npz),[1 0]);
```

```
% Interpolating the function f1 in order to be used in setting the ODE
% of w1.
% See the M-file W1Node.
% ------------------------------------------------------------------------


function value=FH1I(zz)
[z,solinit]=Domain;
f1=fhomogeneous1_New(z,solinit);
BS=f1(1,:);
value=interp1(z,BS,zz);
```

```
% Setting the boundary conditions for the function f1.
% The boundary conditions of f1 are:
% f1 = 1, at z=0,-1. So, when considering f1=FHV(1), the boundary
% conditions can be written as;
% FHVa(1)-1 = 0 at z = -1, the solid boundary.
% FHVb(1)-1 = 0 at z = 0, the free boundary.
% ------------------------------------------------------------------------
```

```
function fh1c=Fh1Nbc(FHVa,FHVb)

fh1c=[ FHVa(1)-1
         FHVb(1)-1];
```

```
% Interpolating the function f2 in order to be used in setting the ODE
% of w2.
% See the M-file W2Node.
% ------------------------------------------------------------------------
function value=FH2I(zz)
[z,solinit]=Domain;
f2=fhomogeneous2_New(z,solinit);
BS=f2(1,:);
value=interp1(z,BS,zz);
```

```
% Setting the boundary conditions for the function f2.
% The boundary conditions of f2 are:
% f2 = -1, at z=-1 and f2 = 1, at z=0. So, when considering f2=FHV(1),
% the boundary conditions can be written as;
% FHVa(1)+1 = 0 at z = -1, the solid boundary.
% FHVb(1)-1 = 0 at z = 0, the free boundary.
% ------------------------------------------------------------------------.

function fh2c=Fh2Nbc(FHVa,FHVb)

fh2c=[ FHVa(1)+1
         FHVb(1)-1];
```

```
% Setting the f homogeneous ode that gives the values of either f1 or f2.
% FHV stands for FH variable.
% The ODE is given by
% [d^2/dz^2 - k^2 -(1/Sc*delt)]f1/2 = 0.
% Take d/dz(f1 or f2)=FHV(2) and f1 or f2=FHV(1).
% The ODE can be witten as;
% d/dz[FHV(2)] = [k^2 + con] FHV(1),
% where con=1/(Sc*delt).
% ------------------------------------------------------------------------

function dFHdz=FhNode(z,FHV)
global k
con=Sc_times_delt;
dFHdz=[FHV(2)
     ((k^2)+con)*FHV(1)];
```

```
% M-file to find the 1st homogeneous solution f1 of the following ODE
% [d^2/dz^2 - k^2 -(1/Sc*delt)]f1 = 0, with the boundary conditions defined as
% f1 = 1, at z=0,-1.
% See the M-files Fhode and Fh1bc.
% ------------------------------------------------------------------------

function f1=fhomogeneous1_New(z,solinit)

solfh1=bvp4c(@FhNode,@Fh1Nbc,solinit);
uE=deval(solfh1,z);
f1(1,:)=uE(1,:);
```

```
% M-file to find the 2nd homogeneous solution f2 of the following ODE
% [d^2/dz^2 - k^2 -(1/Sc*delt)]f2 = 0, with the boundary conditions defined as
% f2 = -1, at z=-1 , the solid boundary.
% f2 = 1, at z=0 , the free boundary.
% See the M-files Fhode and Fh2bc.
% ------------------------------------------------------------------------
function f2=fhomogeneous2_New(z,solinit)

solfh2=bvp4c(@FhNode,@Fh2Nbc,solinit);
uE=deval(solfh2,z);
f2(1,:)=uE(1,:);
```

```
% Interpolating the function F in order to be used in setting the ODE
% of N.
% See the M-file NNode.
% ------------------------------------------------------------------------

function value=FI(zz)
z=Domain;
global F rd
L=rd-1;
BS=F(L,:);
value=interp1(z,BS,zz);
```

```
function value=FJI(zz)
z=Domain;
global FJ Ld
BS=FJ(Ld,:);
value=interp1(z,BS,zz);
```

```
% Interpolating the function fjp in order to be used in setting the ODE
% of fjp.
```

```
% See the M-file FJPode.
% ------------------------------------------------------------------------
function value=FJPI(zz)
z=Domain;
global FJP Ld
I=Ld+1;
BS=FJP(I,:);
value=interp1(z,BS,zz);
```

```
% Setting the boundary conditions of fjp.
% These conditions are:
% fjp = 0, at z=0,-1.
% Consider fjp = FJPV(1). Then, the boundary conditions are
% FJPVa(1) = 0 at z=-1.
% FJPVb(1) = 0 at z=0.
% ------------------------------------------------------------------------

function FJpc=FJPNbc(FJPVa,FJPVb)

FJpc=[ FJPVa(1)
        FJPVb(1)];
```

```
% Setting the fj particular ODE that gives the values of fjp.
% FJPV stands for FJ variable, FJI is fj interpolated and NJI is NJ
% interpolation.
% The particular fj equation is
% [d^2/dz^2 - k^2 - 1/Sc*delt] fjp^(n+1) = - (1/Sc*delt)*fjp^(n) +
% +NJI(z)*((k^4)*(alpha0-1)*beta*NbsI(z)-(k^2)*dNbdzI(z))+...
% (k^2)*(alpha0+1)*beta*(dNbdz2I(z)*NJI(z)+2*dNbdzI(z)*dNdzJI(z)+...
% NbsI(z)*dNdzJ2I(z)).
% Take d/dz(fjp) = FJPV(2), fjp = FJPV(1).
% The above equation can be written as:
% d/dz(FJPV(2))= ((k^2)+con)*FJPV(1)-con*FJI(z)+NJI(z)*((k^4)*(alpha0-1)*beta*NbsI(z)...
% -(k^2)*dNbdzI(z))+(k^2)*(alpha0+1)*beta*(dNbdz2I(z)*NJI(z)+2*dNbdzI(z)*dNdzJI(z)+...
% NbsI(z)*dNdzJ2I(z)),
% where con=1/Sc*delt.
% ------------------------------------------------------------------------

function dFJpdz=FJPNode(z,FJPV)
global k alpha0
con=Sc_times_delt;
beta=beta_number;
dFJpdz=[FJPV(2)
     ((k^2)+con)*FJPV(1)-con*FJI(z)+NJI(z)*((k^4)*(alpha0-1)*beta*NbsI(z)-...
     (k^2)*dNbdzI(z))+(k^2)*(alpha0+1)*beta*(dNbdz2I(z)*NJI(z)+...
```

```
     2*dNbdzI(z)*dNdzJI(z)+NbsI(z)*dNdzJ2I(z))];
```

```
% Interpolating the function fP in order to be used in setting the ODE
% of wp.
% See the M-file WPNode.
% ------------------------------------------------------------------------

function value=FPI(zz)
z=Domain;
global FP rd
BS=FP(rd,:);
value=interp1(z,BS,zz);
```

```
% Setting the boundary conditions of fp.
% These conditions are:
% fp = 0, at z=0,-1.
% Consider fp = FPV(1). Then, the boundary conditions are
% FPVa(1) = 0 at z=0.
% FPVb(1) = 0 at z=-1.
% ------------------------------------------------------------------------

function Fpc=FPNbc(FPVa,FPVb)

Fpc=[ FPVa(1)
        FPVb(1)];
```

```
% Setting the f particular ODE that gives the values of fp.
% FPV stands for F variable, FI is f interpolation and NI is N
% interpolation.
% The particular f equation is
% [d^2/dz^2 - k^2 - 1/Sc*delt] fp^(n+1) = - (1/Sc*delt)*f^(n) -
% Ra*k^2*N^(n+1).
% Take d/dz(fp) = FPV(2), fp = FPV(1).
% The above equation can be written as:
% d/dz(FPV(2))= (k^2 + con)*FPV(1)-con*FI(z)-Ra*(k^2)*NI(z),
% where con=1/Sc*delt.
% See the M-files NI and FI.
% ------------------------------------------------------------------------

function dFpdz=FPNode(z,FPV)
global k
con=Sc_times_delt;
Ra=Ra_number;
dFpdz=[FPV(2)
     ((k^2)+con)*FPV(1)-con*FI(z)-Ra*(k^2)*NI(z)];
```

```
% Interpolating the concentration basic state linearly Nb, at every time step
% using the interp1.m.
% This M-file is needed to set the concentration basic state ODE M_file.
% See the M_file BSNode.

function value=Nbs(zz)
z=Domain;
global rb Nb
L=rb-1;
BS=Nb(L,:);
value=interp1(z,BS,zz);
```

```
% Interpolating the concentration basic state linearly Nb, at every time step
% using the interp1.m.
% See the M_file NNode.

function value=NbsI(zz)
z=Domain;
global Ld Nb
BS=Nb(Ld,:);
value=interp1(z,BS,zz);
```

```
% Interpolating the function N in order to be used in setting the ODE
% of N and Fp.
% See the M-file NNode.
% ------------------------------------------------------------------------

function value=NI(zz)
z=Domain;
global N Ld
BS=N(Ld,:);
value=interp1(z,BS,zz);
```

```
% Interpolating the function NJ in order to be used in setting the ODE
% of fjp and NJ.
% ------------------------------------------------------------------------

function value=NJI(zz)
z=Domain;
global NJ Ld
BS=NJ(Ld,:);
value=interp1(z,BS,zz);
```

```
% Setting the boundary conditions for the function NJ.
```

```
function NJc=NJNbc(NJVa,NJVb)
NJc=[NJVa(2)
     NJVb(2)];
```

```
% Setting the concentration ode that gives the values of NJ.
% NJV stands for NJ variable, NJI stands for NJ intrpolated and WJI is WJ
% interpolated.
% The adjoint equation of the temperature profile is
% [d^2/dz^2 -kappa*d/dz - k^2 - 1/delt] nj^(n+1) = - (1/delt)nj^(n) -
% Ra*wj^(n+1).
% Take d/dz(nj) = NJV(2), nj = NJV(1), the above equation is
% written as:
% d/dz(NJV(2)) = kappa*NJV(2)+((k^2)+(1/delt))*NJV(1)-(1/delt)*NJI(z)+Ra*WJI(z).
% See M-files NJI and WJI.
% ------------------------------------------------------------------------

function dNJdz=NJNode(z,NJV)
global delt k
Ra=Ra_number;
kappa=kappa_number;
dNJdz=[NJV(2)
     -kappa*NJV(2)+((k^2)+(1/delt))*NJV(1)-(1/delt)*NJI(z)+Ra*WJI(z)];
```

```
% Setting the boundary conditions for the function N.
% The boundary conditions of N are:
% -d/dz (N) + kappa*N= 0, at z=0,-1..
% So, when considering N=NV(1) and d/dz(N)=NV(2) the boundary
% conditions can be written as;
% -NVb(2)+kappa*NVb(1)= 0 at z = -1,0.
% ------------------------------------------------------------------------

function Nc=NNbc(NVa,NVb)
kappa=kappa_number;
Nc=[ -NVa(2)+kappa*NVa(1)
     -NVb(2)+kappa*NVb(1)];
```

```
% Setting the concentration ode that gives the values of N.
% NV stands for N variable, NI stands for N intrpolated, WI is W
% interpolated and dNbdzI the interpolation of the 1st derivative of the
% basic concentration prfile w.r.t z.
% The temperature ODE is given by:
% [ d^2/dz^2 - kappa*d/dz - k^2 - 1/delt](N^(n+1)) = - (1/delt)(N^(n))
% + W^(n)*(d/dz)[NBS^(n)] + beta*NBS^(n)*[(1+alpha_{0})*F^(n) + 2*alpha_{0}*k^2*W^(n)].
% Consider d/dz(N^(n+1))=NV(2) and N^(n+1)=NV(1), the above
```

```
% equation is written as:
% d/dz[NV(2)] = kappa*NV(2)+ (k^2 + (1/delt))*NV(1) - (1/delt)*NI(z)+WI(z)*dNbdzI(z)
% - beta*NbsI^(n)*[(1+alpha_{0})*FI^(n) + 2*alpha_{0}*k^2*WI^(n)] .
% See the M-files NI, WI, FI, NbsI and dNbdzI.
% ------------------------------------------------------------------------

function dNdz=NNode(z,NV)
global delt k alpha0
kappa=kappa_number;
beta=beta_number;
dNdz=[NV(2)
     kappa*NV(2)+((k^2)+(1/delt))*NV(1)-(1/delt)*NI(z)+WI(z)*dNbdzI(z)-...
     beta*NbsI(z)*((1+alpha0)*FI(z)+2*alpha0*(k^2)*WI(z))];
```

```
% Setting the boundary conditions for the function w1.
% The boundary conditions of w1 are:
% w1 = 0, at z=0,-1. So, when considering w1=W1V(1), the boundary
% conditions can be written as;
% W1Va(1) = 0 at z = -1, the solid boundary.
% W1Vb(1) = 0 at z = 0, the free boundary.
% ------------------------------------------------------------------------

function WH1bc=W1Nbc(W1Va,W1Vb)
WH1bc=[ W1Va(1)
        W1Vb(1)];
```

```
% Setting the w1 ode that gives the values of w1.
% W1V stands for w1 variable and FH1I stands for interpolated f1.
% The ODE is given by
% [d^2/dz^2 - k^2]w1 = f1.
% Take d/dz(w1)=W1V(2) and w1=W1V(1).
% The ODE can be witten as;
% d/dz[W1V(2)] = (k^2)*W1V(1) + FH1I(z),
% See  FH1I M-files.
% ------------------------------------------------------------------------

function dW1dz=W1Node(z,W1V)
global  k
dW1dz=[W1V(2)
     (k^2)*W1V(1)+FH1I(z)];
```

```
% Setting the boundary conditions for the function w2.
% The boundary conditions of w2 are:
% w2 = 0, at z=0,-1. So, when considering w2=W2V(1), the boundary
% conditions can be written as;
```

```
% W2Va(1) = 0 at z = -1, the solid boundary.
% W2Vb(1) = 0 at z = 0, the free boundary.
% --------------------------------------------------------------------
function WH2bc=W2Nbc(W2Va,W2Vb)
WH2bc=[ W2Va(1)
        W2Vb(1)];
```

```
% Setting the w1 ode that gives the values of w2.
% W1V stands for w2 variable and FH2I stands for interpolated f2.
% The ODE is given by
% [d^2/dz^2 - k^2]w2 = f2.
% Take d/dz(w2)=W2V(2) and w2=W2V(1).
% The ODE can be witten as;
% d/dz[W2V(2)] = (k^2)*W2V(1) + FH2I(z),
% See FH2I M-files.
% --------------------------------------------------------------------
function dW2dz=W2Node(z,W2V)
global  k
dW2dz=[W2V(2)
     (k^2)*W2V(1)+FH2I(z)];
```

```
% M-file to find the solution w1 of the following ODE
% [d^2/dz^2 - k^2]w1 = f1, with the boundary conditions defined as
% w1 = 0, at z=0,-1.
% See the M-files W1Node and W1Nbc.
% --------------------------------------------------------------------

function [W1,DW1]=WH1_New(z,solinit)

solW1=bvp4c(@W1Node,@W1Nbc,solinit);
uWH1=deval(solW1,z);
W1(1,:)=uWH1(1,:);
DW1(1,:)=uWH1(2,:);
```

```
% M-file to find the solution w2 of the following ODE
% [d^2/dz^2 - k^2]w2 = f2, with the boundary conditions defined as
% w2 = 0, at z=0,-1.
% See the M-files W2Node and W2Nbc.
% --------------------------------------------------------------------

function [W2,DW2]=WH2_New(z,solinit)

solW2=bvp4c(@W2Node,@W2Nbc,solinit);
uWH2=deval(solW2,z);
W2(1,:)=uWH2(1,:);
```

```
DW2(1,:)=uWH2(2,:);
```

```
% Interpolating the function W in order to be used in setting the ODE
% of N.
% See the M-file NNode.
% ------------------------------------------------------------------------

function value=WI(zz)
z=Domain;
global W Ld
BS=W(Ld,:);
value=interp1(z,BS,zz);
```

```
% Interpolating the function WJ in order to be used in setting the ODE
% of NJ.
% See the M-file NJNode.
% ------------------------------------------------------------------------

function value=WJI(zz)
global WJ Ld
z=Domain;
F=Ld+1;
BS=WJ(F,:);
value=interp1(z,BS,zz);
```

```
% Setting the boundary conditions for the function wjp.
% The boundary conditions of wjp are:
% wjp = 0, at z=0,-1. So, when considering wjp=WJPV(1), the boundary
% conditions can be written as;
% WJPVa(1) = 0 at z = -1, the solid boundary.
% WJPVb(1) = 0 at z = 0, the free boundary.
% ------------------------------------------------------------------------

function WHJPbc=WJPNbc(WJPVa,WJPVb)
WHJPbc=[ WJPVa(1)
        WJPVb(1)];
```

```
% Setting the wj particular ODE that gives the values of wjp.
% WJPV stands for wj variable and FJPI is fjp interpolation.
% The particular wj equation is
% [d^2/dz^2 - k^2] wjp^(n+1) = fjp^(n+1).
% Take d/dz(wjp) = WJPV(2), wjp = WJPV(1).
% The above equation can be written as:
% d/dz(WJPV(2)) = (k^2)*WJPV(1)+FJPI(z).
% See the M-file FJPI.
```

```
% ------------------------------------------------------------------------

function dWJPdz=WJPNode(z,WJPV)
global  k
dWJPdz=[WJPV(2)
     (k^2)*WJPV(1)+FJPI(z)];
```

```
% Setting the boundary conditions for the function wp.
% The boundary conditions of wp are:
% wp = 0, at z=0,-1. So, when considering wp=WPV(1), the boundary
% conditions can be written as;
% WPVa(1) = 0 at z = -1, the solid boundary.
% WPVb(1) = 0 at z = 0, the free boundary.
% ------------------------------------------------------------------------

function WHPbc=WPNbc(WPVa,WPVb)
WHPbc=[ WPVa(1)
        WPVb(1)];
```

```
% Setting the w particular ODE that gives the values of wp.
% WPV stands for w variable and FPI is fP interpolation.
% The particular w equation is
% [d^2/dz^2 - k^2] wp^(n+1) = fP^(n+1).
% Take d/dz(wp) = WPV(2), wp = WPV(1).
% The above equation can be written as:
% d/dz(WPV(2)) = (k^2)*WPV(1)+FPI(z).
% See the M-file ETAPI.
% ------------------------------------------------------------------------

function dWPdz=WPNode(z,WPV)
global  k
dWPdz=[WPV(2)
     (k^2)*WPV(1)+FPI(z)];
```

```
clear all; close all;


load('beta002.mat')
load('beta004.mat')
load('beta006.mat')
load('beta008.mat')
load('beta01.mat')
load('beta012.mat')
load('beta014.mat')
load('beta016.mat')
```

```
load('beta018.mat')

[M1,I1]=imax(beta002);
[M2,I2]=imax(beta004);
[M3,I3]=imax(beta006);
[M4,I4]=imax(beta008);
[M5,I5]=imax(beta01);
[M6,I6]=imax(beta012);
[M7,I7]=imax(beta014);
[M8,I8]=imax(beta016);
[M9,I9]=imax(beta018);



k(1)=((I1-1)/5)+0.1;
k(2)=((I2-1)/5)+0.1;
k(3)=((I3-1)/5)+0.1;
k(4)=((I4-1)/5)+0.1;
k(5)=((I5-1)/5)+0.1;
k(6)=((I6-1)/5)+0.1;
k(7)=((I7-1)/5)+0.1;
k(8)=((I8-1)/5)+0.1;
k(9)=((I9-1)/5)+0.1;

beta=[0.2; 0.4; 0.6; 0.8; 1; 1.2; 1.4; 1.6; 1.8];

figure
plot(WN,log(beta002),'--','LineWidth',5,'color','k');
hold on
plot(WN,log(beta004),'-.','LineWidth',5,'color','k');
hold on
plot(WN,log(beta006),':','LineWidth',5,'color','k');
hold on
plot(WN,log(beta008),'LineWidth',5,'color','k');
set(gca,'FontSize',34,'FontName','Times New Roman')
xlabel('Wavenumbers k','FontSize',34)
ylabel('log(GE)','FontSize',34)
legend('G=0.2','G=0.4','G=0.6','G=0.8')

figure
plot(WN,log(beta01),'--','LineWidth',5,'color','k');
hold on
plot(WN,log(beta012),'-.','LineWidth',5,'color','k');
hold on
plot(WN,log(beta014),':','LineWidth',5,'color','k');
```

```
hold on
plot(WN,log(beta016),'--','LineWidth',5,'color','k');
hold on
plot(WN,log(beta018),'LineWidth',5,'color','k');
set(gca,'FontSize',34,'FontName','Times New Roman')
xlabel('Wavenumbers k','FontSize',34)
ylabel('log(GE)','FontSize',34)
legend('G=1','G=1.2','G=1.4','G=1.6','G=1.8')

figure
scatter(beta,k,'LineWidth',6);
set(gca,'FontSize',34,'FontName','Times New Roman')
xlabel('The gyrotactic number G','FontSize',34)
ylabel('Wavenumbers k')
```

Bibliography

[1] Addison, P. S. *The Illustrated Wavelet Transform Handbook: Introductory Theory And Applications In Science, Engineering, Medicine and Finance*, 1 ed. IOP Publishing Ltd., 2002.

[2] Addison, P. S. Wavelet transforms and the ECG: a review. *Physiol. Meas. 26* (2005), R155–R199.

[3] Antoine, J. .-P., Murenzi, R., Vandergheynst, P., and Ali, S. T. *Two-Dimensional Wavelets And Their Relatives*, 1 ed. Cambridge University Press, 2004.

[4] Arfken, G. B., Weber, H. J., and Harris, F. E. *Mathematical Methods For Physicists*, 7 ed. Elsevier Inc., 2013.

[5] Arnold, K. E., and Murray, S. N. Relationships between irradiance and photosynthesis for marine benthic green algae *Chlorophyta* of differing morphologies. *J. Exp. Mar. Biol. Ecol. 43* (1980), 183–192.

[6] Articolo, G. A. *Partial Differential Equations And Boundary Value Problems With Maple*, 2 ed. Elsevier Inc., 2009.

[7] Bahouri, H., Chemin, J.-Y., and Danchin, R. *Fourier Analysis And Nonlinear Partial Differential Equations*, 1 ed. Springer−Verlag Berlin Heidelberg, 2011.

[8] Barclay, V. J., Bonner, R. F., and Hamilton, I. P. Application of wavelet transforms to experimental spectra: smoothing, denoising, and data set compression. *Anal. Chem. 69* (1997), 78–90.

[9] Bary, D. *Cell Movements: From Molecules To Motility*, 2 ed. Garland Science, 2000.

[10] Batchelor, G. K. The stress system in a suspension of force−free particles. *J. Fluid Mech. 41*, 3 (1970), 545–570.

[11] Bees, M. A., and Hill, N. A. Wavelength of bioconvection patterns. *J. Exp. Biol. 200* (1997), 1515–1526.

[12] Bees, M. A., and Hill, N. A. Linear bioconvection in suspension of randomly swimming, gyrotactic micro−organisms. *Phys. Fluids 10*, 8 (1998), 1864–1881.

[13] Bees, M. A., and Hill, N. A. Non−linear bioconvection in a deep suspension of gyrotactic swimming micro−organisms. *J. Math. Biol. 38* (1999), 135–168.

[14] Bees, M. A., Hill, N. A., and Pedley, T. J. Analytical approximation for the orientation of small dipolar particales in steady shear flows. *J. Math. Biol. 36* (1998), 269–298.

[15] Berg, H. C., and Anderson, R. A. Bacteria swim by rotating their flagellar filaments. *Nature 245* (1973), 380–382.

[16] Berg, H. C., and Brown, D. A. Chemotaxis in *Escherichia coli* analysed by three−dimensional tracking. *Nature 239* (1972), 500–504.

[17] Berg, P. W., and McGregor, J. L. *Elementary Partial Differential Equations*, 1 ed. Holden−Day, Inc., 1966.

[18] Boggess, A., and Narcowich, F. J. *A First Course In Wavelets With Fourier Analysis*, 2 ed. Jhon Wiley and Sons, INC., 2009.

[19] Brenner, H. Suspension rheology. *Prog. Heat Mass Transfer 5* (1972), 89–129.

[20] Childress, S., Levandowsky, M., and Spiegel, E. A. Pattern formation in a suspension of swimming micro−organisms. *J. Fluid Mech. 63*, 3 (1975), 591–613.

[21] Chui, C. K. *An Introduction To Wavelets, Volume 1 Of Wavelet Analysis And Applications*, 1 ed. Academic Press,Inc, 1992.

[22] Clonda, D., Lina, J. .-M., and Goulard, B. Complex Daubechies wavelets: properties and statistical image modelling. *Signal Processing 84* (2004), 1–23.

[23] Compant, S., Clément, C., and Sessitsch, A. Plant growth−promoting bacteria in the rhizo− and endosphere of plants: Their role, colonization, mechanisms involved and prospects for utilization. *Soil Biol. and Biochem. 42* (2010), 669–678.

[24] Croze, A. O., Ashraf, E. E., and Bees, M. A. Sheard bioconvectio in a horizontal tube. *Phys. Biol. 7* (2010), 1–12.

[25] Czirók, A., Jánosi, I. M., and Kessler, J. O. Bioconvection dynamics: dependence on organism behaviour. *J. Exp. Biol. 203* (2000), 3345–3354.

[26] Daubechies, I. Orthonormal bases of compactly supported wavelets. *Communications on Pure and Applied Mathematics XLI* (1988), 909–996.

[27] Doumenc, F., Boeck, T., Guerrier, B., and Rossi, M. Transient Rayleigh−Bénard−Marangoni convection due to evaporation: a linear non−normal stability analysis. *J. Fluid Mech. 648* (2010), 521–539.

[28] Drautz, H., Baumgartner, A., and Zähner, H. Metabolic products of microorganisms. 224 bafilomycins, a new group of microlide antibiotics production, isolation, chemical structure and biological activity. *The Journal of Antibiotics XXXVII*, 2, 110–117.

[29] Dym, C. L., and Shames, I. H. *Solid Mechanics A Variational Approach*, 1 ed. Springer, 2013.

[30] Eleanor, L. *Henderson's Dictionary Of Biology.* Pearson Education Limitid, 2011.

[31] Falkowski, P. G., Katz, M. E., Knoll, A. H., Quigg, A., Raven, J. A., Schofield, O., and Taylor, F. J. R. The evolution of modern eukaryotic phytoplankton. *Science 305* (2004), 354–360.

[32] Farge, M., Kevlahan, N., Perrier, V., and Éric Goirand. Wavelets and turbulence. *IEEE 84*, 4 (1996), 639–669.

[33] Finlay, B. J., Maberly, S. C., and Cooper, J. I. Microbial diversity and ecosystem function. *Oikos 80* (1997), 209–213.

[34] Foster, K. W., Saranak, J., Patel, N., Zarilli, G., Okabe, M., Kline, T., and Nakanishi, K. A rhodopsin is the functional photoreceptor for phototaxis in the unicellular eukaryote *Chlamydomonas*. *Nature 311* (1984), 756–759.

[35] Fuhrman, J. A. Marine viruses and their biogeochemical and ecological effects. *Nature 399* (1999), 541–548.

[36] Gao, R. X., and Yan, R. *Wavelets: Theory And Applications For Manufacturing*, 1 ed. Springer Science and Business Media, 2011.

[37] Gautschi, W. *Numerical Analysis*, 2 ed. Springer, 2012.

[38] Ghorai, S., Singh, R., and Hill, N. A. Wavelength selection in gyrotactic bioconvection. *Bull. Math. Biol. 77* (2015), 1166–1184.

[39] Gitman, D., Tyutin, I., and Voronov, B. *Self−Adjoint Extensions In Quantum Mechanics General Theory And Applications To Schröodinger And Dirac Equations With Singular Potentials*, 1 ed. Springer, 2012.

[40] Gnansounou, E., and Roman, J. K. Life cycle assessment of algae biodiesel and its co−products. *Applied Energy 161* (2016), 300–308.

[41] Gradshtteyn, I. S., and Ryzhik, I. M. *Table Of Integrals, Series And Products*, english edn, ed. a. jeffery ed. Academic, 1980.

[42] Graps, A. An introduction to wavelets. *IEEE 2*, 2 (1995), 1–18.

[43] Guana, S., Laia, C.-H., and Wei, G. A wavelet method for the characterization of spatiotemporal patterns. *Physics D 163* (2002), 49–79.

[44] Guasto, J., Jhonson, K. A., and Gollub, J. O. Measuring oscillatory velocity fields due to swimming algae. *Physics of Fluids 23* (2011), 1.

[45] Haar, A. Zur theorie der orthogonalen funktionensysteme. *Mathematische Annalen 71* (1911), 38–53.

[46] Häder, D.-P., Rosum, A., Schäfer, J., and Hemmersbach, R. Gravitaxis in the flagellate *Euglena gracilis* is controlled by an active gravireceptor. *J. Plant Physiol. 146* (1995), 474–480.

[47] He, W., Miaob, Q., Azariana, M., and Pechta, M. Health monitoring of cooling fan bearings based on wavelet filter. *Mechanical Systems and Signal Processing 64–65* (2015), 149–161.

[48] Hill, N. A., and Bees, M. A. Taylor dispersion of gyrotactic swimming micro-organisms in a linear flow. *Physics of Fluids 14*, 8 (1998), 2598–2605.

[49] Hill, N. A., and Häder, D. .-P. A biased random walk model for the trajectories of swimming microorganisms. *J. Theor. Biol. 186* (1997), 503–526.

[50] Hill, N. A., Pedley, T. J., and Kessler, J. O. Growth of bioconvection patterns in a suspension of gyrotactic micro−organisms in a layer of finite depth. *J. Fluid Mech. 208* (1989), 509–543.

[51] Hinch, E. J., and Leal, L. G. The effect of Brownian motion on the rheological properties of s suspension of non−spherical particles. *J. Fluid Mech. 52* (1972), 683–712.

[52] Hinch, E. J., and Leal, L. G. Note on the rheology of a dilute suspension of dipolar sheres with weak Brownian couples. *J. Fluid Mech. 56*, 4 (1972), 803–813.

[53] Hong, C. S., Shitashiro, M., Kuroda, A., Ikeda, T., Takiguchi, N., Ohtake, H., and Kato, J. Chemotaxis proteins and transducers for aerotaxis in *Pseudiminas aeruginosa. FEMS Microbiol. lett. 231* (2004), 247–252.

[54] Horan, N. J. *Biological Wastewater Treatment Systems*, 1 ed. John Wiley & Sons Ltd., 1990.

[55] Huang, S. .-J., and Hsien, C. .-T. Application of continuous wavelet transform for study of voltage flicker−generated signals. *IEEE 36*, 3 (2000), 925–932.

[56] Jaffard, S., Meyer, Y., and Ryan, R. D. *Wavelets: Tools For Science And Technology*, 1 ed. SIAM, 2001.

[57] James, J. F. *A Students Guid To Fourier Transforms With Applications In Physics And Engineering*, 3 ed. Cambridge University Press, 2011.

[58] Jeffery, G. B. The motion of ellipsoidal particles immersed in a viscous fluid. *Proceedings of Royal Society of London A* (1922), 161–179.

[59] Jékely, G., Colombelli, J., Hausen, H., Guy, K., Stelzer, E., Nédélec, F., and Arendt, D. Mechanism of phototaxis in marine zooplankton. *Nature 456* (2008), 395–399.

[60] Jeong, G.-T., and Park, D.-H. Optimization of lipid extraction from marine green macro−algae as biofuel resources. *Korean J. Chem. Eng. 32*, 12, 2463–2467.

[61] Karimi, A., and Paul, M. R. Bioconvection in spatially extended domain. *Phys. Rev. E 87:053016* (2013).

[62] Kessler, J. O. Hydrodynamic focusing of motile algal cells. *Nature 313* (1985), 218–220.

[63] Kessler, J. O. The external dynamics of swimming micro−organisms. *Progress in Phycological Res. 4* (1986), 257–307.

[64] Kessler, J. O. The external dynamics of swimming microorganisms. *Progress in Phycological Res. 4* (1986), 257–307.

[65] Kessler, J. O., and Hill, N. A. Complementary of physics, biology and geometry in the dynamics of swimming micro−organisms. *Springer− Verlag Berlin Heidelberg 480* (1997), 325–340.

[66] Koch, D. L., and Subramanian, G. Collective hydrodynamics of swimming microorganisms: Living fluids. *Annu. Rev. Fluid Mech. 43* (2011), 637–659.

[67] Kundra, V., Escobedo, J. A., Kazlauskas, A., Kim, H. K., Rhee, S. G., Williams, L. T., and Zetter, B. R. Regulation of chemotaxis by the platelet−derived growth factor receptor− β. *Nature 367* (1994), 474–476.

[68] Kundu, P. K., and Dowling, I. M. C. D. R. *Fluid Mechanics*, 5 ed. Elsevier, 2012.

[69] Lauga, E. Bacterial hydrodynamics. *Annu. Rev. Fluid Mech. 48* (2016), 105–130.

[70] Lauga, E., and Powers, T. R. The hydrodynamics of swimming microorganisms. *Rep. Prog. Phys. 72* (2009), 1–36.

[71] Lavandowsky, M., Childress, W. S., Spiegel, E. A., and Hutner, S. H. A mathematical model of pattern formation by swimming microorganisms. *J. Protozool. 22*, 2, 296–306.

[72] Leal, L. G., and Hinch, E. J. The rheology of a suspension of nearly spherical particles subject to Brownian rotations. *J. Fluid Mech. 44*, 4 (1972), 745–765.

[73] Lebert, M., Porst, M., Richter, P., and Häder, D.-P. Physical characterization of gravitaxis in *Euglena gracilis*. *J. Plant Physiol. 155* (1999), 338–343.

[74] Lillo, F. D., Cencini, M., Durham, W. M., Barry, M., Stocker, R., Climent, E., and Boffetta, G. Turbulent fluid accelaration generates clusters of gyrotactic microorganisms. *Physical Review Letters 112* (2014), 1–5.

[75] Loefer, J. B., and Mefferd, R. B. Concerning pattern formation by free-swimming microorganisms. *American Society of Naturalists 86* (September 1952), 325–329.

[76] Loefer, J. B., and Mefferd, R. B. Pattern formation in concentrated particulate suspension. *American Society of Naturalists 87* (March 1953), 117–118.

[77] Ma, Z., Wu, Y., Jin, J., Yan, J., Kuang, S., Zhou, M., Zhang, Y., and Guo, A.-Y. Phylogenetic analysis reveals the evolution and diversification of cyclins in eukaryotes. *Molecular Phylogenetics and Evolution 66* (2013), 1002–1010.

[78] Mardia, K. V., and Jupp, P. F. *Directional Statistics*, 2 ed. John Wiley & Sons Ltd., 2000.

[79] Martinez, V. A., Besseling, R., Croze, O. A., Tailleur, J., Reufer, M., Schwarz−Linek, J., Wilson, L. G., Bees, M., and Poon, W. C. K. Different dynamic microscopy: A high−throughput method for characterizing the motility of microorganisms. *Biophysical Journal 103* (2012), 1637–1647.

[80] Mendoza, H., Carmona, L., ao, P. A., Freijanes, K., and de la Jara, A. Variation in lipid extractability by solvent in microalgae. Additional criterion for selecting species and strains for biofuel production from microalgae. *Bioresources Technol. 197* (2015), 369–374.

[81] Merah, M., Abdelmalik, T. A., and Larbi, B. H. R−peaks detection based on stationary wavelet transform. *Computer Methods and Programs in Biomedicine 121* (2015), 149–160.

[82] Misiti, M., Misiti, Y., Oppenheim, G., and Poggi, J. .-M. *Wavelet And Their Applications*, 1 ed. ISTE, 2007.

[83] Okon, Y., Cakmakci, L., Nur, I., and Chet, I. Aerotaxis and chemotaxis of *Azospirillum brasilense*: A note. *Microb. Ecol. 6* (1980), 277–280.

[84] Pedley, T. J., Hill, N. A., and Kessler, J. O. The growth of bioconvection patterns in a uniform suspension of gyrotactic micro−organism. *J. Fluid Mech. 195* (1988), 223–237.

[85] Pedley, T. J., and Kessler, J. O. The orientation of spheroidal microorganisms swimming in a flow field. *Proc. R. Soc. London B 231* (1987), 47–70.

[86] Pedley, T. J., and Kessler, J. O. A new continuum model for suspensions of gyrotactic micro-organisms. *J. Fluid Mech. 212* (1990), 155–182.

[87] Pedley, T. J., and Kessler, J. O. Hydrodynamic phenomena in suspensions of swimming microorganisms. *Annu. Rev. Fluid Mech. 24* (1992), 313–358.

[88] Platt, J. R. "Bioconvection Patterns" in cultures of free-swimming organisms. *Science 133* (1961), 1766–1767.

[89] Plesset, M. S., and Whipple, C. G. Viscous effects in Rayleigh−Taylor instability. *Phys. Fluids 17*, 1 (1974), 1–7.

[90] Plesset, M. S., and Winet, H. Bioconvection patterns in swimming microorganism cultures as an example of Rayleigh−Taylor instability. *Nature 248* (1974), 441–443.

[91] Pons, A. J., S. F. B. M. A., and Søresen, P. G. Quantitative analysis of chemoconvection patterns in the methylen−blue−glucose system. *J. Phys. Chem.B. 106* (2002), 7252–7259.

[92] Popova, T. P., Zaharinov, B. S., Marinova−Garvanska, S. M., and Baykov, B. D. Microbiological evalution of sewage sludge in terms of possibilities of application in soil as a fertilizer. *International Journal of Current Microbiology and Applied Sciences 3*, 3, 984–990.

[93] Porter, J. R. Antony van leeuwenhoek: Tercentenary of his discovery of bacteria. *Bacteriological Reviews 40*, 2, 260–269.

[94] Purcell, E. M. Life at low Reynolds number. *American Jornal of Physics 45*, 1, 3–11.

[95] R. B. Forward, J. Negative phototaxis in crustacean larvae: Possible functional significance. *J. Exp. Mar. Biol. Ecol. 16* (1974), 11–17.

[96] Rallison, J. M. The effect of the Brownian rotations in the a dilute suspension of rigid particles of arbitrary shape. *J. Fluid Mech. 84*, 2 (1978), 237–263.

[97] Rüffer, U., and Nultsch, W. High-speed cinematographic analysis of the movement of *Chlamydomonas*. *Cell Motility 5* (1985), 251–263.

[98] Roberts, A. M., and Deacon, F. M. Gravitaxis in motile micro−organisms: the role of the fore−aft body asymmetry. *J. Fluid Mech. 452* (2002), 405–423.

[99] Rothschild. Measurement of sperm activity befor artificial insemination. *Natural Publishing Group 163* (March 1949), 358–359.

[100] Schmid, P. J., and Henningson, D. S. *Stability And Transition In Shear Flows*, 1 ed. Springer, 2001.

[101] Schopf, J. W. Fossil evidence of archaean life. *Phil. Trans. R. Soc. B. 361* (2006), 869–885.

[102] Shaevits, J. W., Lee, J. Y., and Fletcher, D. A. Spiroplasma swim by a processive change in body helicity. *Cell 122* (2005), 941–945.

[103] Sifuzzaman, M., Islam, M. R., and Ali, M. Z. Application of wavelet transform and its advantages compared to Fourier transform. *The Journal of Physical Sciences 13* (2009), 121–134.

[104] Silflow, C. D., and Lefebvre, P. A. Assembly and motility of eukaryotic cilia and flagella. Lessons from *Chlamydomonas reinhardtii*. *Plant Physiology 127* (2001), 1500–1507.

[105] Son, K., Brumley, D. R., and Stocker, R. Live from under the lens: exploring microbial motility with dynamic imaging and microfluids. *Nature Reviews Microbiology 13* (2015), 761–775.

[106] Spurk, J. H., and Aksel, N. *Fluid Mechanics*, 2 ed. Springer−Verlag Berlin Heidelberg, 2008.

[107] Stocker, R., and Durham, W. M. Tumbling for stealth. *Sience 325* (2009), 400–402.

[108] Taylor, B. L., Zhulin, I. B., and Johnson, M. S. Aerotaxis and other energy−sensing behavior in bacteria. *Annu. Rev. Microbiol. 53* (1999), 103–128.

[109] Thomas, G. B., and Finney, R. L. *Calculus And Analytic Geometry*, 8 ed. Addison−Wesley Publishing Company, Inc., 1992.

[110] (translated by Georg Zimmermann), A. H. On the theory of orthogonal function systems. *C. Heil and D.F. Walnut (eds.), Fundamental Papers in Wavelet Theory, Princeton University Press* (2006), 155–188.

[111] Vanderbei, R. J. *Linear Programming Foundation And Extension*, 4 ed. Springer, 2014.

[112] Verma, R., and Goel, A. Wavelet application in fingerprint recognition. *IJSCE 1* (2011), 129–134.

[113] Viswanathan, P., and Krishna, P. V. Morlet wavelet fingerprint invariant automated authentication system. *IJRTET 4*, 1 (2010), 1–5.

[114] Wager, H. On the effect of gravity upon the movements and aggregation of the *Euglena viridis*, *Ehrb.*, and other microorganisms. *Philos. Trans. R. Soc. London B 201* (1911), 334–390.

[115] Williams, C. R., and Bees, M. A. Photo−gyrotactic bioconvection. *J. Fluid Mech. 678* (2011), 41–86.

[116] Williams, C. R., and Bees, M. A. A tale of three taxes: photo−gyro−gravitactic bioconvection. *J. Exp. Biol. 214* (2011), 2398–2408.

[117] Woese, C. R. On the evolution of cells. *PNAS 99* (2002), 8742–8747.